71-27,606

CRITES, Thomas Richard, 1942-
BACKSCATTER OF NORMALLY INCIDENT INTERMEDIATE ENERGY BREMSSTRAHLUNG FROM SEMI-INFINITE MEDIA OF VARYING ATOMIC NUMBER.

The University of Oklahoma, Ph.D., 1971
Engineering, nuclear

University Microfilms, A XEROX Company, Ann Arbor, Michigan

THE UNIVERSITY OF OKLAHOMA

GRADUATE COLLEGE

BACKSCATTER OF NORMALLY INCIDENT INTERMEDIATE ENERGY BREMSSTRAHLUNG FROM SEMI-INFINITE MEDIA OF VARYING ATOMIC NUMBER

A DISSERTATION

SUBMITTED TO THE GRADUATE FACULTY

in partial fulfillment of the requirements for the

degree of

DOCTOR OF PHILOSOPHY

BY

THOMAS R. CRITES

Norman, Oklahoma

1970

PLEASE NOTE:

Some pages have light
and indistinct print.
Filmed as received.

UNIVERSITY MICROFILMS.

BACKSCATTER OF NORMALLY INCIDENT INTERMEDIATE

ENERGY BREMSSTRAHLUNG FROM SEMI-INFINITE MEDIA

OF VARYING ATOMIC NUMBER

APPROVED BY

Robert G. Nelson

H. J. Fischbeck

Larry Canter

William D. Burnett

James M. Robertson

DISSERTATION COMMITTEE

ACKNOWLEDGMENTS

The author expresses his sincere appreciation to Dr. Robert Y. Nelson, dissertation advisor, and William D. Burnett, research advisor, for their valuable guidance, suggestions, and review throughout this research, which could not have been meaningfully completed without their assistance.

The author is very grateful to his wife, Frances, for the great personal efforts she has made in seeing this work through, and her excellent support in typing and proofreading.

The author is deeply indebted to William H. Kingsley and Harold L. Rarrick for their efforts in making possible the work arrangement under which the dissertation was completed.

Gratitude is extended to the many Sandia Corporation personnel who aided in this project, in particular: Bill L. O'Neal and Donald E. Amos for many fruitful discussions; James H. Renken, Joann H. Flinchum and Kenneth G. Adams for the great amount of work they did in making possible the computer comparisons; Lawrence D. Posey, Jesse

E. Harness, and Dan D. Craig for their support in obtaining data on the 3.5 and 10.5 MeV flash x-ray machine; Robert W. Mottern and S. A. Ravenbyrne at the Van de Graaff facility; and Alvie A. Barrett for his able shop assistance.

Financial aid for this portion of the requirements for the Doctor of Philosophy Degree at the University of Oklahoma was furnished in part by a United States Public Health Service Grant and in major by a United States Atomic Energy Commission prime contractor, Sandia Laboratories, Albuquerque New Mexico.

TABLE OF CONTENTS

LIST OF TABLES

LIST OF TABLES (cont'd)

LIST OF ILLUSTRATIONS

LIST OF ILLUSTRATIONS, (cont'd)

LIST OF ILLUSTRATIONS, (cont'd)

LIST OF ILLUSTRATIONS, (cont'd)

LIST OF ILLUSTRATIONS, (cont'd)

1. INTRODUCTION

The development of x-ray machines of greater output and the extension of accelerators for use outside experimental laboratories, require an accurate knowledge of the surrounding radiation fields. The radiation field about these facilities consists of two sources: transmitted and scattered radiation. Transmission and forward scattering (i.e. build-up) are fairly well documented in low to intermediate energy range photons.

Less well established is scattering in a backward direction, or backscattering. Though very little experimental data exist on the backscattering of bremsstrahlung sources (1), the backscattering of gamma rays from radioisotopes has been studied for a great many sources and scattering materials, and these efforts will be reviewed in Section 2.

The term "albedo" is generally accepted in the study of backscatter as the ratio of the radiation fluence reflected from a surface to the fluence incident on that surface. Unlike the reflection of light (where the term albedo arises) which can be considered a surface phenomenon, photons of MeV energies are much more penetrating. The albedo considered in radiation research takes into account photons that are scattered back out of the medium from several mean free paths below the surface. The albedo determined in the present research effort is an "effective" albedo, consisting of characteristic x-rays, singly scattered and multi-scattered photons, and bremsstrahlung and annihilation radiation from pair production interactions. No attempt has been made to differentiate the contributions of each method, but rather the effort was to determine the overall fluence to obtain the differential albedo from the surface of the backscattering material.

The dissertation investigation studied the angular dependency of backscatter of normally incident broad beam bremsstrahlung of varying energies reflecting from surfaces of varying atomic number. The bremsstrahlung source machines used are discussed in Section 5.2. The reflected fluence was measured by LiF crystal thermoluminescent dosimeters, placed in highly collimated, copper-lined, lead shields to monitor the angular distribution. The scattering media used are common shielding materials of sufficient size to represent semi-infinite bodies, meaning that any increase in slab area or thickness will not result in a change in albedo. The materials used in this work are concrete, steel, and lead.

An extensive comparison of experimental results with results obtained by other methods is made. Computer methods have primarily been used to estimate the extent of backscatter, particularly when complicated incident spectra are involved. Two different computer methods, a discrete ordinates solution to the photon transport equations and Monte Carlo, are used for comparison to the experimental data obtained. As the two computer methods approach the backscatter problem very differently, their results predictably differ somewhat from each other and from the data obtained. These differences are examined in the dissertation.

Nomenclature used in this dissertation is based on the International Commission of Radiological Units and Measurements recommendations in general (2) and the Oak Ridge National Laboratory Neutron and Gamma-Ray Albedos Report (1) in particular.

2. HISTORICAL REVIEW

As forward scattering is well considered elsewhere (3, 4, 5, 6, 7, 8, 9, 10, 11), the following discussion will consider only those experiments which center on backscatter.

2.1 EXPERIMENTAL

The first studies of backscatter gamma-rays were probably made by Imbert and Bertin-Sans in 1896 (12). This and other studies led to the famous work by Compton (13) in 1923 from which he developed his quantum theory of x-ray scattering. Klein and Nishina (14) in 1929 obtained a general expression for the Compton differential scattering and collision cross-sections for initially unbound and stationary electrons. It was not until the development of more sensitive detection equipment and larger sources in the nineteen-fifties, that gamma-ray scattering was studied experimentally in greater depth.

In 1954 Hayward and Hubbell (15), using a collimated cobalt-60 source, studied the energy and scattering angle distribution from wood and steel wool with a collimated scintillation detector. Also in that year, Hine and McCall (16) studied the backscatter of gamma rays from lead, iron, aluminum, wood, and water using mercury-203, cesium-137, and cobalt-60 point sources in contact with the backscattering material. A scintillation gamma-ray spectrometer was again used to investigate the intensity and energy of the back-scattered radiation. These experiments demonstrated the

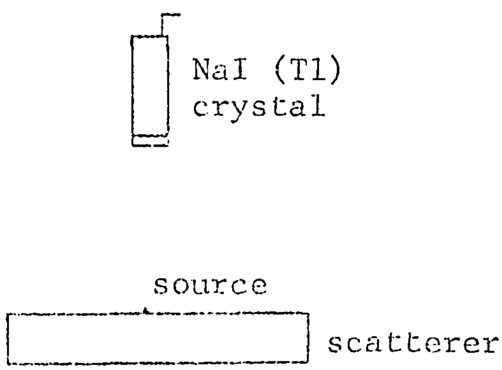

Figure 1. Relative position of detector, source, and scattering medium, Hine and McCall.

anistropy of single-scattering and the isotropy of multi-scattering; the significance of fluorescent radiation for matter of high atomic number, such as lead; and the dependence on incident energy and angle. By varying the thickness of backscatter material, Hine and McCall observed a variation in the amount of radiation scattered.

Bulatov and Garusov (17) in 1958 studied a very wide range of backscattering materials using cobalt-60 and gold-198 sources of gamma-rays located some distance from the scattering media. By collimating the beam they were able to vary the angle of incidence of the gamma-rays and study this effect upon backscatter intensity. They, as did Hine and McCall, varied the thickness of the back-scatterer and then expressed the dependence of the energy albedo on scatterer thickness as

$$\eta(d) = \eta(\infty)(1 - e^{-d/a}) \qquad \text{Eq. 2.1}$$

where:

$\eta(d)$ = the value of the albedo for a scatter thickness, d

$\eta(\infty)$ = the limiting value of the albedo for "infinite" scatterer thickness

d = the scatterer thickness in gm/cm^2

a = a constant

From their work, Bulatov and Garusov formed an empirical relation to describe the variance of the albedo as a function of the primary beam energy, E; the angle of incidence at the surface of the scatterer, α; the effective atomic number, Z, of the scatterer material; and its density, ρ,

$$\eta(E,\alpha,Z,\rho) = 3.2 \frac{1}{E} \frac{1}{\cos \alpha} \frac{\rho}{Z^2} \pm 20\% \quad \text{Eq. 2.2}$$

Hyodo (18), in 1962, extended the work of Hine and McCall. He measured the spectra of backscattered radiation from semi-infinite slabs by means of a scintillation spectrometer as a function of the measuring angle. His sources were cobalt-60 and cesium-137 in close contact to slabs of paraffin, aluminum, iron, tin, and lead. Hyodo's work gives a comprehensive study of the energy and number albedos, the angular distributions of scattered energy and number of photons, and the energy distributions for the combinations of the gamma sources and scatterer materials used. Hyodo also studied the effect of thickness of scatterer material upon his results and, because of his geometry, arrived at a slightly lower value for "infinitely thick" than did Bulatov and Garusov. Hyodo's later work with Fujita et al. (19) and Nakamura (20) studied in greater detail the effect of scatterer thickness using iron as a backscatterer and cobalt-60 as a source in close contact with the iron. They arrived at the empirical relationship

$$A(\theta,x) = A(\theta,\infty)(1 - e^{-cx}) \qquad \text{Eq. 2.3}$$

where:

$A(\theta,x)$ = the fraction of photons emergent at angle θ per steradian for one primary photon incident to the scatterer of thickness x

x = the slab thickness

Their value for "c" differs from that of "$\frac{1}{a}$" in the Bulatov-Garusov development by about a factor of two. This study of the effect of thickness on backscattering was extended in 1967 by Hyodo, Matsumoto, and Mizukami (21) to cover polyethylene, aluminum, and lead, still using the point cobalt-60 source in contact with the slab. A least squares fit of their data against

$$A(x) - b = [A(\infty) - b](1 - e^{-cx}) \qquad \text{Eq. 2.4}$$

was made with good result. The terms here are the same as in Eq. 2.3, with "c" and "b" constants dependent upon experiment design. Their work, along with that of Bulatov and Garusov indicated that a thickness of material greater than two mean free paths of the source radiation would constitute an "infinite" thickness.

The first detailed backscatter work done with concrete as the scatter material was carried out in 1963 by Clarke and Batten (22). They used uncollimated point sources of cobalt-60 and iridium-192 at varying heights above a concrete slab. An uncollimated ionization chamber detector was placed at various distances from the source and the concrete to determine the effect of concrete on the dose measured. This work was extended by Hendee and Ellis (23) in 1965,

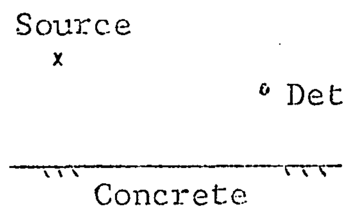

Figure 2. Experimental arrangement used by Clarke and Batten

using uncollimated cobalt-60 and cesium-137 sources scattered from semi-infinite slabs of concrete, lead, and water.

Jones, et al., (24, 25), in 1964, using cobalt-60 and cesium-137 as plane-parallel beam sources, studied the backscatter from concrete, aluminum, and steel as a function of the incident and the reflected angle with a scintillation detector. From their results, Jones, et al., developed the empirical formula

$$A_d(\Omega) = c \exp(-m\theta_s) + b' \qquad \text{Eq. 2.5}$$

where:

$A_d(\Omega)$ = the differential dose-rate ratio

$$A_d(\Omega) = \frac{D}{D_o} \qquad \text{Eq. 2.6}$$

with:

D = the reflected dose per unit solid angle at d

D_o = the incident dose rate at the center of the slab's surface

"c", "m", and "b" in Eq. 2.5 are constants which they determined for each source, backscatterer, and incident angle. θ_s was the Compton scattering angle. Steyn and Andrews (26) in their experiments of 1967, did a very complete study, extending this work using gold-198, cesium-137, and cobalt-60 point sources one meter from graphite, aluminum, high density concrete, iron, nickel, tin, lead, and uranium. A highly collimated scintillation spectrometer was used as the detector to determine angular and energy dependence of the backscattered photons. The expression chosen by Steyn to best fit his data is

$$d\,A_D = a_o + a_1 x + a_2 x^2 \qquad \text{Eq. 2.7}$$

where:

$d\,A_D$ = the differential dose albedo;

$$x = 1 + \cos \theta_s \qquad \text{Eq. 2.8}$$

θ_s = scattering angle as in Figure 5.

"a_o", "a_1", and "a_2" are constants dependent upon the conditions of the experiment.

The integrated dose albedo empirical expression is represented by

$$\alpha_D = 3a_o + a_1 + \frac{a_2}{2} \qquad \text{Eq. 2.9}$$

where the constants have the same values as in Eq. 2.7. Both equations 2.7 and 2.9 neglect fluorescent x-ray dose contributions.

Data in the literature concerning the backscatter of x-rays in the source energy regions covered by the above papers show similar results (27, 28, 29, 30, 31, 32, 33).

The backscatter of high energy bremsstrahlung was first studied by Kruglov and Lopatin (34) in 1959, when they were concerned about energy losses in using absorption calorimetry for calibrating the beam output of an 85-MeV accelerator.

Pruitt (35) in 1964 was the first to consider backscatter from megavolt photons in the albedo sense. Using a scintillation spectrometer as a detector and backscatter media of carbon, magnesium, copper, tin, and lead, he determined the energy albedo for normally incident bremsstrahlung with a maximum photon energy of 90 MeV, and for lead at 25, 50, and 170 MeV maximum.

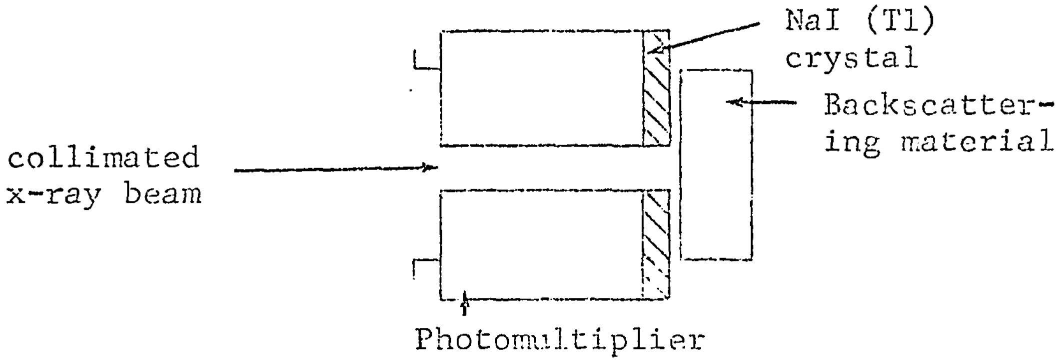

Figure 3. Experimental arrangement used by Pruitt.

In 1967, Sugiyama and Tomimasu (36), using lower energy (11.3 to 23.2 MeV maximum) bremsstrahlung, studied the angular distribution of the energy albedo from lead, copper, and Duralumin.

Karzmark and Capone (37), in 1968, performed a cursory look at radiation scattered from concrete by a 6 MeV linear accelerator.

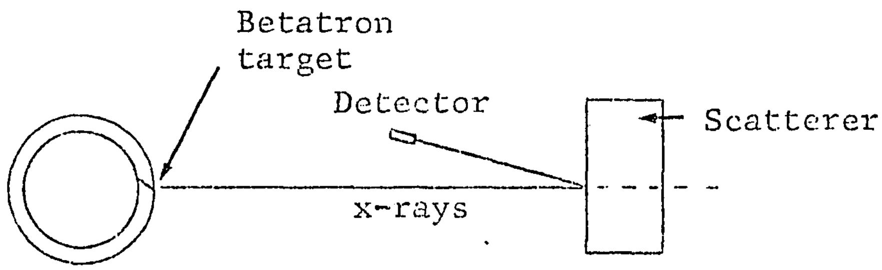

Figure 4. Experimental arrangement used by Sugiyama and Tomimasu.

2.2 NUMERICAL

The development of numerical estimates of albedo followed the gathering of experimental data. After the work of Compton (13) and Klein and Nishina (14) which described the basic scattering interaction, several years passed until sufficient data was collected to formulate empirical estimates. During this period the Monte Carlo technique of random sampling and high speed computers were developed, presenting another method of numerically estimating the photon backscatter from a surface. Hayward and Hubbell (38) were among the first to employ the Monte Carlo technique; using a desk calculator they estimated the albedo of various materials for 1 MeV photons in 1954. The next year, Perkins (39) with an IBM computer repeated their process with normally incident photons of 1 MeV on concrete. Berger's

(40) Monte Carlo calculations in 1957 were based on an experimental design (Figure 2) to be tested eight years later by Clarke and Batten (21).

Wells (41) in 1959, developed, by Monte Carlo techniques, a very complete study of the angular distribution and energy spectra of gamma-ray scatter from concrete. He postulated source energies of 0.6 MeV to 7.0 MeV incident at five different angles to the slab. His calculations include the effects of single and multiple scatter interactions, the photoelectric effect, and pair production reactions. As the cross-section data have since been largely revised (42), Wells repeated his analysis in 1964 (43). In 1962, Davisson and Beach (44) extended this type of calculation to include water, iron, and lead as backscatter media. In 1963, two studies were made which probably represent the best Monte Carlo examinations of photon backscatter from concrete available to date. Raso (45) and Leimdorfer (46) each worked on the reflection of photons from concrete in the energy range 1 to 10 MeV. While Raso allowed the angle of incident to vary and studied that effect, Leimdorfer used normal incidence and studied the variance of reflector thickness on albedo. Both considered photoabsorption, Compton interactions, and pair production. Their works are considered as standards against which experimental results are often compared. Each of the above works considered only monoenergetic photons.

Bulatov and Leipunski (47) in 1961 were among the earliest to formulate quantitative expressions for albedo from experimental data. Based on experimental information gathered earlier by Bulatov (17), they expressed number and energy albedo as a function of build-up and build-up as a function of media thickness. Later in 1966, Bulatov (48) developed engineering formulas and nomograms for determining quantities of scattered gamma-radiation. These were based on three geometries: a narrow beam striking a scattering material, an isotropic source in contact with a surface, and a plane unidirectional flow of gamma quanta. Values are given primarily for cobalt-60 and gold-198 sources scattered from lead, iron, and aluminum. Some values for carbon and concrete are included.

In 1963, Chilton and Huddleston (49) developed a semi-empirical formula for the differential dose albedo from gamma-rays incident on concrete, which has been very useful in this field. The energy ranges covered are from 0.2 to 10 MeV in a geometry as shown in Figure 5.

Their development considers single scattering as expressed by the Klein-Nishina representation and pair production annihilation and multiple scattering components

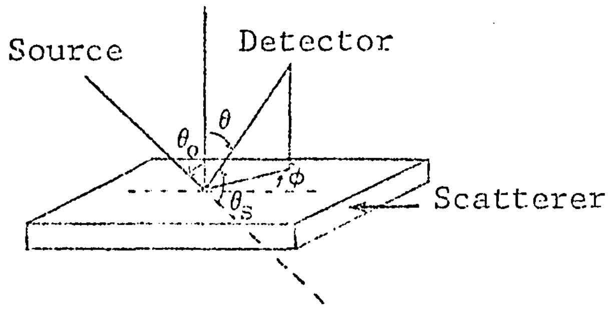

Figure 5. Relative position of source, detector, and scatterer for the Chilton-Huddleston development.

as isotropic sources at the surface of the backscatterer. The relationship they derived is given by

$$\alpha_d(\theta_o, \theta, \phi) = \frac{C\ K(\theta_s)\ .10^{26} + C'}{1 + \cos\ \theta_o\ \sec\ \theta} \qquad \text{Eq. 2.10}$$

where:

$\alpha_d(\theta_o, \theta, \phi)$ = the differential dose albedo

C and C' = parameters to be adjusted for each incident energy

$K(\theta_s)$ = the Klein-Nishina value of the energy scattering cross-section per electron

$\cos\ \theta_s = \sin\ \theta_o\ \sin\ \theta\ \cos\ \phi - \cos\ \theta_o\ \cos\ \theta$

Values for C and C' are given in their report. A number of comparisons are made with the results of this equation and results from Monte Carlo estimates and existing experimental data. Chilton (50) extended this work in 1965 to calculate the total albedo. Also in 1965, Chilton and Davisson (51) published values for the constants in Equation 2.10 for concrete, water, iron, and lead.

Huddleston (52) in 1964 updated some of the original Chilton-Huddleston values and examined more closely those values near gold-198, cesium-137, cobalt-60, and sodium-24 gamma energies. With Shoemaker, he (53) set up a series of isoalbedo contours for engineering applications. In 1966, due to more accurate Monte Carlo information, Chilton (54) revised their formula to more closely represent available data. The new formula is

$$\alpha(\theta_o,\theta,\phi) = F(\theta_o,\theta,\phi)\,\frac{C.10^{26}K_e(E_o,\theta_s) + C'}{1 + \cos\theta_o \sec\theta\left[1 + 2E_o(1 - \cos\theta_s)\right]^{\frac{1}{2}}}$$

Eq. 2.11

where

$$F(\theta_o, \theta, \phi) = A_1 + A_2(1-\cos\ \theta_o)^2 + A^3(1-\cos\ \theta)^2$$

$$+ A_4(1-\cos\ \theta_o)^2(1-\cos\ \theta)^2 + A_5(1-\cos\ \theta_o)(1-\cos\ \theta)(1-\cos\ \phi)$$

Eq. 2.12

and the other parameters are as defined for the original equation 2.10. Thus far, only values for the constants with cesium-137 and cobalt-60 sources have been established. In 1967 Chilton (55) revised these particular numbers.

Recently several other techniques have been developed to estimate albedo (56, 57, 58, 59) and the method of discrete ordinates (as developed by Carlson [60]) deserves special mention. For some time neutron distributions have been calculated by discrete ordinates methods, while photon distributions had been calculated by Monte Carlo methods. In 1965 Lathrop (61) investigated the possibility of using the faster (computer time-wise) discrete ordinates method for photon distribution calculations. His investigation showed excellent agreement with Monte Carlo methods and pointed the way for further development of the discrete ordinates method. Renken and Adams (62) in 1967 expanded

Lathrop's work on photon scatter. Multiple scattering and fluorescence are extensively covered.

Pair production annihilation contributions were written into the program two years later (63). Their program (DTF) allows a rapid calculation of photon densities as a function of angle, radius, and energy. Input parameters may be widely varied with little resultant run-time penalty.

2.3 SUMMARY

Except for the few examples discussed, backscatter of bremsstrahlung above a few MeV has not been investigated experimentally. The experimental configuration used by Pruitt did not allow the investigation of angular distribution. Both works were somewhat limited as to the energy range studied and choice of backscatterer materials. The present research provides information on energy regions not yet studied, and develops a method for determining albedo dose and angular distributions from pulse-type bremsstrahlung sources.

The notation used in this section is in each case that of the author discussed and definitions are given at that point.

3. THEORETICAL CONSIDERATIONS

3.1 INTRODUCTION

As the research topic deals with a continuous spectrum bremsstrahlung having a leading spectrum edge of intermediate energy (1 to 10 MeV), all the familiar photon interactions are of interest.

In the lower energy regions of the bremsstrahlung spectrum, photoelectric absorption is the predominant interaction. Electrons released by the photoelectric effect are of low energy and are not considered further. (Their ionization losses far outweigh their radiation loss.) In filling the K- and L- orbital vacancies left by photoelectric absorption, K- and L- x-rays, respectively, are given off. These x-rays are given off isotropically from the point they arise.

Characteristically a sharp drop occurs in the absorption cross-section of the material at energies just below the capture edge. The x-rays generated fall in this "depressed" cross-section region and consequently contribute significantly to backscatter yields.

Compton interactions are highly anisotropic, with angle and energy distributions calculated by Klein-Nishina formulas. In high energy Compton scattering events, the scattered photon distribution is largely in the forward direction. However, multiple Compton scattering events occur to create an isotropic photon fluence from this source. Large energy transfers can occur to create Compton electrons. These electrons can then give up their energy through bremsstrahlung which will add to the photon fluence in the backscatter media.

Photons of energies greater than a few MeV can react in the field of a nucleus or an electron to create an electron-positron pair. The cross-section for these reactions increases with incident photon energies and increasing target mass number. The energy of the photon (in excess of that required for formation of the electron-positron pair) goes into kinetic energy of the created pair (or triplet if in the field of an electron). The angular distribution of the positron and negatron is mainly forward for incident photons of high energy. Each gives up its kinetic energy by ionization, excitation, and bremsstrahlung. As the positron slows down it will recombine with an electron giving rise to two 0.511 MeV annihilation photons at that point. The bremsstrahlung and annihilation radiation will contribute isotropically to the backscatter fluence.

Coherent, or Rayleigh, scattering occurs in the energy regions where atomic electron binding effects must be considered in Compton scattering. The photon does not transfer energy to the atom while it is interacting. In the high energy regions where Rayleigh scattering need be considered (around 1 MeV) the majority of the photons are scattered by less than 5° and in the lower energy regions the cross-section for photoelectric absorption greatly overshadows the coherent scattering effect.

The energy region employed for this study encompasses the photonuclear absorption resonance regions. However, the photonuclear cross-sections of the backscatter materials studied are small and the resultant photoneutron fluence would be quite small relative to the photon fluence. The effect of the photoneutron fluence on the detectors used will be discussed later in this section.

Other photon interactions of minor importance, resonance scattering and Thomson scattering by the nucleus, Compton scattering by nucleons, meson production, resonance scattering associated with meson production, Delbruck scattering, and nucleon-antinucleon production, will not be considered (3, 64).

The detection instruments used in this work are thermoluminescent crystals and a scintillation spectrometer. Each is differential with respect to angular distribution; i.e. neither covers the entire emission field in the experimental set-up chosen, and the spectrometer is differential also with respect to energy. Methods of using the output of these detectors in a manner suitable for comparison with prior numerical estimates will be discussed in greater depth.

Each of these topics will now be reviewed in depth to assess their contribution to albedo as considered in this study. It is not the purpose of the following sections to derive a rigorous theoretical solution to the backscattering of intermediate energy bremsstrahlung, but rather they are given in an effort to point out sources of photons which contribute to the backscatter field and consider their relative importance.

3.2 PHOTON INTERACTIONS

3.2.1 Photoelectric Absorption (3, 11)

As pointed out in the introduction, photoelectric absorption is the predominant interaction for photons of low energy. The cross-section for this reaction is heavily Z dependent. For high Z target nuclei, photoelectric absorption may remain the predominant interaction to about

900 KeV. Although no longer the predominant interaction, a cross-section does continue to exist for photoelectric absorption to high photon energies (1.41×10^{-2} barn/atom at 100 MeV in Pb [65]). This reaction will occur primarily with the low energy region of the incident bremsstrahlung and with photons being scattered back from some depth in the backscatter medium.

The photoelectric effect is not easily treated theoretically due to bound electron considerations and outer orbital shielding effects. Estimates have been made for cross-sections in the energy range 0.2 MeV to 100 MeV using

$$\tau_K \approx Z^5 \sum_{N=1}^{4} \frac{a_n + b_n Z}{1 + c_n Z} E_o^{-p_n} \text{ barn/atom} \quad \text{Eq. 3.1}$$

where:

τ_K = the K-shell photoelectric cross-section in barns per atom

Z = the atomic number of the target nuclei

a_n, b_n, c_n, p_n = constants chosen for an empirical fit

To add in the effect of other orbital electron interactions

$$\frac{\tau_{pe}}{\tau_K} \approx 1 + 0.01481 \ln^2 Z - 0.000788 \ln^3 Z \qquad \text{Eq. 3.2}$$

is used where:

τ_{pe} = the total photoelectric cross-section in barns per atoms

In lower energy ranges absorption edges vary the cross-section greatly. At these edges the cross-section shows discontinuous jumps because the photon energy becomes smaller than the binding energy of some of the electrons. At this point the number of electrons which the photon is energetically capable of ejecting is suddenly decreased.

The photoelectrons resulting from this interaction tend to be ejected at right angles to the incident photon path, showing preference for the forward direction with increasing photon energy.

After the ejection of an orbital electron, a vacancy exists which must be filled. Generally an electron in a higher orbit gives up energy to drop into the deficient orbit. The energy given up is in the form of characteristic x-rays and can be estimated by

$$h\nu = 13.6\, Z^2 \left[\frac{1}{n_1^2} - \frac{1}{n_2^2}\right] \text{eV} \qquad \text{Eq. 3.3}$$

where:

$h\nu$ = the emitted photon energy in eV

n_1 and n_2 are the principle quantum numbers for the initial and final electron vacancies. This radiation is given off in a truly isotropic distribution. The number of emitted photons by this process is dependent upon incident photon energy and the target material; the energy of each photon is dependent only upon the material. This energy range is such that the primary interactions these x-rays will undergo is photoelectric absorption. They are thus attenuated approximately exponentially from the point they arise until they exit from the surface of the backscatter media.

From these considerations, one can now derive an expression for the contribution to the backscatter fluence due to the photoelectric effect

$$
{}_{pe}\phi_N\ (\phi_o, E_o, Z, r) = \frac{\rho N.Z}{4\Pi r^2 M} \int_d \int_A \Big\{ \phi_o \exp[-\mu_t(E_o Z)d]\ \tau_{pe}(E_o Z)
$$

$$
+ \phi_c(d)\ \tau_{pe}(E_c Z) + \phi_{pp}(d)\ \tau_{pe}(0.511, Z) \Big\}
$$

$$
\Big[\exp[-\mu_t(E_{pe}, Z)d(\sec\ \theta_s)] \Big]\ dd\ dA \qquad \text{Eq. 3.4}
$$

where:

$_{pe}\phi_N(\phi_o, E_o, Z, r)$ = the number fluence from the photoelectric effect at some point r from the surface of a backscatter material with atomic number Z

ϕ_o = the incident fluence of photons at energy E_o

$\tau_{pe}(E_o, Z)$ = the photoelectric microscopic cross-section of the incident bremsstrahlung fluence

$\tau_{pe}(E_c, Z)$ = the photoelectric microscopic cross-section of photons having undergone Compton scattering interactions

$\tau_{pe}(0.511, Z)$ = the photoelectric cross-section of photons created by pair production

d = the depth in the backscatter media being considered

$\mu_t(E_o, Z)$ = the total attenuation coefficient for the incident bremsstrahlung fluence

$\phi_c(d)$ = the fluence due to Compton scattered photons at a depth d

$\phi_{pp}(d)$ = the fluence due to pair production at d

A = incident beam area

r is assumed much greater than the beam radius at the surface of the backscatterer.

The energy fluence under the same conditions is found to be

$$_{pe}\phi_N(\phi_o, E_o, Z, r) = {}_{pe}\phi_N \sum_n h\nu \qquad \text{Eq. 3.5}$$

where: $_{pe}\phi_N$ is given by Eq. 3.4 and $h\nu$ by Eq. 3.3

Using a detection system which is capable of differentiating energies, one would expect to observe an energy grouping due to these characteristic x-rays.

Fink, et al. (66) list extensive experimental results on fluorescence yields and energies.

3.2.3 Compton Scattering (3,11)

In the energy region approximately 0.5 to 5 MeV the dominant photon interaction is incoherent scattering from electrons, the Compton effect (67). Over this energy range the cross-section for the Compton effect is given by the Klein-Nishina equation

$$_e\sigma = \frac{2\Pi e^4}{m_o^2 c^4}\left\{\frac{1+\alpha}{d^2}\,\frac{2(1+\alpha)}{1+2\alpha} - \frac{1}{\alpha}\ln(1+2\alpha)\right.$$

$$\left. + \frac{1}{2\alpha}\ln(1+2\alpha) - \frac{1+3\alpha}{(1+2\alpha)^2}\right\}\frac{cm^2}{electron} \qquad \text{Eq. 3.6}$$

where:

$_e\sigma$ = the probability of removal of a photon from a collimated beam while passing through an absorber containing one electron/cm^2

e = the electronic charge (4.8×10^{-10} statcoulomb)

m_o = the electron mass (9.1083×10^{-28} gm)

c = the velocity of light (2.998×10^{10} cm/sec)

and $$\alpha = \frac{E_o}{m_o c^2} \qquad \text{Eq. 3.7}$$

where E_o is the incident photon energy. This equation is based on interaction with an unbound electron. In those cases where the photon energy is comparable with the binding energy of the atomic electrons, the photoelectric cross-section usually greatly exceeds the Compton scattering cross-section (11) which is given by

$$
{}_e\sigma_s = \frac{2\pi e^4}{m_o^2 c^4}\left[\frac{4\alpha^2}{3(1+2\alpha)^3} - \frac{(1+\alpha)}{\alpha^2(1+2\alpha)^2}(1+2\alpha-2\alpha^2) + \frac{1}{2\alpha^3}\ln(1+2\alpha)\right] \qquad \text{Eq. 3.8}
$$

with terms as defined in Eq. 3.7.

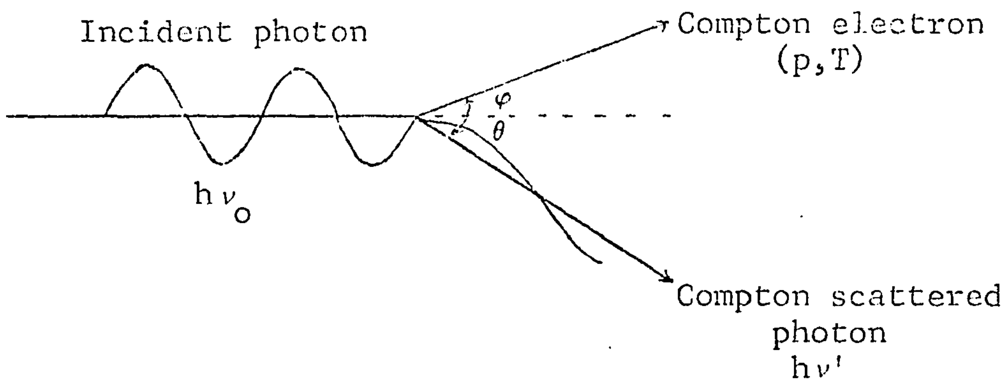

Figure 6. Compton Scattering

The energy of the incident photon will be shared after the collision by a scattered photon and the struck electron. The energy of the scattered photon is given by

$$h\nu' = \frac{m_o c^2}{1 - \cos\theta + \left(\frac{1}{\alpha}\right)} \qquad \text{Eq. 3.9}$$

and the kinetic energy of the struck electron

$$T = h\nu_o \frac{2\alpha \cos^2 \varphi}{(1+\alpha)^2 - \alpha \cos \varphi} \qquad \text{Eq. 3.10}$$

The direction of the scattered photon is given by

$$\frac{d({}_e\sigma)}{d\theta} = \frac{d({}_e\sigma)}{d\Omega} \, 2\Pi \sin\theta \, \frac{\text{cm}^2}{\text{electron}} \qquad \text{Eq. 3.11}$$

where:

$\frac{d({}_e\sigma)}{d\theta}$ = the number of photons scattered at angle θ per electron per cm^2 per incident $h\nu$

$\frac{d({}_e\sigma)}{d\Omega}$ = the number of scattered photons per unit solid angle given by

$$\frac{d({}_e\sigma)}{d\Omega} = \frac{e^4}{m_o^2 c^4}\left(\frac{h\nu'}{h\nu_o}\right)^2\left(\frac{h\nu_o}{h\nu'} + \frac{h\nu'}{h\nu_o} - \sin^2\theta\right) \qquad \text{Eq. 3.12}$$

with terms as defined before. Inspection of graphs of these functions by Evans (11) shows that as incident photon energy increases, scattering becomes greater in the forward direction.

The direction of the Compton electron is given by

$$\frac{d({}_e\sigma)}{d\varphi} = \frac{d({}_e\sigma)}{d\Omega'}\ 2\,\Pi \sin\varphi \qquad \text{Eq. 3.13}$$

where:

$$\frac{d({}_e\sigma)}{d\Omega'} = \frac{d({}_e\sigma)}{d\Omega}\ \frac{\sin\theta\ d\theta}{\sin\varphi\ d\varphi} \qquad \text{Eq. 3.14}$$

The distribution of struck electrons also shows peaking in the forward direction with increased incident photon energy.

The number-energy distribution of the Compton electrons can be represented as

$$\frac{d({}_e\sigma)}{dT} = \frac{d({}_e\sigma)}{d\Omega}\ \frac{2\,\Pi}{\alpha^2 m_o c^2} \left[\frac{(1+\alpha)^2-\alpha^2\cos^2\varphi}{(1+\alpha)^2-\alpha(2+\alpha)\cos^2\varphi}\right]^2 \qquad \text{Eq. 3.15}$$

From applying the conservation of momentum and energy in the Compton interaction one may write

$$\frac{1}{h\nu'} - \frac{1}{h\nu_o} = \frac{1}{m_o c^2}(1 - \cos\theta) \qquad \text{Eq. 3.16}$$

From an examination of Eq. 3.16 it follows that, for a given scatter angle, higher energy incident photons suffer a greater energy change than do lower energy incident photons. Since the energy gained by the struck electron is

$$T = h\nu_o - h\nu' \qquad \text{Eq. 3.17}$$

Compton scattering favors energy transfer to electrons in the higher energy ranges. However, since the Compton process only predominates through about 5 MeV, the bremsstrahlung from these electrons will be of moderate energy and will be emitted isotropically. The ratio of energy lost by these electrons by bremsstrahlung to energy lost by ionization is approximated by

$$\frac{\left(\frac{dT}{ds}\right)_{rad}}{\left(\frac{dT}{ds}\right)_{ion}} \approx Z\left(\frac{m_o}{M_o}\right)^2\left(\frac{T}{1400\ m_o c^2}\right) \qquad \text{Eq. 3.18}$$

where M_o is the rest mass of the particle near which the energy loss occurs and the other terms are as previously defined. For this radiation to then be contributed to the backscatter fluence, it must pass through some thickness, d, from the point of origin to the surface of the backscatter medium.

The degraded photon can then undergo further Compton scatter to be emitted at the surface also. Previous experiments (16, 23) using monoenergetic photon sources have been able to differentiate between these multiply scattered photons and those singly scattered. Since the sources used for this research were bremsstrahlung spectra, this differentiation was not possible.

The contributions to backscatter fluence due to Compton interaction will be then

$$_{C}\phi_N(\phi_o, E_o, Z, r) = {}_{SC}\phi_N + {}_{MC}\phi_N + {}_{BC}\phi_N \qquad \text{Eq. 3.19}$$

where:

$_{SC}\phi_N(\phi_o, E_o, Z, r)$ = the number fluence due to singly Compton scattered photons at some point, r, from the surface of a backscattering medium with atomic number Z when exposed to a photon fluence ϕ_o of energy E_o, given by

$$_{SC}\phi_N(\phi_o, E_o, Z, r) = \int_d \int_A \frac{\phi_o(E_o)\ \exp[-\mu_t(E_o, Z)d]}{r^2}$$

$$\frac{d(_e\sigma_s)}{d\Omega}\ \frac{\rho N_o Z}{M}\ \exp[-\mu_t(E_c, Z)d(\sec\ \theta_s)]\ dd\ dA$$

Eq. 3.20

where:

$\phi_o(E_o)$ = the incident photon fluence

$\mu_t(E_o, Z)$ = the total attenuation coefficient to the incident photons

d = the depth in the backscatterer being considered

$\frac{d(_e\sigma_s)}{d\Omega}$ = the number of photons being scattered into the solid angle of concern

$\mu_t(E_c, Z)$ = the total attenuation coefficient to the scattered photons

$_{MC}\phi_N(\phi_o, E_o, Z, r)$ is the number fluence contribution due to multiply Compton scattered photons at some point, r, given here for twice Compton scattered:

$$_{MC}\phi_N(\phi_o, E_o, Z, r) =$$

$$\iint_{A\,(t,\alpha,\beta)} \iint_{d\,d'} \phi_o(E_o)\ \exp[-\mu_t(E_o,Z)d']\ {}_e\sigma_s(E_o)\ \frac{\rho N.Z}{M}$$

$$\exp[-\mu_t(E_c,Z)t]\ \frac{1}{4\Pi t^2}\ \frac{d({}_e\sigma_s)}{d\Omega}\ (E_c)\ \frac{\rho N.Z}{M}$$

$$\frac{\exp[-\mu_t(E_{DC},Z)d\ \sec\ \theta_s]}{r^2}\ dd'\ dd\ td\alpha t\ \sin\alpha\ d\beta\, dt$$

Eq. 3.21

where:

d' = the depth into the backscatter medium until the first Compton interaction

${}_e\sigma_s\ (E_o)$ = the Compton microscopic scattering cross-section for the incident photons

$\mu_t(E_o Z)$ = the total attenuation coefficient to the once Compton scattered photons

t = the distance between the first and second Compton scatter events

$\frac{d({}_e\sigma_s)}{d\Omega}(E_c)$ = the number of photons being scattered into the solid angle of concern dependent upon the energy of the once Compton scattered photons

$\mu_t(E_{DC},Z)$ = the total attenuation coefficient for the double Compton scattered photons d = the depth in the backscatter medium to the second Compton event

(α, β) = angles defining the direction of first Compton scattering

and the rest of the terms are as previously defined. Higher order scattering would be handled similarly.

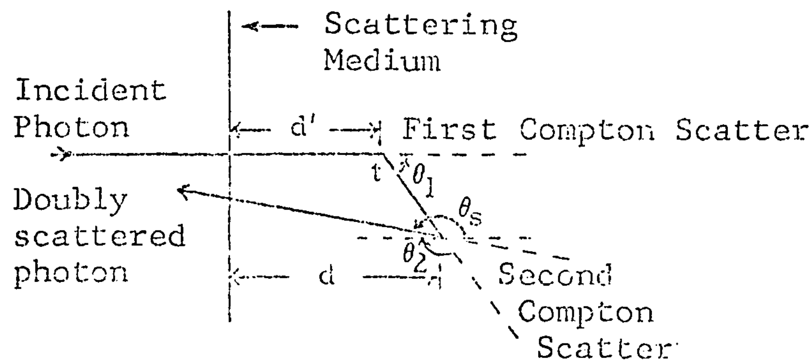

Figure 7. Multiple Compton Scattering

Finally, ${}_{BC}\phi_N$, the number fluence contribution due to bremsstrahlung produced by Compton scattered electrons, can more easily be represented by ${}_{BC}\phi_E$, the energy of photons contributed to the backscatter fluence by the bremsstrahlung of Compton electrons, which can be given by

$$_{BC}\phi_E(\phi_o,E_o,Z,r) = \int_d \int_{d'} \int_A \int_{E_B} \phi_o(E_o)\ \exp[-\mu_t(E_o,Z)d']$$

$$e^{\sigma}\ \frac{\rho N_o Z}{M}\ \frac{\left(\frac{dT}{ds}\right)_{rad}}{\left(\frac{dT}{ds}\right)_{rad} + \left(\frac{dT}{ds}\right)_{ion}}$$

$$\frac{\exp[-\mu_t(E_B,Z)d\ \sec\ \theta_s]}{4\Pi r^2}\ dE_B\ dA\ dd'\ dd \qquad \text{Eq. 3.22}$$

where:

$_{BC}\phi_E$ = the energy contributed to the backscatter fluence by the bremsstrahlung of Compton electrons at the point r

$\mu_t(E_B,Z)$ = the total attenuation coefficient to the bremsstrahlung radiation

and the rest of the terms are as previously defined.

The highest energy photon one might see emergent from the scattering surface due to Compton interaction, with the sources used in this dissertation, would be that due to a large number of Compton scatter events resulting in a photon emerging at 90^{o} to the incident beam. The larger the number of scatterings required the lower the probability of the photon surviving. A 10 MeV photon undergoing three Compton scatterings of 30° each would emerge with an energy of 1.13 MeV.

3.2.3 Pair Production (3, 11)

In the energy region of 5 MeV for high Z materials and 10 MeV for intermediate Z materials, the cross-section for pair production interactions becomes important. The energy threshold for pair production is 1.022 MeV in the field of a nucleus and 2.044 MeV in the field of an electron.

The cross-section for this interaction in the field of a nucleus is estimated by

$$K_n = \left[K_n(\text{Born, unscreened}) - S^{HFS}\right]\left[1 + \Delta(\text{rad. corr.})\right]$$

$$- \Delta(\text{empirical}) \cdot \Delta K_n^{DBM} \qquad \text{Eq. 3.23}$$

where: K_n(Born, unscreened) is an approximation represented by

$$K_n(\text{Born}) \approx \frac{4Z^2 r_e^{\;2}}{137} \ln (183\ Z^{-1/3})$$

$$\left[(1-\frac{2}{k})(1+\frac{K}{k}) - \frac{\mu}{6} - \frac{2}{k} + \frac{\mu}{k^2} - \frac{2\mu}{3k^3} - \frac{2K}{k}\frac{\left(1+\frac{\mu K}{k}\right)}{\sqrt{1+\frac{4K}{k}}} \ln \frac{\sqrt{1+\frac{4K}{k}} + 1 - \frac{2}{k}}{\sqrt{1+\frac{4K}{k}} - 1 + \frac{2}{k}}\right]$$

Eq. 3.24

with

$$r_e = \frac{e^2}{m_o c^2} \qquad \text{Eq. 3.25}$$

$$k = \frac{E_\gamma}{0.511} \qquad \text{Eq. 3.26}$$

$$\mu = \frac{4}{3} + \left[9 \ln (183\ Z^{-1/3})\right]^{-1} \qquad \text{Eq. 3.27}$$

and

$$K = \frac{255\ Z^{-1/3}}{(15.6 - 4/3 \ln Z)} \qquad \text{Eq. 3.28}$$

in Eq. 3.23.

S^{HFS} = the Sorenssen screening correction

$1 + \Delta(\text{rad. corr.})$ = the Mork-Olsen radiative correction factor

$\Delta(\text{empirical})$ = a correction factor for high-energy Coulomb effects as is Δk_n^{DBM}

Values for each of these are found in the literature (3).

The cross-section for pair production in the field of an electron is estimated by

$$K_e = \frac{r_o^2}{137} \left\{ \frac{28}{9} \ln (2k) - \frac{218}{27} - \frac{1}{k} \left[\frac{4}{3} \ln^3(2k) - 3 \ln^2(2k) + 6.84 \ln(2k) - 21.51\right] \right\}$$

Eq. 3.29

with terms as defined above. The energy of the incident photon is shared by the electron-positron pair.

$$h\nu = (T_- + m_o c^2) + (T_+ + m_o c^2) \qquad \text{Eq. 3.30}$$

where T_- and T_+ are the kinetic energy of the electron and positron respectively. The kinetic energy of the positron is slightly greater than that of the electron when they are created in the field of a nucleus. This difference being, at most, about

$$T_+ - T_- = \frac{2\ Ze^2}{(h/2\,\Pi\, m_o c^2)} = 0.0075\ Z \quad \text{Eq. 3.31}$$

The angular distribution of the pair peaks in the forward direction for high energy incident photons (68).

For pair production in the field of an electron the photon's energy is divided among three particles (the created positron and electron and the electron involved in the interaction).

All particles here lose energy by radiation, ionization, and excitation. The contribution of the bremsstrahlung can be considered in the same manner as described for the Compton electrons previously. As the positron slows down it will combine with an electron to create two annihilation photons of 0.511 MeV, which are emitted isotropically. This radiation is expected to comprise the major portion of the backscatter fluence due to pair production interactions (46, 69, 70).

The fluence contribution, due to pair production interactions, at some point, r, can then be represented by

$$_{PP}\phi_N\ (\phi_o, E_o, Z, r) = {}_{BPP}\phi_N + {}_A\phi_N \qquad \text{Eq. 3.32}$$

where $_{BPP}\phi_N$ is the number fluence due to bremsstrahlung of the electrons and positrons and is to be represented in the same manner as $_{BC}\phi_N$.

$_A\phi_N$ is the number fluence contribution due to annihilation radiation, expressed here as

$$_A\phi_N\ (\phi_o, E_o, Z, r) = \int_d \int_{d'} \int_A \phi_o(E_o)\, \frac{\exp[-\mu_t(E_o, Z)d']}{4\,\Pi\, r^2}$$

$$2\ \tau_K\ \frac{\rho N.Z}{M} \exp[-\mu_t(0.511, Z)d \sec\ \theta_s]\ dA\ dd'\ dd$$

Eq. 3.33

where:

$\phi_o(E_o)$ = the incident fluence

$\mu_t(E_o,Z)$ = the total attenuation coefficient to the initial fluence in the back-scatterer of atomic number Z

d' = the distance from the surface to the pair production interaction

$\mu_t(0.511,Z)$ = the total attenuation coefficient to the annihilation radiation

d = the distance from the point of positron annihilation to the surface of the backscatterer

k_T = the pair production microscopic cross-section

A = area of incident beam

The rest of the terms are as previously defined.

To obtain an idea of the photon energy to emerge under this interaction one can consider bremsstrahlung from the most probable electron energy to be produced in the pair production interaction

$$E_{e^-} = \frac{1}{2}(h\nu - 1.022) \text{ MeV} \qquad \text{Eq. 3.34}$$

Bremsstrahlung resulting from this electron will have a maximum leading edge equal to the energy of the electron. With the sources used, a photon energy of 4.64 MeV might be observed from the 10.5 MeV machine.

3.2.4 Rayleigh Scattering and Photonuclear Interactions

Although Rayleigh (coherent) scattering may be of some consequence in scattering radiation from a beam for transmission measurements, the angle of deflection is always (11) small, and can be estimated by

$$\theta_c = 2 \arcsin \frac{0.0133\ Z^{1/3}}{E_o(\text{MeV})} \qquad \text{Eq. 3.25}$$

where θ_c is the opening half angle of a cone containing at least 75% of the coherent-scattered photons. The number of Rayleigh scattering events necessary to reflect a photon reduces the probability of this contribution below the level to be considered here. Rayleigh scattered photons might well undergo further reactions to send them back out of the reflector, but since the total distance traveled by the photon will be nearly the same as the distance into the medium and nearly no energy is lost in the Rayleigh scattering process, for purposes of this report coherent scattering will not be considered further.

Although the photonuclear giant resonance peaks occur in the energy region of interest, their cross-sections are small (5% to 10%) compared to those for the Compton effect and for absorption by nuclear pair production. The most probable result of photonuclear absorption is the emission of a neutron. At present only experimental data is available for determining cross-sections.

Considering the materials chosen for this work:

-- Lead has a photonuclear threshold of about 6.8 MeV and reaches its resonance peak at 13.7 MeV. The cross-section at this peak is 0.81 barns/atom.

-- Iron has a photonuclear threshold of 11.2 MeV and resonance peak at 18.0 MeV, with a cross-section of 0.075 barns/atom at that energy (71).

-- The principle components of concrete, oxygen and silicon, being of lower Z have higher threshold energies, and cross-sections at their resonance peaks are considerably smaller (0.02 - 0.03 barns/atom). (72)

Since the photonuclear cross-sections are a couple of orders of magnitude below the cross-section for pair production at the same energy, the decrease to the photon fluence due to photonuclear absorption will not be considered. However, it is necessary to consider the neutron fluence which arises. The number of neutrons arising can be calculated as

$$N_n = \int_{B_n}^{E_m} \int_{\alpha} \sigma_{(\gamma,n)}(E,ZA)\left(\frac{\rho N_o}{M}\right)\phi_N(E)\, d\alpha\, dE \quad \text{Eq. 3.36}$$

where:

$\sigma_{(\gamma,n)}(E,ZA)$ = the photonuclear cross-section at energy E in a material of atomic number Z and atomic mass A

$\phi_N(E)$ = the photon number fluence at the point of interest

B_n = the threshold energy

E_m = the maximum energy at which nuclear capture occurs or the maximum energy of the incident beam, whichever is smaller

a = incident beam area

The neutron number fluence at a point of interest, r, can be calculated

$$
{}_n\phi_N\,(\phi_o, E_o, r, ZA) = \int_d \int_{B_n}^{E_m} \int_A \frac{\phi_o(E_o)}{4\Pi r^2} \exp[-\mu_t(E_o,Z)d]
$$

$$
\sigma_{(\gamma,n)}(E,ZA)\, \frac{\rho N_o}{M}\; \exp[-\Sigma_r(E,ZA)d]\; dA\; dE\; dd
$$

Eq. 3.37

where:

$\phi_o(E_o)$ = the incident photon fluence

$\mu_t(E_o, Z)$ = the total attenuation coefficient to the incident fluence

d = the distance from the surface of the backscatter medium to the point of nuclear absorption

$\Sigma_r(E, ZA)$ = the removal cross-section to the emitted neutrons

and the other terms are as previously defined. Photons having undergone one of the interactions previously discussed will not have sufficient energy for photonuclear capture and their fluence is not added in this calculation.

For the materials and energies used in this dissertation,

$$_n\phi_N(\phi_o, E_o, r, ZA) \ll {}_{pp}\phi_N + {}_C\phi_N + {}_{pe}\phi_N \qquad \text{Eq. 3.38}$$

where:

$_{pe}\phi_N$ is given by Eq. 3.4

$_C\phi_N$ is given by Eq. 3.19

$_{pp}\phi_N$ is given by Eq. 3.32

Therefore no neutron response correction will be made for the TLD readings obtained.

Photofission is not considered for the materials chosen at the energies used for this research (73, 74).

3.2.5 Summary

The total energy fluence at some point, r, can then be represented as the sum of the previously calculated fluence.

$$\phi_E = {}_{pe}\phi_N \sum_n h\nu + F(E_c)\ {}_C\phi_N + 0.511\ {}_{pp}\phi_N \qquad \text{Eq. 3.39}$$

where:

${}_{pe}\phi_N \sum_n h\nu$ is given in Eq. 3.5

${}_C\phi_N$ is given by Eq. 3.19 and $F(E_c)$ is the distribution of the Compton scattered photons, and

${}_{pp}\phi_N$ is given by Eq. 3.32

The exposure-dose distribution may be determined from the energy distribution above by

$$D = \int \left(\frac{\mu(E)}{\rho}\right) \phi_E \, dE \qquad \text{Eq. 3.40}$$

where $\left(\frac{\mu(E)}{\rho}\right)$ is the energy mass absorption coefficient for water (since water is often used as a dose standard, any material could, of course, be chosen).

3.3 DETECTION INSTRUMENTATION

3.3.1 Scintillation Spectrometer

The scintillation detector used in this research was a 5" D x 3" right cylindrical NaI (Tl) crystal of Isotopes Inc. production with its photomultiplier package. A Nuclear Data 512 channel instrument was used as the multi-channel pulse height analyzer and data display device. The analyzer used has a "dead" time of (5 + 0.25N) μsec, where N is the channel number, and an internal delay time of 2 μsec. A detailed discussion of the operation of a scintillation spectrometer may be found in references 75 and 76.

Due to system "dead" time, the scintillation spectrometer could not be used in the experiments with the flash x-ray devices.

It was not possible to sufficiently "detune" the 2.0 MeV Van de Graaff to make a measurement of the beam spectrum. Even at the maximum distance allowed by the radiographic bay and with a very small opening collimator, the detector system was swamped out. Some measurements were made of the reflected spectra and these results are found in Appendix D for comparison with spectra generated by the two computer programs used.

Spectral data are given in Appendix D.

3.3.2 Thermoluminescent Detectors

The thermoluminescent detectors used in this research were Harshaw produced LiF crystals. Two sizes (1/8" x 1/8" x 0.035" and 6mm x 1mm x 0.9mm) were used to check for systematic errors arising from crystal size considerations.

Particular characteristics of the LiF thermoluminescent detector are:

-- a very linear response over a wide energy range (77) though with some under-response at low energies (40 KeV) to be discussed in greater detail in Appendix E;

-- fading of the "glow curve" is less than 5% per year (78) after an initial stabilizing period of a few hours;

-- linear response (±3%) to accumulated doses of about 700 R (79) and doesn't saturate until doses of about 10^5 R (77);

-- lower limits of detection (with the detectors used) of approximately 5 MR (80);

-- and dose rate independence in response to rates up to 2×10^{11} rad/sec ±10% (81, 82).

These characteristics make the LiF thermoluminescent detectors nearly ideal for the research undertaken, and certainly better than other, existing, passive detectors (83, 84).

The detectors used have some neutron response. TLD-100 (Harshaw manufactured LiF) shows a response of about 1:37::thermal neutron:gamma exposure. The response to fast neutrons is much less (85, 86).

By placing these small detectors at various points from the surface of the backscattering material, one can determine the angular dependency of the scattered photons. Due to the integrating nature of the detector, they do not readily lend themselves to a determination of the energy of the backscattered fluence.

Much work has been done on various methods of obtaining data from TLD's. A variety of annealing and read-out procedures have been proposed (87, 88, 89, 90, 91), to accomplish greater statistical accuracy, reproducibility, handling convenience, etc. In the present research an Eberline TLD Reader Model TLR-5 was employed with the LiF crystals previously discussed. The reader allows the operator to control the time (0 - 60 seconds) and temperature (0 - 400°C) of both a "pre-heat" cycle and an "integrate" cycle. Nitrogen is purged through the chamber at one liter per minute during read-out to lower the instrument background. A modification of the reader was made by connecting an additional variable rheostat in series with the photo-multiplier gain adjust to allow greater accuracy in setting the gain to a desired level. Appendix F discusses the method by which the read-out and annealing procedures were chosen.

The theory of thermoluminescent dosimetry is well documented elsewhere (92, 93).

3.3.3 Attenuation Methods of Spectral Determination

Various methods have been used to attempt to gain information about the spectral distribution of x-rays (94). The method to be discussed here is that of graphically fitting three exponentials to an attenuation curve. It is felt that three extractions are all that can be made from a single attenuation curve with accuracy (95).

The clearest use of the attenuation curve comes from plotting the logarithm of the fraction transmitted (ordinate) verses the depth in the attenuating material (abscissa). If the absorber material is thick enough, the attenuation curve will approach a straight line at greater depths in the material. Extrapolation of this portion of the curve back to zero absorber thickness and subtraction from the original attenuation curve removes the high energy component of the incident fluence. The intercept of this portion of the curve on the ordinate axis gives the fraction of incident radiation contributed by the high energy component. This extraction procedure can then be repeated as diagramed below.

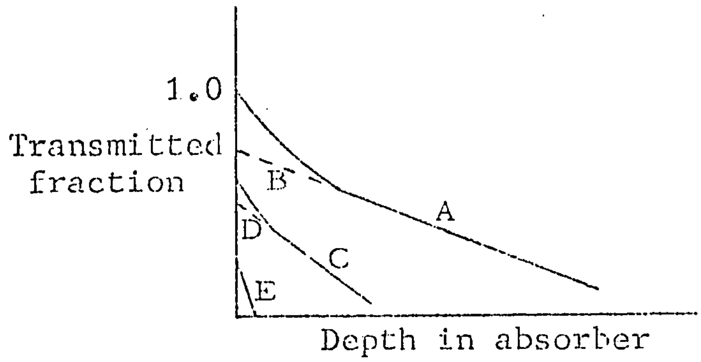

Figure 8. Attenuation extractions

Curve A is the original attenuation information, curve B the high energy component extracted, curve C that portion remaining after removal of the high energy contribution, curve D the intermediate energy extraction, and curve E is the remaining low energy component (after Greening - 94). Using the slopes of the linear curves, one can determine the linear attenuation coefficients of the various energy components in the particular absorber material used. From this an energy assignment can be made from values such as given in Attix, et al. (42). Having the energy and the fraction of the incident flux contributed by that energy, one can generally characterize the beam in a three-energy representation. Greening (96) also discusses a method of incident energy spectrum determination from absorption data using Laplace transforms. A recent attempt has been made to computerize absorption data in an effort to obtain better energy representations (97).

Several difficulties arise in applying this method to determining the spectral output and reflected spectra for the machines used. The reflected intensity is so low as to be near the limit for statistically reliable measurement with TLD's. Any method which requires the attenuation of this intensity through several half values is impractical. The focal point for the electron beam striking an x-ray target is not precisely controlled on flash x-ray devices. It is therefore necessary to make a very large number of measurements with well collimated detectors to gain a meaningful absorption curve. This curve will then represent an average for the particular machine and not precisely represent any one shot. The spectral unfold for absorption data generated by bremsstrahlung spectra of the energy span covered in this dissertation becomes quite severe. A number of extensive measurements of spectra have been published (98, 99, 100, 101, 102, 103, 104, 105). These spectra represent a compilation of information gathered from Compton scatter devices, absorption data, electron spectra-target codes, etc. In general previously published spectra are used in this report for computer program inputs. Appendix D discusses the spectra information generated in this work compared to previously published work. Sample albedo results with each are given to study the effect of different spectra inputs.

4. NUMERICAL ANALYSIS METHODS

4.1 EMPIRICAL METHODS

Of the empirical methods for calculating albedo, only the Chilton-Huddleston (49) development attempts to go beyond a few MeV. For that reason, theirs will be the only one discussed in this section. The initial development was limited to scatter from concrete.

The geometry of the Chilton-Huddleston (C-H) derivation is given in Figure 9.

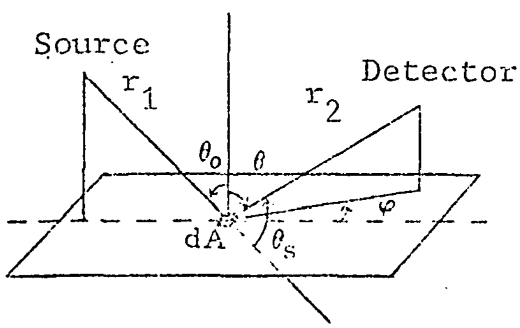

Figure 9. Geometry of the Chilton-Huddleston derivation

Starting with the formula for differential dose at a point, from single scattering

$$dD = \frac{D_1 \alpha_d \cos \theta_o \, dA}{r_1^2 r_2^2} \qquad \text{Eq. 4.1}$$

where:

dD = the differential dose at point of measurement

D_1 = dose at reference point one unit distance from point source

α_d = dose albedo

θ_o = polar angle of incidence radiation

dA = differential area of reflecting surface

r_1 = distance from source to differential area

r_2 = distance from differential area to detector.

They develop a representation of single scattering dose albedo

$$\alpha_{dS} = \frac{B\,K(\theta_s)}{\bar{\mu}_1 + \bar{\mu}_2 \cos \theta_o \sec \theta} \qquad \text{Eq. 4.2}$$

where:

α_{dS} = the single scattering dose albedo

B = a collection of factors which depend only on the reflecting material or are constant

$K(\theta_s)$ = the Klein-Nishina value of the energy scattering cross-section per electron

$\bar{\mu}_1$ and $\bar{\mu}_2$ = the mass absorption coefficient for the gamma radiation before and after scattering, respectively.

Their representation of the contribution by annihilation radiation is of similar form but without the Klein-Nishina factor, since annihilation radiation is produced isotropically.

$$\alpha_{di} = \frac{B_1'}{\bar{\mu}_1 + \bar{\mu}_2' \cos\theta_o \sec\theta} \qquad \text{Eq. 4.3}$$

where:

α_{di} = annihilation dose albedo

B_1' = a collection of factors which depend only on the reflecting material or are constant

$\bar{\mu}_2'$ = the energy absorption coefficient at the average energy of the isotropically produced radiation

Neglecting other contributions as being below the level of influence in this approximation, the over-all differential albedo is given as the sum of 4.2 and 4.3 with appropriate changes in the constants.

$$\alpha_d(\theta_o, \theta, \phi) = \frac{B_3 K(\theta_s)}{\bar{\mu}_1 + \bar{\mu}_2 \cos\theta_o \sec\theta} + \frac{B_2'}{\bar{\mu}_1 + \bar{\mu}_2' \cos\theta_o \sec\theta}$$

Eq. 4.4

In the case of lead, and several other high Z materials, ignoring the photoelectric contribution results in low albedo estimates.

By assuming the attenuation coefficients are not greatly energy dependent and incorporating them into the constant terms, one arrives at the much simplified equation

$$\alpha_d(\theta_o, \theta, \phi) = \frac{CK(\theta_s) \cdot 10^{26} + C'}{1 + \cos\theta_o \sec\theta} \qquad \text{Eq. 4.5}$$

Where C and C' are the C-H parameters which must be adjusted for each incident photon energy. Comparison with Monte Carlo results appear to justify this assumption (though since the parameters C and C' are obtained from a least-squares fit to Monte Carlo data, this would follow). Their first paper (49) gave values of C and C' only for concrete at incident energies of 0.2, 0.5, 1, 2, 4, 6, and 10 MeV.

In 1965, Chilton and Davisson (51) published values for the C-H parameters in water, concrete, iron, and lead for incident photons of energies up to 6.13 MeV.

A later paper by Chilton (54) revised the formula, to that shown in Eq. 2.11, to more closely match updated Monte Carlo runs. However, only values for 0.662 and 1.25 MeV reflected from concrete have been published. Consequently the revised formula cannot be used in this development.

Appendix N considers these empirical developments with "effective" x-ray energies from the machines used in this dissertation.

Leimdorfer (46) has developed an analytical expression for the total albedo (not considering the angular distribution and making much the same assumptions as Chilton-Huddleston). His development covers the same area as that of Chilton and Huddleston and lacks some of their flexibility; further work with it is not considered.

4.2 MONTE CARLO METHODS

The Monte Carlo method is a computerized experiment in which individual photon "case histories" are compiled until a statistically valid distribution is obtained. An individual photon enters the program at a given energy. On the basis of this energy, a probability generating subroutine assigns an interaction with energy loss, change of direction, etc. This process is continued until the photon is emitted from the material (transmitted or backscattered) or drops in energy below some pre-set cut-off level. At this point a new photon is introduced into the program.

Raso (45), in 1963, published values of total dose rate albedo from concrete with incident photon energies of 0.2 to 10.0 MeV. However, the data of Wells (43) published in 1964, is of a format more nearly that of this research. His data gives differential dose albedos for photon reflection from concrete. Source energies of 0.6, 1, 2, 4, and 7 MeV are used with angles of incidence of $\theta_o = 0^o$, 30^o, 45^o, 60^o, and 75^o.

His representation of the differential dose albedo is given by the relation

$$a(\theta_o, \theta, \phi, E_o) = \frac{D(\theta_o, \theta, \phi, E_o)}{F(E_o) \sec \theta_o} \qquad \text{Eq. 4.6}$$

where:

$\alpha(\theta_o, \theta, \phi, E_o)$ = the ratio of the dose rate current reflected per steradian in the θ, ϕ direction to the dose rate per photon of energy incident upon the slab surface at an angle θ_o

$D(\theta_o, \theta, \phi, E_o)$ = the scattered photon rate current per steradian leaving the concrete surface in the direction θ, ϕ per photon incident at an angle θ_o per unit area on the concrete surface

$F(E_o) \sec \theta_o$ = the dose rate incident to the surface per photon per cm^2 crossing the surface in the direction θ_o.

The cited literature deals only with monoenergetic incident sources. The author finds no published results of Monte Carlo runs having been made for bremsstrahlung, and since each bremsstrahlung spectrum would be a function of the particular generating machine, information of this type would be of limited value.

For comparison purposes in this dissertation, a number of Monte Carlo runs have been made and their results plotted. The program used (Appendix K) is based on a publication by K. G. Adams and C. R. Mehl (106) as updated generally in April, 1968, by Adams and with specific update features by Adams, August, 1970, for adaptation to the specific energies and materials encountered in the present problem. A study of results from this particular Monte Carlo program with comparisons from DTF results (to be discussed in Section 4.3) and previously published experimental results is given in Appendix M.

4.3 METHOD OF DISCRETE ORDINATES

The method of discrete ordinates is a numerical procedure used to solve the Boltzmann transport equation. The solution of transport problems using the method of discrete ordinates is a well-established technique in neutron problems. These techniques have been adapted to photon transport problems at Sandia Laboratories (62) and other installations dealing with shielding or energy deposition problems.

The particular program (DTF-69) used in this research (Appendix L) was written by J. H. Renken and K. G. Adams (63) with updates specific to the problem of the dissertation by J. H. Flinchum of Sandia Corporation.

In any particular DTF run, the incident photon spectrum is divided into a finite number of energy groups (i.e. a multigroup approximation). The monoenergetic transport equation for each group is then solved numerically by finite difference equations. The photon energy loss due to scattering is accounted for by the transfer of photons from one group to another of lower energy. Within the limitations of the numerical nature of the solution, the result of this procedure is believed to be a rigorous solution of the transport equation.

A number of other codes based on the same principle are presently in use. A comprehensive review of the "state-of-the-art" as regards the method of discrete ordinates may be obtained from the Radiation Shielding Information Center (107).

Runs have been made for each experimental configuration for comparison purposes. These results are presented in the discussion of experimental data in Section 6.2.

Various spectra were used as input. These spectra and results are discussed in Appendix D.

As with the Monte Carlo program, a number of runs were made for comparison with previously published experimental data with results presented in Appendix M.

5. EXPERIMENTAL DESIGN

5.1 BACKSCATTER MATERIALS

5.1.1 Introduction

For results of various experiments to be comparable, it is necessary that variance in the dimensions of the back-scatterer not affect the amount of radiation reflected. To this end experimenters generally use a "semi-infinite" slab of material, meaning that any increase in the irradiated slab area or the slab thickness must not result in a change in the albedo for the viewed area. Though all are agreed upon this principle, few are agreed upon what is necessary to constitute a semi-infinite piece of material. In the high energy bremsstrahlung experiments discussed previously (35, 36), variations from thicknesses of seven mean free path lengths and diameters of nine mean free path lengths to thickness of one half a mean free path length and less than one half a mean free path length in diameter are used.

Experiments with gamma ray sources have generally shown (12, 17, 18, 21) that increasing the thickness of backscatter medium beyond two mean free path lengths does not significantly alter the albedo measured. Lateral dimensions are less well established however, perhaps because of variation in experimental design.

Hine (16) has demonstrated that for diameters of less than two mean free path lengths, variation in surface area significantly alters the measured albedo. Mizukami et al. (20) indicate that a surface area less than four mean free path lengths in diameter is inadequate, but that at a diameter of seven mean free path lengths no change in albedo will be observed by increasing the surface area. Steyn (12) feels that five mean free path lengths form an adequate surface. Other experimenters using gamma-ray sources (17, 24, 25) do not discuss the problem and use scatter surfaces of three to six mean free path lengths in diameter.

To insure that slabs used in this research were "semi-infinite", they were generally chosen to be two mean free path lengths thick at the point of minimum absorption for the energy spectrum being used and three and one half mean free path lengths from the edge of the viewed area (Appendix B) to any edge of the reflector. A number of measurements were made to insure the adequacy of the following calculations. These results are reported in Appendix G.

5.1.2 Lead

Lead exhibits a minimum mass attenuation coefficient of 0.0410 cm^2/gm to 3.4 MeV photons. This corresponds to a mean free path length of 2.15 cm or 0.845 inches. A lead slab having adequate dimensions at this energy would be "semi-infinite" for any of the energies used in this work. Lead slabs 1.75 inches thick and 12.0 inches square were used for albedo measurements. The surface was uniformly irradiated (Appendix H).

5.1.2 Iron

Iron has a minimum mass attenuation coefficient of 0.0299 cm^2/gm for photons at 8.5 MeV. This gives a mean free path length of 4.25 cm or 1.67 inches. Thus, a slab 3.34 inches thick and of diameter 11.69 inches plus viewed diameter (Appendix B) could be called "semi-infinite". For the majority of this research, a slab of this size would be larger than necessary. With a bremsstrahlung maximum energy of 2.0 MeV, a slab 2.32 inches thick and 8.14 inches plus viewed diameter would be semi-infinite. A slab 3.50 inches thick and 14.0 inches square was used for albedo measurements at 2.0 and 3.5 MeV, a slab 18.0 x 18.0 x 4.50 inches was used for 7.0 and 10.5 MeV.

5.1.3 Concrete

Normal density concrete (2.30 gm/cm^3) has a minimum absorption coefficient of 0.0204 or maximum mean free path length of 21.31 cm or 8.39 inches near 30 MeV. The energies considered in the present research are not that high and the absorption coefficient would therefore be somewhat higher. Also considerable differences exist in the atom densities of various concrete, depending upon how and where they are made. The concrete used was that typical of this area, poured with fine aggregate, stirred to prevent voids and formed without reinforcement steel to avoid high Z pertubation. The atom densities of this concrete are compared with other concretes in Table 1. The effect of differing concrete atom densities on albedo is studied through use of the discrete ordinates computer program at an incident bremsstrahlung energy of 2.0 MeV maximum in Figure 10. Aluminum is often used for computer comparisons to concrete due to the closeness in density, atomic number (Z), etc., and the relative ease of calculating one Z vs 10-13 Z. The effective atomic number of the concrete used here was 12.1, the density 2.16 gm/cm^3.

A slab 8 inches thick and 32 inches square was used as the concrete reflector at 2.0 and 3.5 MeV, a 10 inch thick, 36 inches square slab at 10.5 MeV. No concrete backscatter surface was used in the 7.0 MeV experiments due to the lack of handling equipment in that facility.

TABLE 1

CONCRETE COMPOSITIONS

ATOM DENSITIES (atoms/cm^3)

ELEMENT	CONCRETE USED IN THIS DISSERTATION	O R N L STANDARD CONCRETE	RADIATION RESEARCH ASSOCIATES CONCRETE
H	2.177×10^{21}	8.50×10^{21}	9.886×10^{21}
C	4.355×10^{21}	2.02×10^{22}	6.913×10^{20}
O	3.986×10^{22}	3.55×10^{22}	4.473×10^{22}
Na	3.473×10^{20}	1.63×10^{19}	9.1×10^{20}
Mg	2.6×10^{19}	1.86×10^{21}	9.922×10^{20}
Al	1.284×10^{20}	5.56×10^{20}	2.64×10^{21}
Si	1.775×10^{22}	1.70×10^{21}	1.355×10^{22}
P	0	0	3.326×10^{19}
S	0	0	3.326×10^{19}
K	1.257×10^{19}	4.03×10^{19}	5.862×10^{20}
Ca	2.274×10^{21}	1.11×10^{22}	4.334×10^{21}
Ti	0	0	9.577×10^{19}
Fe	2.515×10^{19}	1.93×10^{20}	7.794×10^{20}
Cu	5.156×10^{18}	0	0
Zn	4.872×10^{19}	0	0
Sr	2.406×10^{18}	0	0

Figure 10 Albedo dependence on concrete composition
for 2.0 MeV Bremsstrahlung

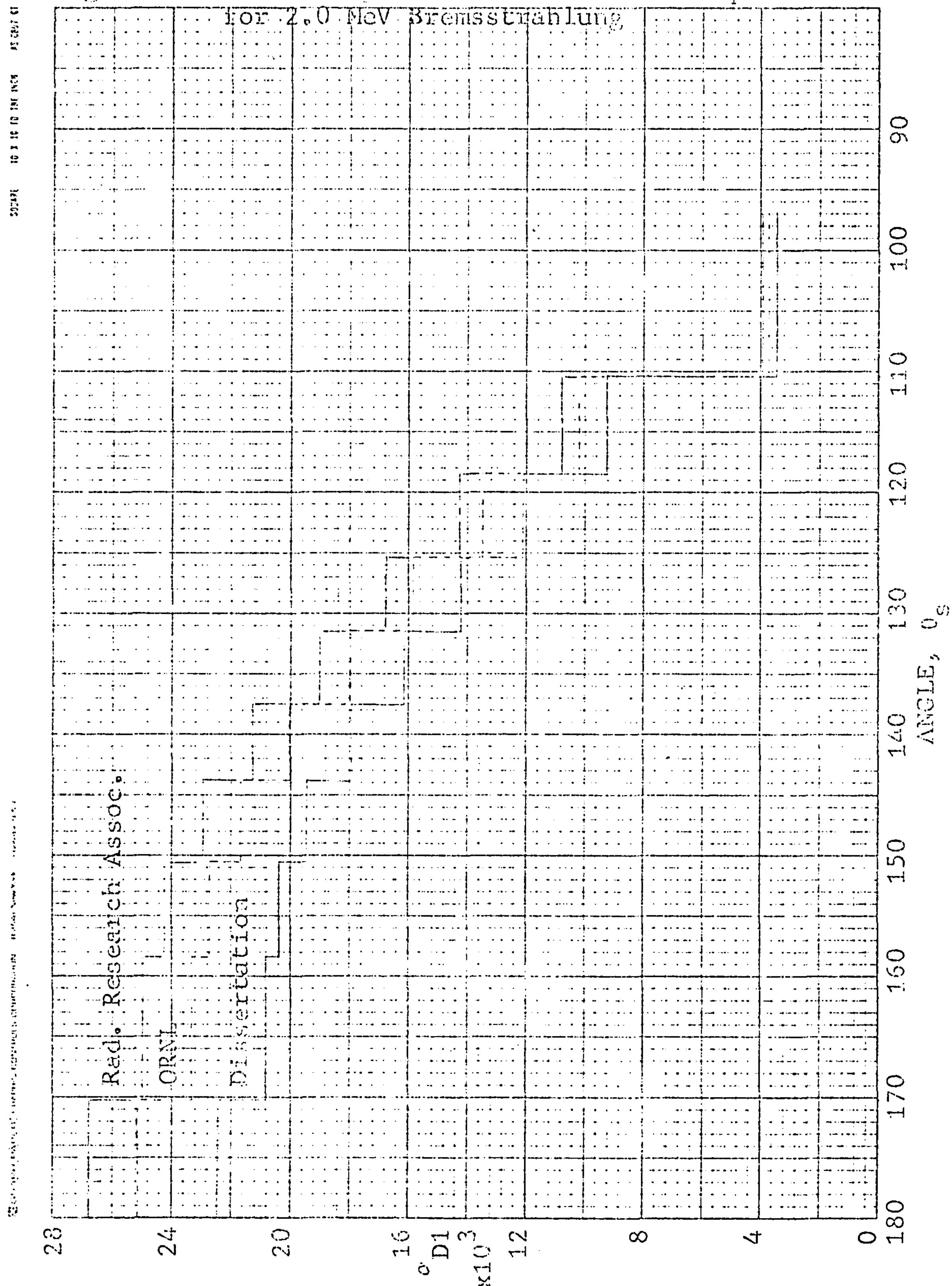

5.2 PHOTON SOURCES

5.2.1 Van de Graaff

The 2.0 MeV bremsstrahlung source used in this research was generated by an industrial radiographic Van de Graaff of High Voltage Engineering manufacture. The accelerating voltage is adjustable from 0.75 to 2.0 MeV, with sensitivity of ±40 KeV over 95% of a two hour period at 2.0 MeV. The electron beam current is adjustable from 0.01 to 0.25 milliamperes, with ±5 μamp at 0.250 milliamperes. The device generates 85 roentgens per minute at one meter. The accelerator is mounted with three degrees of freedom in a radiographic bay 19 feet wide, 26 feet high, and 26 feet from tube head to farthest wall.

Basic design and operating theory of Van de Graaffs are well discussed elsewhere (108, 109).

Beam divergence at the backscatter location is discussed in Appendix H for this and the following machines.

A previously published measured spectrum from this type of generator is given in Table 5. Rough absorption measurements were made with copper absorbers to determine an "effective energy for the beam used. These results are shown in Appendix D.

5.2.2 Flash x-ray devices (110, 111)

The 3.5, 7.0, and 10.5 MeV bremsstrahlung spectra were generated by high-energy flash x-ray generators. The major components of these machines are a low-inductance Marx generator, a Blumlein transmission line, and a field-emission vacuum tube. These components are housed within a steel cylinder filled with transformer oil for insulation.

During the charging cycle, storage capacitors are functionally placed in parallel with spark gaps acting as open circuits. When the desired charging voltage has been achieved, the power supply is electrically disconnected from the capacitor bank, and a high-voltage signal is initiated on the trigger line. Adjoining spark gaps are successively overvolted, causing the Marx generator to erect full output voltage. The negative voltage output of the Marx generator is placed on the intermediate cylinder of a folded Blumlein transmission line. During Blumlein charging, the outer and central cylinders, across which the tube is electrically located, are held near ground potential. When the Marx generator has erected to approximately 90 percent of its full output voltage, the Blumlein switch, between the central and intermediate cylinders, experiences self-breakdown, launching a traveling wave in the inner coaxial line. The voltage pulse formed by the Blumlein structure is impressed across the x-ray tube which consists of an insulating and vacuum-holding structure, a field emission cathode, and an anode.

The x-ray mode anode is a thick, high-Z target (generally tungsten) for maximum efficiency in generation of bremsstrahlung radiation by deceleration of the electrons. A thick aluminum plate filters the remaining electrons and low energy x-rays from the beam as it is extracted into the experimental area. The output characteristics of the machine are dependent upon numerous parameters, including charge voltage, anode-cathode gap configuration, Blumlein oil gap, switch spacing, and the post-pulse switch position. Because of the complexity of calculations and measurements of these quantities and the large number of combinations of machine parameters, photon intensity and spectrum as a function of position and time are not totally available either in experimental or theoretical form. That which is known of the beam produced by the machine used in this research is discussed in the following sections.

5.2.2.1 3.5 MeV Generator

The Relativistic Electron Beam Accelerator (REBA) is a Sandia Corporation designed, Sandia built experimental device. The primary purpose of this device is to study the deposition of energy in material by electron beams. By placing a high Z plate in the beam one can generate a bremsstrahlung photon spectrum. The time during which the experiments of this dissertation were carried out, is essentially the only time at which REBA has been operated in the x-ray mode. There exists, therefore, very little information about the x-ray beam. Various spectra for possible photon distributions are given in Appendix D. A few measurements were made with copper absorbers to give some idea of the beam quality. A plot of this determination is shown in Figure 41.

The beam intensity per burst of REBA at the point of backscatter was lower than required for good measurement. Therefore, a number of shots were made for each measurement to acquire sufficient dose. This had the effect of averaging out the machine's performance, as generators of this sort tend not to reproduce exactly from burst to burst. A sample set of shot parameters (tube voltage, V_T; and tube current, I_T) are given for REBA in Table 2. Tube voltage varied from averages of 3.38 to 3.52 MeV in the sets of experiments run for this paper. There is reason to believe (112) that these voltages may be high by as much as 10-15 percent. The tube output was monitored and normalized for each set as discussed in Section 6.

REBA consists of a single capacitor bank system which may dump into either of two Blumlein transmission lines (Figure 11). The irradiation cell in which the experiments discussed here were conducted was 14 feet wide, 15 feet from tube head to opposite wall and essentially open topped.

TABLE 2

REBA SHOT CHARACTERISTICS

TUBE VOLTAGE V_T (Mv)	TUBE CURRENT I_T (kA)
3.50	40.0
3.40	38.2
3.35	38.6
3.40	38.2
3.27	38.2
3.37	38.2
3.25	35.0
3.53	39.8
3.54	39.1
3.54	38.2
3.54	38.2
3.26	38.2
3.62	41.0
3.26	36.8
3.54	39.6

$$(V_T)\ \text{avg} = 3.42 \pm 0.13\ (3.71\%)\ \text{Mv}$$

$$(I_T)\ \text{avg} = 38.49 \pm 1.40\ (3.64\%)\ \text{kA}$$

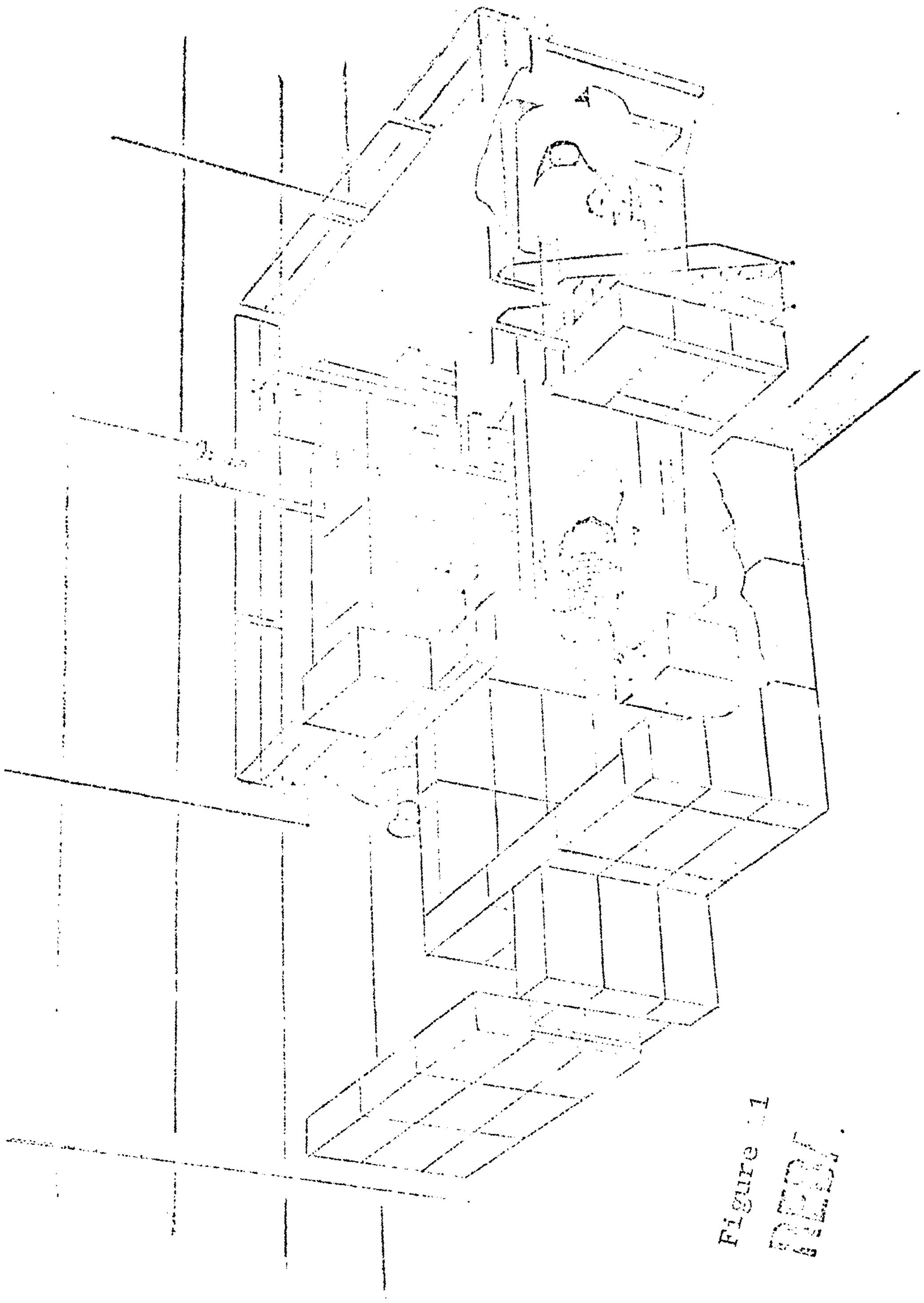

Figure 1

5.2.2.2 7.0 MeV Generator

The Transient Radiation Effects Facility (TREF) (113) is an Air Force Special Weapons Center laboratory designed for conducting transient radiation effects experiments to assess the survivability of systems in a prompt gamma radiation environment. The facility is perhaps less generator development oriented than Sandia, but due to the high priority of systems requiring tests in these environments, and the operating expense (~$1000/day) little more is known about the x-ray beam of the 7.0 MeV PulseRad 1590 (Figure 12) than that of the two other flash x-ray machines (REBA and HERMES II). Some absorption measurements have been made with absorbers of various atomic number which indicate an effective value of 4.1 - 4.2 MeV (114). Filtration of the output beam of TREF is somewhat (0.7934 cm Al and 0.076 cm Ta) heavier than that of REBA or HERMES (at the time of these measurements). To the primary purpose of these machines, this excess is of little consequence. The effect of reducing the low energy component of the incident bremsstrahlung through filtration of the beam (Figures 49 and 50), may be of greater importance (Figure 46) to albedo measurements. These figures indicate that, as pointed out by Zol'nikov and Sukhanova (115), specification of the

PULSERAD 1590

GAMMA SIMULATOR

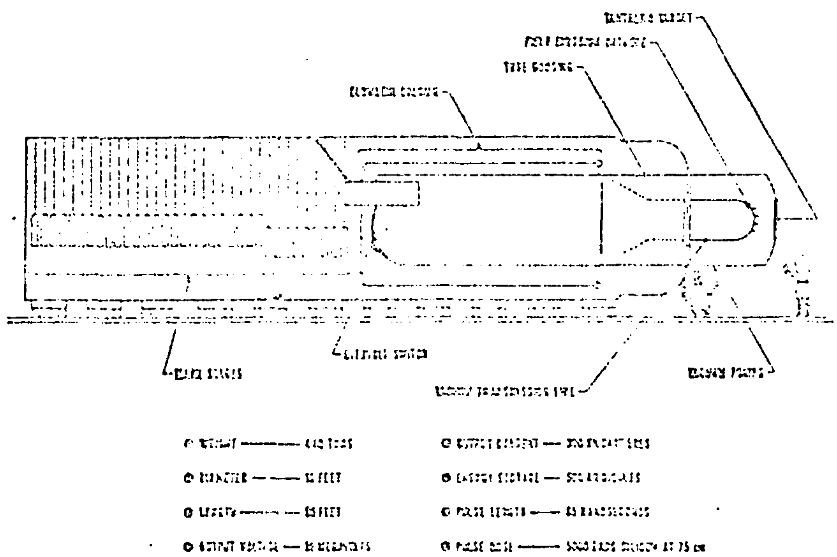

Figure 12

bremsstrahlung peak may give little information as regards albedo. This will be discussed more fully in Section 6.

The experimental area of TREF is separated from the flash x-ray device by a 10 foot high, 12 foot wide, 20 foot long RF shielded room. Facility design was such as to preclude the ready handling of the massive concrete slab used for previous backscatter experiments. Results are reported in Section 6 for iron and lead only.

Dose output for the PulseRad 1590 is rated at 4,000 rads in water at 75 centimeters per pulse. One pulse per experimental set-up was, therefore, adequate. Tube voltage varied from 6.48 to 7.10 MeV with an average of 6.98 ± 0.18 (2.57%) MeV for the shots made in this work.

5.2.2.3 10.5 MeV Generator

The second High Energy Radiation Megavolt Electron Source (HERMES II) is a Sandia designed and built flash x-ray device similar to those discussed previously. Somewhat more is known about the beam characteristics of this machine. Spectra and beam divergence are discussed in Appendix D and by Chodorow (110). Figures 13 and 14 detail the device and experimental area. Dose per pulse is about 2,500 Rad in water at one meter, and again only one burst per experimental set up was required to obtain adequate dose

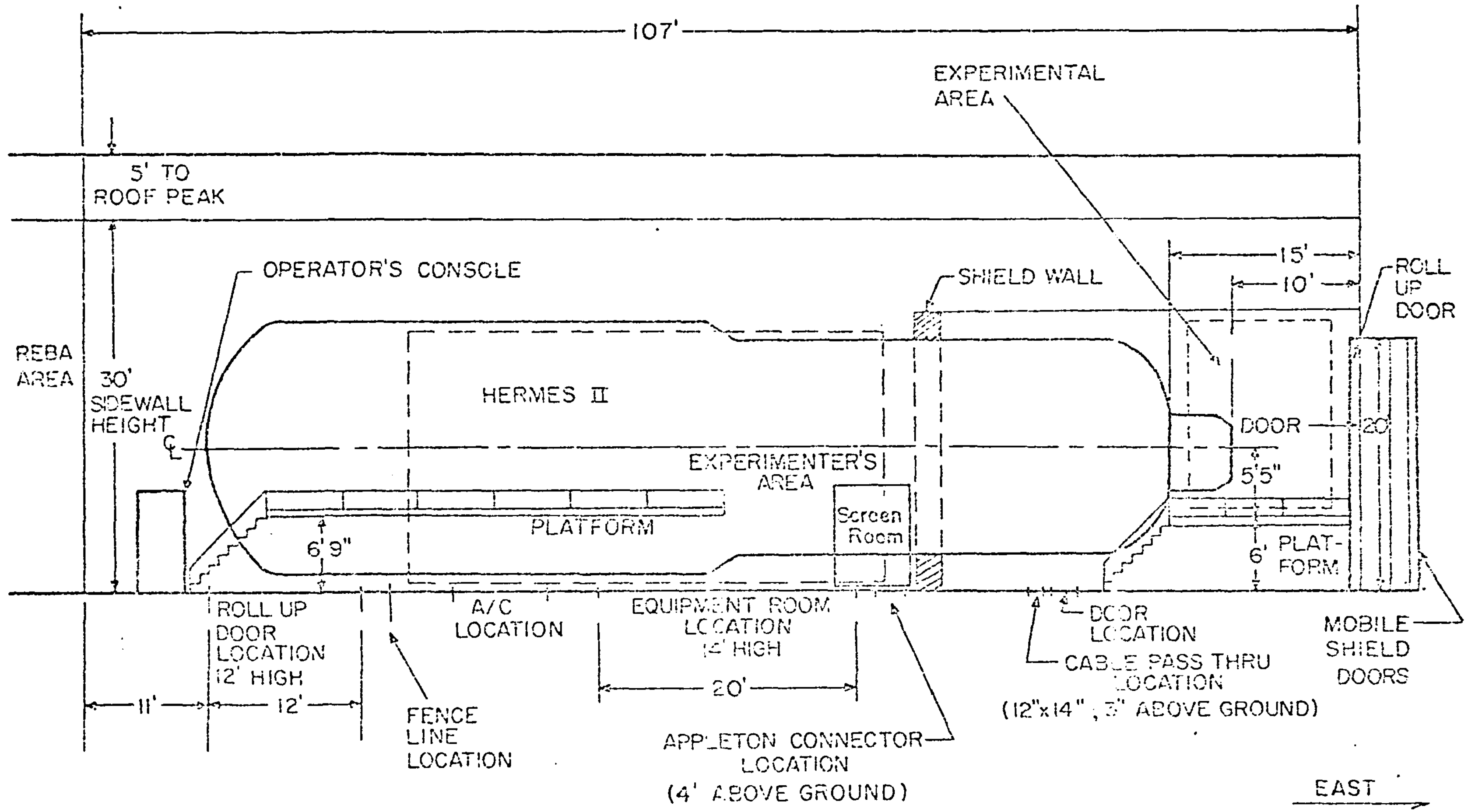

Figure 13 HERMES II

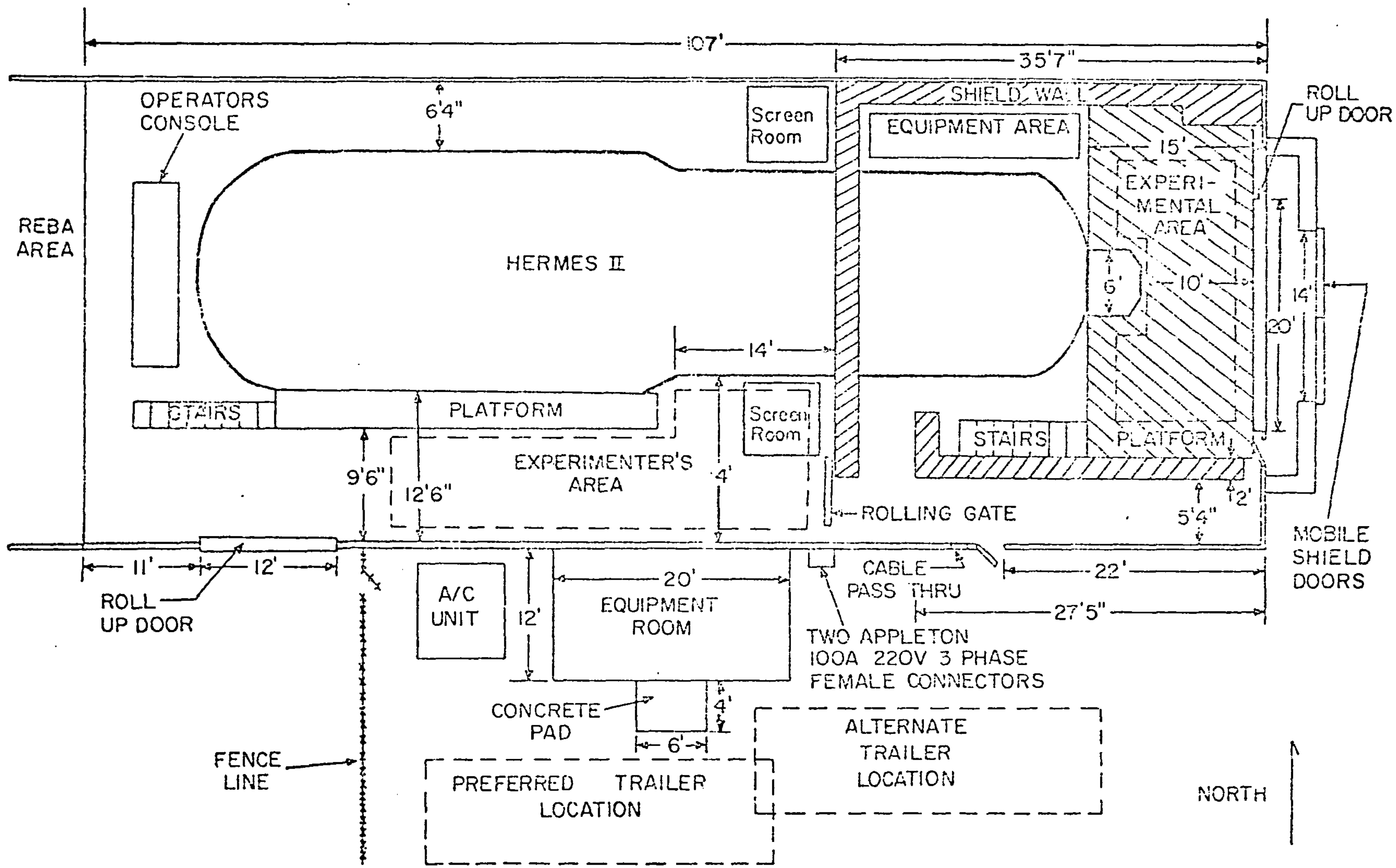

Figure 14 HERMES II

levels. Experimental configurations were repeated a number of times for statistical purposes. Peak tube voltage varied from 9.95 to 10.9 MeV with an average of 10.56 ± 0.28 (2.68%) MeV for runs made in this experiment.

5.3 BACKSCATTER SURFACE, COLLIMATOR, AND DETECTOR POSITION

The basic experimental design is diagramed in Figure 15.

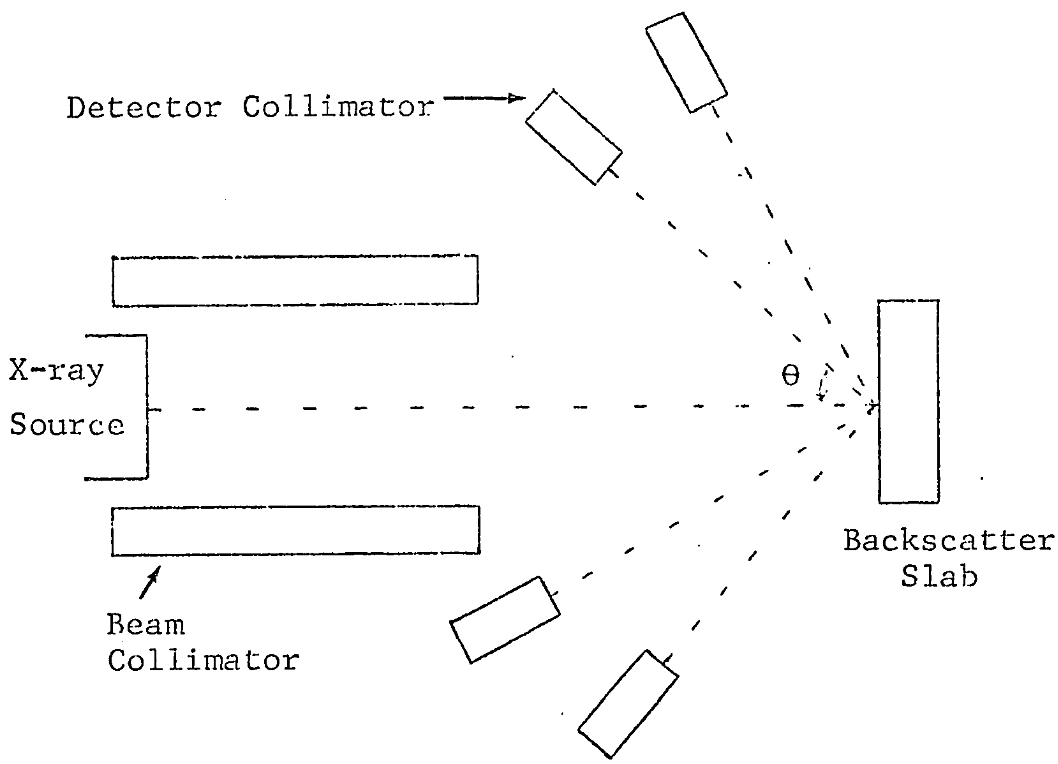

Figure 15. Experimental configuration

The x-ray source was shielded, not to restrict the beam, but to reduce air scatter at the detector locations. The beam was monitored at the center line and near the end of the beam collimator for normalization of each run.

The backscatter slab was placed normal to the x-ray beam axis at a distance adequate for uniform irradiation of the surface.

The detector collimators were placed as close to the backscatter slab as possible, without interrupting the incident beam. Distance from the slab and the angle between the slab and collimator axis determined the length of collimator required to restrict the viewed area sufficiently to maintain an "infinite" surface area slab. To provide flexibility in positioning the detector collimators and varying their length, the collimators were made up in segments. Standard lead bricks (2" x 4" x 8") were center drilled with 1.00" ID holes. One inch diameter copper rod was cut into 2.0, 3.0 and 4.0 inch lengths and center drilled with 0.50" ID holes. 0.25" slugs were cut from the copper rod to provide back-up shields. The copper was then pressure fitted to the lead and un-drilled lead bricks used around the assembly for additional shielding.

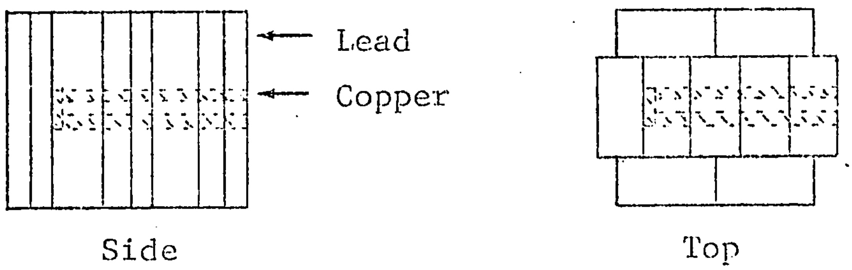

Figure 16. Detector collimator

The thermoluminescent dosimeters were packaged in polyethene bags and centered at the back of the detector collimator. The dosimeters were calibrated to Co-60 in the same configuration, so all results are measured in dose in LiF equivalent to Co-60.

The collimator lengths and detector distances used in individual measurements are given with the TLD data in Appendix I.

6. EXPERIMENTAL RESULTS

6.1 DATA ANALYSIS

The Radiation Shielding Information Center's report on Neutron and Gamma-Ray Albedos (1) defines three types of differential albedos for which the particle flux has been weighted by a dose response function: $\alpha_{D1}(E_o, \theta_o, \theta, \phi)$, differential current out (in dose units) per incident flux (in dose units); $\alpha_{D2}(E_o, \theta_o, \theta, \phi)$; differential current out (in dose units) per incident current (in dose units); and $\alpha_{D3}(E_o, \theta_o, \theta, \phi)$; differential flux out (in dose units) per incident flux (in dose units). As the incident beam is normal to the reflecting slab ($\theta_o = 90^o$), α_{D1} and α_{D2} are identical for the present research and may be defined as the ratio of the particle current (in dose units, $\mathcal{D}_R$, per steradian reflected in the direction θ, ϕ) to the dose, D_o, due to incident particles of energy, E_o.

$$\alpha_{D1} = \alpha_{D2} = \frac{\mathcal{D}_R}{D_o} \qquad \text{Eq. 6.1}$$

The experimental determination of D_R and D_O, and transformation to a form comparable to computer estimates, is not straight forward. Measurement of the incident dose at the backscatter surface would result in a measurement of the incident dose plus a reflected dose, which is substantial due to the solid angle intercepted by the detectors being located at the scatter surface. (This is the quantity defined by Johns [109] as backscatter.) Therefore, two runs were made for each individual albedo measurement, one background and the other backscatter. During the background run, thermoluminescent dosimeters (TLD's) were located at the point where the center of the backscatter slab was to be placed for the albedo measurement, another set of TLD's was located midway between the x-ray target and the backscatter slab, and TLD's were located in each collimator to measure the background for that particular configuration due to air scatter, shield penetration, etc. The dosimeter positions were the same for albedo measurements less the set at the backscatter location (Figure 15). The TLD's monitoring the beam between the x-ray target and backscatter slab were never less than thirty inches to the slab. At this point the backscatter contribution was less than 0.5%. The dose actually deposited at the slab's surface was then calculated from measurements made during each of the runs.

$$DD = DI \left(\frac{BCS}{BCG}\right) \left[\frac{_{inc}\left(\frac{\mu_{en}}{\rho}\right)_{slab}}{_{inc}\left(\frac{\mu_{en}}{\rho}\right)_{LiF}} \right] \qquad \text{Eq. 6.2}$$

where:

DD = dose deposited at slab surface center during backscatter measurement

DI = dose deposited in TLD's during background run at same distance from x-ray target as DD

BCS = dose in TLD at some point between backscatter slab and x-ray target

BCG = dose in TLD at same point as BCS during background run

$_{inc}\left(\frac{\mu_{en}}{\rho}\right)_{slab}$ = mass energy-absorption coefficient for the slab material and the incident beam

$_{inc}\left(\frac{\mu_{en}}{\rho}\right)_{LiF}$ = mass energy-absorption coefficient for LiF and the incident beam

The dose to the slab surface was then averaged over the viewed area to account for beam divergence (Appendix H) to obtain D_o.

$\left(\frac{\mu_{en}}{\rho}\right)_{inc}$ is an effective value for the particular incident beam (Appendix D) considered and is estimated by:

$$\left(\frac{\mu_{en}}{\rho}\right)_{inc} = \frac{\sum_i \left(\frac{\mu_{en}}{\rho}\right)_i E_i}{\sum_i E_i} \qquad \text{Eq. 6.3}$$

where $\left(\frac{\mu_{en}}{\rho}\right)_i$ is the mass energy-absorption coefficient at the average energy of the "i"th energy interval and E_i is the amount of energy in that interval.

The backscatter measurement was corrected for a background normalized to the backscatter input dose and expressed in terms of water dose.

$$BS = \left[DR - DBG\left(\frac{BCS}{BCG}\right)\right]\left[\frac{\text{ref}\left(\frac{\mu_{en}}{\rho}\right)_{H_2O}}{\text{ref}\left(\frac{\mu_{en}}{\rho}\right)_{LiF}}\right] \qquad \text{Eq. 6.4}$$

where:

BS = dose in water reflected by the backscatter slab at some angle and distance

DR = dose in TLD measured at same position as BS during backscatter run

DBG = dose in TLD measured at same position as BS during background run

$_{ref}\left(\frac{\mu_{en}}{\rho}\right)_{H_2O}$ = mass energy-absorption coefficient for water and reflected beam

$_{ref}\left(\frac{\mu_{en}}{\rho}\right)_{LiF}$ = mass energy-absorption coefficient for LiF and the reflected beam

$\left(\frac{BCS}{BCG}\right)$ as defined in Eq. 6.2

$_{ref}\left(\frac{\mu_{en}}{\rho}\right)$ is an effective value for the particular reflected beam spectrum (Appendix D) considered.

To determine the backscattered dose per steradian, BS was divided by the effective viewed solid angle of the particular collimator system used.

$$\Omega_\epsilon = \frac{A_\epsilon}{d^2} \qquad \text{Eq. 6.5}$$

where: A_ϵ = effective viewed area normal to the collimator axis (Appendix B)

d = detector to slab distance

The differential dose current per steradian is given by:

$$\mathcal{D}_R = \frac{BS}{\Omega_\epsilon} \cos \theta \qquad 6.6$$

where θ is the angle between the incident beam center line and the detector collimator axis. $\mathcal{D}_R$ has no meaning in the true physical sense, but is the form traditionally used in comparing albedo data. The differential current dose albedo per steradian, α_{D1}, may then be calculated by Equation 6.1.

Beam intensity, for machines of the nature discussed in Section 5, is most frequently given as Rad in water per burst or per unit time at some point in the beam. Calculation of the dose in any particular shielding material involves detailed information as to incident beam energy spectra. Lacking such information, another expression of albedo might be more useful in shielding calculations.

$$\alpha_{D3(H_2O)} = \frac{\mathcal{D}_{R(H_2O)}}{D_{o(H_2O)}} \qquad \text{Eq. } 6.7$$

Derivation of Eq. 6.7 would follow as Eq. 6.1 above with

$_{inc}\left(\frac{\mu_{en}}{\rho}\right)_{H_2O}$ replacing $_{inc}\left(\frac{\mu_{en}}{\rho}\right)_{slab}$ and the reflected dose being expressed as flux rather than current, a quantity with real physical meaning, useful in actual shielding calculations.

6.2 PRESENTATION OF RESULTS

Figures 17 through 27 compare the values of α_{D1} obtained experimentally with those obtained by the Monte Carlo program (Appendix K), the DTF program (Appendix L) and the Chilton-Huddleston formulation (Appendix N).

Error limits on the experimental points are discussed in Appendix J. Error bars for the Monte Carlo runs are not shown in an effort to avoid cluttering the graphs. In each plot, 200,000 case histories were run with a deviation of around ±8.5% for iron at 10.5 MeV to about ±16.2% for lead at 2.0 MeV. The precise error value was dependent upon the number of photons falling in a given angular spread. These errors are much increased when requesting an energy differentiation as plotted in Appendix D. DTF and the Chilton-Huddleston representations do not have readily representable error limits.

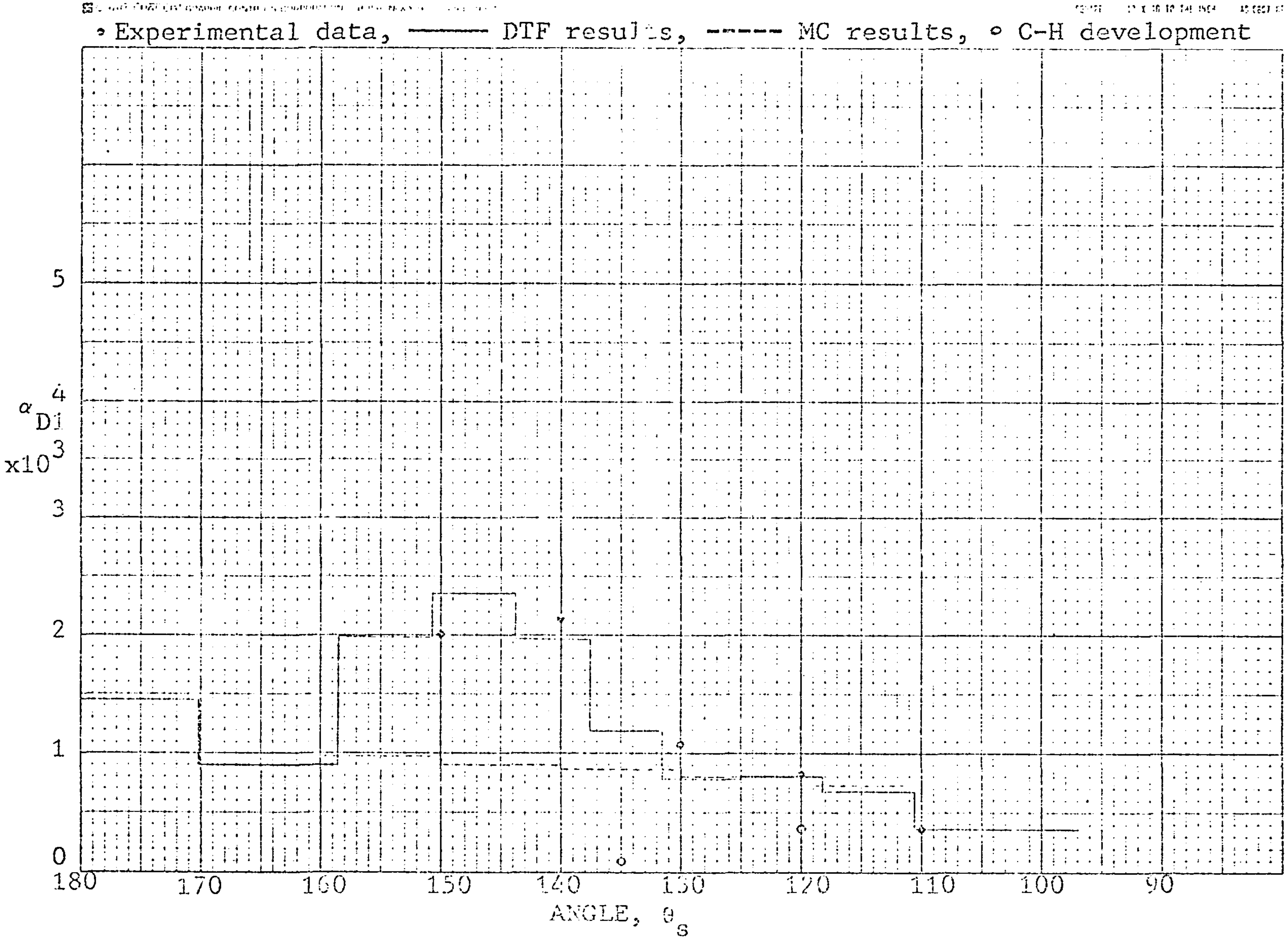

Figure 17 2.0 MeV lead scatterer α_{D1} vs Angle

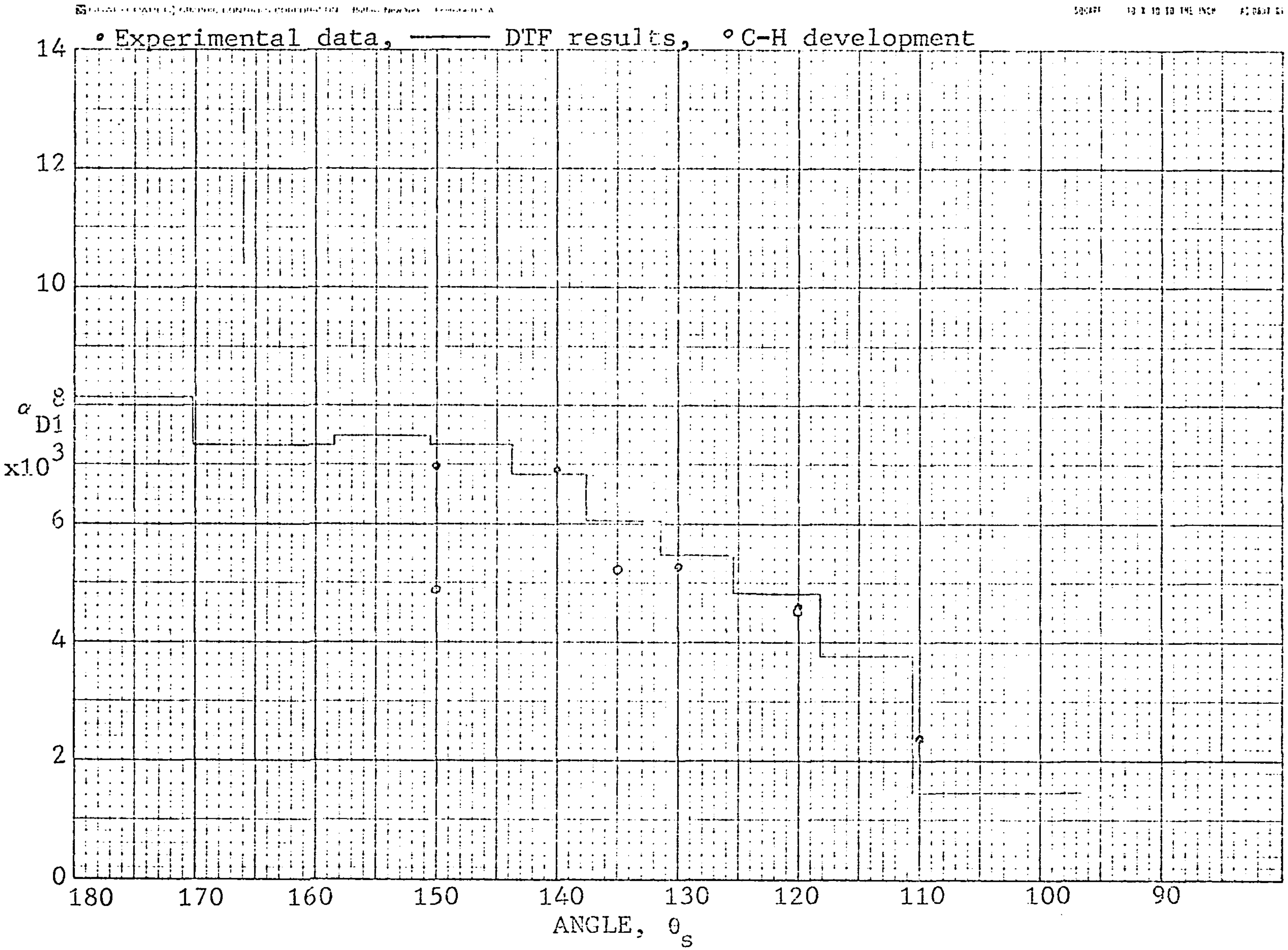

Figure 18 2.0 MeV iron scatterer α_{D1} vs Angle

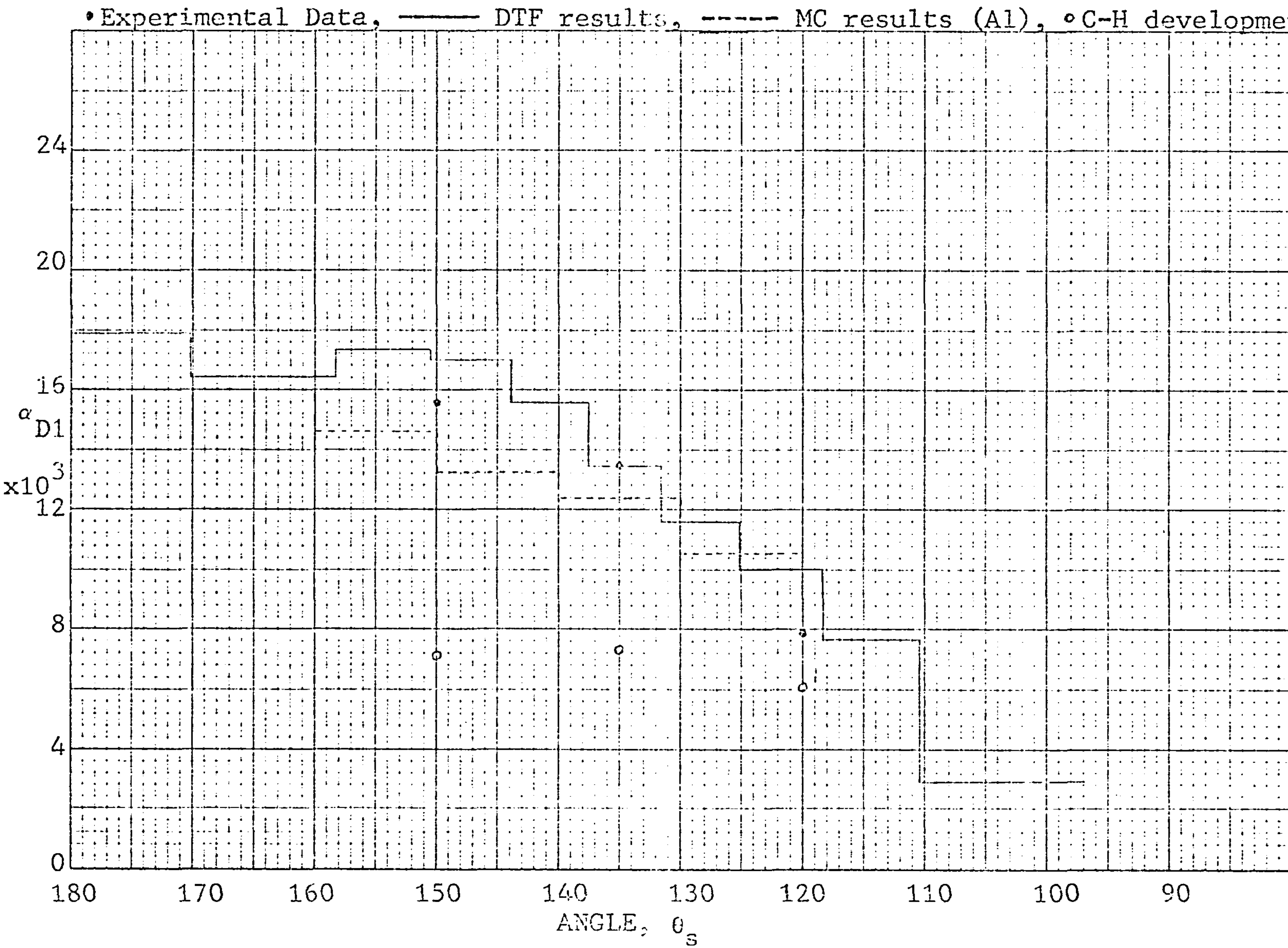

Figure 19 2.0 MeV concrete scatterer α_{D1} vs Angle

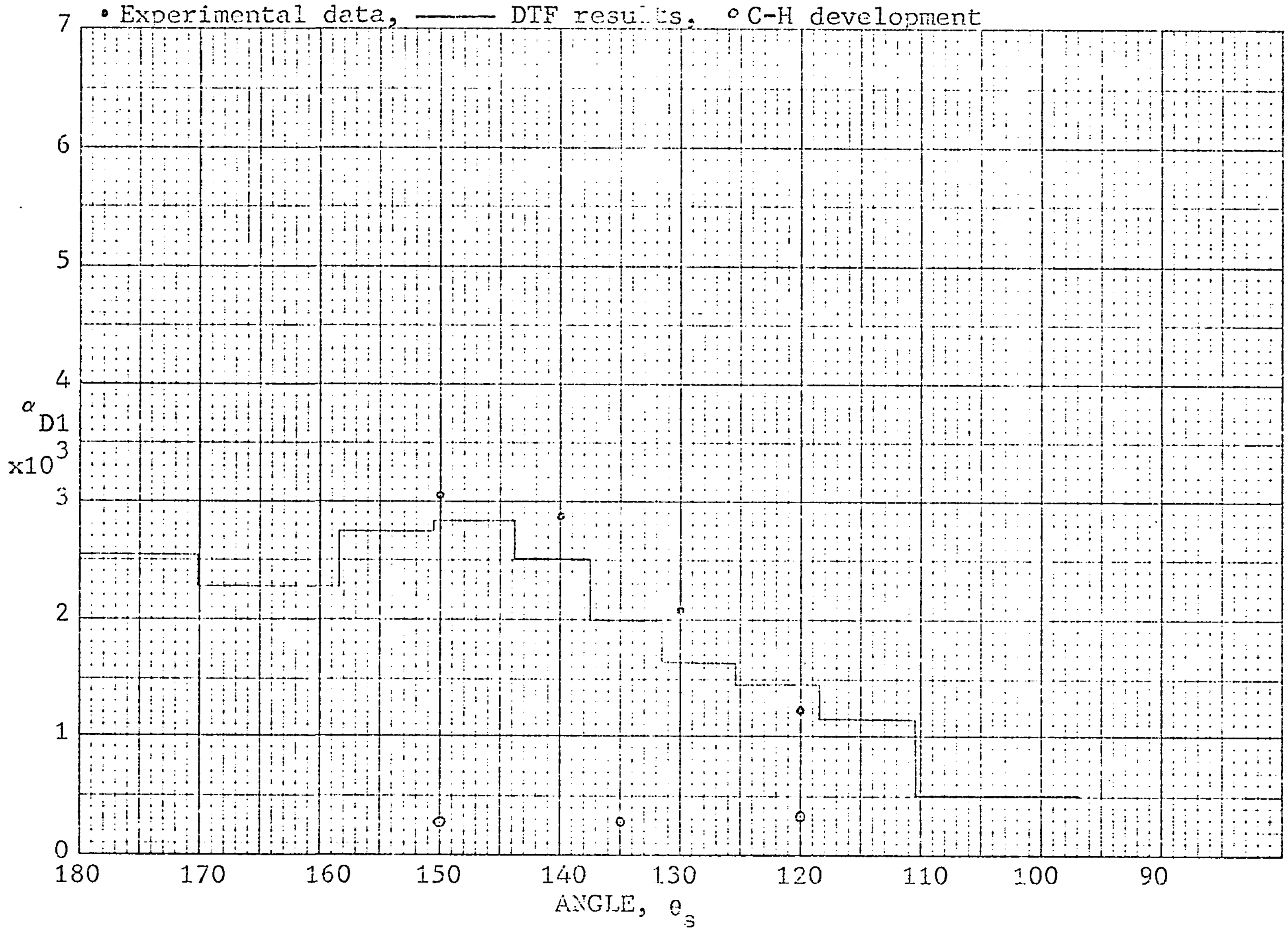

Figure 20 3.5 MeV lead scatterer α_{D1} vs Angle

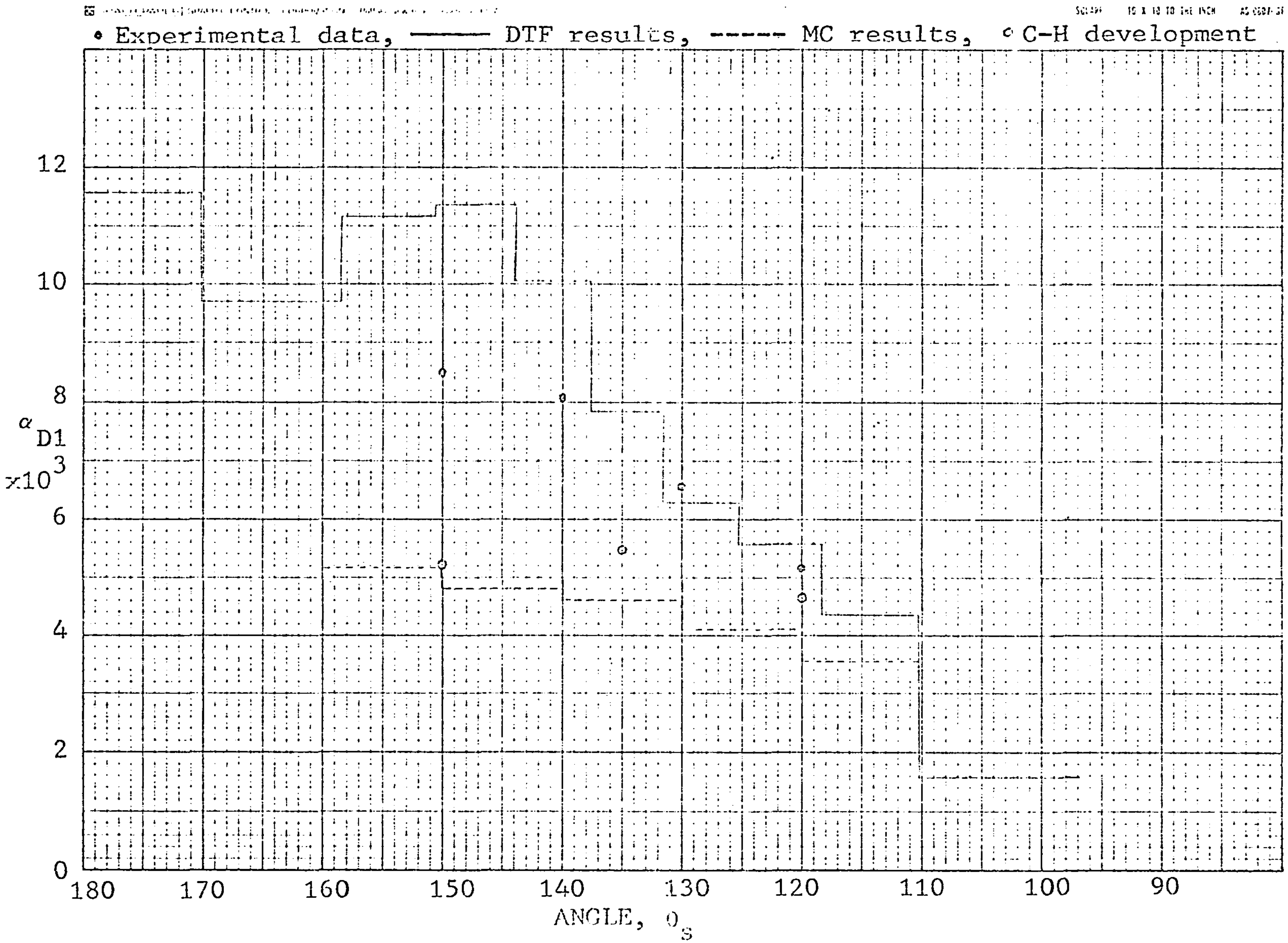

Figure 21 3.5 MeV iron scatterer α_{D1} vs Angle

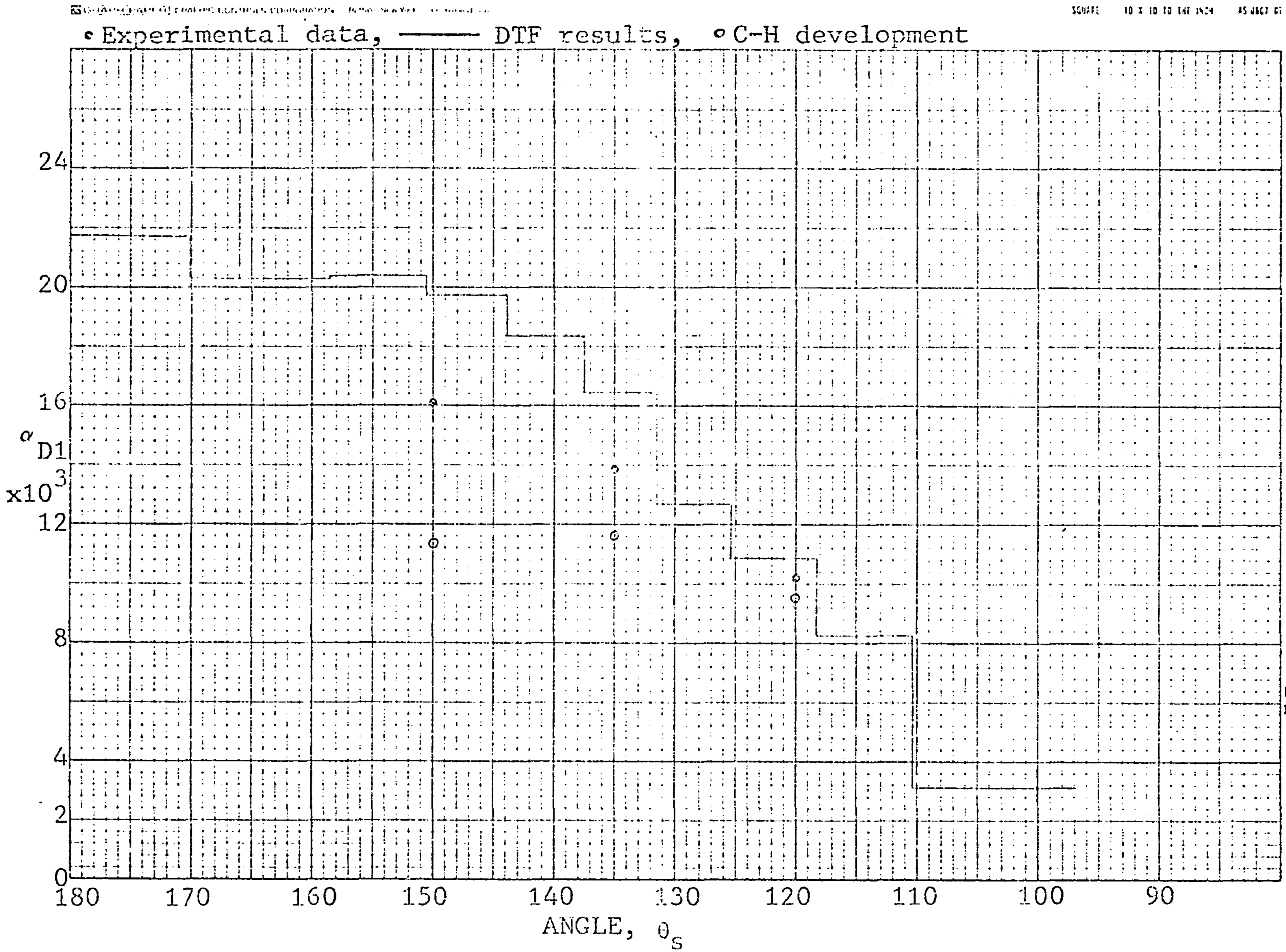

Figure 22 3.5 MeV concrete scatterer α_{D1} vs Angle

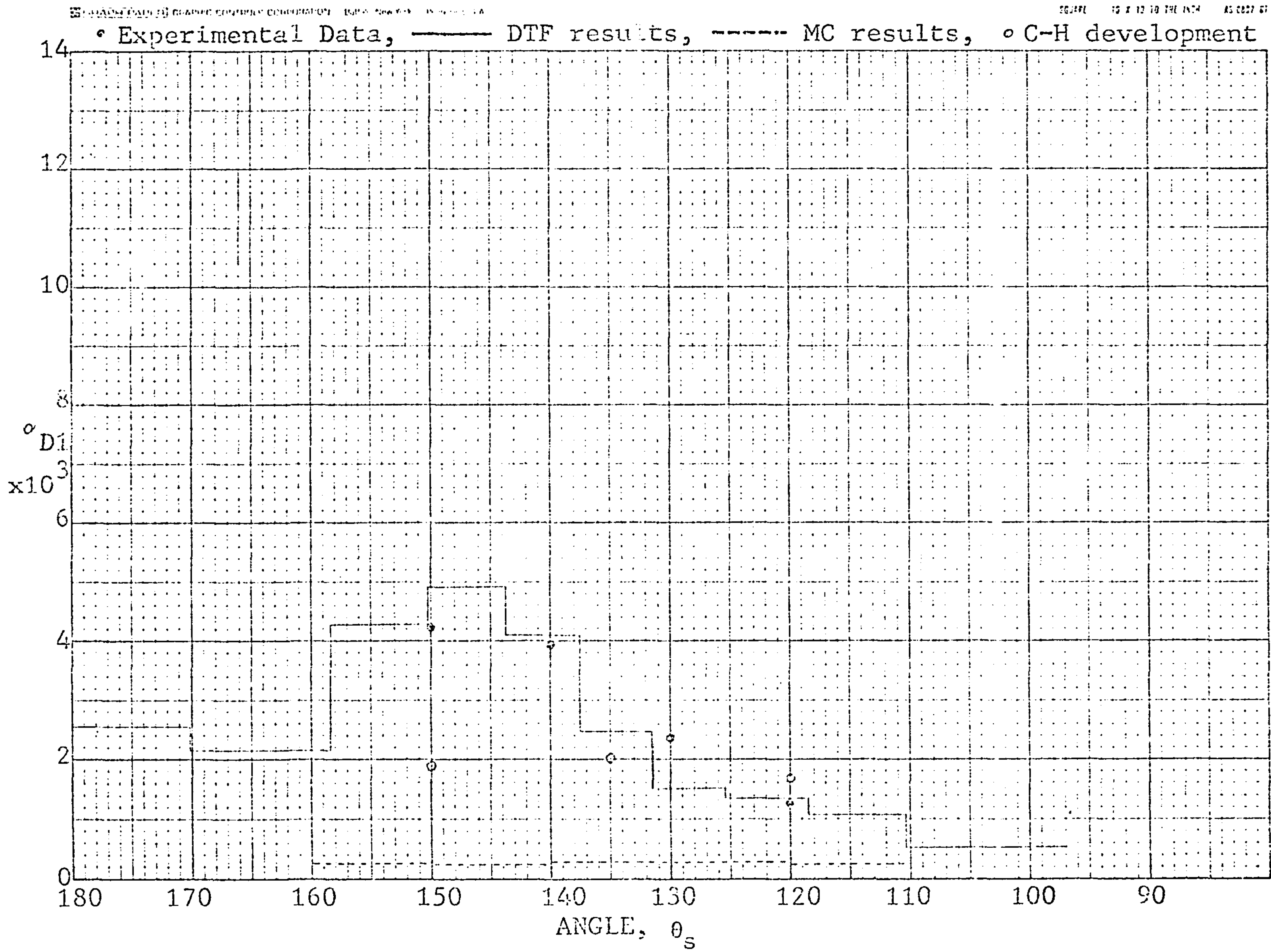

Figure 23 7.0 MeV lead reflector σ_{D1} vs Angle

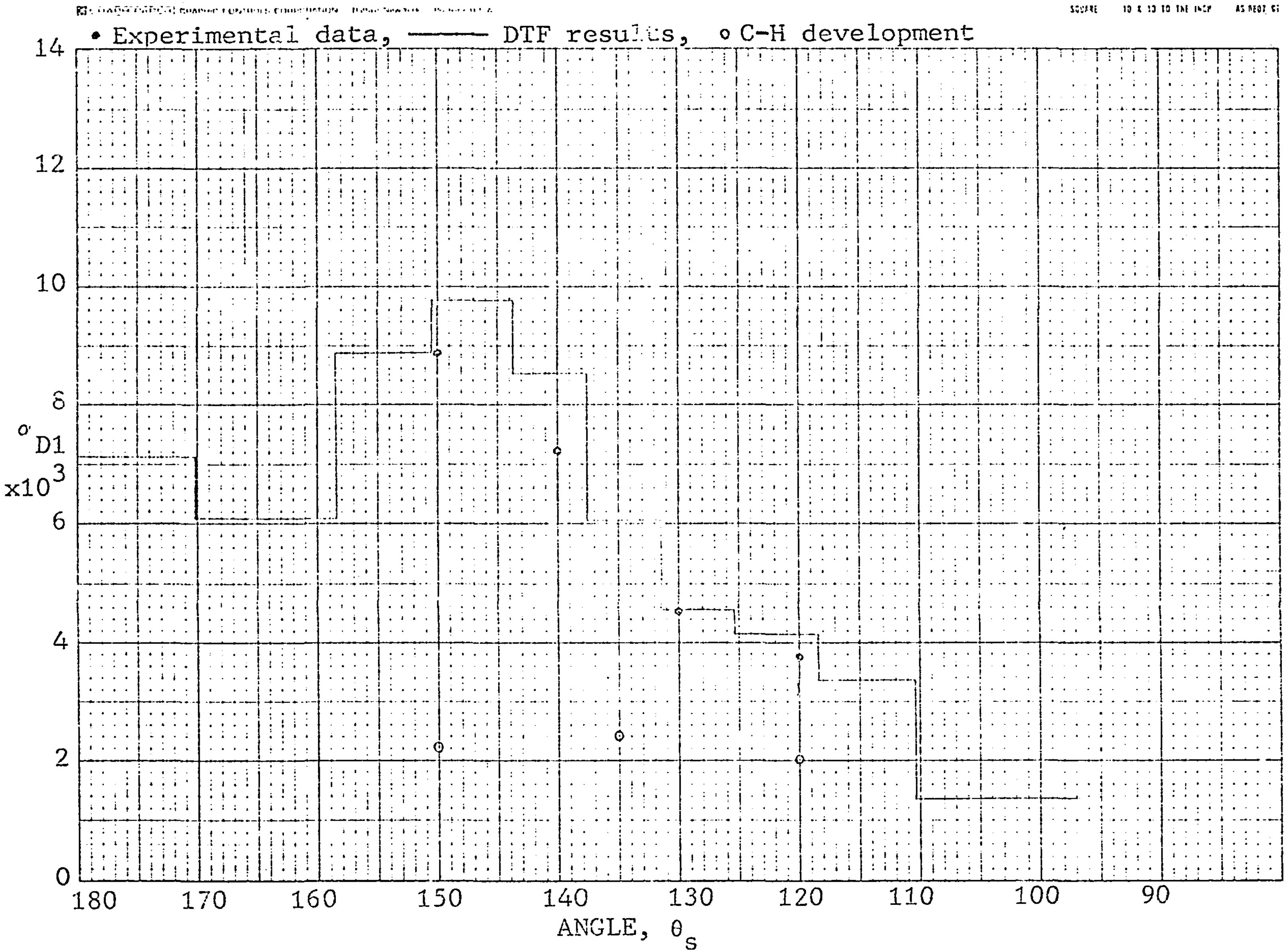

Figure 24 7.0 MeV iron reflector σ_{D1} vs Angle

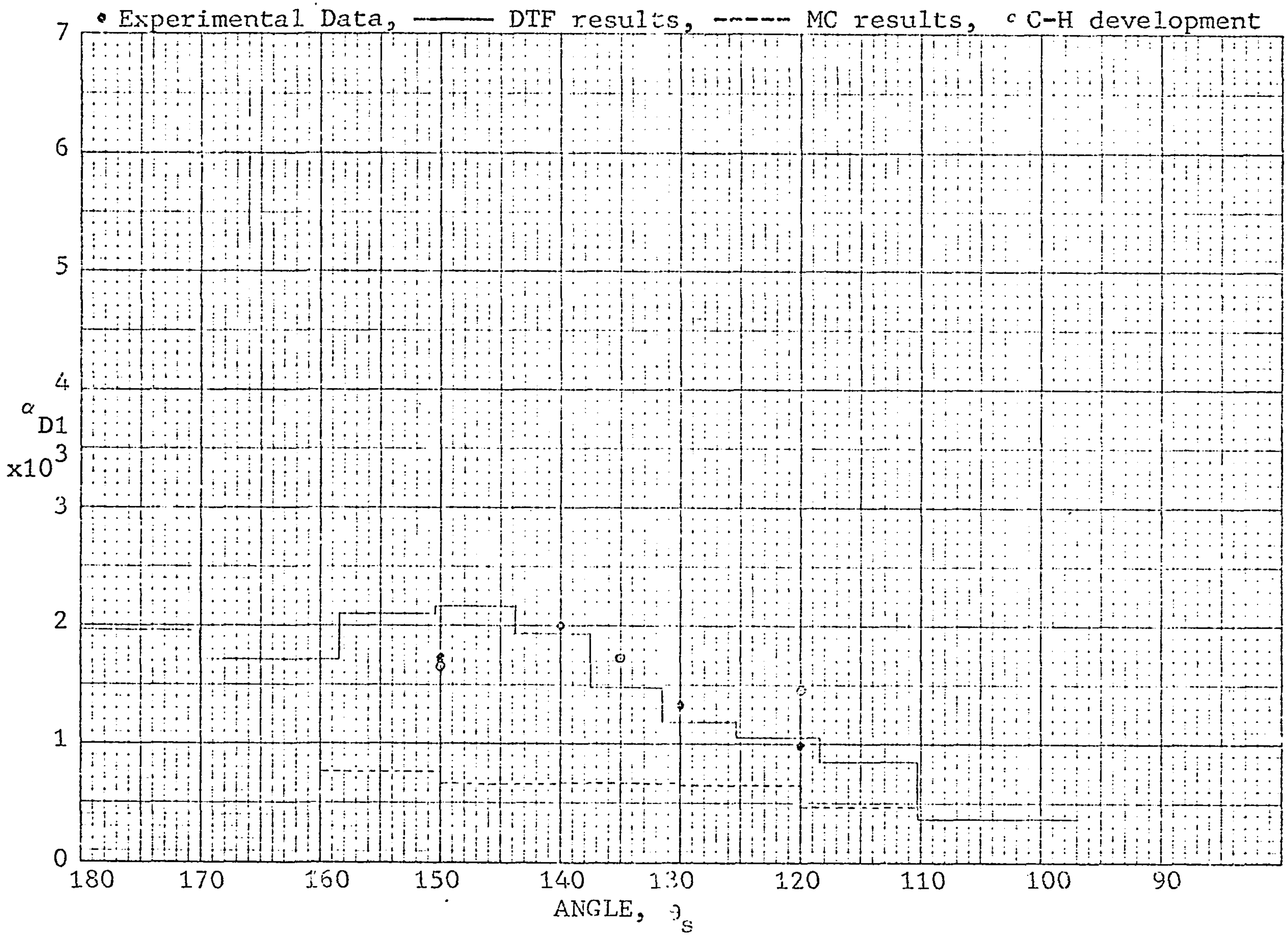

Figure 25 10.5 MeV lead scatterer α_{D1} vs Angle

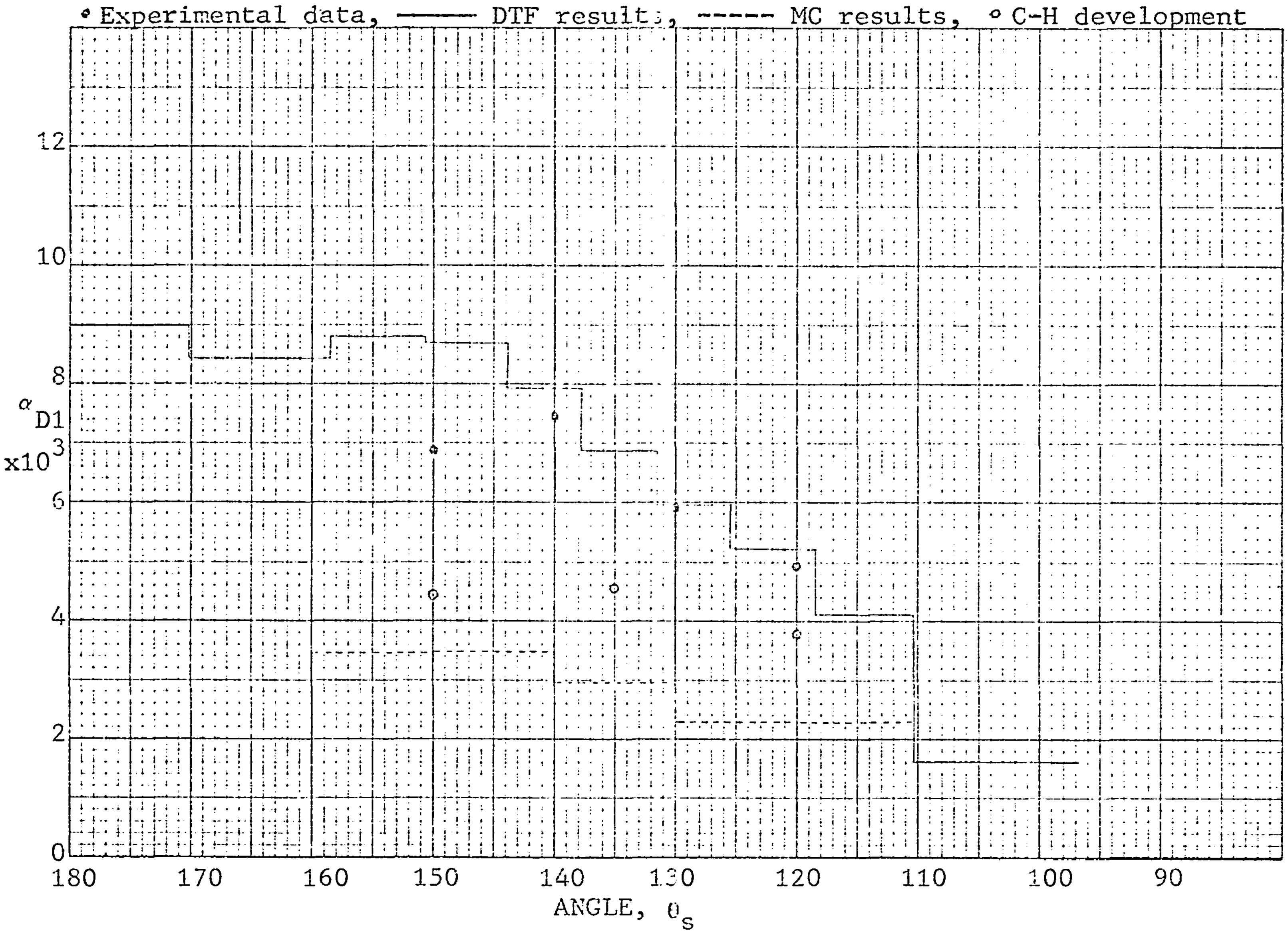

Figure 26 10.5 MeV iron scatterer α_{D1} vs Angle

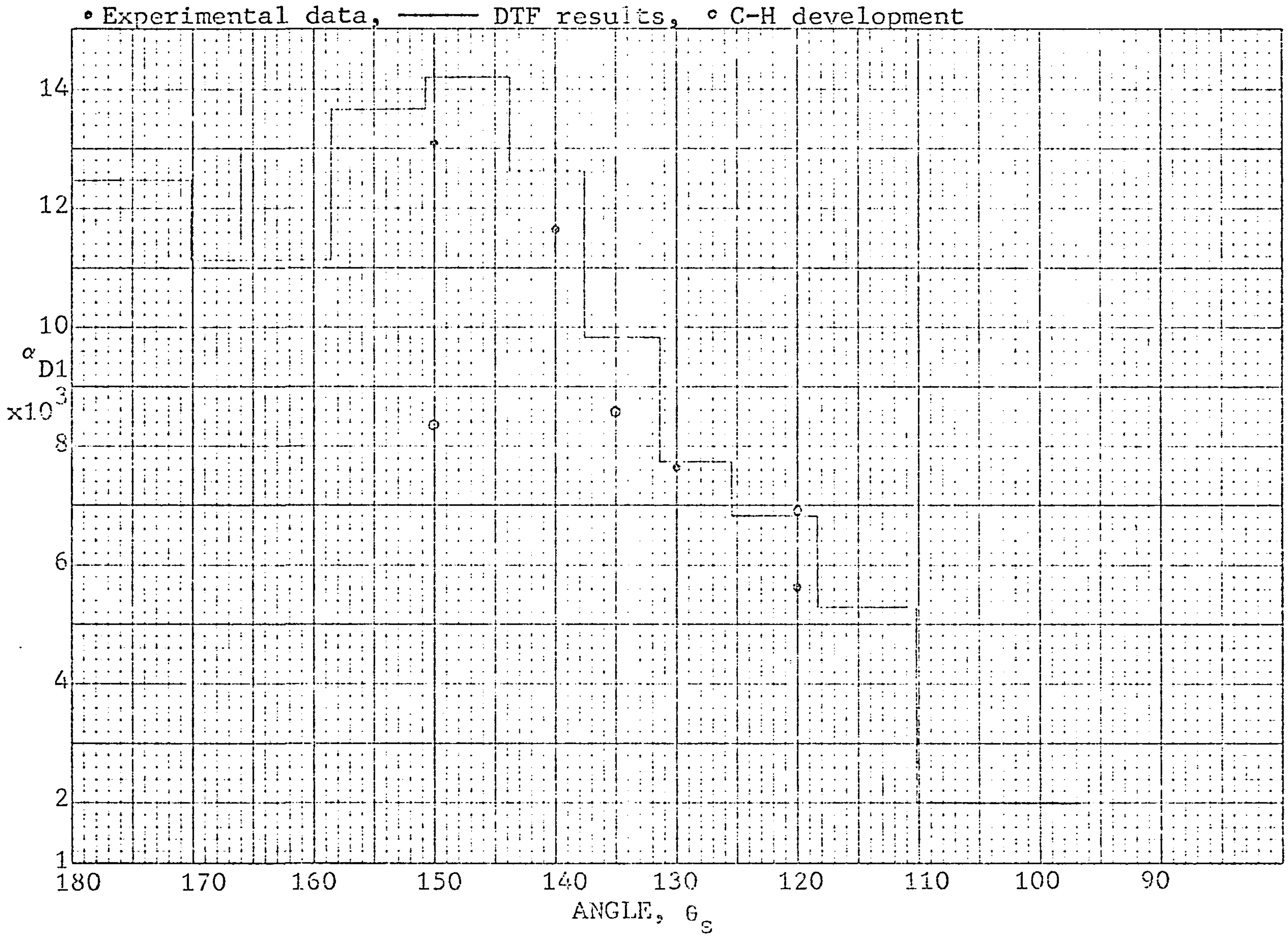

Figure 27 10.5 MeV concrete scatterer α_{D1} vs Angle

Table 3 lists the values of the differential dose in water flux albedo, $\alpha_{D3(H_2O)}$, obtained experimentally.

TABLE 3

$\alpha_{D3(H_2O)} \times 10^3$

ANGLE OF SCATTER	SCATTER MATERIAL		
2.0 MeV			
θ_s	Lead	Iron	Concrete
150°	19.10 ± 8.5%	14.05 ± 8.9%	17.96 ± 8.6%
140°	24.12 ± 9.6%	14.72 ± 9.7%	
135°			19.06 ± 14.2%
130°	14.43 ± 10.9%	14.44 ± 9.1%	
120°	19.98 ± 9.5%	15.73 ± 6.6%	15.55 ± 9.9%
110°	7.95 ± 13.0%	17.30 ± 10.4%	
3.5 MeV			
θ_s	Lead	Iron	Concrete
150°	29.76 ± 9.5%	14.17 ± 15.3%	14.99 ± 12.9%
140°	31.96 ± 13.0%	15.34 ± 11.2%	
135°			18.23 ± 9.5%
130°	27.72 ± 9.0%	14.97 ± 9.5%	
120°	10.79 ± 9.6%	15.19 ± 12.9%	19.33 ± 11.5%
7.0 MeV			
θ_s	Lead	Iron	
150°	71.26 ± 21.3%	45.19 ± 13.6%	
140°	75.98 ± 9.2%	41.58 ± 12.9%	
130°	61.79 ± 11.2%	31.08 ± 10.0%	
120°	38.11 ± 31.7%	33.18 ± 15.2%	
10.5 MeV			
θ_s	Lead	Iron	Concrete
150°	21.91 ± 13.7%	7.64 ± 11.0%	10.11 ± 16.0%
140°	29.07 ± 10.1%	9.36 ± 15.4%	10.30 ± 18.7%
130°	23.03 ± 7.4%	9.03 ± 9.4%	8.08 ± 17.1%
120°	22.55 ± 8.5%	9.83 ± 11.2%	7.80 ± 16.1%

For purposes of examining $\alpha_{D3(H_2O)}$ as a function of atomic number and maximum bremsstrahlung energy, the albedo currents are "integrated" over the angular range studied so as to have one value, $A_{D1(H_2O)}$, for each material-energy combination. This value should not be confused with A_{DJ} values published elsewhere, as the dose references differ and $A_{D1(H_2O)}$ is the current dose summed across ten degree averages for measurements of dose reflected only from 115° to 155°. Figure 28 is a plot of $A_{D1(H_2O)}$ against the bremsstrahlung peak energy and Figure 29 against atomic number.

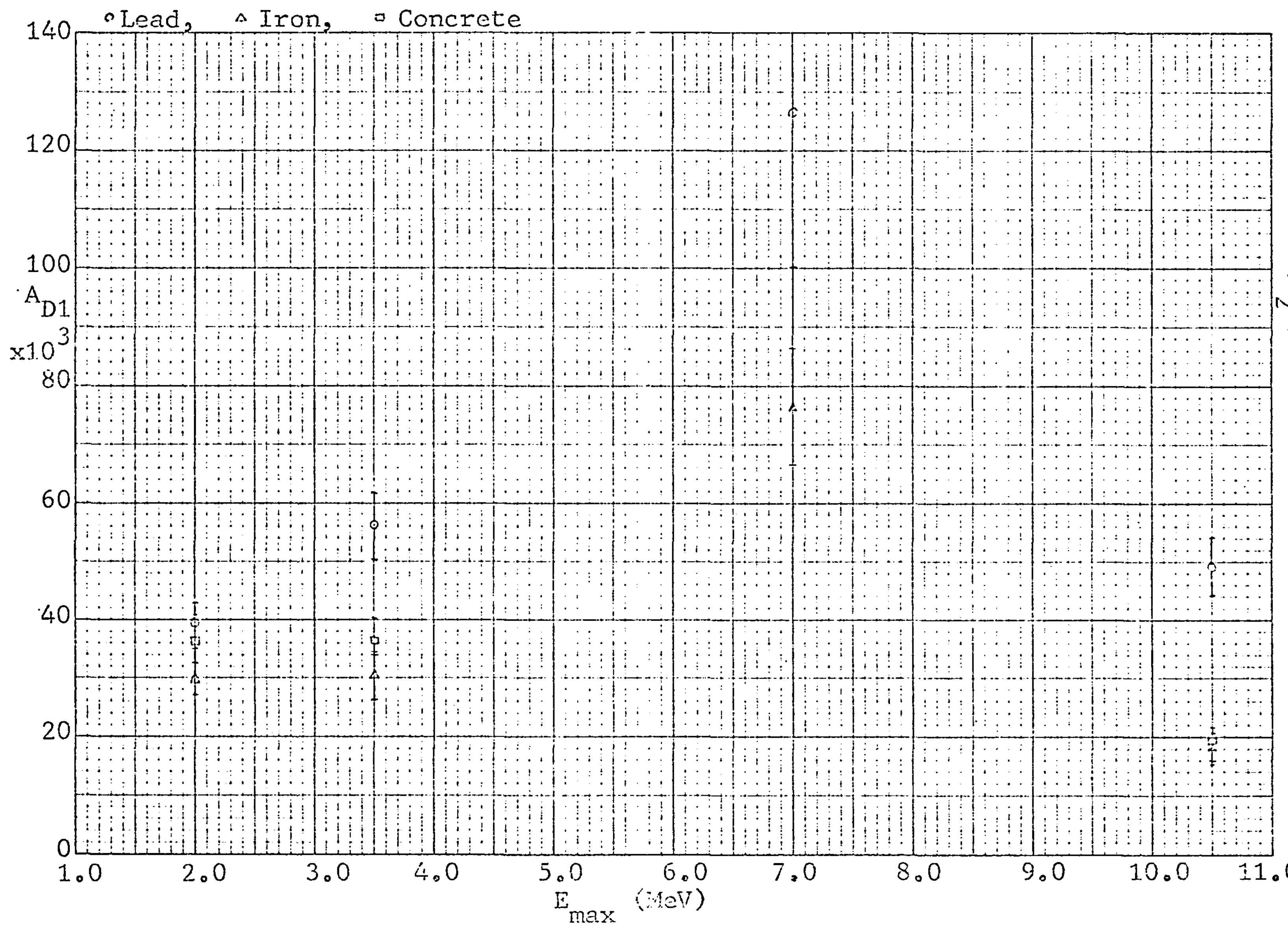

Figure 28 $A_{D1}(H_2O)$ vs E_{max}

Figure 29 $A_{D1(H_2O)}$ vs Atomic Number

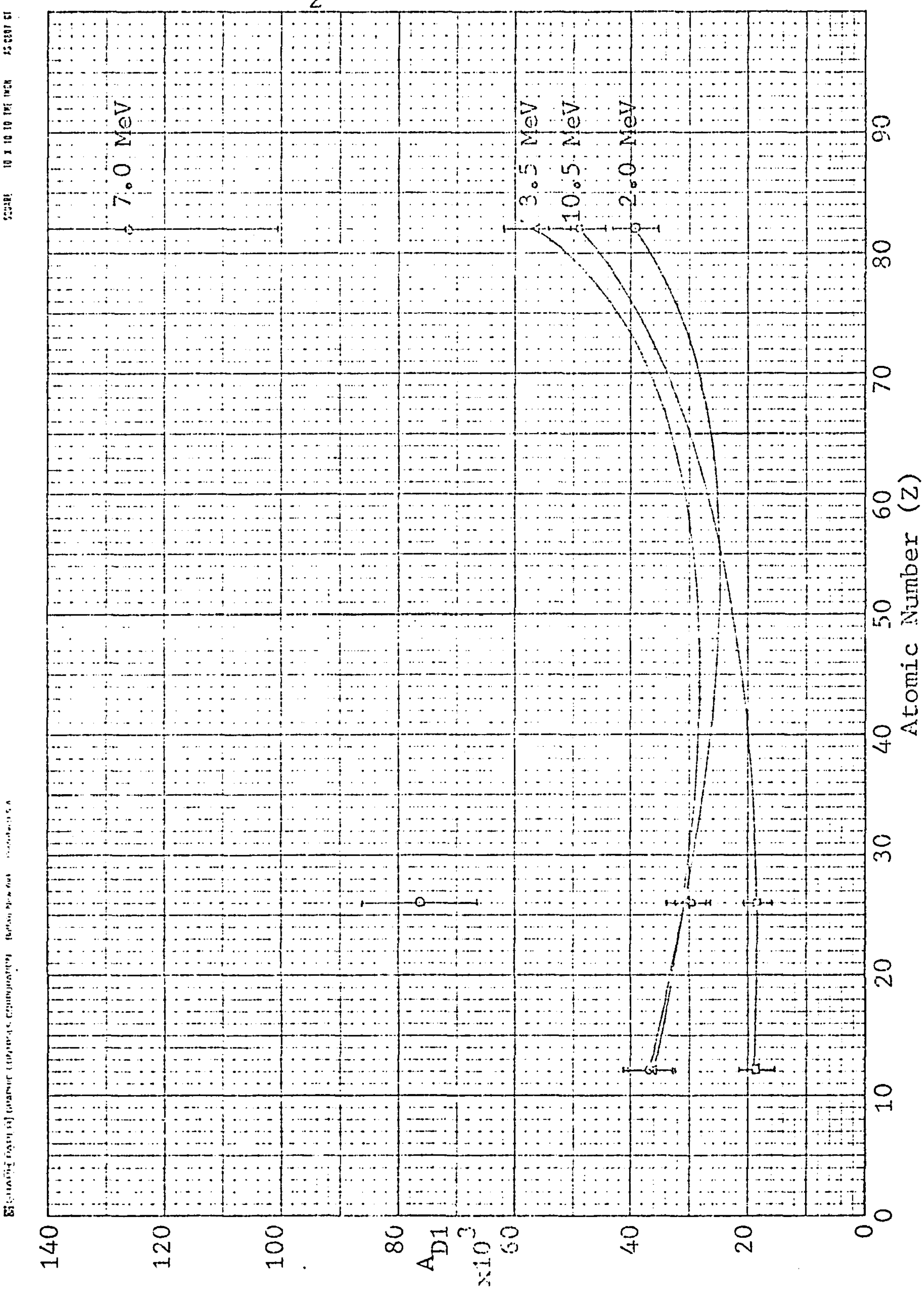

6.3 DISCUSSION OF RESULTS

In general the experimental values determined for α_{D1}, the differential dose current albedo, quite closely follow the estimate obtained from DTF, the discrete ordinate computer solution. No error limits are specified on the experimental points plotted in Figures 17 through 27 due to their very strong dependence, through the function

$$\frac{{}_{inc}\left(\frac{\mu_{en}}{\rho}\right)_{slab}}{{}_{inc}\left(\frac{\mu_{en}}{\rho}\right)_{LiF}}$$, upon the incident energy spectra

considered. Errors due to measurement are discussed in Appendix J and are similar to those given in Table 3 of Section 6.2.

Results of the Chilton-Huddleston approximation are generally lower than the experimental data, in particular at the higher scattering angles. Still these numbers are within the order of error often accepted in radiation shielding estimates and though unfortunately low, they are not as low as results obtained with the Monte Carlo program used here. As fluorescence is not considered in the Chilton-Huddleston development, the generally poor fit with lead might be expected.

Error limits for the $\alpha_{D3(H_2O)}$ values in Table 3 are given with each value. This limit includes those errors considered in Appendix J and the error introduced by

$$\left[\frac{{}_{inc}\left(\frac{\mu_{en}}{\rho}\right)_{H_2O}}{{}_{inc}\left(\frac{\mu_{en}}{\rho}\right)_{LiF}}\right]$$

due to various incident energy spectra.

This factor is not nearly so variant as $\left[\frac{{}_{inc}\left(\frac{\mu_{en}}{\rho}\right)_{slab}}{{}_{inc}\left(\frac{\mu_{en}}{\rho}\right)_{LiF}}\right]$

due to the absorption coefficient of LiF rather closely following that of H_2O throughout the spectra (Appendix E).

$$\left[\frac{{}_{ref}\left(\frac{\mu_{en}}{\rho}\right)_{H_2O}}{{}_{ref}\left(\frac{\mu_{en}}{\rho}\right)_{LiF}}\right]$$

is the same in either data set and also

does not widely vary (~ 5% over the reflected spectra considered in Appendix D).

The values for $A_{D1(H_2O)}$ are for comparison within this data set only and the error limits given in those plots are an indication of the measurement errors only, not considering the practice of integrating over a small number of data points. The summation performed does, however, provide a single value for each (Z,E) combination, formed under the same conditions, by which Table 3 values may be considered for materials of different atomic number, exposed to different incident energies.

The plot of $A_{D1(H_2O)}$ against the maximum incident bremsstrahlung energy (Figure 28) tends to confirm the Zol'nikov, et al. report (115) that albedos have little dependence upon E_{max} in the bremsstrahlung spectra. The plot against atomic number (Figure 29) is very similar to other plots made from data obtained with mono-energetic sources (1). The closeness of points obtained from different reflecting materials and different incident spectra is perhaps the most interesting feature of this graph. The points at 7.0 MeV maximum, that spectrum reported to have a small low energy component, are an exception, perhaps indicating the energy contributions below a few hundred KeV to be more important in albedo considerations than the rest of the spectrum. This concept is explored, by computer, in Appendix D.

7. CONCLUSIONS AND RECOMMENDATIONS

Differential dose flux albedos were measured experimentally for broad-beam, normally incident bremsstrahlung spectra photons reflected from common shielding materials. These values were translated, through dose absorption ratios and angular relationships, to differential dose current albedos for comparison to various methods of estimating albedo. The comparison of experimental data to results of the discrete ordinates computer program (DTF) output was excellent, though the reliability of this fit is unknown due to the limited spectra information available on the generating devices studied. The results of the Chilton-Huddleston development, applied to the effective energies of the spectra studied, fall between the two computer estimates made and compare much better to the experimental results (generally within a factor of two) than might be expected considering the assumptions of this formulation. (Lead scatterers compare less well.)

The current albedo, though widely used in albedo studies, is an awkward form for shielding use as it lacks physical meaning. Typical dose albedos, where the incident dose is based on energy deposition in the reflecting body, differ considerably from albedos calculated with the normally reported incident beam dose (based on water). These differences are dependent upon the reflecting material and can be interchanged only through an accurate knowledge of the energy spectra involved. To be of greatest value to those performing shielding calculations, results of this dissertation are reported as differential flux dose in water albedo.

The albedos reported in Table 3 are much less dependent upon reflector material and bremsstrahlung peak energy than might be expected. Figure 29 indicates the low energy make-up of the incident bremsstrahlung spectra to be of considerable importance.

In addition to the primary subject of the dissertation: a DTF modification is presented which yields results in a form more convenient to radiation protection use (Appendix L); and a thermoluminescent dosimeter annealing procedure is developed which greatly facilitates dosimeter handling, while losing none of the advantages of other procedures in terms of reliability and stability (Appendix F).

The following areas might be of interest for future experimental study:

a) Backscattering measurements to determine the influence of the low energy portion of an incident bremsstrahlung spectrum, as more information as to the beam character in that region becomes available.

b) A study of the effect of surface areas much smaller than "semi-infinite" on albedo to examine the trend indicated in Figures 74 and 76.

c) Backscattering measurements with materials of atomic numbers between 26 and 82, which though not generally of radiation protection interest, have value to others.

d) Angles of beam incidence, other than normal.

8. BIBLIOGRAPHY

1. Selph, Wade E. Neutron and Gamma-ray Albedos. Oak Ridge National Laboratory, Oak Ridge, Tennessee; February, 1968.

2. International Commission on Radiological Units. Report 11, September 1, 1968.

3. Jaeger, R. G.; Eisenlake, H. A., et al., editors. Shielding Fundamentals and Methods. Vol. I of Engineering Compendium on Radiation Shielding. Sponsored by International Atomic Energy Agency.

4. National Bureau of Standards. Safety Standard for Non-Medical X-ray and Sealed Gamma-ray Sources. Part I. General. Handbook 93. U. S. Government Printing Office, 1966.

5. National Bureau of Standards. Shielding for High-Energy Electron Accelerator Installations. Handbook 97. U. S. Government Printing Office, 1964.

6. Rockwell, T. III, editor. Introduction and Outline of Basic Shielding Theory. Reactor Shielding Design Manual.

7. Walker, R. L. and Grotenhuis, M. A Summary of Shielding Constants for Concrete. Argonne National Laboratory; November, 1961.

8. Kirn, Frederick S. and Kennedy, Robert J. "How Much Concrete for Shielding?" Nucleonics, Vol. 12, No. 6 (June, 1954), pp. 44-48.

9. Murray, Kenneth M. "Shielding Moderate-Energy Electron Accelerators," Nucleonics, Vol. 22, No. 2 February, 1964, pp. 61-67.

10. Raso, D. J. "Transmission of Scattered Gamma-Rays Through Concrete and Iron Slabs," Health Physics, Vol. 5 (1961), pp. 126-141.

11. Evans, R. D. The Atomic Nucleus. New York: McGraw-Hill, 1955.

12. Steyn, Julian Jack. "Backscatter of Normally Incident Gamma Photons from Semi-Infinite Media of Varying Atomic Number." Thesis, University of Toronto, Canada, 1966.

13. Compton, A. H. Phys. Rev. 21, 5 (1923), pg. 483.

14. Klein, D. and Nishina, Y. Zeit Fur Physik 52, (1929), pg. 853.

15. Hayward, E. and Hubbell, J. A. "The Backscattering of Co^{60} Gamma Rays from Infinite Media," J. Applied Physics, 25, 4, (April, 1954).

16. Hine, J. and McCall, R. C. "Gamma-ray Backscattering," Nucleonics 12, No. 4 (April, 1954), pp. 27-30.

17. Bulatov, B. P. and Garusov, E. A. "^{60}Co and ^{198}Au Gamma-ray Albedo of Various Material," Journal of Nuclear Energy, Part A: Reactor Science, Vol. 11, (1960), pp. 159-64.

18. Hyodo, T. "Backscattering of Gamma Rays," Nucl. Sci. & Eng., 12, (1962), pp. 178-84.

19. Fumita, H.; Kobayashi, K.; and Hyodo, T. "Backscattering of Gamma Rays from Iron Slabs," Science and Engineering, 19: 437-440, 1964.

20. Nakamura, T. and Hyodo, T. "Radial Distribution of Photons Backscattered from the Surface of Semi-infinite Scatterer," Nucl. Sci. & Technol. 6[3], pp. 143-152, March, 1969.

21. Mizukami, K.; Matsumoto, T.; and Hyodo, T. "Backscattering of Gamma Rays from Polyethylene, Aluminum and Lead Slabs,: Journal of Nuclear Science and Technology, 4 (12), pp. 607-613, (December, 1967).

22. Clarke, E. T. and Batten, J. F. "Gamma-ray Scattering by Concrete Surfaces," Nuclear Science and Engineering, 17:125-30, (1963).

23. Hendee, W. R. and Ellis, J. L. "Scattering of Gamma Radiation from Semi-Infinite Slabs," Health Physics, Vol. 12, (1966), pp. 673-681.

24. Jones, T. H.; Scofield, N. E.; Haggmark, L. G.; and Gurney, W. J. Experimental Determination of the Gamma-ray Angular Dose Albedos of Concrete, Aluminum, and Steel. U. S. Naval Radiological Defense Laboratory, San Francisco, California 94135, (#USNRDL-TR-790), 6 October 1964.

25. Haggmark, L. G.; Jones, T. H.; Scofield, N. E.; and Gurney, W. J. "Differential Dose-Rate Measurements of Backscattered Gamma Rays from Concrete, Aluminum, and Steel," Nucl. Sci. & Eng., 23:138-149, (1965).

26. Steyn, J. J. and Andrews, D. G. "Experimental Differential Number, Energy and Exposure Albedos for Semi-Infinite Media, for Normally Incident Gamma Photons," Nucl. Sci. & Eng., 27:318-327, (1967).

27. Cormack, D. V.; Burke, D. G.; and Davitt, W. E. "Spectral Distributions of 140 KVP X-rays," Radiology, 70 (1958), pg. 91.

28. Cormack, D. V. and Mak, S. "Spectra of Scattered Radiation at Points off the Beam Axis," Radiology, 72 (1959), pg. 107.

29. Jones, H. E. and Skarsgard, L. D. "The Spectral Distribution of Scattered Radiation Produced in a Water Phantom by X-rays in the Range 100 KV to 1.25 MeV," Rad. Research, 9, (1958), pg. 135.

30. Baran, J. A.; Faw, R. E.; and Kimel, W. R. "Reflection of Co^{60} Gamma Rays from Concrete," Nucl. Inst. and Methods, 75, (1969), pp. 141-148.

31. Kitazume, Mitsuyaki. "Gamma-ray Scattering from Point Sources by Infinite Plane Surfaces," Journal of Nuclear Science and Technology, 5, (3), (March, 1968), pp. 98-103.

32. Pozdnew, D. B.; Churin, S. A.; and Gokhshtein, L. F. "Backward Scattering of Y-Radiation from Aluminum Barriers of Finite Thickness," Atomnaya Energiya, Vol. 22, No. 4, April, 1967.

33. Viktorov, A. A.; Efimenko, B. A.; Zolotukhin, V. G.; Klimanov, V. A., and Mashkovich, V. P. "Differential Albedo for Gamma Rays from a Point Unidirectional Source," Atomnaya Energiya Vol. 23, No. 3, pp. 187-191 (Sept., 1967.)

34. Kruglov, S. P., and Lopatin, S. P. "A Study of the Dispersion of the Energy of an Impact Radiation Beam from an Absorption Calorimeter," Zhurnal Tekhnicheskoi Fiziki, Vol. 30, No. 4, (April, 1960), pp. 424-432.

35. Pruitt, J. S. "High Energy X-ray Photon Albedo," Nucl. Inst. and Methods, 27, (1964), pp. 23-28.

36. Sugiyama, S. and Tomimasu, T. "High Energy X-ray Albedo for Pb, Cu and Duralumin," Nucl. Inst. and Methods, 53, (1967), pp. 346-348.

37. Karzmark, C. J. and Capone, T. "Measurements of 6 MV X-rays; II: Characteristics of Secondary Radiation," Br. J. Radiol., 41, (March, 1968), pp. 222-226.

38. Hayward, E. and Hubbell, J. "The Albedo of Various Materials for 1-MeV Photons," The Physical Review, Second Series, Vol. 93, No. 5, March 1, 1954.

39. Perkins, J. G. "Monte Carlo Calculation of Gamma-ray Albedos of Concrete and Aluminum," Journal of Applied Physics, Volume 26, No. 6, June, 1955.

40. Berger, J. J. "Calculation of Energy Dissipation by Gamma Radiation near the Interface between Two Media," J. Applied Physics, 28, Vol. 12, (1957) pp. 1502-1508.

41. Wells, M. B. "Air and Concrete Scattering of Gamma Rays," Convair; ANP Doc. No. NARF-59-11T MR-N-29 (20 March 1959).

42. Attix and Roesch, editors, Radiation Dosimetry, Volume 1, 1968.

43. Wells, M. B. "Differential Dose Albedos for Calculation of Gamma-ray Reflection from Concrete," Radiation Research Associate Document RRA-T46, December, 1964.

44. Davisson, Charlotte and Beach, L. A. "A Monte Carlo Study of Backscattered Gamma Radiation," Trans. Am. Nucl. Soc. Vol. 5, No. 2, (1962), pg. 391.

45. Raso, Dominic J. "Monte Carlo Calculations on the Reflection and Transmission of Scattered Gamma Rays," Nucl. Sci. & Eng. 17:411-418 (1963).

46. Leimdorfer, Martin. "The Backscattering of Gamma Radiation from Plane Concrete Walls," Nucl. Sci. & Eng., 17:345-351, (1963).

47. Bulatov, B. P. and Leipunski, O. I. "The Albedo of X-rays and the Reflection Build-up Factor," Soviet J. At. Energy, 7, (1961), pg. 1015.

48. Bulatov, B. P. "Method of Calculating the Intensity of Backscattered Gamma Radiation," Translated from Atomnaya Energiya, Vol. 21, No. 5, (November, 1966), pp. 345-356.

49. Chilton, A. B. and Huddleston, C. M. "A Semi-empirical Formula for Differential Dose Albedo for Gamma Rays on Concrete," Nucl. Sci. & Eng., 17:419-424 (1963).

50. Chilton, A. B. "Backscattering of Gamma Rays from Point Sources by an Infinite-Plane Concrete Surface," Nucl. Sci. & Eng., 21:194-200 (1965).

51. Chilton, A. B.; Davisson, C. M.; and Beach, L. A. "Parameters for C-H Albedo Formula for Gamma Rays Reflected from Water, Concrete, Iron and Lead," Trans. Am. Nucl. Soc. 8, (1965), pg. 656.

52. Huddleston, C. M. Comparison of Experimental and Theoretical Gamma Ray Albedo - An Interim Report. U. S. Naval Civil Engineering Laboratory, Point Hueneme, California, Doc. TN-567, 10 January 1964.

53. Huddleston, C. M. and Shoemaker, N. F. A Mathematical Derivation of Contour Lines for Constant Albedo of Gamma Rays on Concrete. U. S. Naval Civil Engineering Laboratory, Point Hueneme, Calif. Doc. TN-539.

54. Chilton, A. B. "A Modified Exposure Albedo Formula for Gamma Rays Reflected from Concrete," (1966 Winter Meeting American Nuclear Society), Trans. Am. Nucl. Soc., Vol. 9, No. 2, Pg. 368.

55. Chilton, A. B. "The Close-in Exposure Field from Point Isotropic Gamma-ray Sources Located at an Air-Ground Interface," Nucl. Sci. & Eng., 27: 403-410, (1967).

56. Eisenhauer, C. "An Image Source Technique for Calculating Reflection of Gamma Rays or Neutrons," Health Physics, Vol. II (1965) pp. 1145-1154.

57. Kaiser, R. E. and Mingle, J. O. "Reflections of High-Energy Photons from Semi-Infinite Homogeneous Slabs by Invariant Imbedding Techniques," Am. Nucl. Soc. Trans., Vol. 10, No. 2.

58. Doggett, W. O. and Bryan, F. A. "Theoretical Dose Transmission and Reflection Probabilities for 0.2 - 10.0 MeV Photons Obliquely Incident on Finite Concrete Barriers," Nucl. Sci. & Eng. Vol. 39, pp. 92-104 (1970).

59. Trubey, D. K. "The Single-scattering Approximation to the Solution to the Gamma-Ray Air-scattering Problem," Nucl. Sci. & Eng., 10, (1961), pp. 102-116.

60. Carlson, B. G.; Lee, C. E.; and Worlton, W. J. "The DSN and TDC Neutron Transport Codes," USAEC Document MAMS-2346 (1959).

61. Lathrop, K. D. "Use of Discrete-Ordinates Methods for Solution of Photon Transport Problems," Nucl. Sci. and Eng., 24:381-388, (1966).

62. Renken, James H. and Adams, K. G. Application of the Method of Discrete Ordinates to Photon Transport Calculations: A Research Report; Sandia Laboratories, SC-RR-67-419, June, 1967.

63. Renken, J. H. and Adams, K. G. An Improved Capability for Solution of Photon Transport Problems by the Method of Discrete Ordinates; Sandia Laboratories, SC-RR-739, December, 1969.

64. Segre, E., editor. Experimental Nuclear Physics. Vol. 1. New York: John Wiley and Sons, Inc. 1953.

65. Pratt, R. H. "Atomic Photoelectric Effect at High Energies," Physical Review, 117, (1960), pg. 1017-28.

66. Fink, R. W.; Jopson, R. C.; Mark, H.; and Swift, C. D. "Atomic Fluorescent Yields," Rev. Mod. Phys. Vol. 38, No. 3, June, 1966, pp. 513-540.

67. Morgan, K. Z. and Turner, J. E., editors. Principles of Radiation Protection. New York: John Wiley and Sons, 1967.

68. Bethe, H. A. and Heitler. Proc. Roy. Soc., (London). 146, (1934), pg. 83.

69. Berger, J. J.; Hubbel, J. H.; and Reingold, I. H. "Contribution of Annihilation Radiation to the Gamma Ray Flux in Lead," Physical Review, Vol. 113, No. 3 (Feb., 1959), pp. 857-862.

70. Motz, J. W.; Olsen, H. A.; and Koch, H. W. "Pair Production by Photons," Reviews of Modern Physics, Vol. 41, No. 4, pp. 581-591 (Oct., 1969).

71. Johns, H. E.; Katz, L.; Douglas, R. A.; and Haslam, R. N. H. "Gamma-Neutron Cross Section," Physical Review, 80, 6, (1950), pp. 1062-1068.

72. Baldwin, G. C. and Koch, H. W. "Threshold Measurements on the Nuclear Photo-effect," Physical Review, 67 (1945), pp. 1-11.

73. Weinstock, E. V. and Halpern, J. "Systematics of Photoproton Reaction," Physical Review, 94, 6, (1954), pp. 1651-54.

74. Levinger, J. S. Nuclear Photo-Disintegration. Oxford Univ. Press, 1960.

75. Price, W. J. Nuclear Radiation Detection. New York: McGraw-Hill, 1964.

76. Attix, F. H. and Roesch, W. C., editors. Radiation Dosimetry, Vol. II. Academic Press, 1966.

77. Attix, R. H. Present Status of Dosimetry by Radiophotoluminescence and Thermoluminescence Methods. U. S. Naval Research Laboratory Document NRL-6145, September, 1964.

78. Hendee, W. R.; Ibbott, G. S.; and Gilbert, D. B. "Effects of Total Dose on Energy Dependence of TLD-100 LiF Dosimeters," International Journal of Applied Radiation and Isotopes, Vol. 19, (1968), pp. 431-437.

79. Durke, R. K.; Lucas, A. C.; York, N. B.; Dahlstrom, T. S.; and Blair, G. E. Energy and Rate-Dependence Studies, Edgerton, Germeshauser, and Grier, Inc. Document EGG-S-237-R.

80. Schayes, R.; Brooke, C.; Kozlowitz, I.; and Lheureux, M. "New Developments in Thermoluminescent Dosimetry," Health Physics, Vol. 14 (1968), pp. 251-263.

81. Tochilin, E. and Goldstein, N. Dose Rate and Spectral Measurements from Pulsed X-ray Generators, U. S. Naval Radiological Defense Laboratory Document DASA-1703, December, 1965.

82. Bernstein, B. H. "Pulsed X-ray Prompt Gamma Simulation," U. S. Air Force Document BSD-TR 66-386, November, 1966.

83. Storm, E. and Shlaer, S. "Development of Energy-Independent Film Badges with Multi-Element Filters," Health Physics, Vol. 11, pp. 1127-1144.

84. Yokota, R.; Nakajima, S.; and Sakai, E. "High Sensitivity Silver-Activated Phosphate Glass for the Simultaneous Measurement of Thermal Neutrons, γ- and/or β-Rays," Health Physics, Vol. 5, pp. 219-224.

85. Endres, G. W. R. and Kocher, L. F. "The Response of Selected Thermoluminescent Materials to Fast-Neutron Exposures," Proceedings of Second International Conference on Luminescent Dosimetry; Conf-680920, September, 1968.

86. Reddy, A. R.; Ayyangar, K.; and Brownell, G. L. "Thermoluminescence Response of LiF to Reactor Neutrons," Rad. Research Vol. 40, pp. 552-562 (1969).

87. Zimmerman, D. W.; Rhyner, C. R.; and Cameron, J. R. "Thermal Annealing Effects on the Thermoluminescence of LiF," Health Physics, Vol. 12, (1966), pp. 525-531.

88. Carlsson, C. A. "Thermoluminescence of LiF: Dependence of Thermal History," Phys. Med. Biol. 1969, Vol. 14, No. 1, pp. 107-118.

89. Martensson, B. K. A. "Thermoluminescence of LiF: A Statistical Analysis of the Influence of Pre-Annealing on the Precision of Measurement," Phys. Med. Biol., 1969, Vol. 14, No. 1, pp. 119-130.

90. Harshaw Chemical Co. "High Sensitivity Ribbon Lithium Fluoride Thermoluminescent Dosimeters," Standard Data Sheets 074, 060, and 045.

91. Cameron, J. R.; Zimmerman, D.; Kenney, G.; Buck, R.; Bland, R.; and Grant, R. "Thermoluminescent Radiation Dosimetry Utilizing LiF," Health Physics, Vol. 10, pp. 25-29.

92. Randall, J. T. and Wilkins, M. H. F. "Phosphorescence and Electron Traps I and II; The Study of Trap Distribution," Proc. Roy. Soc. (London), Vol. 184, (1945), pp. 347-433.

93. Attix, F. H., editor. Proceedings of International Conference on Luminescence Dosimetry, June, 1965.

94. Greening, J. R. "The Derivation of Approximate X-ray Spectral Distribution and an Analysis of X-ray 'Quality' Specification," Brit. J. Radiol. Vol. 34, No. 425, (May, 1963), pp. 363-371.

95. Silberstein, L. "Determination of the Spectral Composition of X-ray Radiation from Filtration Data," J. Opt. Soc. Amer., 22, (1932), pg. 265.

96. Greening, J. R. "The Determination of X-ray Wavelength Distributions from Absorption Data," Proc. Phys. Soc., (London), 63A, (1950), pp. 1227-1234.

97. Twidell, J. W. "The Determination of X-ray Spectra Using Attenuation Measurements and a Computer Program," Phys. Med. Biol., 1970, Vol. 15, No. 3, pp. 529-539.

98. O'Dell, A. A., Jr.; Sandifer, C. W.; Knowles, R. B.; and George, W. D. Measurement of Absolute Thick-Target Bremsstrahlung Spectra, EG&G, Inc. 1183-2139, May 19, 1967.

99. Edelsack, E. A.; Kreger, W. E.; Mallet, W.; and Scofield, N. E. "Experimental Investigation of Thick-Target Bremsstrahlung Radiation Produced by Electrons of 1.00, 1.50, and 2.00 MeV," Health Physics, Vol. 4, pp. 1-15.

100. Pace, A. L. "Radiographic Characteristics of High Energy X-rays," Non-Destructive Testing, March-April, 1953.

101. Sandifer, C. W. and George, W. D. Radiation Calibration of a 20-MeV Linac, EG&G, Inc. # S-333-R May, 1965.

102. Goldie, C. H.; Wright, K. A.; Anson, J. H.; Cloud, R. W.; and Trump, J. G. "Radiographic Properties of X-rays in the Two-to-Six-Million-Volt Range," ASTM Bulletin, October, 1954.

103. Evans, W. W.; Granke, R. C.; Wright, K. A.; and Trump, J. G. "Absorption of 2-MeV Constant Potential Roentgen Rays by Lead and Concrete," Dept. of Elect. Eng., M.I.T, October, 1951.

104. Motz, J. W.; Miller, W.; and Wyckoff, H. O. "Eleven-MeV Thick Target Bremsstrahlung," Physical Review, Vol. 89, No. 5, March, 1953.

105. Hoffman-Pinther, P. X-ray Distribution from Sources Operating at Five to Fifteen Million Electron Volts, OTAC-RR-45.

106. Adams, K. G. and Mehl, C. R. Calculation of the Deposition of Energy by Photons, Sandia Laboratories, SC-RR-66-666, October, 1966.

107. Trubey, D. K. and Maskewitz, B. F. A Review of the Discrete Ordinates Sn Method for Radiation Transport Calculations, USAEC Document ORNL-RSIC-19-UC-80, March, 1968.

108. Kaplan, I., Nuclear Physics, Addison-Wesley Publ. Co., Inc. 1963.

109. Johns, H. E. and Cunningham, J. R. The Physics of Radiology; Charles C. Thomas, Publisher, 1969.

110. Chodorow, A. M. HERMES II Experimenters' Manual, Sandia Laboratories, SC-M-70-242, June, 1970.

111. Bernstein, B. H. Pulsed X-ray Prompt Gamma Simulator, BSD-TR-66-386, Nov., 1966, Air Force Systems Command.

112. Johnson, D. L., Sandia Corporation, private communication, April, 1970.

113. TREF, Technical Planning Document, Dept. of Air Force Headquarters; Air Force Special Weapons Center, Kirtland Air Force Base, Albuquerque, New Mexico.

114. Dye, D. Air Force Special Weapons Center, Private Communication, April, 1970.

115. Zol'nikov, P. P. and Sukhanova, K. A. "Energy and Space Distribution of Backscattered γ-Radiation," Atomnaya Energiya, Vol. 25, No. 6, pg. 518, December, 1968.

116. Dahlstrom, T. S. and Thompson, W. E. "The Angular Distribution of Dose Rate from Gamma Rays Scattered Through Various Thicknesses of Iron and Aluminum," USNRDL-TR-558, April 19, 1962.

117. Plimpton, J. D. Sandia Corporation, Private communication, September, 1970.

118. Mather, R. L. "Gamma-Ray Collimator Penetration and Scattering Effects," Journal of Applied Physics, Vol. 23, No. 10, October, 1957.

119. Martin, T. H. A Computerized Method of Predicting Electron Beam Bremsstrahlung Radiation with Specific Application to High Voltage Flash X-ray Machines. Sandia Corporation; SC-RR-69-241, May, 1969.

120. Bonzon, L. L. and Rivard, J. B. Method for Calculation of Bremsstrahlung and Neutron Production from Electron Driven Target. Sandia Corporation SC-TM-70-629, December, 1970.

121. Golden, J. C., Jr. Analytical Expressions for Bremsstrahlung Spectra Emitted by Highly Filtered Thick High-Z Targeted X-ray Devices from 2 to 20 MeV. Sandia Corporation; SC-TM-67-2900, December, 1967.

122. Bailey, F. A. Sandia Corporation, Private communication, October 26, 1970.

123. Buckalew, W. Sandia Corporation, Private communication, August, 1970.

124. Tochilin, E.; Goldstein, N.; and Lyman, J. T. "The Quality and LET Dependence of Three Thermoluminescent Dosimeters and Their Potential Use as Secondary Standards," Proceedings of the Second International Conference on Luminescence Dosimetry, Conf-680929, September, 1968.

125. Almond, P. R. et al. "The Energy Response of LiF, CaF_2, and $Li_2B_4O_7$:Mn from 26 KeV to 22 MeV," Luminescence Dosimetry, USAEC Doc., April, 1967.

126. Almond, P. R.; McCray, K.; Espejo, D.; and Watanabe, S. "The Energy Response of LiF, CaF_2, and $Li_2B_4O_7$:Mn from 26 KeV to 22 MeV," Proceedings of the Second International Conference on Luminescence Dosimetry, Conf-680920, September, 1968.

127. Frank, M. "Thermoluminescent Dosimetry with LiF and Energy Dependence of Thermoluminescent Dosimeters of CaF_2:Mn and LiF," Kernenergie, 6, 76, (1963).

128. Barford, N. C. Experimental Measurements: Precision, Error and Truth. Addison-Wesley Publishing Co. 1967.

A. NOMENCLATURE

A_ϵ	=	effective viewed area normal to the collimator axis
a	=	collimator radius
$\alpha_{D1}\ (E_o, \theta_o, \theta, \phi)$	=	differential current out (in dose units) per incident flux (in dose units)
$\alpha_{D2}\ (E_o, \theta_o, \theta, \phi)$	=	differential current out (in dose units) per incident current (in dose units)
$\alpha_{D3}\ (E_o, \theta_o, \theta, \phi)$	=	differential flux out (in dose units) per incident flux (in dose units)
$A_{D1}\ (E_o, \theta_o)$	=	total dose albedo, defined by integration of α_{D1} over all θ, ϕ
$A_{D2}\ (E_o, \theta_o)$	=	total dose albedo, defined by integration of α_{D2} over all θ, ϕ
$D_{D3}\ (E_o, \theta_o)$	=	total dose albedo, defined by integration of α_{D3} over all θ, ϕ

α_E and A_E are defined as above for energy albedo

α and A are defined as above for particle albedo

$\alpha(H_2O)$	=	albedo determined when both dose terms are calculated for deposition in water

$\alpha = \dfrac{E_o}{m_o c^2}$

BCG = dose in TLD at some point between backscatter slab location in absence of slab and x-ray target

BCS = dose in TLD at some point between backscatter slab and x-ray target

BS = dose in water reflected by the backscatter slab at some angle and distance

c = the velocity of light -- 2.998×10^{10} cm/sec, or collimator length, dependent upon use

d = collimator to slab distance

D_o = incident dose

$\mathcal{D}_R$ = dose reflected per steradian

DBG = dose in TLD measured at same position as BS during background run

DD = dose deposited at backscatter surface center

DI = dose deposited at backscatter surface location in absence of reflector

DR = dose in TLD measured at same position as BS during backscatter run

e = the electronic charge -- 4.8×10^{-10} statcoulomb

E = photon energy

exp = exponential

$h\nu$ = photon energy

K = Boltzmann's constant

$_eK(\theta_s)$ = Klein-Nishina energy scattering cross-section per electron

ln = natural logarithm

m_o = the electronic mass -- 9.1083×10^{-28} gms

$\left(\frac{\mu_{en}}{\rho}\right)$ = mass energy-absorption coefficient

μ_T = total attenuation coefficient

Ω = solid angle disignation

Π = 3.14159..........

ϕ = the angle between the projection on the surface of the backscatter material of the incident radiation beam and the projection of the reflected radiation

Φ = fluence

$_e\sigma$ = total microscopic Compton interaction cross-section

$_e\sigma_s$ = the Compton scattering coefficient

$\sigma_{(\gamma,n)}$ = photonuclear absorption coefficient for the emission of a single neutron

Σ_r = removal cross-section for neutrons

T = kinetic energy of a particle or temperature, dependent upon use

τ_K = the K-shell photoelectric cross-section in barns per atom

τ_{pe} = the total photoelectric cross-section in barns per atom

θ = the angle between the reflected radiation and the perpendicular to the surface of the backscatter material

θ_o = the angle between the incident radiation beam and the perpendicular to the surface of the backscatter material

θ_s = the angle between the transmitted beam axis and the reflected radiation

Additional specialized abbreviations are defined at the point of their use.

B. VIEWED AREA CONSIDERATIONS

The area of a slab, normal to the collimator, viewed by a TLD crystal at the back of the collimator is the envelope of the family of circles generated by considering each point on the crystal.

If one considers a plane of origin through the leading edge of the collimator (Figure 30) such that a circle of radius "a" (the collimator radius) is defined in the plane, 1, another parallel plane, 2, at distance "c" (the collimator length) in the positive direction, and a third parallel plane, 3, at a negative distance "d" (the distance from the collimator to the scattering center), he may derive the equation of the envelope defining the viewed area.

The collimator radius, a, will appear in Plane 3 as

$$r = \frac{(c + d)\ a}{c} \qquad \text{Eq. B.1}$$

with center displacement $\bar{x}$ and $\bar{y}$ given by

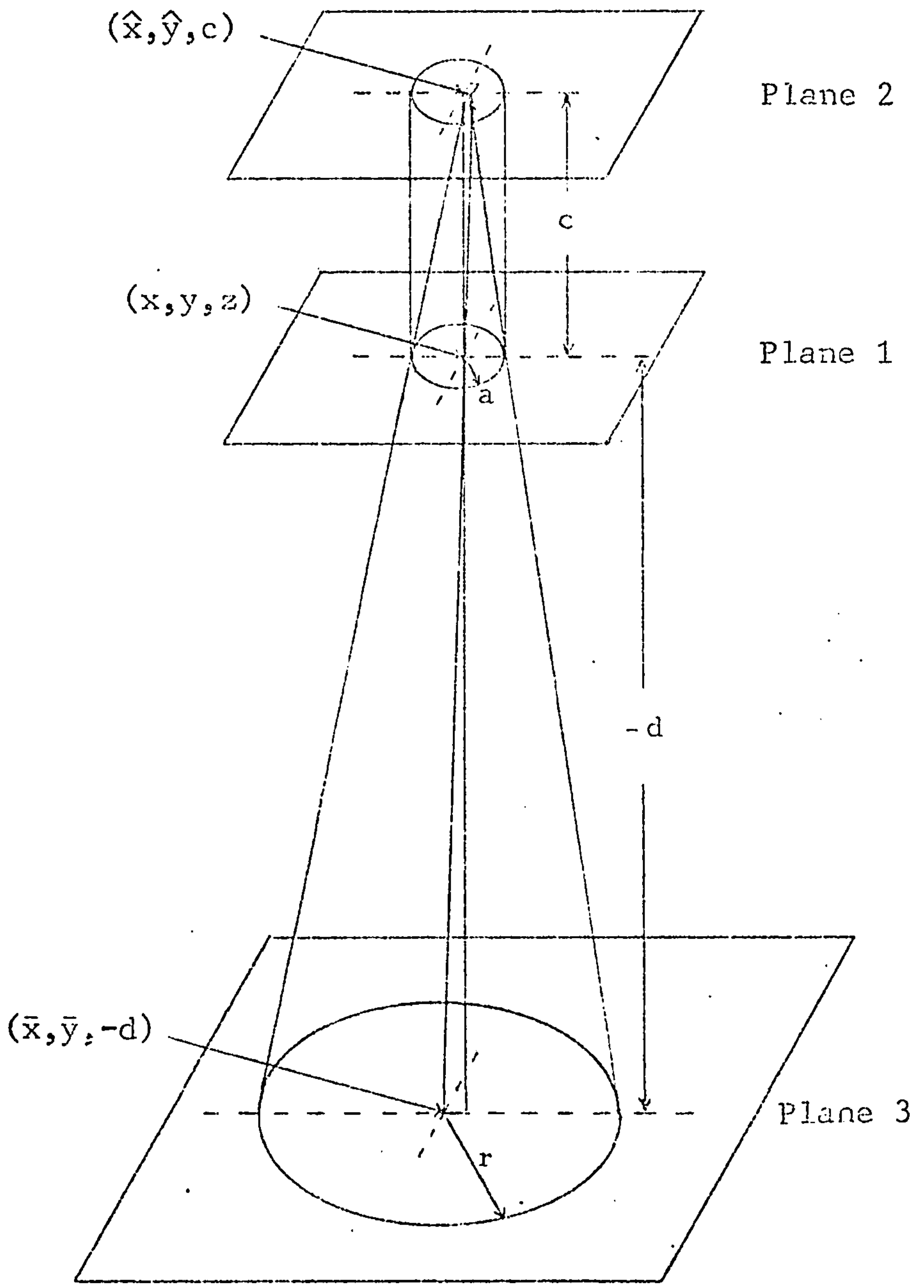

Figure 30. Viewed area geometry

$$\bar{x} = -\frac{\hat{x}\,d}{c} \qquad \text{Eq. B.2}$$

$$\bar{y} = -\frac{\hat{y}\,d}{c} \qquad \text{Eq. B.3}$$

from $(\hat{x},\hat{y})$ in Plane 2.

The equation of the circle in Plane 3 defined by point $(\hat{x},\hat{y})$ on the detecting crystal in Plane 2 and the collimator opening specified in Plane 1 is

$$(x - \bar{x})^2 + (y - \bar{y})^2 = r^2 \qquad \text{Eq. B.4}$$

or, substituting equations B.2 and B.3,

$$\left(x + \frac{\hat{x}d}{c}\right)^2 + \left(y + \frac{\hat{y}d}{c}\right)^2 = r^2 \qquad \text{Eq. B.5}$$

The envelope of the set of circles generated by tracing the outline of the detector is the outside boundary of the desired area.

Setting

$$\hat{x} = \hat{x}\,(t) \qquad \text{Eq. B.6}$$

and $$\hat{y} = \hat{y}\,(t) \qquad \text{Eq. B.7}$$

The equation for the general circle will then be:

$$\left(x + \frac{\hat{x}(t)d}{c}\right)^2 + \left(y + \frac{\hat{y}(t)d}{c}\right)^2 = r^2 \qquad \text{Eq. B.8}$$

To find the envelope of a set of lines, the general equation of the generating line is set equal to zero, differentiated with respect to the variable and the variable then eliminated between the two equations.

$$F(t) = \left(x + \frac{\hat{x}(t)d}{c}\right)^2 + \left(y + \frac{\hat{y}(t)d}{c}\right)^2 - r^2 = 0$$

$$\text{Eq. B.9}$$

$$\frac{dF(t)}{dt} = 2\left(x + \frac{\hat{x}(t)d}{c}\right)\frac{d}{c}\,\hat{x}'\,(t)$$

$$+ 2\left(y + \frac{\hat{y}(t)d}{c}\right)\frac{d}{c}\,\hat{y}'\,(t) = 0 \qquad \text{Eq. B.10}$$

In the particular case being considered, several special cases arise as follows:

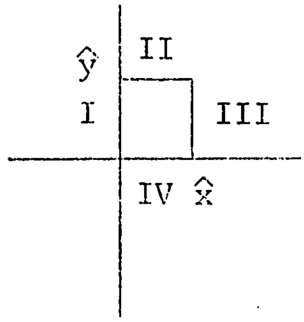

Figure 31. Crystal geometry considerations

Case I

$$\hat{x} = 0 \qquad \text{Eq. B.11}$$

and

$$\hat{x}' = 0 \qquad \text{Eq. B.12}$$

So

$$F(t) = x^2 + \left(y + \frac{\hat{y}(t)d}{c}\right)^2 - r^2 = 0 \qquad \text{Eq. B.13}$$

$$\frac{F(t)}{dt} = 2\left(y + \frac{\hat{y}(t)d}{c}\right)^2 \frac{d}{c}\,\hat{y}'(t) = 0 \qquad \text{Eq. B.14}$$

$$\hat{y} = -\frac{c}{d}\,y \qquad \text{Eq. B.15}$$

Substituting back into F(t):

$$x^2 + (y - y)^2 - r^2 = 0 \qquad \text{Eq. B.16}$$

$$x = \pm r \qquad \text{Eq. B.17}$$

Therefore, a set of circles has been generated parallel to the y-axis of radius "r" along the x-axis.

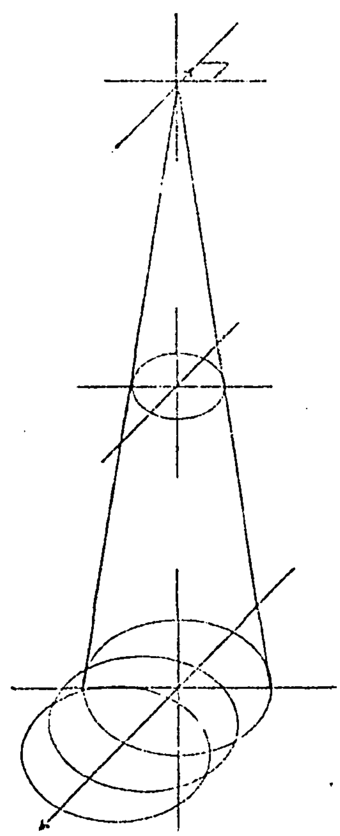

Figure 32. Edge generated envelope

The total envelope in Case I is then the set of parallel lines joining the circles formed by viewing points at the first two corners of the crystal.

Case II is similar in a perpendicular direction along a line parallel to the x-axis at distance $-\bar{y}$. The envelope has equation

$$y = \pm r \qquad \text{Eq. B.18}$$

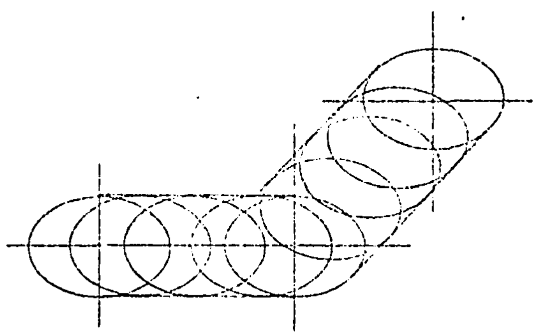

Figure 33. Envelope generated by two edges

Cases III and IV close the viewed area with a resultant figure:

curvature of radius, $r = \frac{(c + d)}{c} a$ Eq. B.19

center line separation of (crystal length)$\left(\frac{d}{c}\right)$ Eq. B.20

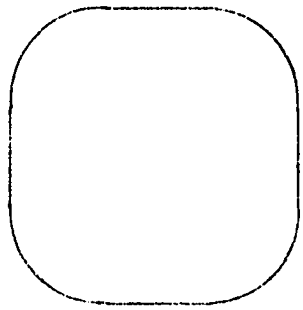

Figure 34. Total viewed area

This area includes the area seen by any point on the crystal. Only a fraction of this is seen by every point on the crystal (umbra), the rest being seen by a decreasing amount of the crystal (penumbra). The umbral region is defined by the area determined by the common area of the circles defined by points originating at the greatest extents of the detector (i.e. the four corners).

To find the umbral area consider the four defining circles:

Circle 4

Circle 1

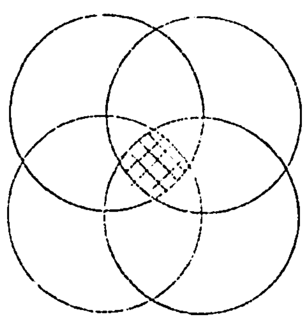

Circle 3

Circle 2

Figure 35. Umbral area

$$\text{Circle 1;} \quad x^2 + y^2 = r^2 \qquad \text{Eq. B.21}$$

$$\text{Circle 2;} \quad x^2 + (y + \bar{y})^2 = r^2 \qquad \text{Eq. B.22}$$

$$\text{Circle 3;} \quad (x + \bar{x})^2 + (y + \bar{y})^2 = r^2 \qquad \text{Eq. B.23}$$

$$\text{Circle 4;} \quad (x + \bar{x})^2 + y^2 = r^2 \qquad \text{Eq. B.24}$$

The intersection of Circles 1 and 2 provides the least value of x:

$$\text{Circle 1 - Circle 2:} \quad y^2 - (y + \bar{y})^2 = 0 \qquad \text{Eq. B.25}$$

$$y^2 - y^2 - 2\bar{y}y - \bar{y}^2 = 0 \qquad \text{Eq. B.26}$$

$$2y = -\bar{y} \qquad \text{Eq. B.27}$$

$$y = -\left(\frac{\bar{y}}{2}\right) \qquad \text{Eq. B.28}$$

$$x^2 + \left(-\frac{\bar{y}}{2}\right)^2 = r^2 \qquad \text{Eq. B.29}$$

$$x^2 = r^2 - \left(\frac{\bar{y}}{2}\right)^2 \qquad \text{Eq. B.30}$$

$$x = \pm\sqrt{r^2 - \left(\frac{\bar{y}}{2}\right)^2} \qquad \text{Eq. B.31}$$

the negative solution for x being the one of interest. The intersection of either Circles 1 and 4 or Circles 2 and 3 provides a mid-point value of x.

$$\text{Circle 1 - Circle 4:}\quad x^2 - (x + \bar{x})^2 = 0 \qquad \text{Eq. B.32}$$

$$x^2 - x^2 - 2x\bar{x} - \bar{x}^2 = 0 \qquad \text{Eq. B.33}$$

$$x = -\left(\frac{\bar{x}}{2}\right) \qquad \text{Eq. B.34}$$

Solution of the intersection of Circles 3 and 4 would yield the right-most boundary of x, but is not necessary as the two halves are symmetrical.

The total area of the umbra may then be found by:

$$A_u = 2\int_{-\sqrt{r^2 - \left(\frac{\bar{y}}{2}\right)^2}}^{-\left(\frac{\bar{x}}{2}\right)} [(\text{Circle 2 boundary})-(\text{Circle 1 boundary})]\,dx \qquad \text{Eq. B.35}$$

$$\text{Circle 1:}\quad y = \pm\sqrt{r^2 - x^2} \qquad \text{Eq. B.36}$$

the negative radical being of interest.

Circle 2: $y^2 + 2y\bar{y} + (\bar{y}^2 + x^2 - r^2) = 0$ Eq. B.37

$$y = \frac{-2\bar{y} \pm \sqrt{4\bar{y}^2 - 4\bar{y}^2 - 4x^2 + 4r^2}}{2} \qquad \text{Eq. B.38}$$

$$y = -\bar{y} \pm \sqrt{r^2 - x^2} \qquad \text{Eq. B.39}$$

the positive radical being of interest.

Eq. B.35 then becomes:

$$A_u = 2\int_{-\sqrt{r^2 - \left(\frac{\bar{y}}{2}\right)^2}}^{-\left(\frac{\bar{x}}{2}\right)} \left(-\bar{y} + 2\sqrt{r^2 - x^2}\right) dx \qquad \text{Eq. B.40}$$

$$A_u = -2\bar{y}x\Bigg|_{-\sqrt{r^2-\left(\frac{\bar{y}}{2}\right)^2}}^{-\left(\frac{\bar{x}}{2}\right)} + 4\int_{-\sqrt{r^2-\left(\frac{\bar{y}}{2}\right)^2}}^{-\left(\frac{\bar{x}}{2}\right)} \sqrt{r^2 - x^2}\, dx \qquad \text{Eq. B.41}$$

$$A_u = -2\bar{y}\left[\frac{\bar{x}}{2} + \sqrt{r^2 - \left(\frac{\bar{y}}{2}\right)^2}\right]$$

$$+ 4\left[\frac{x}{2}\sqrt{r^2 - x^2} + \frac{r^2}{2}\arcsin\frac{x}{r}\right]\Bigg|_{-\sqrt{r^2 - \left(\frac{\bar{y}}{2}\right)^2}}^{-\left(\frac{\bar{x}}{2}\right)}$$

Eq. B.42

$$A_u = \bar{y}\bar{x} - 2\bar{y}\sqrt{r^2 - \left(\frac{\bar{y}}{2}\right)^2} + 2\Bigg\{\left[\left(-\frac{\bar{x}}{2}\right)\sqrt{r^2 - \left(\frac{\bar{x}}{2}\right)^2}\right.$$

$$\left. + r^2 \arcsin\left(-\frac{\bar{x}}{2r}\right)\right]$$

$$- \left[-\sqrt{r^2 - \left(\frac{\bar{y}}{2}\right)^2}\sqrt{r^2 - r^2 + \left(\frac{\bar{y}}{2}\right)^2} + r^2 \arcsin\frac{-\sqrt{r^2 - \left(\frac{\bar{y}}{2}\right)^2}}{r}\right]\Bigg\}$$

Eq. B.43

$$A_u = \bar{y}\bar{x} - 2\bar{y}\sqrt{r^2 - \left(\frac{\bar{y}}{2}\right)^2} - \bar{x}\sqrt{r^2 - \left(\frac{\bar{x}}{2}\right)^2} + 2r^2 \arcsin\left(- \frac{\bar{x}}{2r}\right)$$

$$+ \bar{y}\sqrt{r^2 - \left(\frac{\bar{y}}{2}\right)^2} - 2r^2 \arcsin\left(\frac{-\sqrt{r^2 - \left(\frac{\bar{y}}{2}\right)^2}}{r}\right) \qquad \text{Eq. B.44}$$

$$A_u = \bar{y}\bar{x} - \bar{y}\sqrt{r^2 - \left(\frac{\bar{y}}{2}\right)^2} - \bar{x}\sqrt{r^2 - \left(\frac{\bar{x}}{2}\right)^2}$$

$$+ 2r^2 \left[\arcsin\left(- \frac{\bar{x}}{2r}\right) - \arcsin \frac{-\sqrt{r^2 - \left(\frac{\bar{y}}{2}\right)^2}}{r}\right]$$

Eq. B.45

Substituting absolute values from Eqs. B.1, B.2, and B.3 to obtain the actual area of interest, Eq. B.45 becomes:

$$A_u = \hat{x}\hat{y}\left(\frac{d}{c}\right)^2 - \frac{\hat{y}d}{c}\sqrt{\frac{(c+d)^2}{c^2}a^2 - \frac{\hat{y}^2d^2}{4c^2}}$$

$$- \frac{\hat{x}d}{2}\sqrt{\frac{(c+d)^2a^2}{c^2} - \frac{\hat{x}^2d^2}{4c^2}}$$

$$+ 2\,\frac{(c+d)^2a^2}{c^2}\left[\arcsin\left(-\frac{\hat{x}d}{2a(c+d)}\right) - \arcsin\frac{-\sqrt{\frac{(c+d)^2a^2}{c^2} - \frac{\hat{y}^2d^2}{4c^2}}}{\frac{(c+d)a}{c}}\right]$$

Eq. B.46

The penumbral area is most easily found by determining the total enclosed area and subtracting the umbral area.

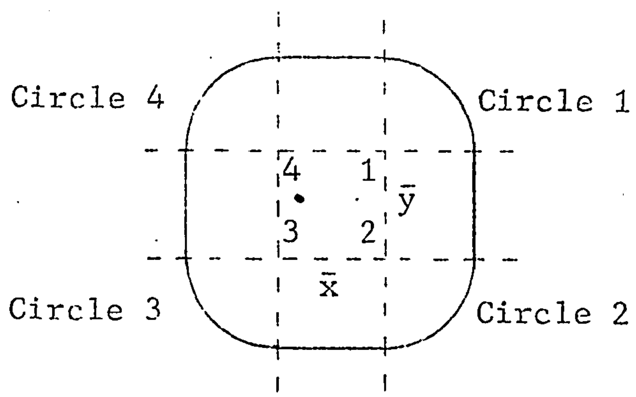

Figure 36. Total enclosed area

The total area can be seen by examination to be:

$$A_T = \Pi r^2 + \bar{y}\bar{x} + 2\bar{x}r + 2\bar{y}r \qquad \text{Eq. B.47}$$

$$A_T = \Pi r^2 + \bar{y}\bar{x} + 2r\ (\bar{x} + \bar{y}) \qquad \text{Eq. B.48}$$

Using absolute values for $\bar{x}$ and $\bar{y}$ from Equations B.1, B.2 and B.3, Eq. B.48 becomes

$$A_T = \frac{\Pi a^2(c+d)^2}{c^2} + \hat{x}\hat{y}\left(\frac{d}{c}\right)^2 + \frac{2a(c+d)}{c}(\hat{x} + \hat{y})\left(\frac{d}{c}\right) \qquad \text{Eq. B.49}$$

and $$A_p = A_T - A_u \qquad \text{Eq. B.50}$$

As pointed out by Dahlstrom and Thompson (116) and demonstrated by Steyn (12), radiation originating in the penumbra is not as effective as that from the umbra and either must be weighted as such or the area weighted in such a manner as to accomplish the same end. The method chosen by Dahlstrom and Thompson was to consider the radiation density as decreasing linearly to zero between the umbra and penumbra limits and choosing an "effective area" which, emitting a constant radiation density, would emit the same amount as the true umbral and penumbral areas.

$$A_\epsilon \rho_o = A_u \rho_o + \int dA_p \, \rho(r) \qquad \text{Eq. B.51}$$

with ρ_o = a constant radiation density

$\rho(r)$ = penumbral radiation density

A_ϵ = an effective viewed area

Steyn carried out a more detailed consideration of the intersected detector area and found that a numerical integration of Eq. B.51 (since it does not reduce to an exact solution) compared to within 0.005% of the area determined by a point detector viewing the same surface. As the detector used in his calculations occupied the full back of the collimator the error involved would be greater than that for which a smaller detector is used (other dimensions remaining comparable).

Field and experimental use of a variety of detector shapes in collimators of differing aperture configurations (117) indicate the error between a precise solution of Equation B.51 and the point detector approximation to be in the order of the square of the ratio of the greatest detector dimension to the collimator length. In the worst case of the data used here, that would be:

$$\left(\frac{0.236}{6.00}\right)^2 \text{ or } 0.155\%$$

In view of these considerations and the untractable form the preceding development takes when considering other than normally viewed surfaces, the point source estimate is used in the actual data reduction. The maximum error involved is far below the statistical variation of the thermoluminescent dosimeter readings.

B.2 POINT DETECTOR VIEWED AREA

The area of a slab viewed by a point detector located in a collimator is determined by the detector to slab distance (c + d), the collimator length (c) and radius (a), and the angle (θ) between the collimator axis and a normal to the slab.

$$x = h(\sec \theta) \qquad \text{Eq. B.52}$$

$$y = (c+d) - g \qquad \text{Eq. B.53}$$

$$\frac{a}{c} = \frac{h}{g} \qquad \text{Eq. B.54}$$

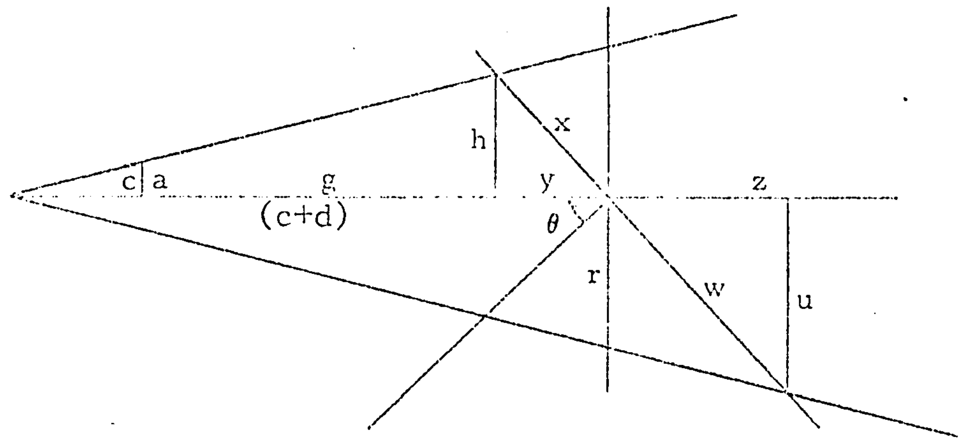

Figure 37. Point detector viewed area

$$g = \frac{c}{a} h \qquad \text{Eq. B.55}$$

$$y = h \tan \theta \qquad \text{Eq. B.56}$$

$$h \tan \theta = (c+d) - \frac{c}{a} h \qquad \text{Eq. B.57}$$

$$h = \frac{(c+d)}{\tan \theta + \frac{c}{a}} \qquad \text{Eq. B.58}$$

$$\cos \theta = \frac{h}{x} \qquad \text{Eq. B.59}$$

$$x = \frac{(c+d)\ \sec\ \theta}{\tan\ \theta + \left(\frac{c}{a}\right)} \qquad \text{Eq. B.60}$$

$$x = \frac{\left(\frac{a}{c}\right)(c+d)\ \sec\ \theta}{1 + \left(\frac{a}{c}\right)\ \tan\ \theta} \qquad \text{Eq. B.61}$$

$$x = \frac{r\ \sec\ \theta}{1 + \left(\frac{a}{c}\right)\ \tan\ \theta} \qquad \text{Eq. B.62}$$

$$\frac{a}{c} = \frac{u}{(c+d) + z} \qquad \text{Eq. B.63}$$

$$\tan\ \theta = \frac{z}{u} \qquad \text{Eq. B.64}$$

$$z = u\ \tan\ \theta \qquad \text{Eq. B.65}$$

$$\frac{a}{c} = \frac{u}{(c+d) + u\ \tan\ \theta} \qquad \text{Eq. B.66}$$

$$\left(\frac{a}{c}\right)(c+d) + u\left(\frac{a}{c}\ \tan\ \theta\right) = u \qquad \text{Eq. B.67}$$

$$\left(\frac{a}{c}\right)(c+d) = u\ [1 - \left(\frac{a}{c}\right)\ \tan\ \theta] \qquad \text{Eq. B.68}$$

$$u = \frac{\left(\frac{a}{c}\right)(c+d)}{1 - \left(\frac{a}{c}\right) \tan \theta} \qquad \text{Eq. B.69}$$

$$\cos \theta = \frac{u}{w} \qquad \text{Eq. B.70}$$

$$w = u \sec \theta \qquad \text{Eq. B.71}$$

$$w = \frac{\left(\frac{a}{c}\right)(c+d) \sec \theta}{1 - \left(\frac{a}{c}\right) \tan \theta} \qquad \text{Eq. B.72}$$

$$w = \frac{r \sec \theta}{1 - \left(\frac{a}{c}\right) \tan \theta} \qquad \text{Eq. B.73}$$

$$G = \text{semi-major ellipse} = \tfrac{1}{2}(w + x) \qquad \text{Eq. B.74}$$

$$G = \tfrac{1}{2}\left[\frac{r \sec \theta}{1 - \left(\frac{a}{c}\right) \tan \theta} + \frac{r \sec \theta}{1 + \left(\frac{a}{c}\right) \tan \theta}\right] \qquad \text{Eq. B.75}$$

$$G = \frac{r \sec \theta}{1 - \left(\frac{a}{c}\right)^2 \tan^2 \theta} \qquad \text{Eq. B.76}$$

$$H = \text{semi-minor ellipse} = r \qquad \text{Eq. B.77}$$

$$A = \text{area of ellipse} = \Pi\, HG \qquad \text{Eq. B.78}$$

$$A = \frac{\Pi\, r^2 \sec^2 \theta}{1 - \left(\frac{a}{c}\right)^2 \tan^2 \theta} \qquad \text{Eq. B.79}$$

The area viewed on the reflecting slab by a point detector where:

a = collimator radius

c = collimator length

r = detector to scattering center distance

θ = angle between collimator axis and a normal to the slab

C. COLLIMATOR EFFECTS

One of the most complete and most frequently referenced works on collimator penetration and scattering is by Mather (118). He develops expressions which give the amount of radiation passing through a cylindrical hole in a slab of material, including the amount of radiation which penetrates the edges of the hole and that due to scattering from the walls of the collimator.

In Mather's report, it is shown, that to a first approximation, the results are the same as the geometric aperture for a like diameter hole in a similar slab with one mean free path of material removed from each side.

Figure 38 details the collimator construction where c is the collimator length, specified in Appendix I for each measurement made.

A copper liner was pressure-fitted to the lead in an effort to eliminate any lead fluorescence response in the TLD's due to the shield.

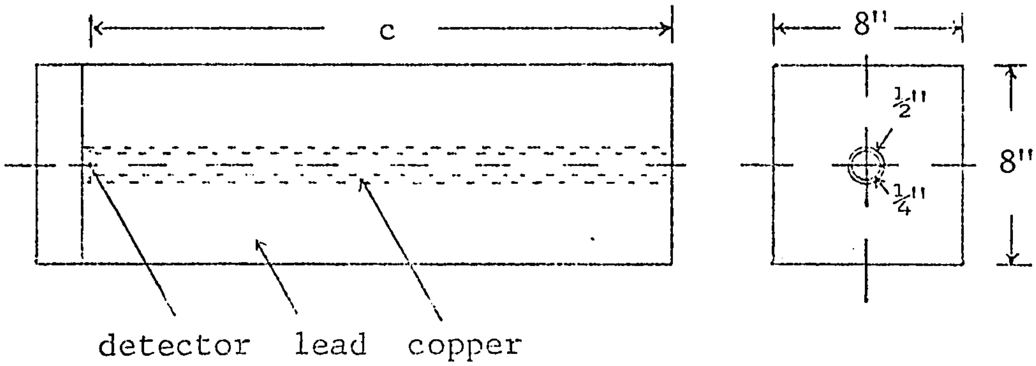

Figure 38. Collimator detail

The mean free path was calculated by the standard equation (11):

$$(\text{mfp}) = \frac{1}{\mu_o} \qquad \text{Eq. C.1}$$

where: μ_o is the total linear attenuation coefficient (as found in Reference 38).

Since the reflected radiation is certainly not monoenergetic (see Appendix D, Figures 49 - 66 for example spectra) a μ_{eff} must be used.

$$\mu_{eff} = \frac{\sum_i \mu_{o_i} E_i}{\sum_i E_i} \qquad \text{Eq. C.2}$$

where E_i is the amount of energy emitted in the "i"th energy interval. μ_{o_i} is the total attenuation coefficient at the average energy of the "i"th energy interval.

The computer-generated spectra in Appendix D were used to obtain the following table.

TABLE 4

DETECTOR COLLIMATOR CORRECTION

Incident Bremsstrahlung Spectra Max. (MeV)	Scatterer Material	Collimator Correction (Inches)
2.0	Lead	0.11
	Iron	0.32
	Concrete	0.15
3.5	Lead	0.15
	Iron	0.31
	Concrete	0.18
7.0	Lead	0.20
	Iron	0.31
10.5	Lead	0.26
	Iron	0.32
	Concrete	0.26

D. SPECTRA CONSIDERATIONS

D.1 INPUT SPECTRA

In order to obtain a computer solution to the back-scatter problem, one must have some knowledge of the incident beam energy spectra. Spectra for the machines studied in this dissertation are quite difficult to obtain. For the purposes of gaining some computer comparison to the experimental data, the author has relied heavily on previously published spectra. At 2.0, 3.5, and 10.5 MeV, very rough absorption measurements were made to have an "effective" energy measurement for comparison to the published spectra in DTF runs. Copper was used in the absorption study and calibrated against Co-60 and Cs-137. Absorption measurements at 7.0 MeV had been made previously by facility operators.

Figure 39 was obtained from copper absorption of the 2.0 MeV Van de Graaff beam. An effective energy (determined by the method of Greening [96]) of 0.85 MeV was used as input to the DTF program. These results are compared in

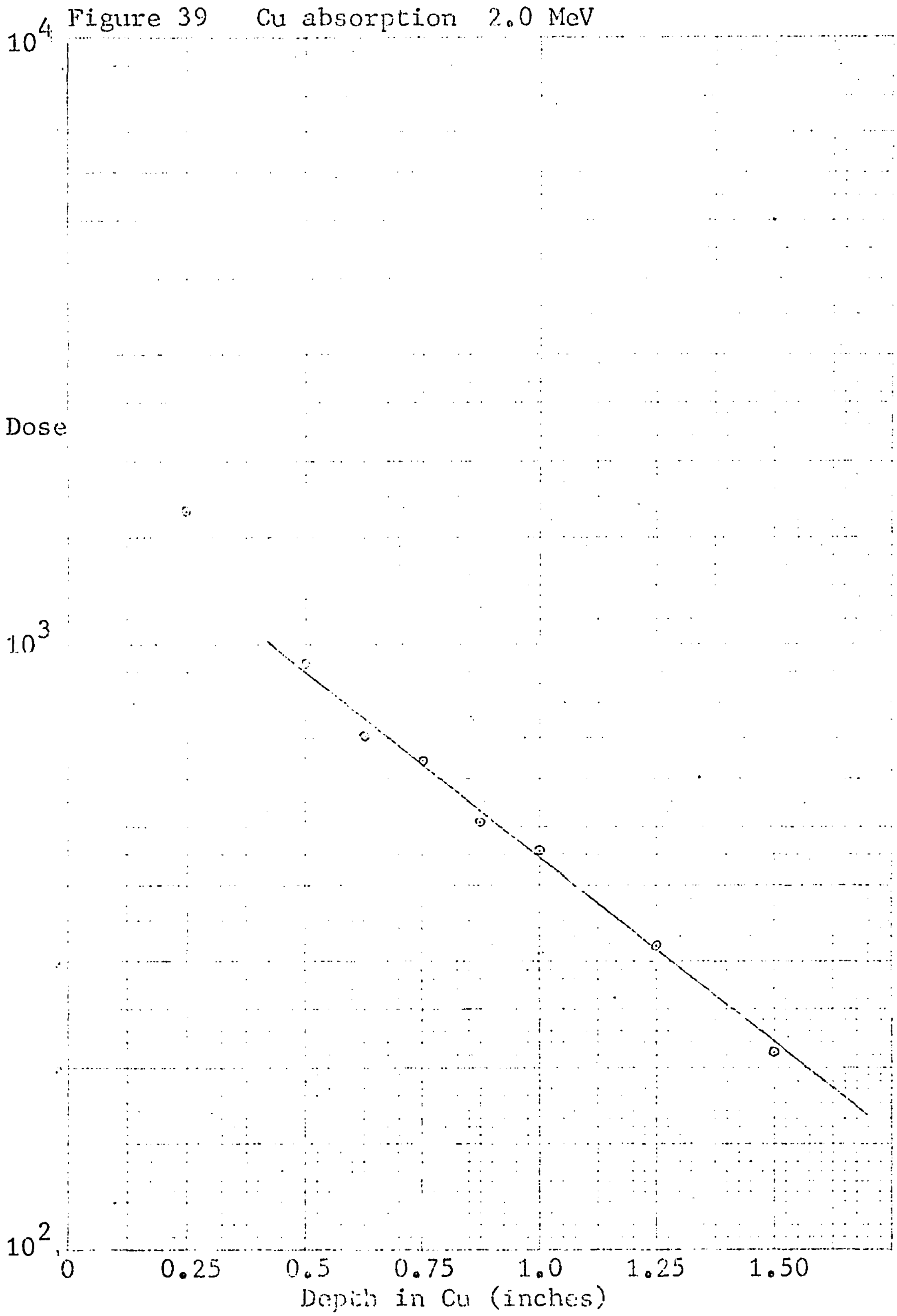
Figure 39 Cu absorption 2.0 MeV
10^4
Dose
10^3
10^2
0
0.25
0.5
0.75
1.0
1.25
1.50
Depth in Cu (inches)

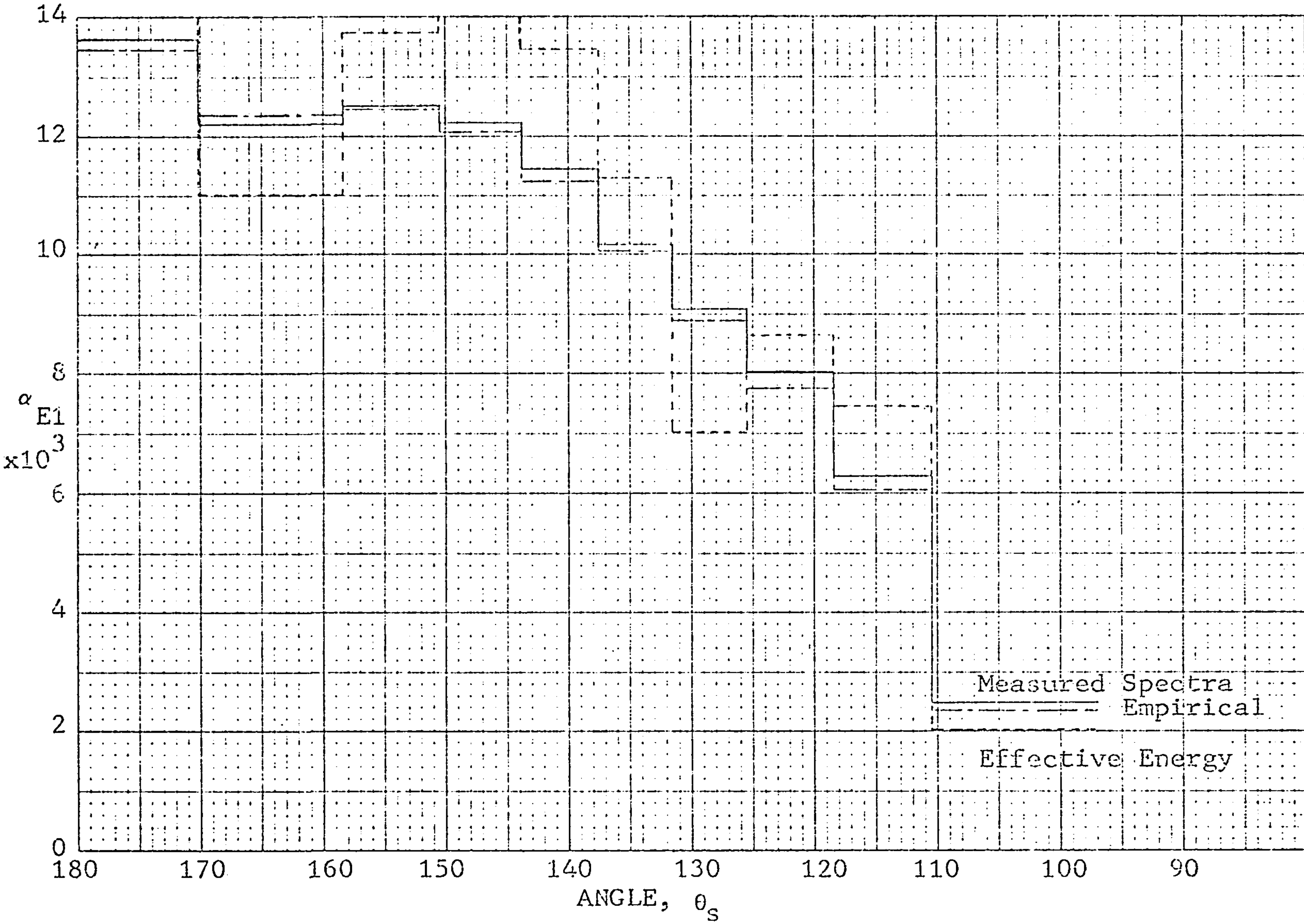

Figure 40 2.0 MeV iron scatterer (DTF)

Figure 40 with DTF results obtained when inputting a measured 2.0 MeV spectrum (Table 5). Iron was used as an example reflecting material.

TABLE 5

2.0 MeV MEASURED SPECTRA (99, 100)

GROUP BOUNDS (MeV)	INPUT FLUX (Photons/MeV)
2.0	5.6
1.5	13.6
1.02	22.0
0.80	35.0
0.60	60.0
0.52	65.0
0.50	68.0
0.44	75.0
0.38	85.0
0.32	87.0
0.28	90.0
0.25	90.0
0.225	90.0
0.20	80.0
0.175	70.0
0.15	60.0
0.13	50.0
0.12	40.0
0.10	40.0
0.088	40.0
0.07684	40.0
0.07664	35.0
0.68	35.0
0.060	30.0
0.055	25.0
0.050	20.0
0.045	15.0
0.040	10.0
0.035	5.0
0.030	

A similar process was carried out on the 3.5 MeV flash x-ray machine. Figure 41 shows the absorption curve, Figure 42 the DTF results, and Table 6 the measured spectra (102) used for comparison. By Greening's technique the 3.5 MeV beam was estimated to be 43.2% 0.24 MeV and 56.8% 1.34 MeV. The measured spectra in this case are somewhat rougher than before as they were used for input to both the Monte Carlo program and DTF. The Monte Carlo spectra input is limited to twenty-five energy groups. The scattering material is again iron.

TABLE 6

3.5 MeV MEASURED SPECTRA (102)

GROUP BOUNDS (MeV)	INPUT FLUX (Photons/MeV)
3.5	0.0143
3.3	0.0845
3.1	0.1194
2.75	0.1746
2.35	0.2553
1.95	0.3692
1.55	0.5355
1.36	0.6471
1.15	0.8261
0.78	1.2821
0.68	1.4412
0.58	1.6724
0.48	1.875
0.38	1.5789
0.32	0.312
0.30	0.0
0.10	0.0
0.06	0.0
0.03	

Figure 41 3.5 MeV Cu absorption

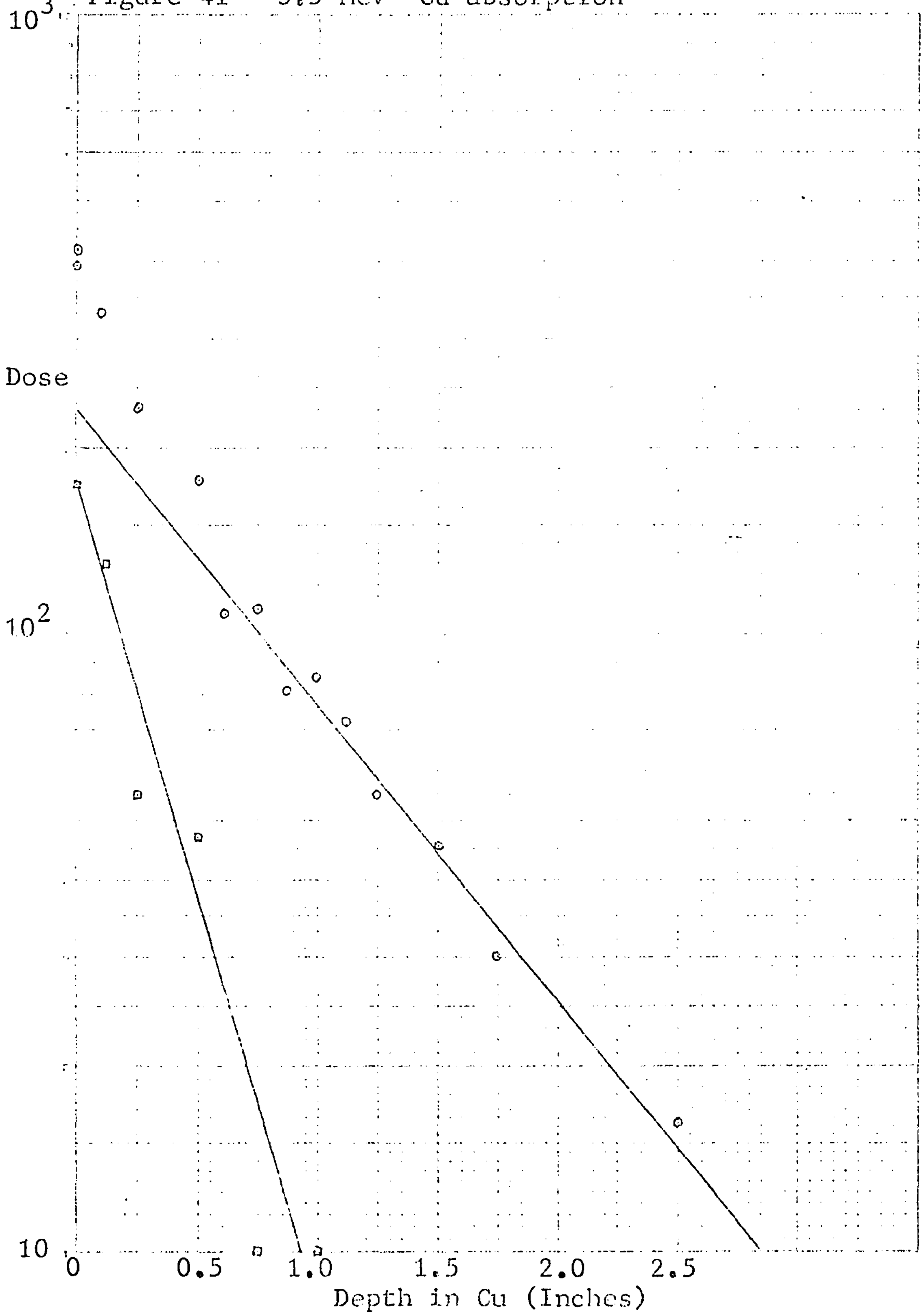

Figure 42 DTF 3.5 MeV iron scatterer

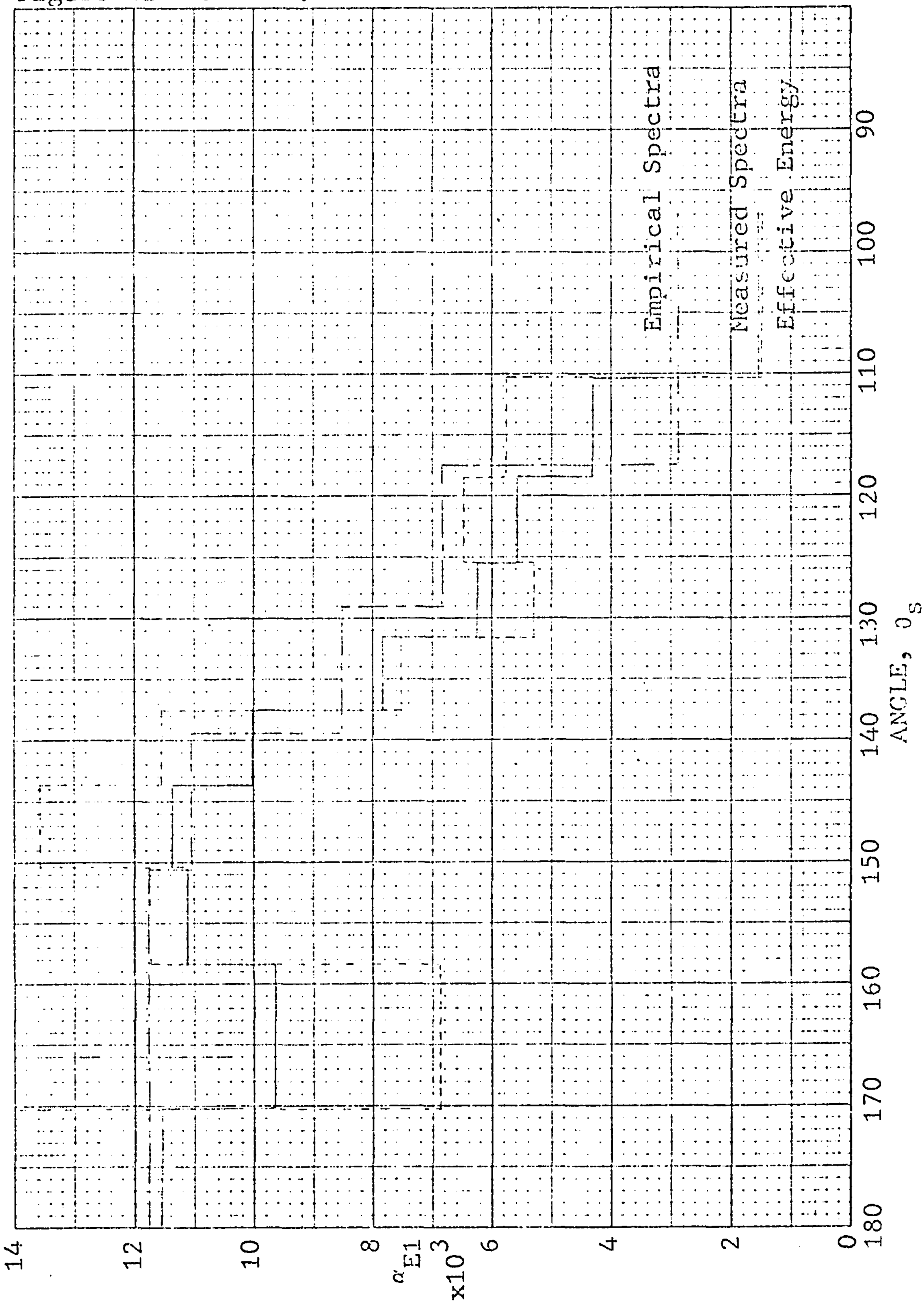

Due to the relative scarcity of measured spectra from flash x-ray devices, several methods of calculating spectra have been derived. Most of these are computerized methods of studying electron transport in a target material. (119, 120). One (121), however, is based on an analytical approximation requiring only a maximum and minimum energy input to obtain a spectra guess. The measured spectrum reported for a 3.5 MeV machine (not that used in this work) is compared with the spectrum obtained from an electron transport code (122) and the empirical approximation spectra in Figure 43. Normalization of the three curves differs to more clearly show each. Results of the empirical method are compared with results previously discussed in Figures 40 and 42. The spectra are given in Tables 7 and 8. The results obtained using the empirical spectra with 7.0 MeV and 10.5 MeV are compared with measured spectra inputs for the same energies in Figures 44 and 45. Lead is used as a reflector in these examples. The input spectra used are found in Tables 9, 10, 11, and 12.

Figure 43 Various 3.5 MeV input spectra

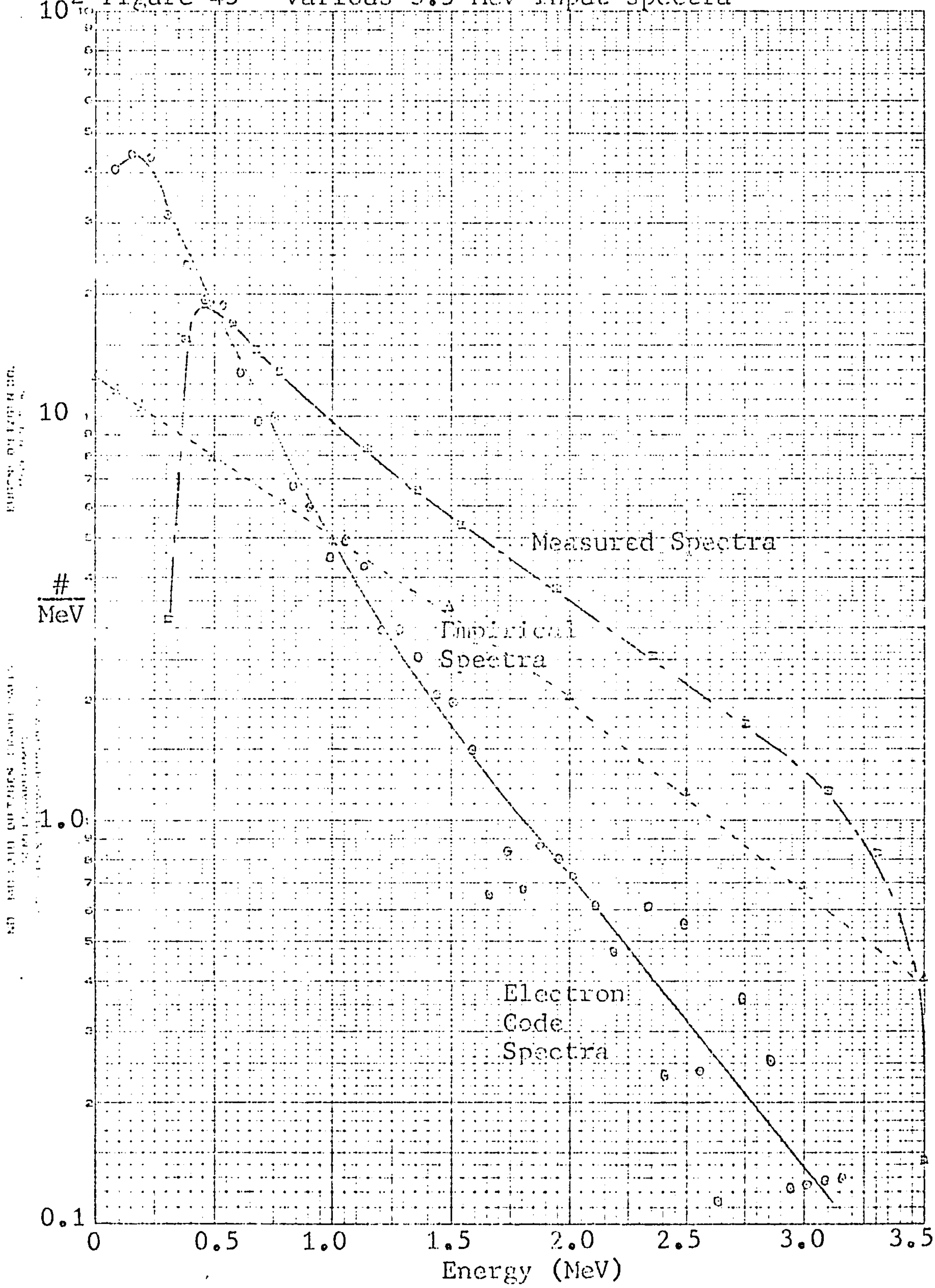

TABLE 7

2.0 MeV EMPIRICAL SPECTRA

GROUP BOUNDS (MeV)	INPUT FLUX (Photons/MeV)
2.00	0.15186
1.50	0.38412
1.02	0.72064
0.80	1.06659
0.60	1.37958
0.52	1.51365
0.50	1.63223
0.44	1.82633
0.38	2.04373
0.32	2.24355
0.28	2.39530
0.25	2.52180
0.225	2.64268
0.20	2.76940
0.175	2.90216
0.15	3.02695
0.13	3.11310
0.12	3.20190
0.10	3.29921
0.08805	3.37152
0.07684	3.40500
0.07664	3.43588
0.068	3.48987
0.060	3.53260
0.055	3.56580
0.050	3.59940
0.045	3.63320
0.040	3.66740
0.035	3.70200
0.030	

TABLE 8

3.5 MeV EMPIRICAL SPECTRA

GROUP BOUNDS (MeV)	INPUT FLUX (Photons/MeV)
3.5	0.040306
3.0	0.068831
2.5	0.117541
2.0	0.200724
1.5	0.338811
1.02	0.48852
0.8	0.61139
0.6	0.70908
0.52	0.74785
0.50	0.78068
0.44	0.83246
0.38	0.88767
0.32	0.93638
0.28	0.97209
0.25	1.0111
0.225	1.02083
0.2	1.05614
0.175	1.0848
0.15	1.1112
0.13	1.1292
0.12	1.14747
0.1	1.16727
0.088	1.18183
0.077	1.19135
0.068	1.20536
0.060	1.21377
0.055	1.22029
0.050	1.22683
0.045	1.23342
0.040	1.24003
0.035	1.24669
0.030	

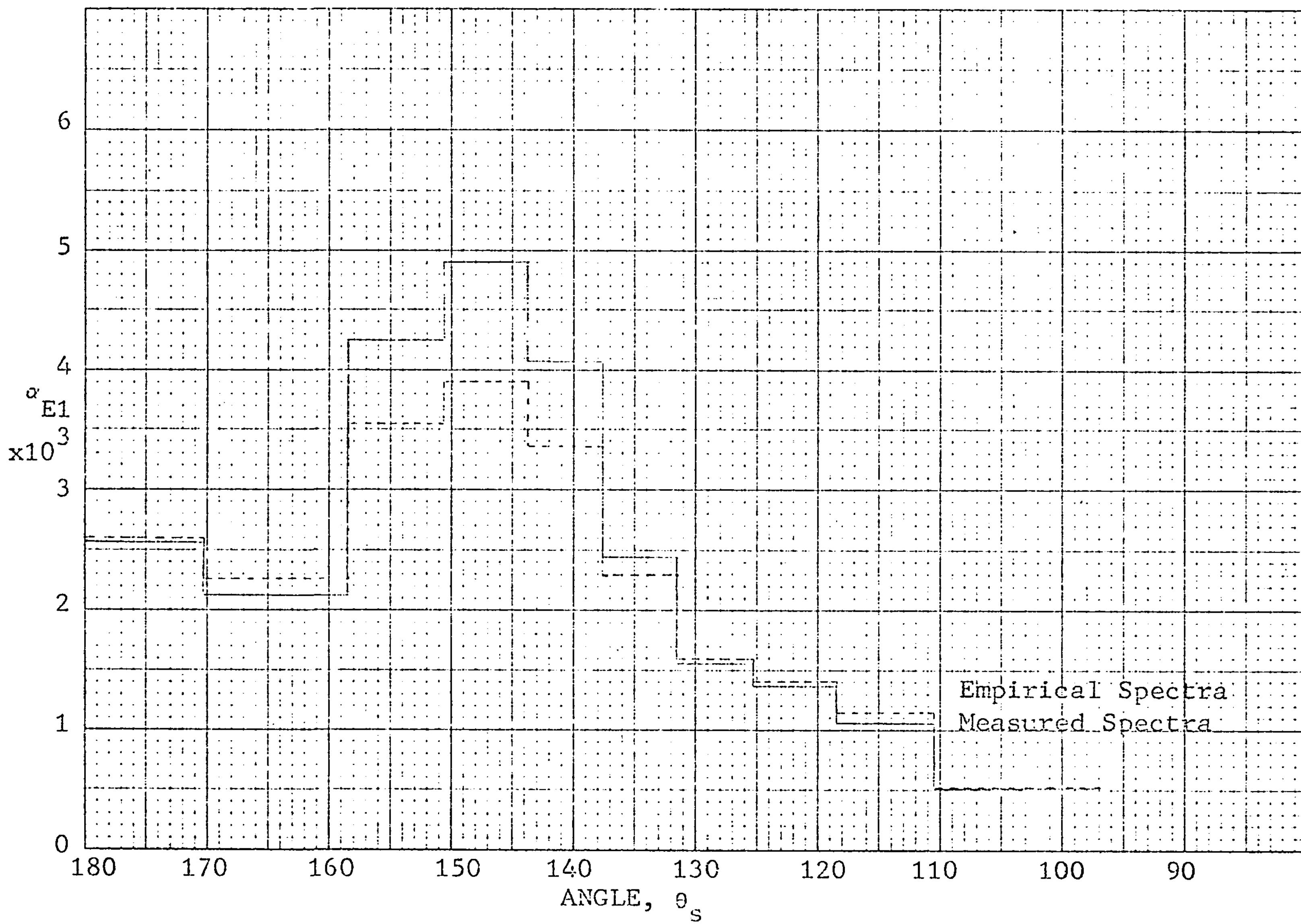

Figure 44 DTF 7.0 MeV lead scatterer

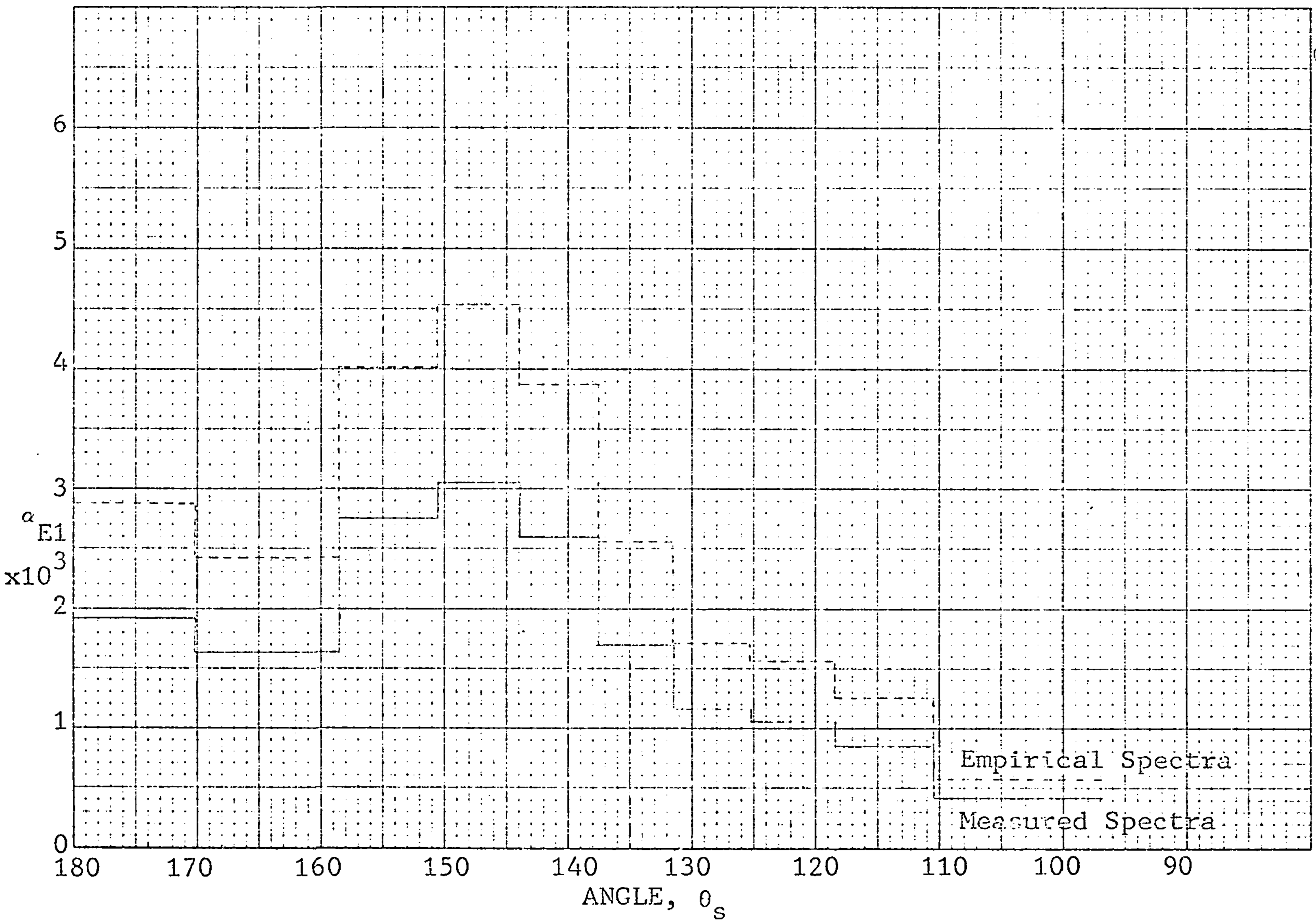

Figure 45 DTF 10.5 MeV lead scatterer

TABLE 9

7.0 MeV MEASURED SPECTRA (105)

GROUP BOUNDS (MeV)	INPUT FLUX (Photons/MeV)
7.0	1.4286
6.63	4.5249
6.12	6.5359
5.61	8.7344
5.1	10.784
4.59	13.508
4.08	16.667
3.57	21.008
3.06	26.471
2.55	34.118
2.04	46.078
1.53	63.399
1.275	76.471
1.02	93.137
0.765	95.425
0.51	107.840
0.40	0.0
0.30	0.0
0.10	0.0
0.06	0.0
0.03	

TABLE 10

7.0 MeV EMPIRICAL SPECTRA

GROUP BOUNDS (MeV)	INPUT FLUX (Photons/MeV)
7.0	0.0100723
6.0	0.0172003
5.0	0.0293728
4.0	0.0501598
3.0	0.0742656
2.5	0.0970494
2.0	0.126823
1.5	0.164807
1.02	0.198325
0.8	0.221891
0.6	0.239058
0.52	0.245523
0.5	0.250845
0.44	0.25903
0.38	0.267482
0.32	0.274729
0.28	0.279921
0.25	0.28407
0.225	0.287896
0.2	0.291773
0.175	0.295703
0.15	0.299285
0.13	0.301695
0.12	0.304128
0.10	0.306742
0.088005	0.308649
0.07684	0.309588
0.07664	0.310322
0.068	0.311706
0.06	0.312792
0.055	0.31363
0.05	0.314471
0.045	0.315313
0.04	0.316158
0.035	0.317005
0.03	

TABLE 11

10.5 MeV MEASURED SPECTRA (110)

GROUP BOUNDS (MeV)	INPUT FLUX (Photons/MeV)
10.5	1.18
10.0	2.3
9.5	5.3
9.0	12.5
8.0	18.5
7.0	24.0
6.0	31.0
5.0	38.0
4.5	46.0
4.0	53.0
3.5	70.0
3.0	87.0
2.5	125.0
2.0	190.0
1.5	300.0
1.2	450.0
1.02	640.0
0.8	760.0
0.6	830.0
0.52	870.0
0.5	900.0
0.44	980.0
0.38	1112.0
0.32	1500.0
0.28	1500.0
0.25	1500.0
0.225	1112.0
0.2	980.0
0.175	900.0
0.15	450.0
0.13	0.0
0.12	0.0
0.10	0.0
0.0880	0.0
0.07684	0.0
0.07664	0.0

TABLE 11 (cont'd)

GROUP BOUNDS (MeV)	INPUT FLUX (Photons/MeV)
0.070	0.0
0.06	0.0
0.05	0.0
0.04	0.0
0.03	

TABLE 12

10.5 MeV EMPIRICAL SPECTRA

GROUP BOUNDS (MeV)	INPUT FLUX (Photons/MeV)
10.5	0.035003
10.0	0.045268
9.0	0.065839
8.0	0.0957568
7.0	0.13927
6.0	0.202555
5.0	0.294598
4.0	0.428466
3.0	0.564976
2.5	0.681355
2.0	0.821707
1.5	0.987151
1.02	1.12425
0.8	1.2162
0.6	1.28143
0.52	1.30561
0.5	1.32535
0.44	1.35547
0.38	1.38629
0.32	1.41248
0.28	1.43111
0.25	1.44593
0.225	1.45954
0.2	1.47327
0.175	1.48713
0.15	1.49972
0.13	1.50816
0.12	1.51666
0.10	1.52578
0.088005	1.53241
0.07684	1.53567
0.07664	1.53764
0.07	1.54244
0.06	1.54823
0.05	1.55404
0.04	1.55988
0.03	

Absorption measurements by Kirtland Air Force personnel indicate an effective energy of 4.1 - 4.2 MeV for the 7.0 MeV flash x-ray machine, as discussed in Section 5.

Absorption measurements of the HERMES II beam are shown in Figures 46 and 47. The curve in Figure 46 was made with a 70 mil tantalum x-ray target and 0.3125 inch aluminum filter while Figure 47 was made with a 60 mil tantalum target and 0.4 inch aluminum filter. The effect of the additional filter in "hardening" the beam can be seen. In the first case one gets a 58% component at 3.8 to 4.2 MeV and a 42% component of 0.27 - 0.28 MeV. The second set-up indicates about 75% at 4.9 - 5.5 MeV and 25% at 0.11 - 0.15 MeV. The tube configuration at the time data was taken for this research was a 60 mil tantalum target backed by a 0.3125 inch aluminum plate.

None of the measured spectra referenced give photon flux for less than 200 - 300 KeV. There is considerable debate as to the amount of energy carried in the low energy range of the spectra. Some (123) feel that the low energy count goes significantly higher than any other portion of the spectra, while others (104, 105) indicate a drop to zero below 100 KeV. Something in between these two views

Figure 46 10.5 MeV Copper absorption

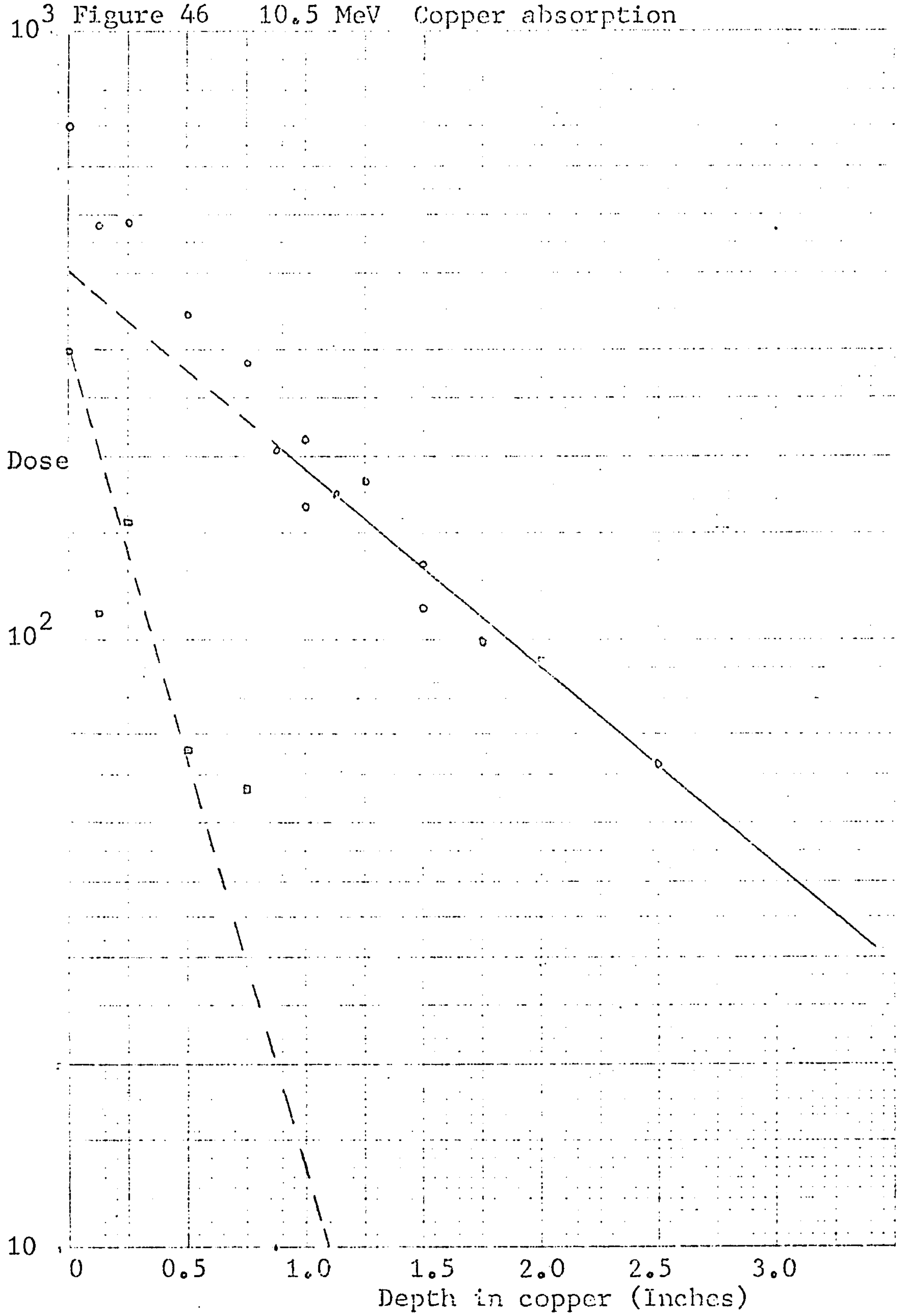

Figure 47 10.5 MeV copper absorption

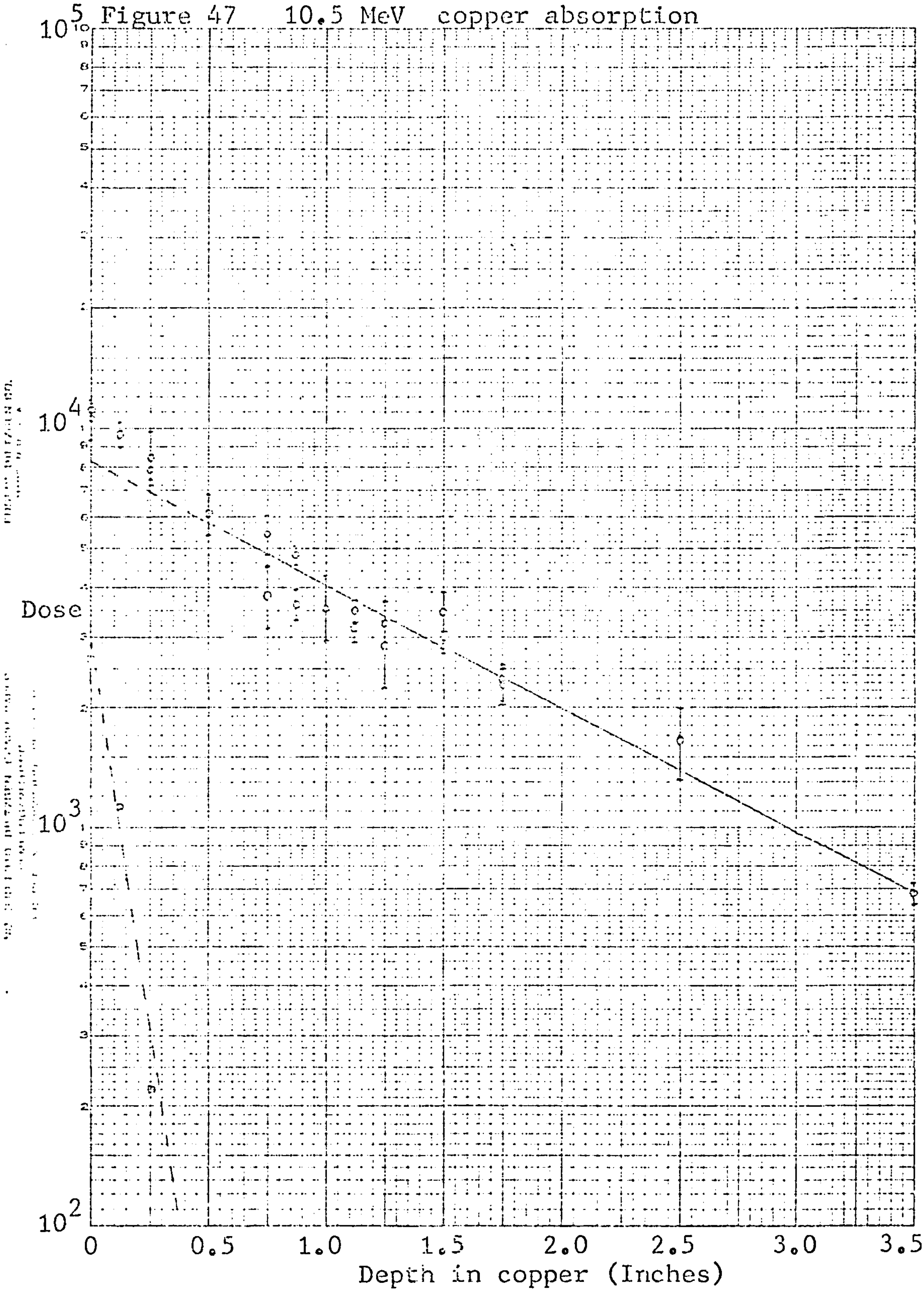

is probably more nearly the correct representation. To the primary mission of the x-ray devices studied (i.e. dose deposition inside a steel-encased body) the question of low energy population is largely academic. The effect on the present experiments is shown in Figure 48. The input spectra for these curves are given in Table 13. The total energy albedo from iron is reduced 31.8% by increasing the low energy component of the beam by the amounts shown. The difference the additional filter used at 7.0 MeV would make on the 10.5 MeV spectrum is shown in Figures 49 and 50.

Figure 48 DTF 10.5 MeV iron scatterer

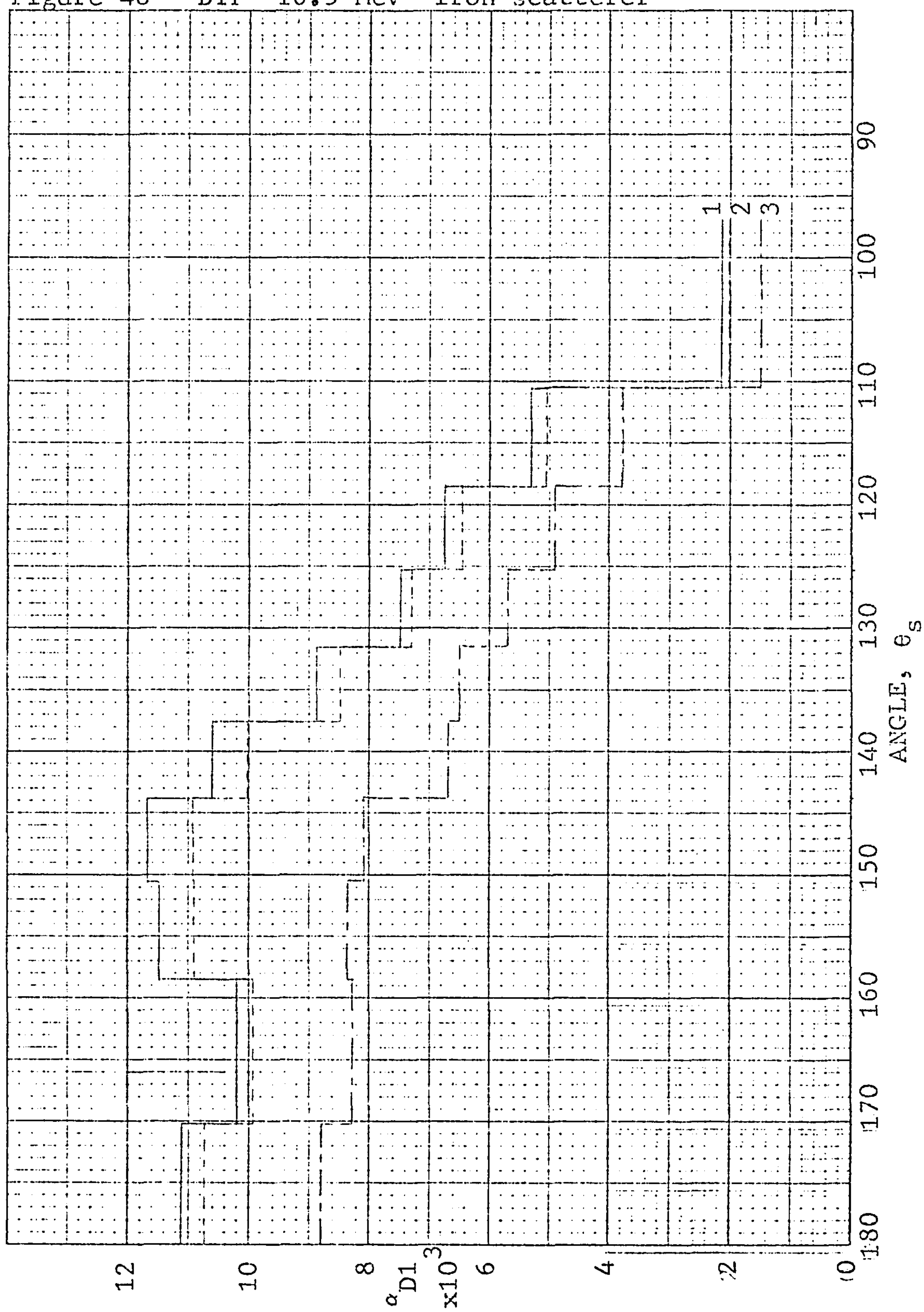

TABLE 13

10.5 MeV SPECTRA

GROUP BOUNDS (MeV)	INPUT FLUX 1 (Photons/MeV)	INPUT FLUX 2 (Photons/MeV)	INPUT FLUX 3 (Photons/MeV)
10.5	1.18	1.18	1.18
10.0	2.3	2.3	2.3
9.5	5.3	5.3	5.3
9.0	12.5	12.5	12.5
8.0	18.5	18.5	18.5
7.0	24.0	24.0	24.0
6.0	31.0	31.0	31.0
5.0	38.0	38.0	38.0
4.5	46.0	46.0	46.0
4.0	53.0	53.0	53.0
3.5	70.0	70.0	70.0
3.0	87.0	87.0	87.0
2.5	125.0	125.0	125.0
2.0	190.0	190.0	190.0
1.5	300.0	300.0	300.0
1.2	450.0	450.0	450.0
1.02	640.0	640.0	640.0
0.8	760.0	760.0	760.0
0.6	830.0	830.0	830.0
0.52	870.0	870.0	870.0
0.5	900.0	900.0	900.0
0.44	980.0	980.0	980.0
0.38	1112.0	1112.0	1112.0
0.32	1500.0	1500.0	1500.0
0.28	1500.0	1500.0	1800.0
0.25	1500.0	1500.0	2600.0
0.225	1112.0	1500.0	3000.0
0.20	980.0	1500.0	4000.0
0.175	900.0	1500.0	5600.0
0.15	450.0	1500.0	8000.0
0.13	0.0	1500.0	10000.0
0.12	0.0	1500.0	13000.0
0.10	0.0	1500.0	17000.0
0.088	0.0	1500.0	18500.0
0.07684	0.0	1500.0	19000.0
0.07664	0.0	1500.0	19000.0
0.07	0.0	1500.0	19500.0
0.06	0.0	1500.0	20000.0
0.05	0.0	1500.0	21500.0
0.04	0.0	1500.0	22500.0

Figure 49   10.5 MeV   Spectra 1

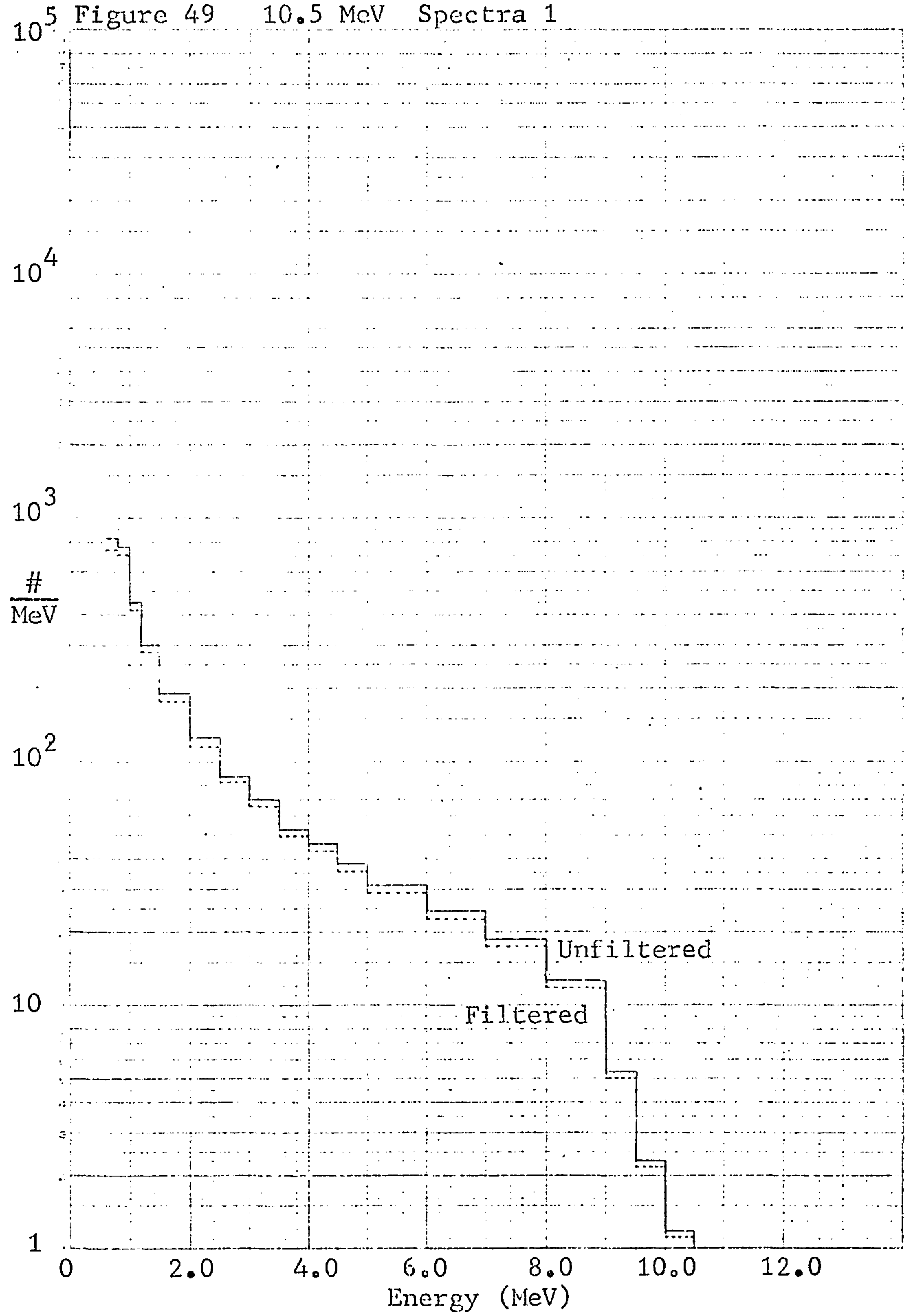

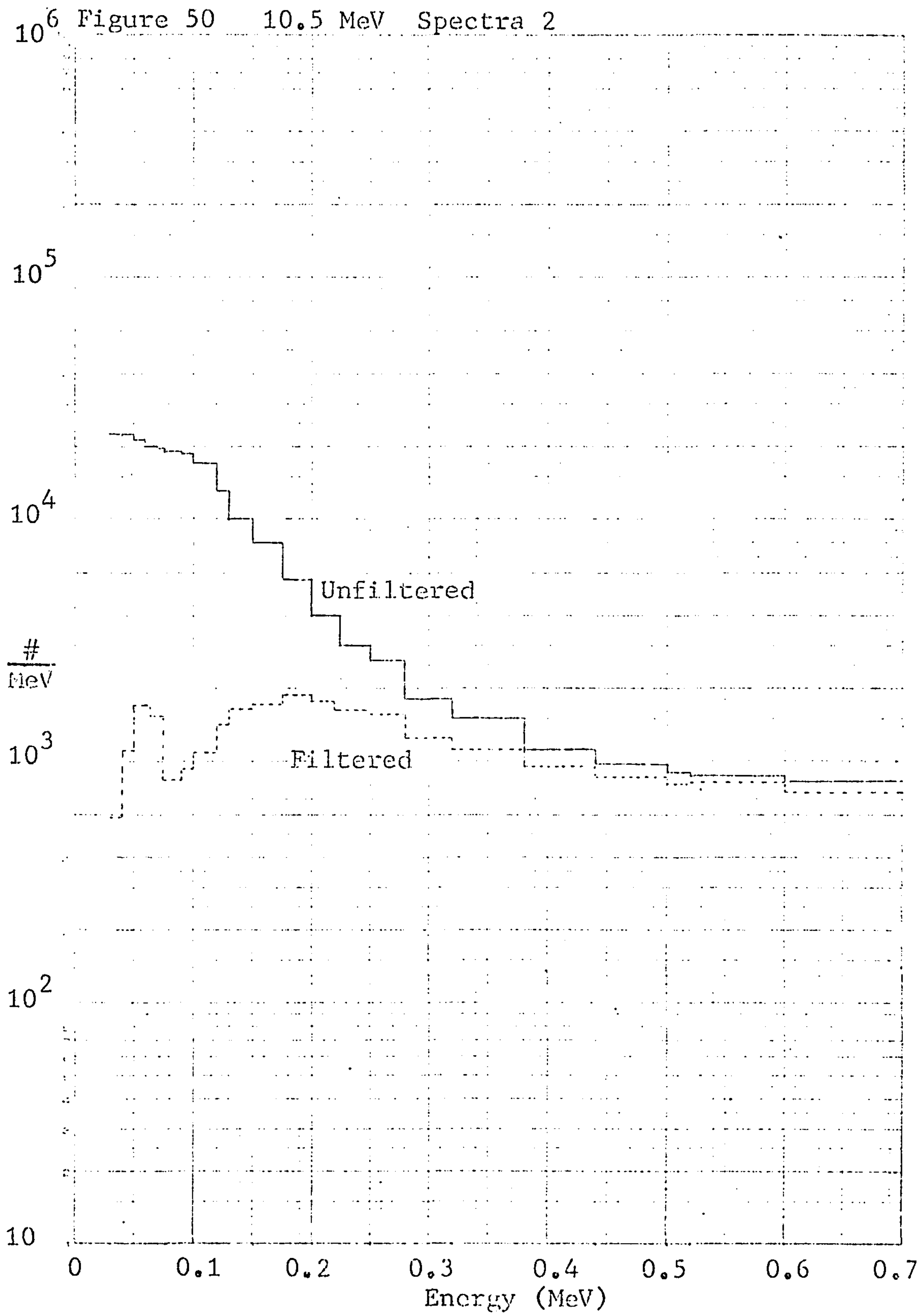
Figure 50 10.5 MeV Spectra 2
10^6
10^5
10^4
#/MeV
10^3
10^2
10
Unfiltered
Filtered
0
0.1
0.2
0.3
0.4
0.5
0.6
0.7
Energy (MeV)

Differential albedo plots for input bremsstrahlung spectra of different peak energies are given in Figure 51 with concrete as the scattering medium. As the input energy increases, DTF can be seen to predict a somewhat cyclic variation with angle. This tendency is more pronounced with higher Z materials and is shown to be quite distinct in Figure 45. This variation is also evident with single energy spectra inputs and is at odds with experimental data previously published for gamma sources. A comparison of DTF and Monte Carlo results with experimental data published elsewhere is shown in Figures 88 and 89.

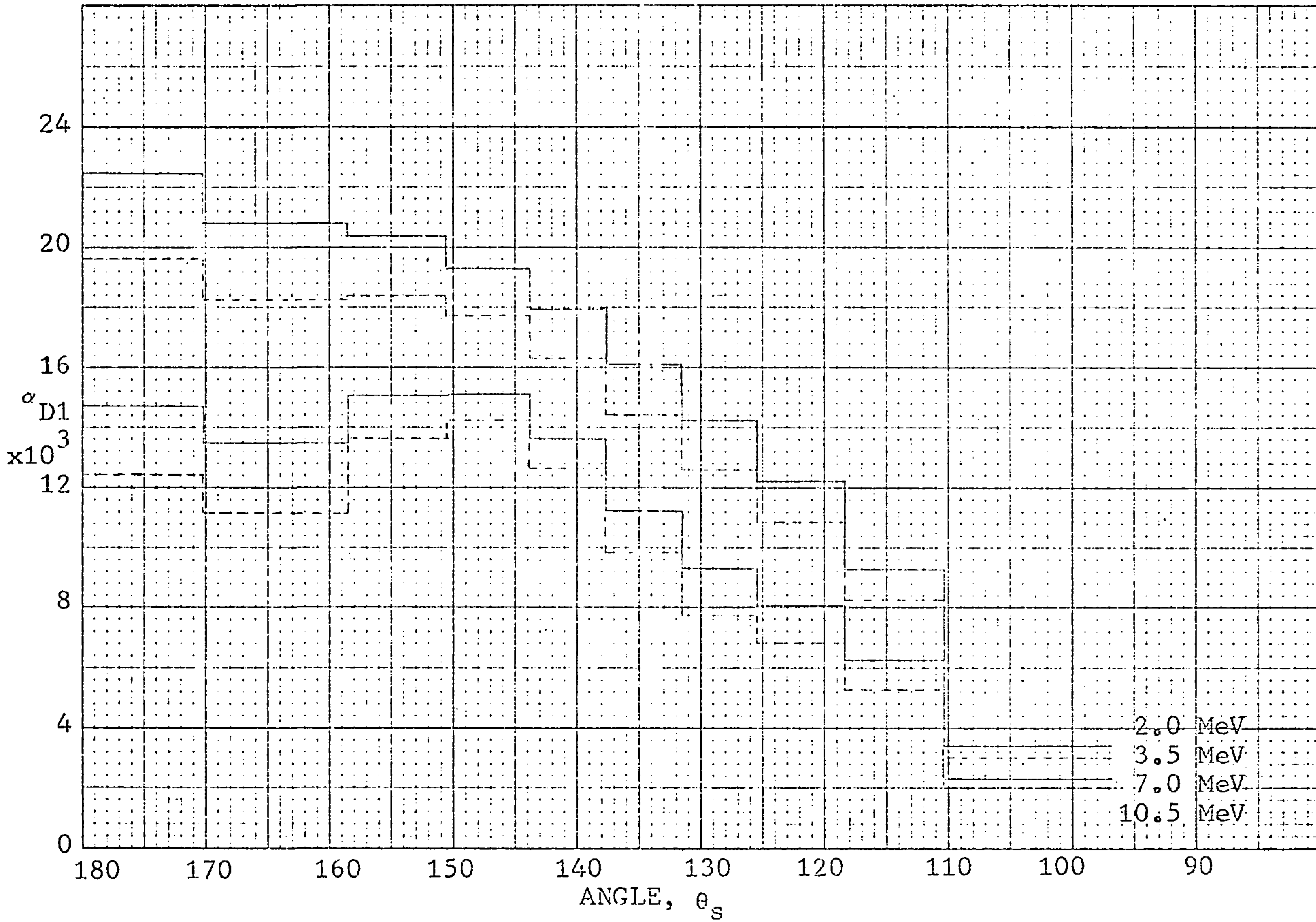

Figure 51 DTF Various E_{max} concrete scatterer

D.29 REFLECTED SPECTRA

Physical measurement of the reflected spectra for backscatter flux with the flash x-ray machines was not possible, as is discussed in Section 3. Due to the steady-state operation mode of the Van de Graaff, some scintillation measurements of reflected spectra were possible at 2.0 MeV. The crystal used (described in Section 3) was canned in 0.032" aluminum which gives a transmission of about 65% at 70 KeV decreasing to 12% at 30 KeV. Due to the rapidly shifting gain evidenced by the detector system functioning in the high radiation background existing in the radiographic bay, no effort was made to correct the spectra obtained. Figures 52 and 53 are examples of the spectra obtained.

Greater spectra information is necessary to make collimator length and TLD response corrections. Spectral results from DTF and Monte Carlo runs are plotted in Figures 54 to 71 for the materials and energies used in this work. These spectra were used for the corrections discussed in Appendices C and E.

Figure 52 2.0 MeV measured 60° concrete scatterer

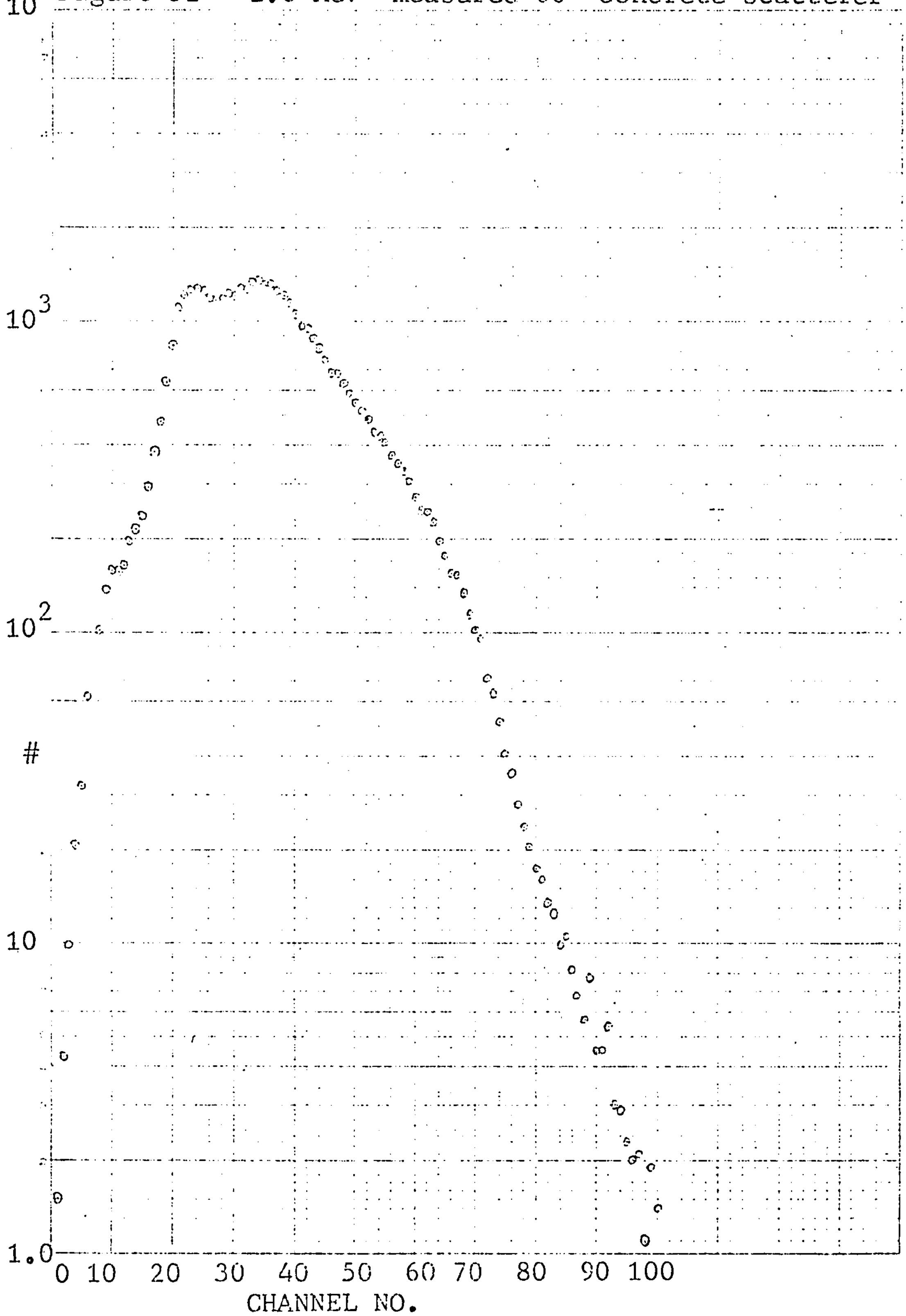

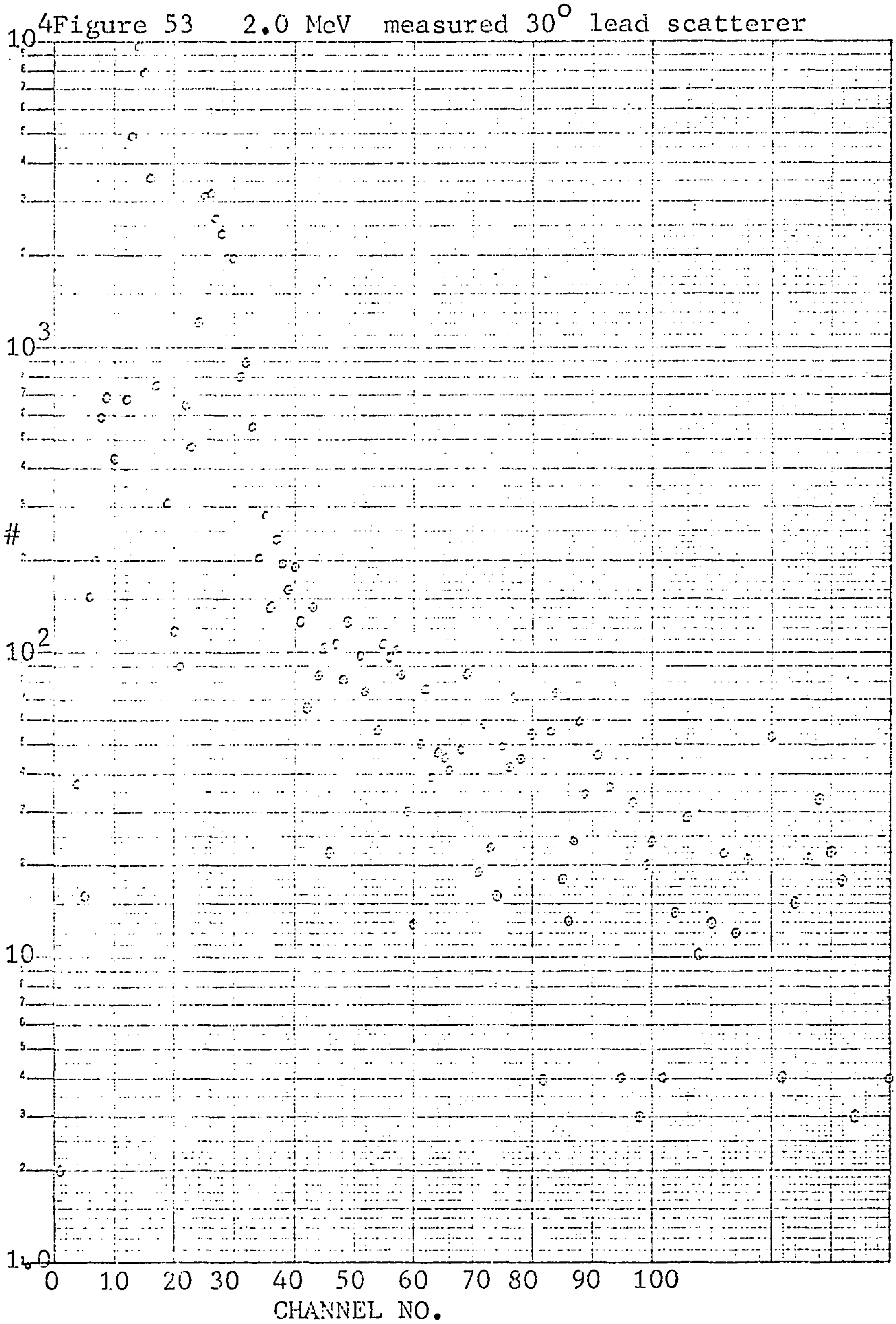
Figure 53 2.0 MeV measured 30° lead scatterer
10^4
10^3
#
10^2
10
1.0
0 10 20 30 40 50 60 70 80 90 100
CHANNEL NO.

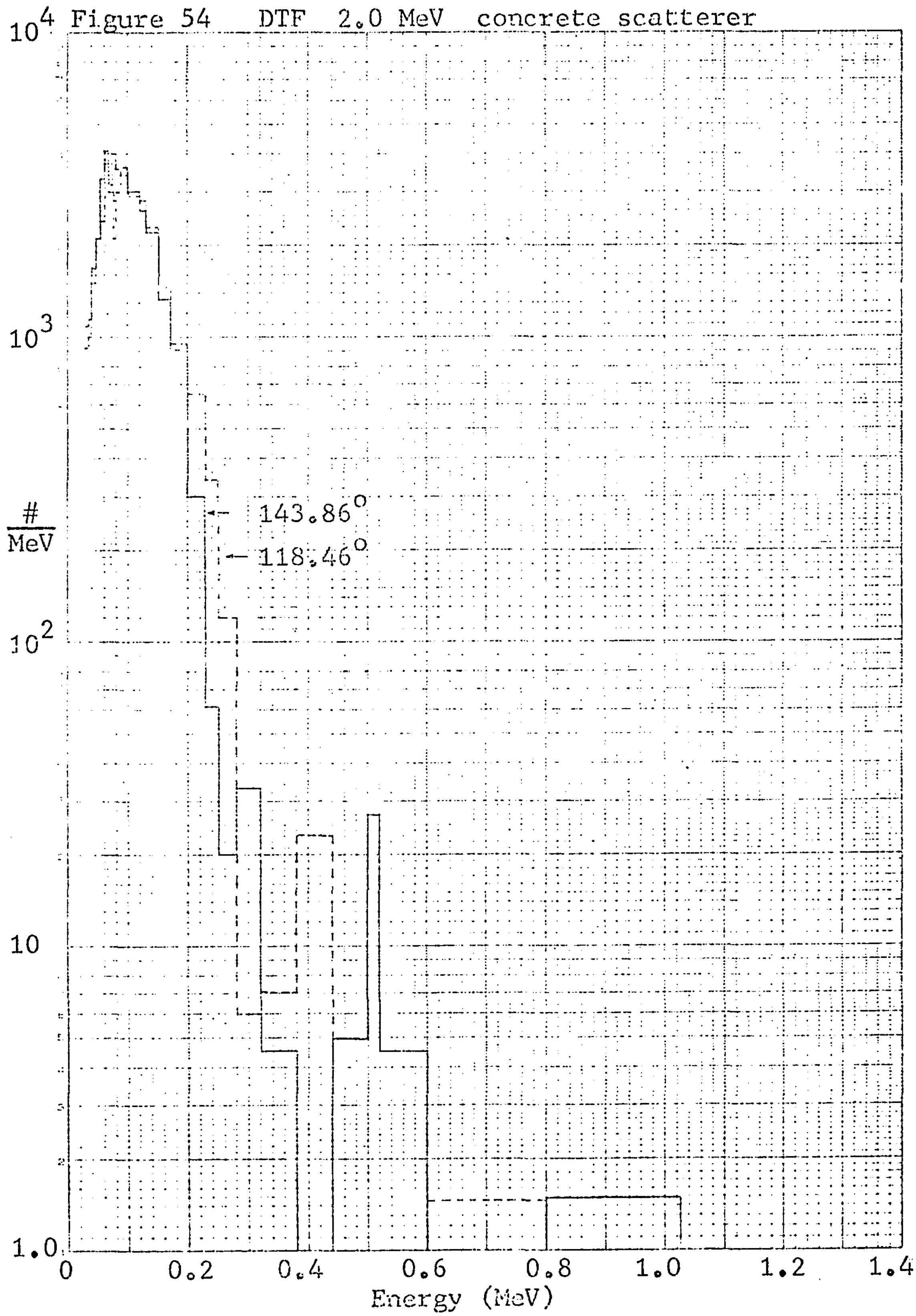

10^4 Figure 54 DTF 2.0 MeV concrete scatterer
10^3
$\frac{\#}{MeV}$
143.86°
118.46°
10^2
10
1.0
0
0.2
0.4
0.6
0.8
1.0
1.2
1.4
Energy (MeV)

Figure 55 DTF 2.0 MeV iron scatterer

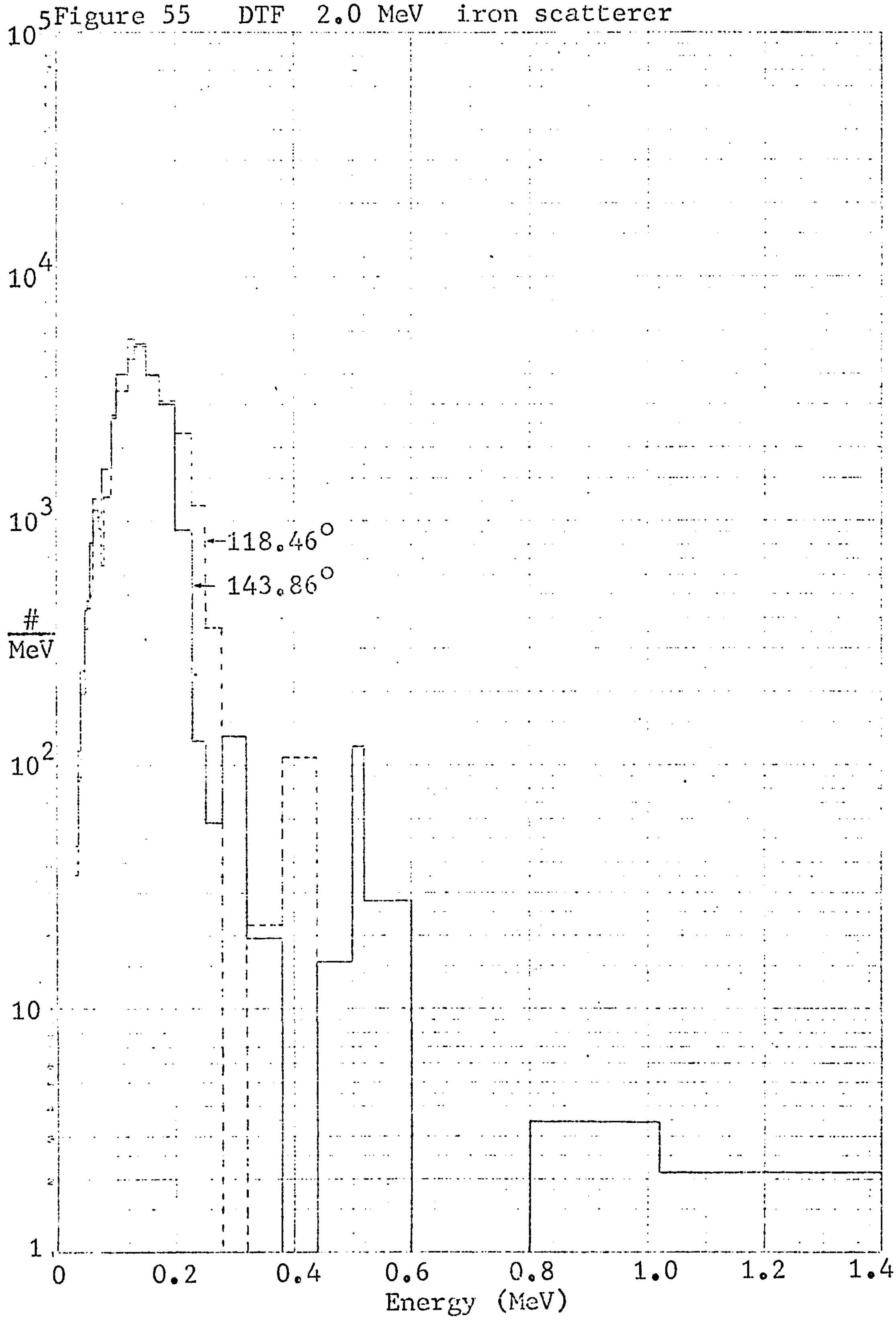

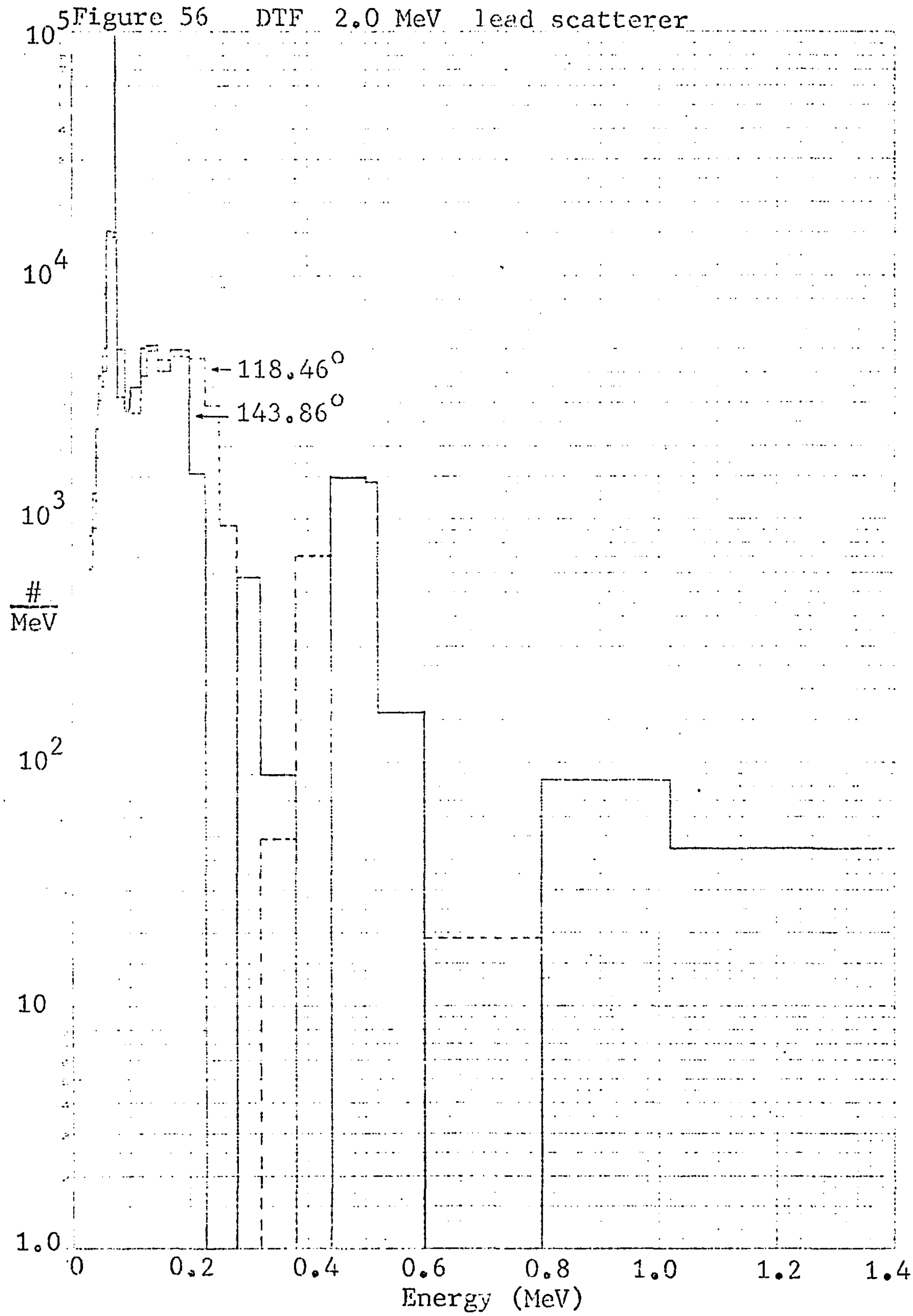
Figure 56 DTF 2.0 MeV lead scatterer
10^5
10^4
10^3
10^2
10
1.0
#/MeV
118.46°
143.86°
0
0.2
0.4
0.6
0.8
1.0
1.2
1.4
Energy (MeV)

Figure 57 Monte Carlo 2.0 MeV aluminum scatterer

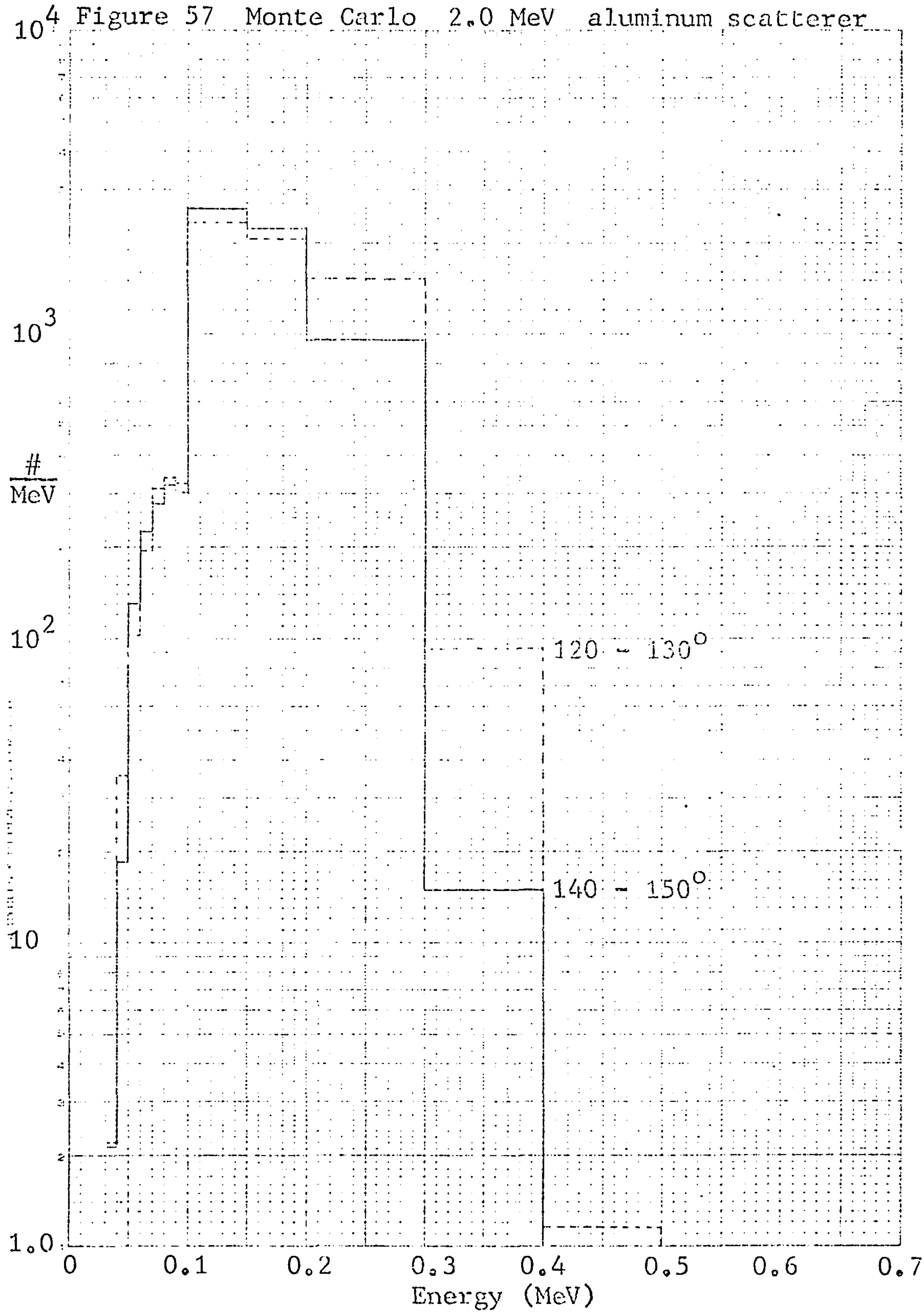

Figure 58 Monte Carlo 2.0 MeV lead scatterer

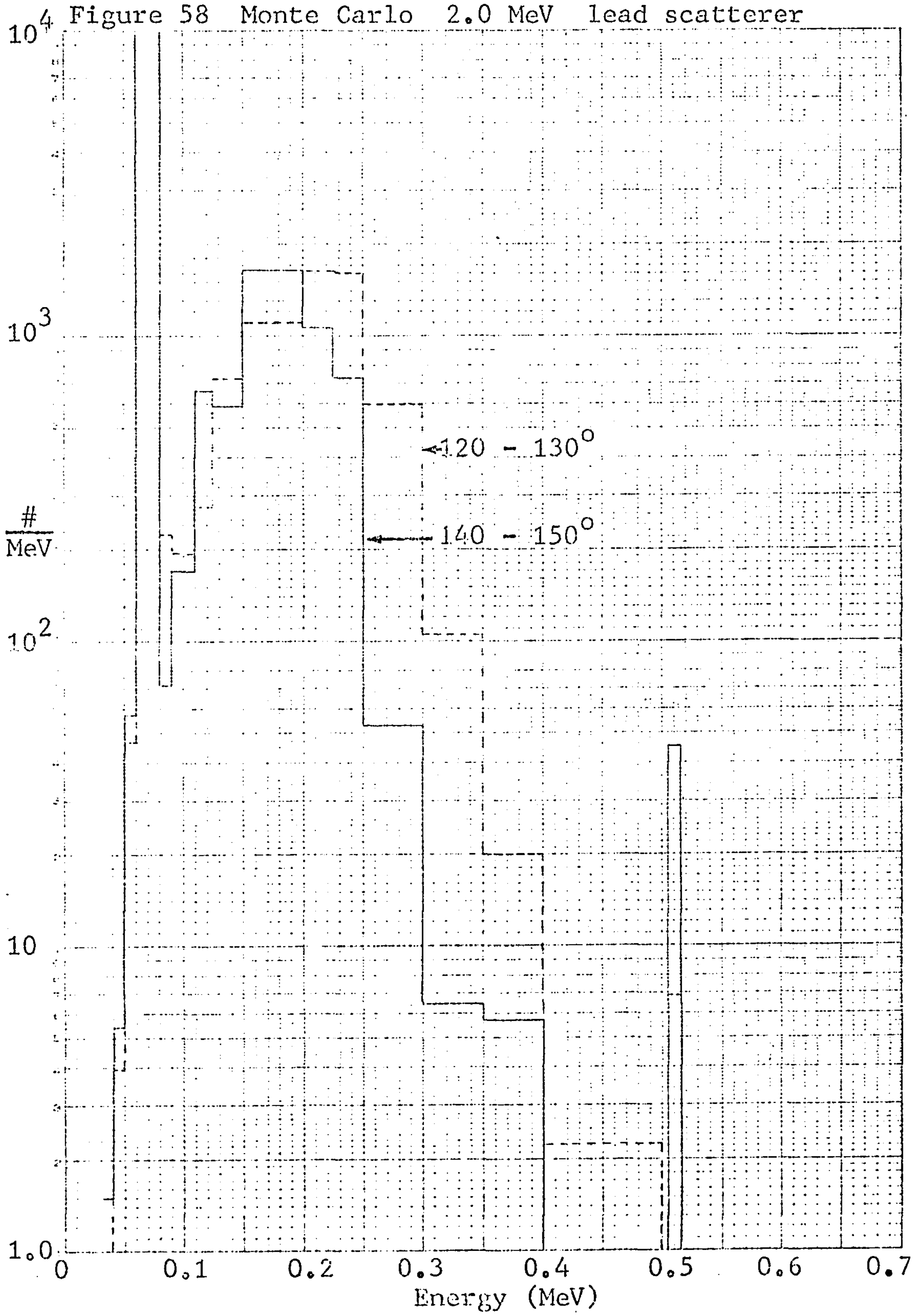

Figure 59 DTF 3.5 MeV concrete scatterer

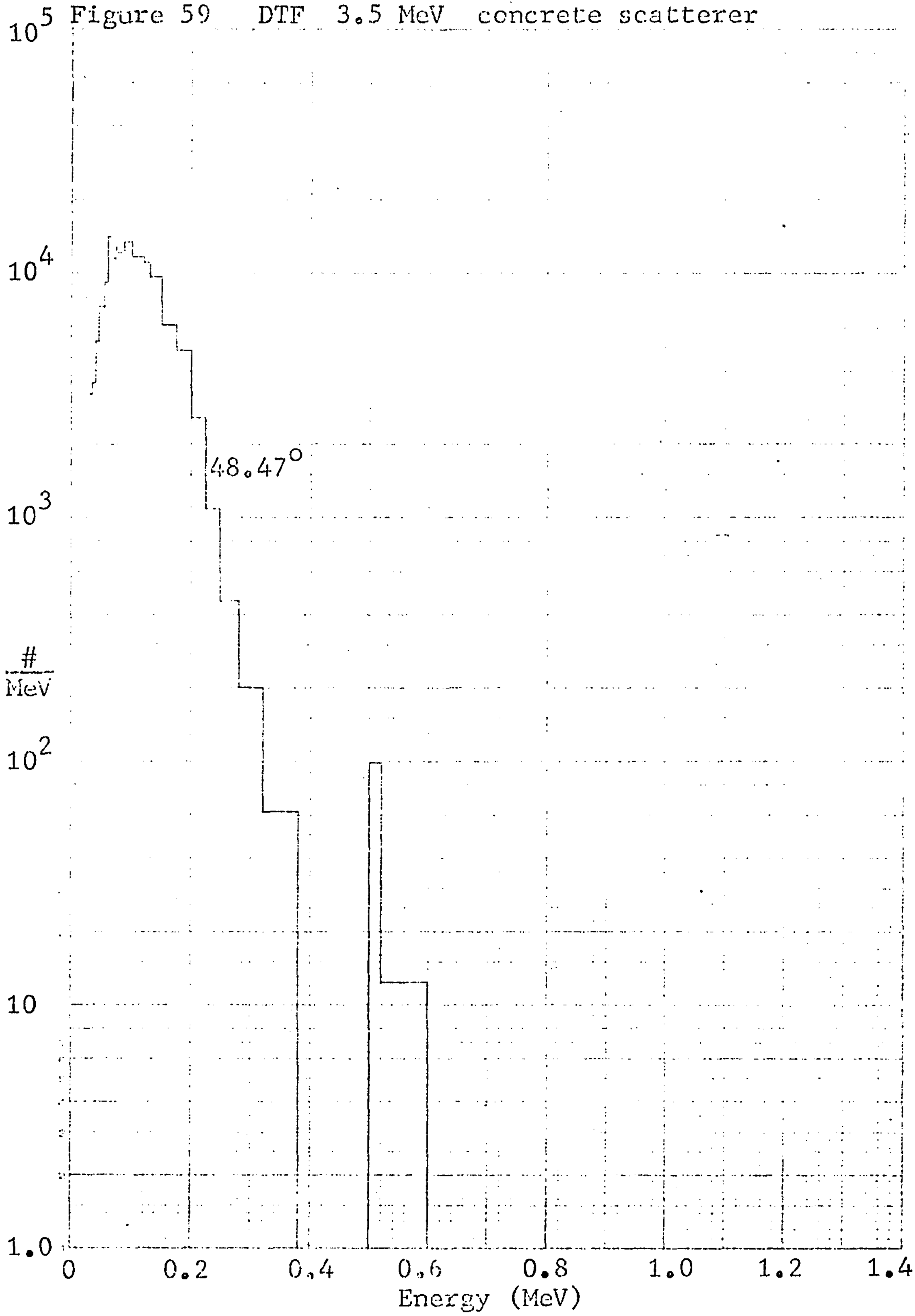

Figure 60 DTF 3.5 MeV iron scatterer

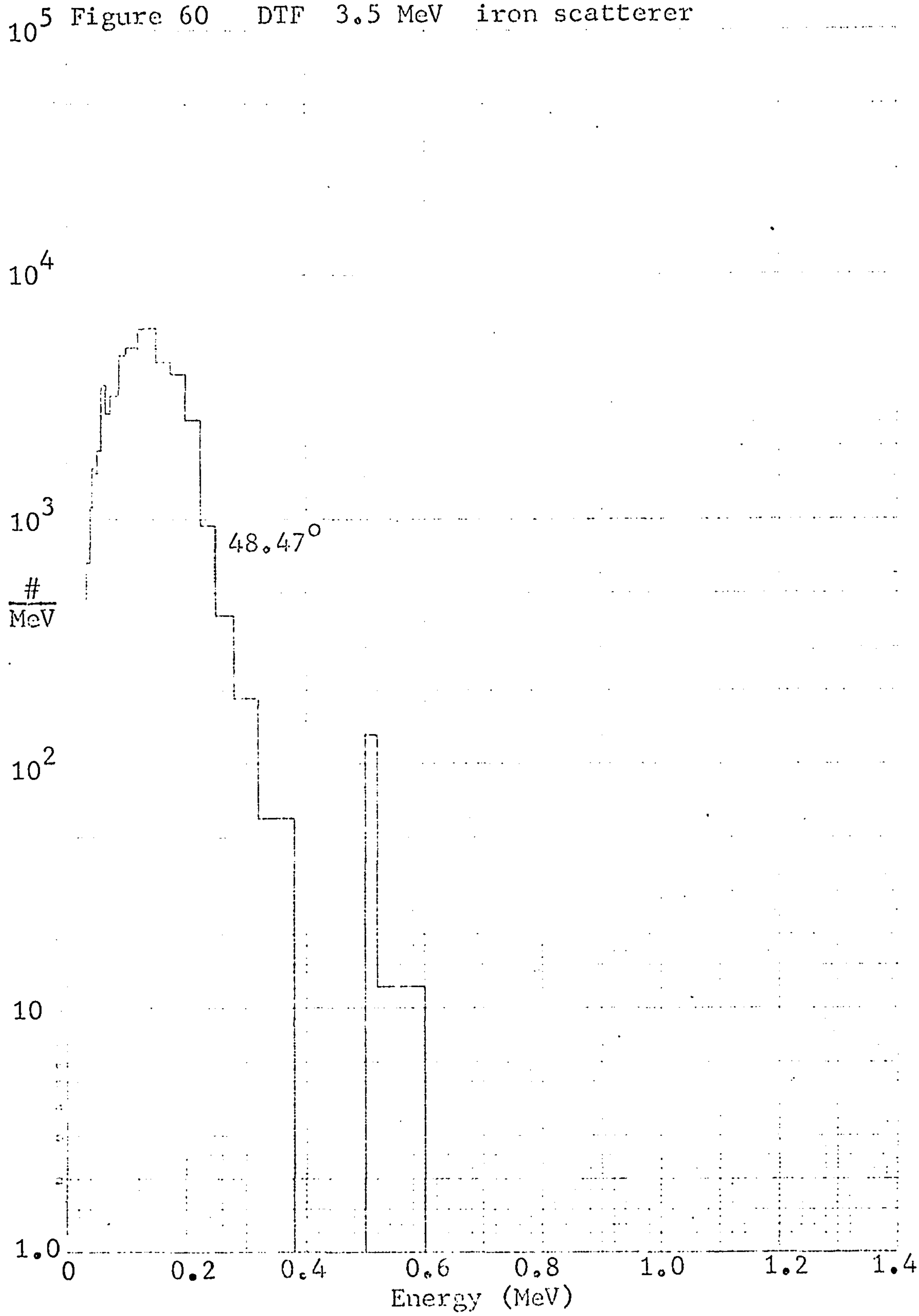

Figure 61 DTF 3.5 MeV lead scatterer

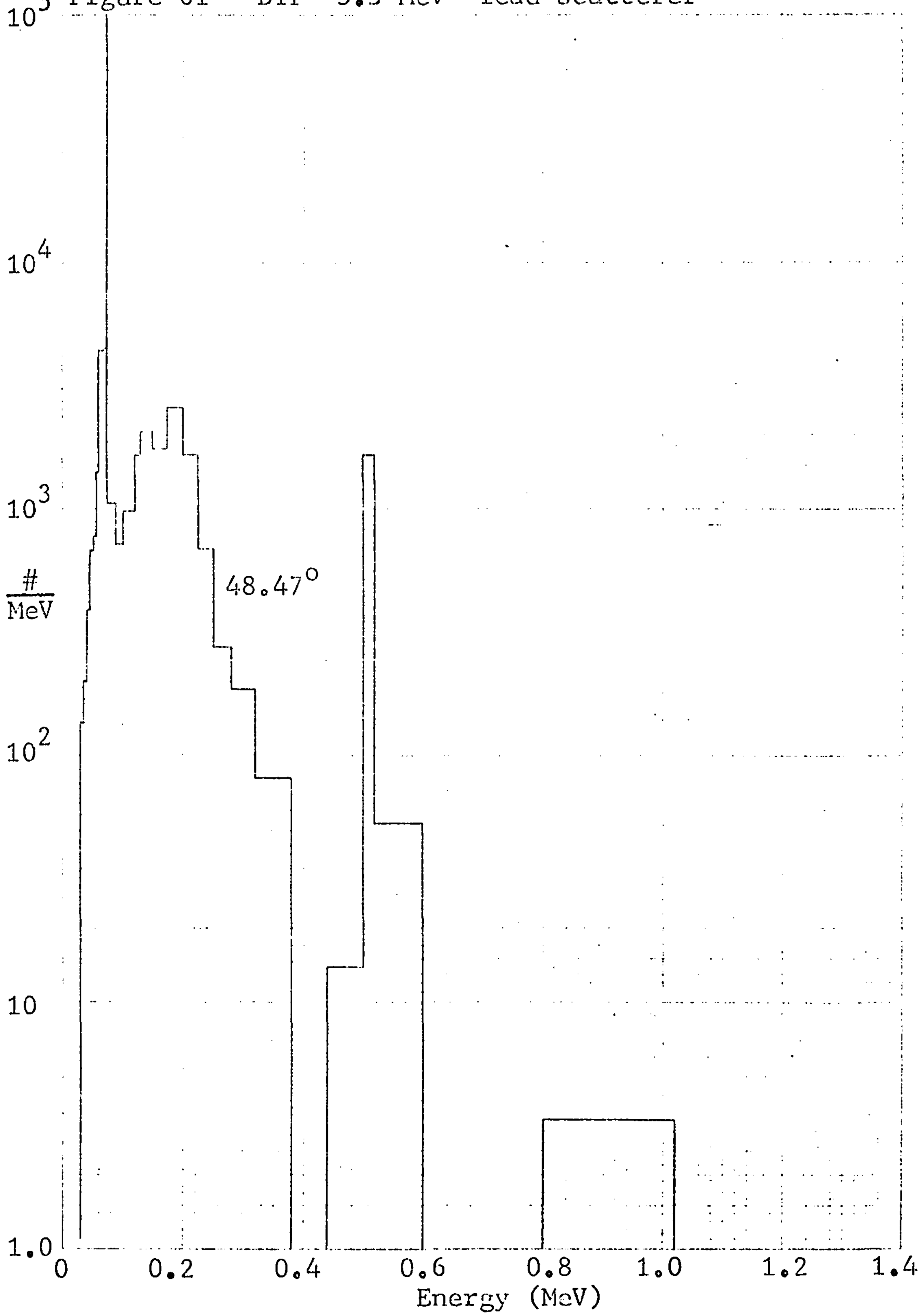

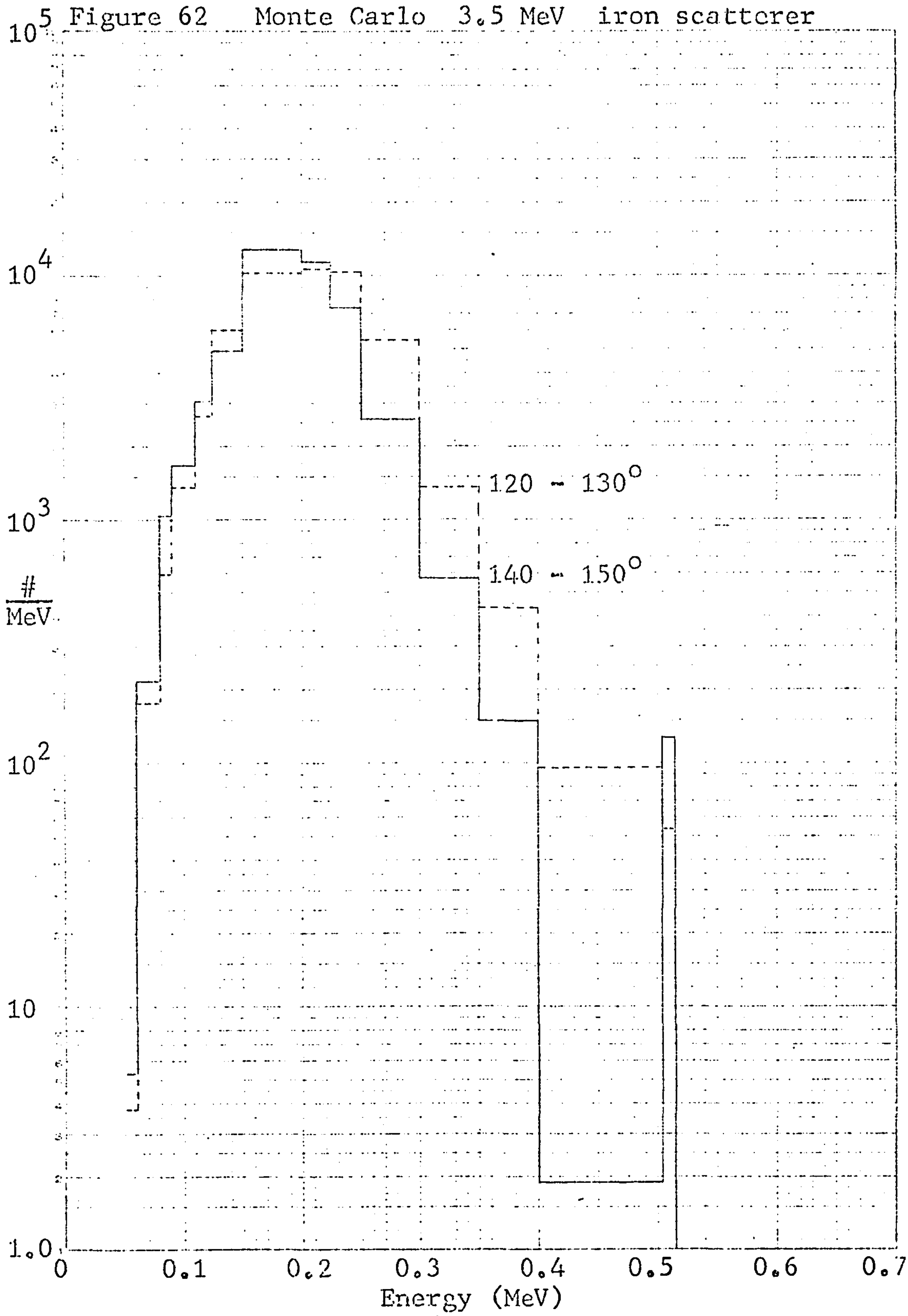

Figure 62 Monte Carlo 3.5 MeV iron scatterer
10^5
10^4
10^3
10^2
10
1.0
#/MeV
120 - 130°
140 - 150°
0
0.1
0.2
0.3
0.4
0.5
0.6
0.7
Energy (MeV)

Figure 63 DTF 7.0 MeV concrete scatterer

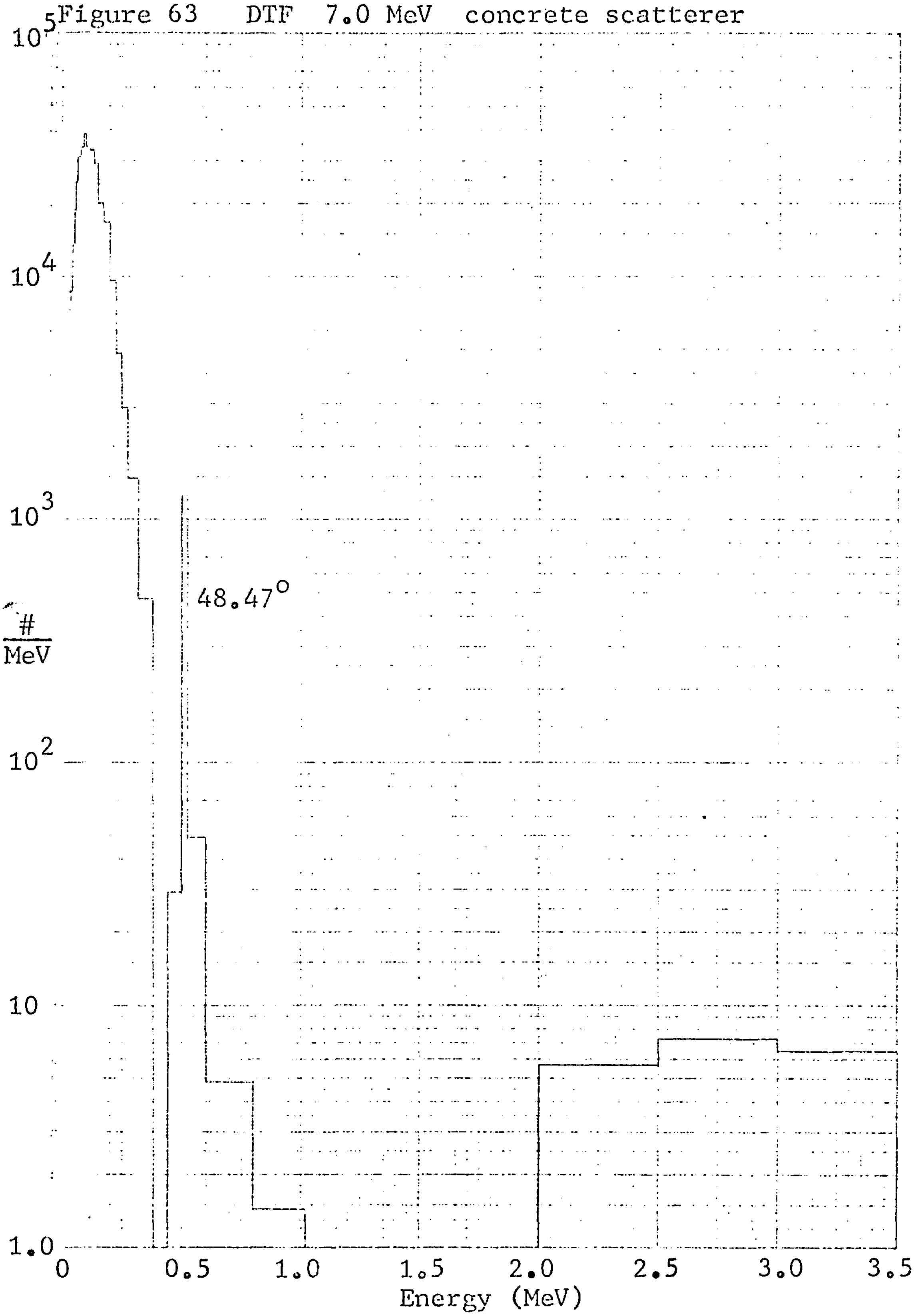

Figure 64 DTF 7.0 MeV iron scatterer

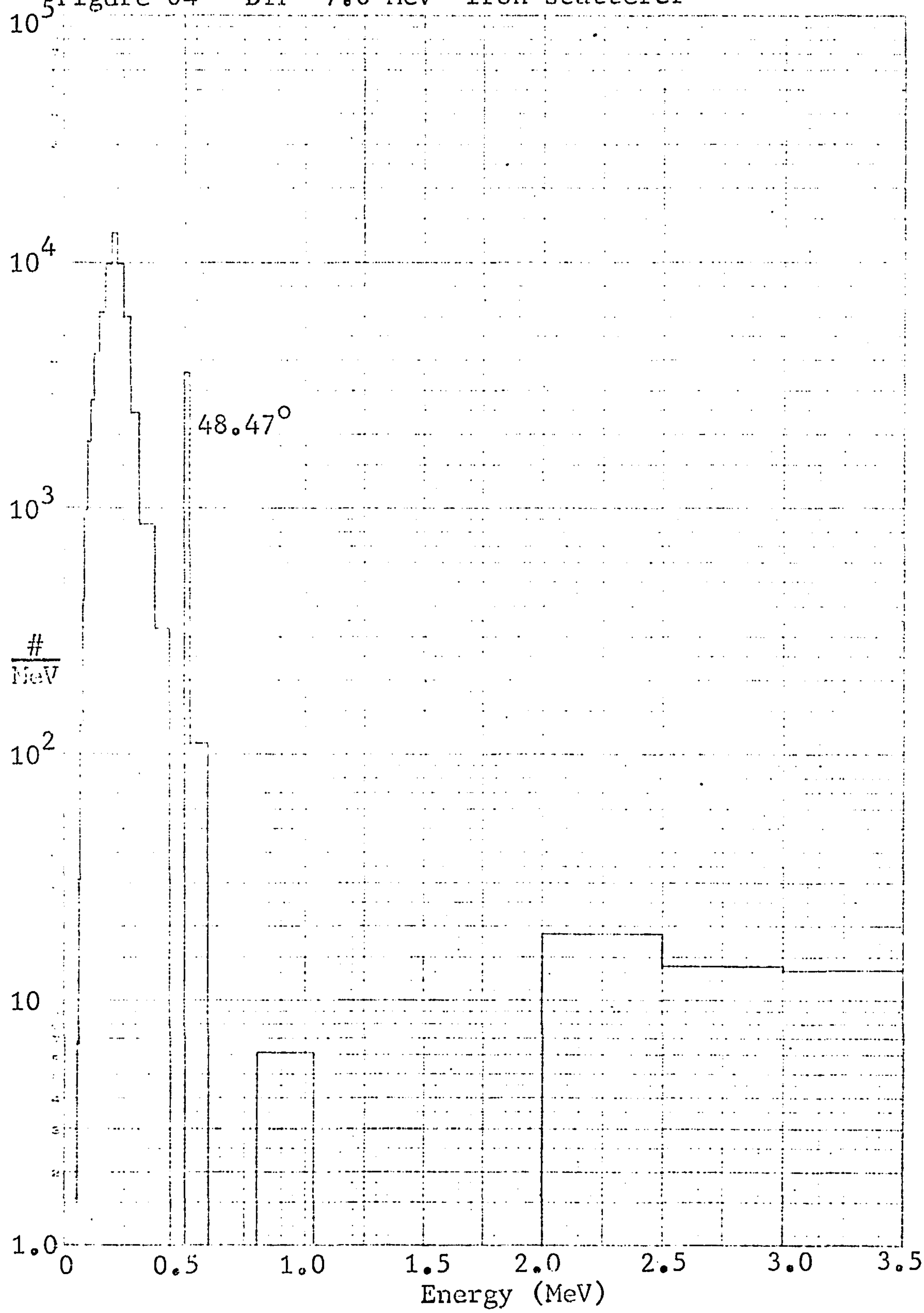

Figure 65 DTF 7.0 MeV lead scatterer

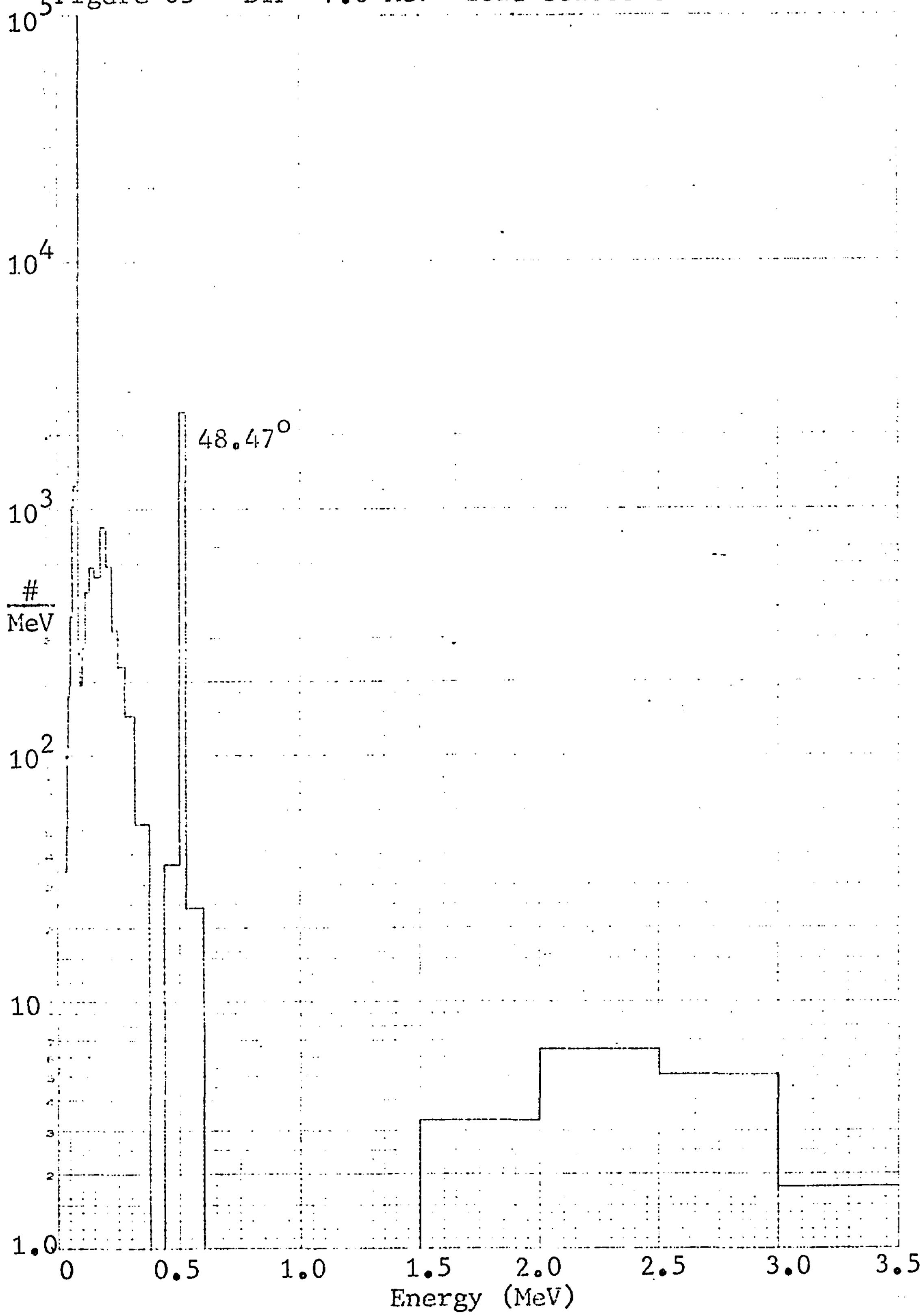

Figure 66 Monte Carlo 7.0 MeV lead scatterer

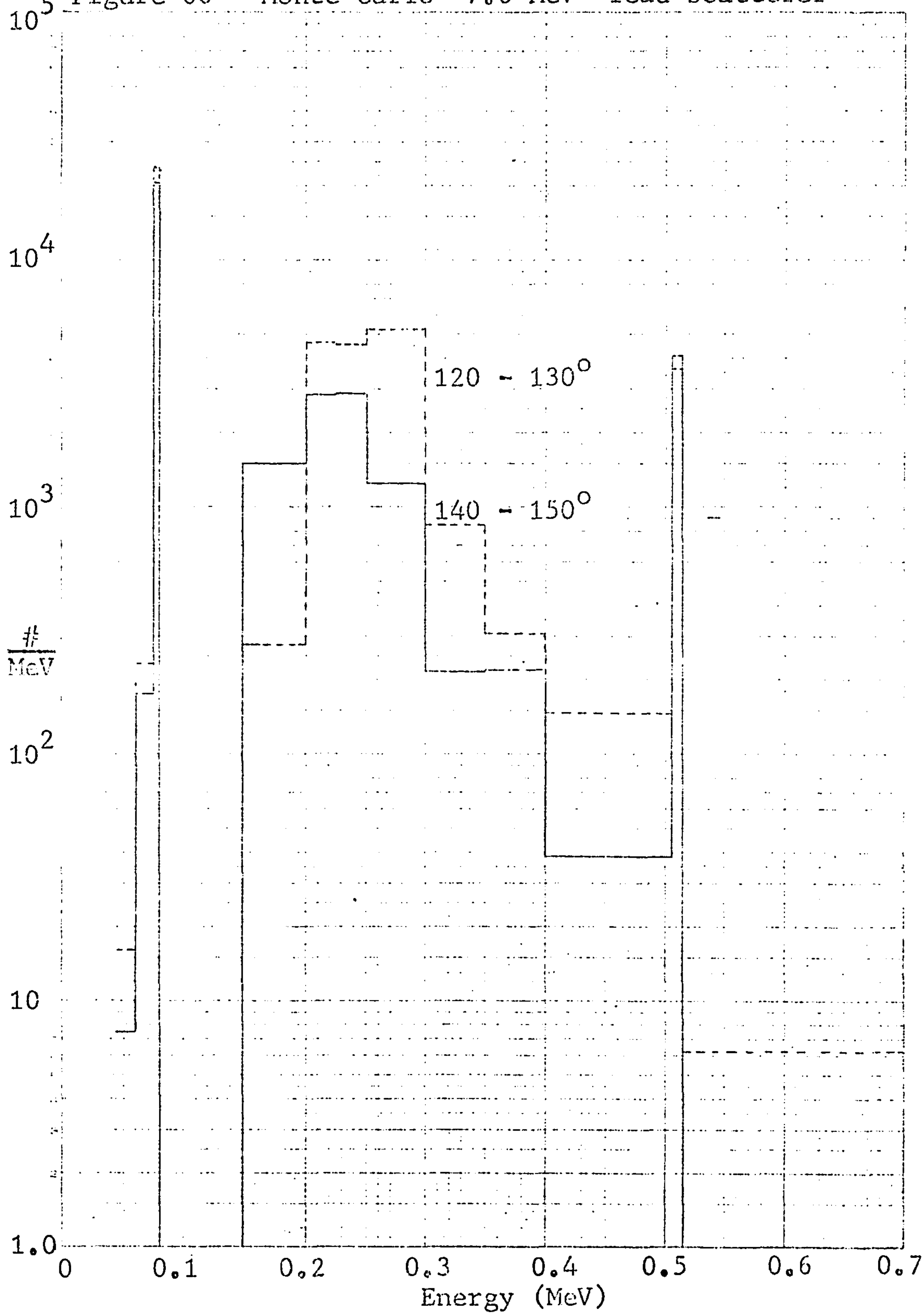

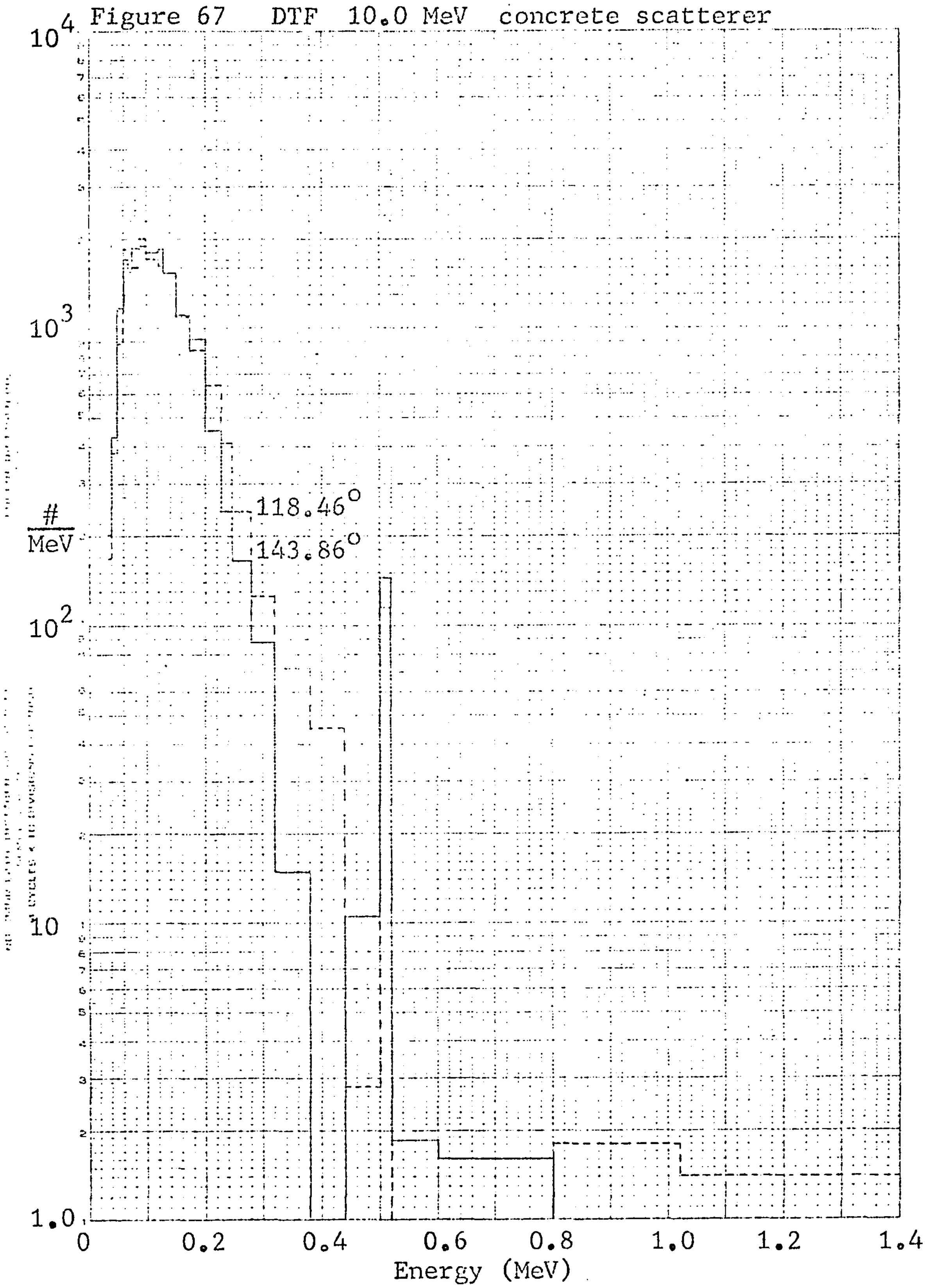
Figure 67 DTF 10.0 MeV concrete scatterer
10^4
10^3
10^2
10
1.0
#/MeV
118.46°
143.86°
0
0.2
0.4
0.6
0.8
1.0
1.2
1.4
Energy (MeV)

Figure 68 DTF 10.5 MeV iron scatterer

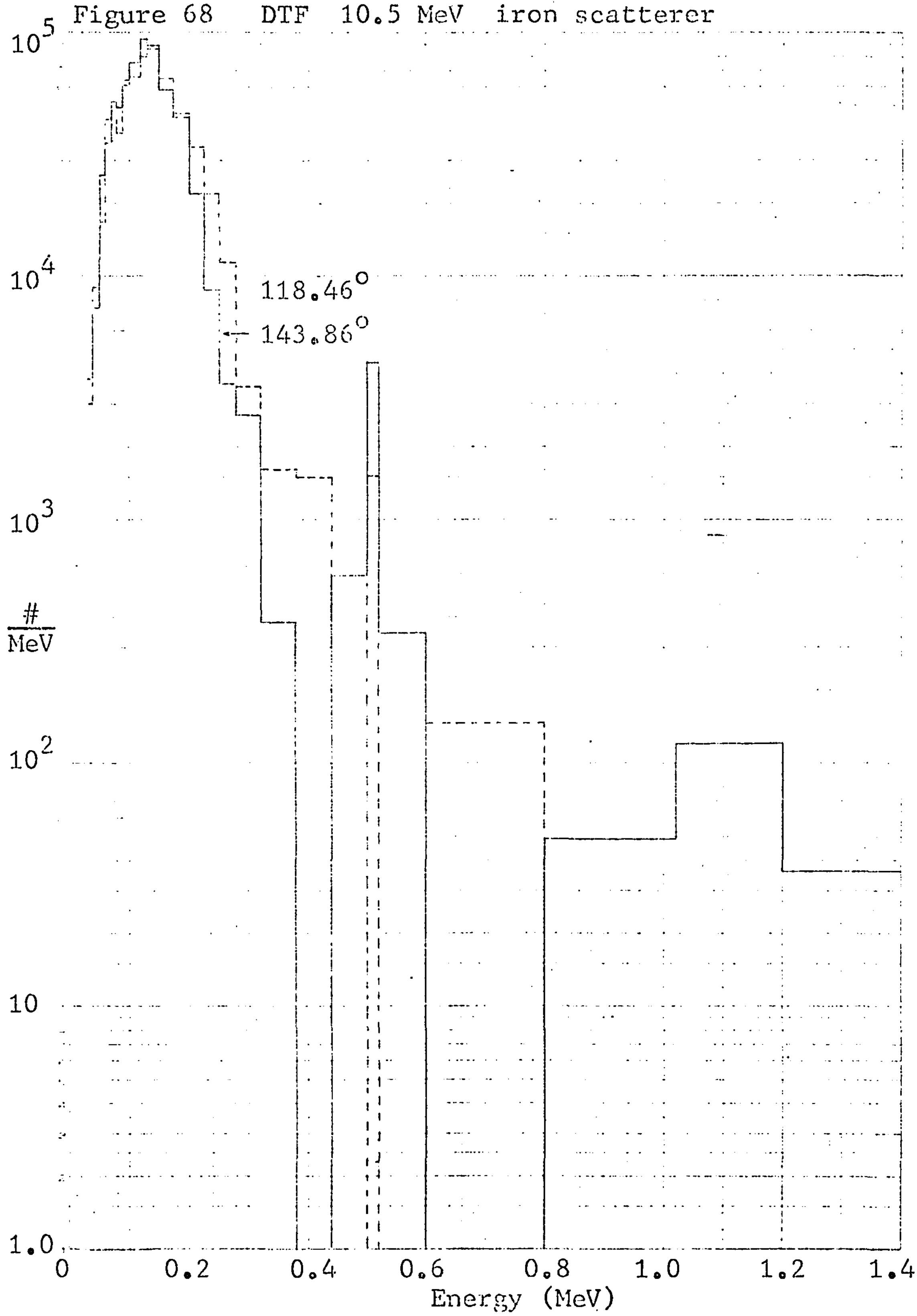

Figure 69 DTF 10.5 MeV lead scatterer

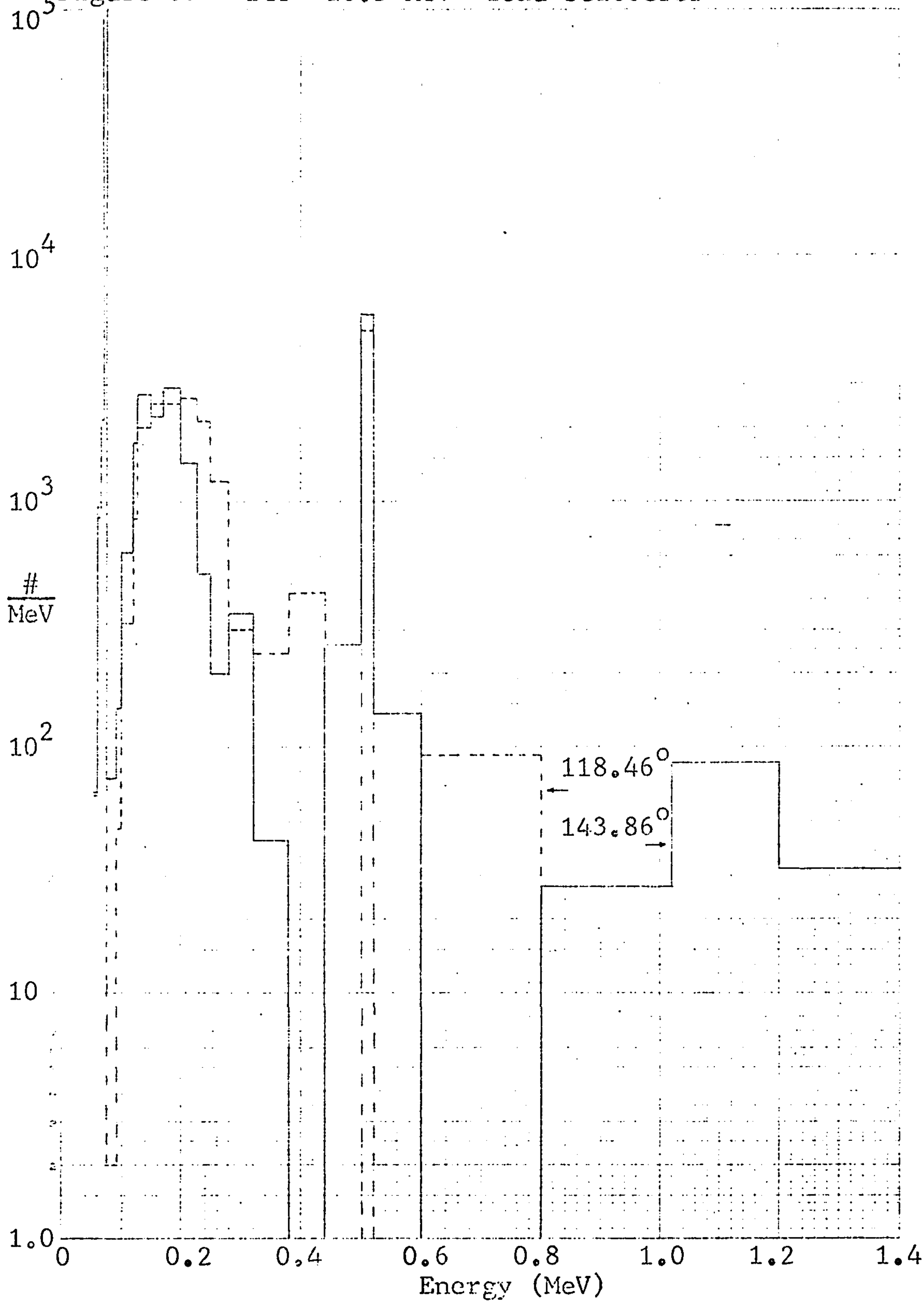

Figure 70 Monte Carlo 10.5 MeV iron scatterer

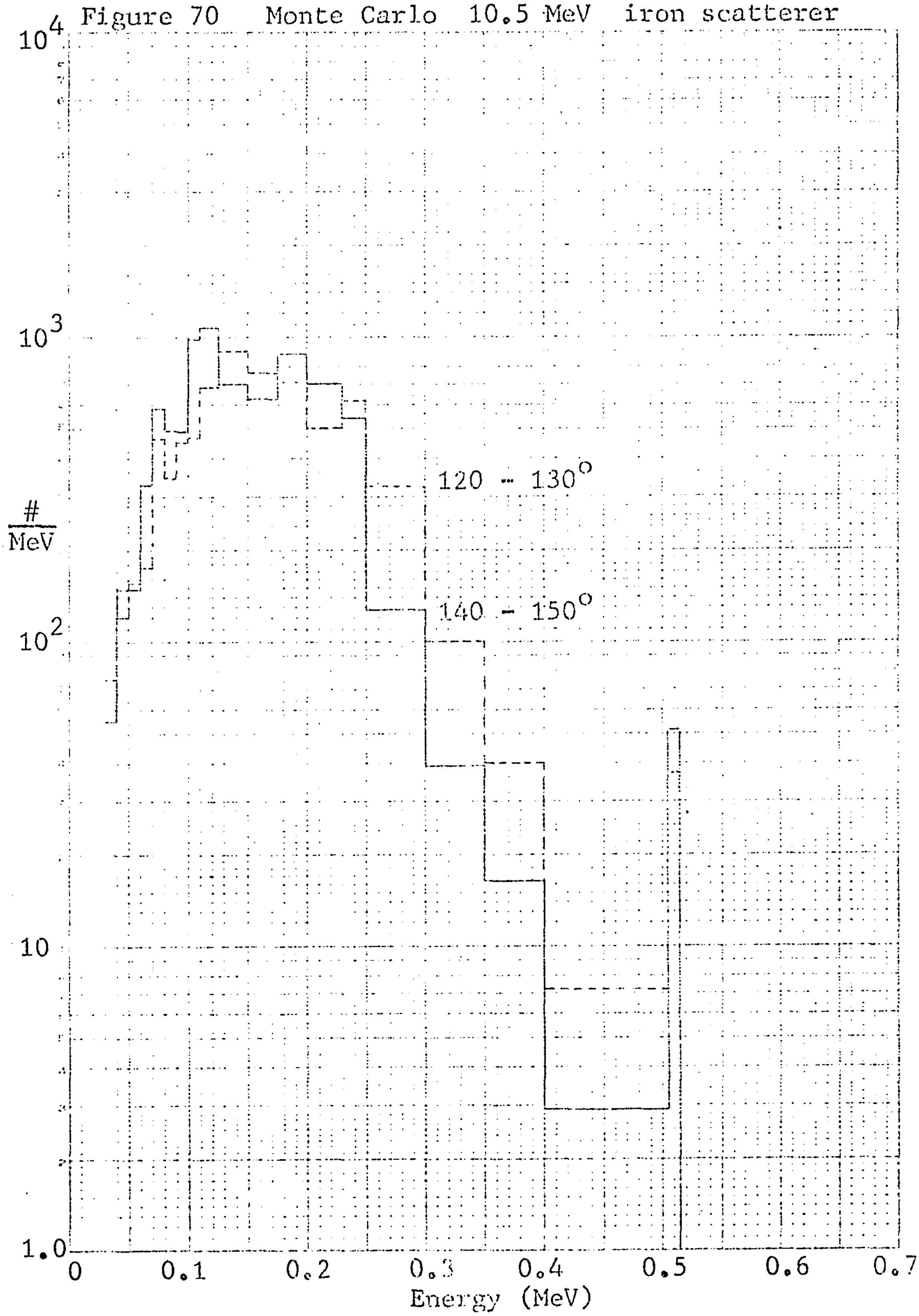

Figure 71 Monte Carlo 10.5 MeV lead scatterer

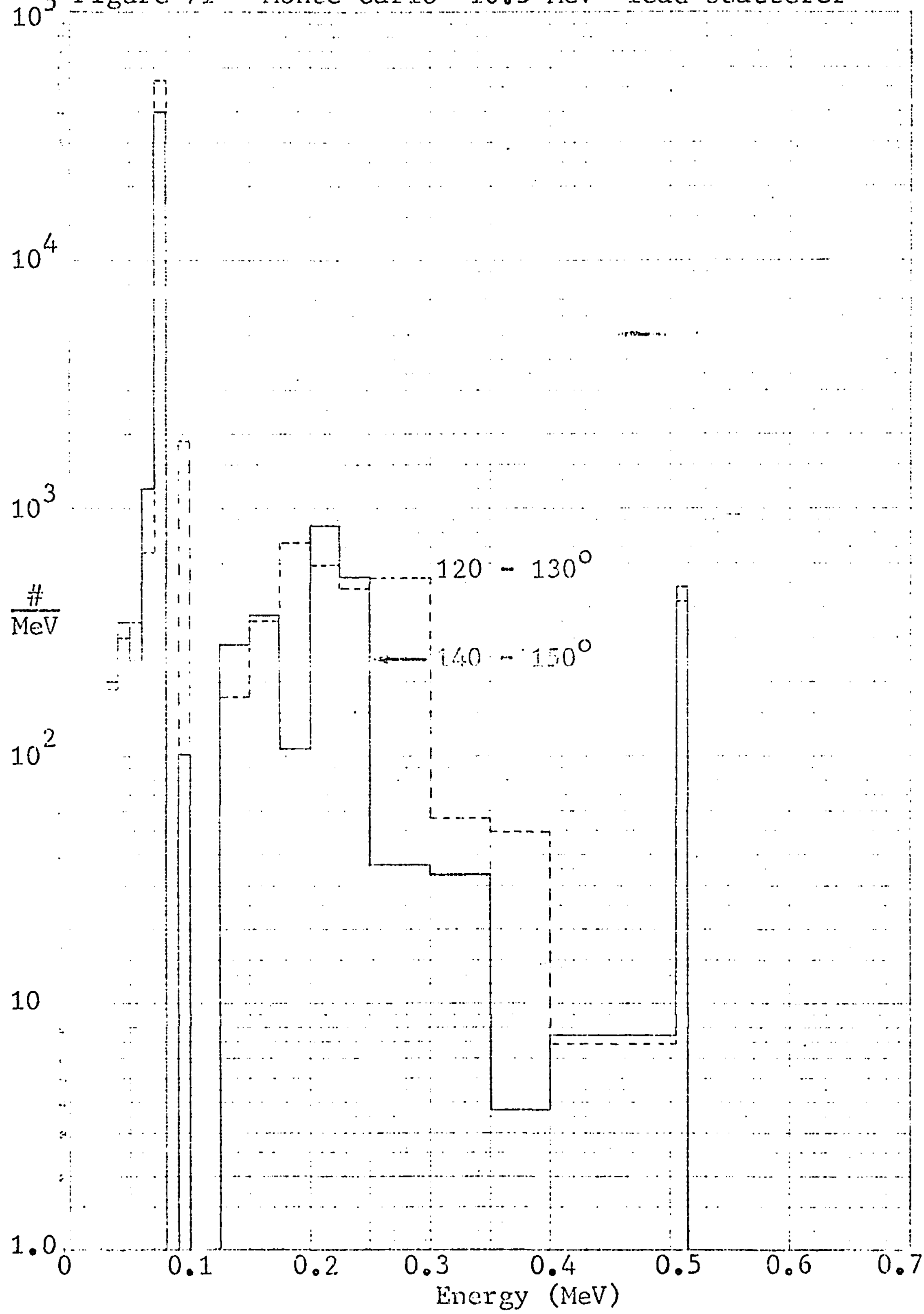

E. LiF ENERGY DEPENDENCY

A large number of experiments have been carried out in an effort to determine the relative response of LiF as a function of energy (79, 81, 91, 93, 124, 125, 126, 127, 128). Though there is some disagreement in the literature, the response is well enough understood for a large number of private and government agencies to adopt thermoluminescent dosimetry for personnel exposure documentation and to consider it for use as a secondary standard in radiation measurement.

Energy dependency of TLD's is most frequently plotted as "Thermoluminescent response per R relative to that for Co-60" vs "Energy", and in this form shows a marked over-response at energies below 100 KeV (Figure 72).

This dissertation, however, is concerned with the measurement of dose albedos. A plot of energy dependency as "Response of LiF per rad in water" vs "Energy" is therefore a more visible representation of the energy dependency of the present measurements.

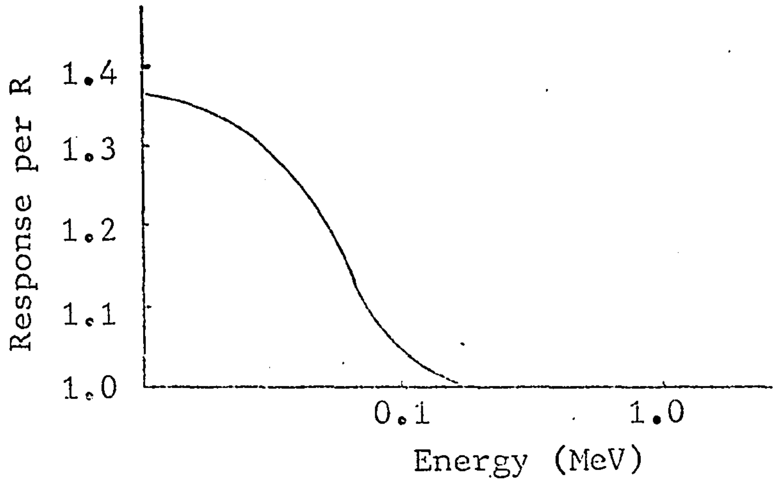

Figure 72. TLD energy response per R (81)

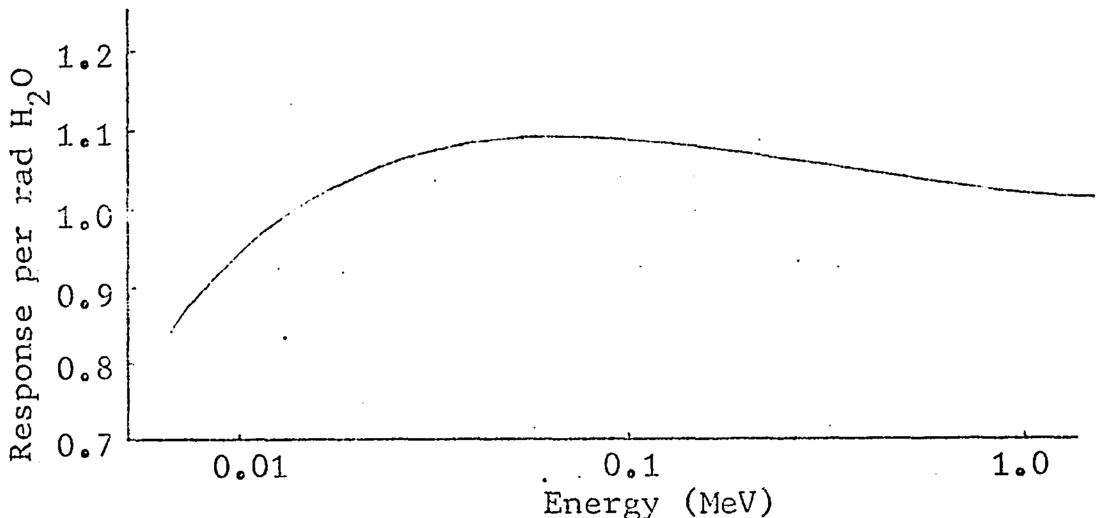

Figure 73. TLD energy response per rad (H_2O) (123)

The TLD response per rad (H_2O), essentially the

$$\left[\frac{\left(\frac{\mu}{\rho}\right)_{H_2O}}{\left(\frac{\mu}{\rho}\right)_{LiF}}\right]$$

function discussed in Section 6 inverted, is energy independent above 40 KeV. Reportedly (78) the dosimeters are even less energy sensitive at high dose levels.

Correction to the TLD data for calculation of "water dose" albedos is therefore relatively small and not rapidly varying as a function of x-ray spectra.

F. THERMOLUMINESCENT DOSIMETER READ-OUT AND ANNEALING PROCEDURES

A series of experiments were carried out to determine the most convenient annealing - read-out procedure, with results comparable to "standard" procedures, using the available equipment. The experimental procedure consisted of adjusting the time and temperature of the "Pre-heat" and "Integrate" cycles by means of glow curves, to insure that essentially all the thermoluminescence was given off in as short a time and with as low a temperature as possible.

Groups consisting of fifteen to twenty TLD's were treated according to several "standard" pre-irradiation annealing procedures (80, 87, 89, 90), exposed to 1 R ±5% of ^{60}Co radiation, treated according to their corresponding post-irradiation annealing procedure and read out in the "Integrate" cycle. The time and temperature of the "Pre-heat" cycle were then adjusted, by means of glow curves, to eliminate the lower temperature traps, and thus serve effectively as a post-irradiation annealing procedure. Upon establishment of a suitable "Pre-heating" cycle, groups of 15 TLD crystals were pre-irradiation annealed according to a particular "standard" procedure, exposed to 1 R ^{60}Co, read out in the determined cycle and compared statistically to the groups which received a post-irradiation annealing before read-out. To verify the results more substantially, the experiment was repeated using fifty dosimeters in each procedure.

The read-out cycle, as determined by the use of glow curves, consisted of a "Pre-heat" period of 7 seconds at 165°C and an "Integrate" period of 15 seconds at 250°C. The time interval allows the dosimeter to be read out and the heating element to cool back to an acceptable level in approximately 30 seconds with a minimum amount of dark current.

The data for that "standard" annealing cycle recommended for use with those TLD crystals used and the abbreviated annealing cycle developed here were compared statistically and found to be equivalent at the 99.5% confidence level under chi square testing. Compared with other "standard" annealing procedures, the abbreviated procedure yielded as great a mean sensitivity (light units/R) and was quite comparable in accuracy.

Table 14 lists the annealing procedures studied and the results obtained with each, using twenty-five dosimeters per set. Table 15 summarizes the mean sensitivity and standard deviation obtained with each set. Individual TLD readings are found in Appendix I.

TABLE 14

TLD ANNEALING PROCEDURES

1) 1 hr. 400°C Pre-anneal
2 hr. 100°C
10 min. 100°C Post-anneal
No Pre-heat cycle
15 sec. 250°C Integrate
Mean = 718.5
% = 3.53

2) 1 hr. 400°C Pre-anneal
2 hr. 100°C
10 min. 100°C Post-anneal
7 sec. 165°C Pre-heat
15 sec. 250°C Integrate
Mean = 696.8
% = 6.50

3) 1 hr. 400°C Pre-anneal
2 hr. 100°C
No Post-anneal
7 sec. 165°C Pre-heat
15 sec. 250°C Integrate
Mean = 711
% = 3.40

4) 1 hr. 400°C Pre-anneal
24 hr. 80°C
No Post-anneal
No Pre-heat
15 sec. 250° Integrate
Mean = 704
% = 2.98

5) 1 hr. 400°C Pre-anneal
24 hr. 80°C
No Post-anneal
7 sec. 165°C Pre-heat
15 sec. 250°C Integrate
Mean = 706
% = 2.94

6) 1 hr. 400°C Pre-anneal
24 hr. 80°C
10 min. 100°C Post-anneal
No Pre-heat
15 sec. 250°C Integrate
Mean = 695
% = 2.94

7) 1 hr. 400°C Pre-anneal
24 hr. 80°C
10 min. 100°C Post-anneal
7 sec. 165°C Pre-heat
15 sec. 250°C Integrate
Mean = 672
% = 5.12

8) 1 hr. 400°C Pre-anneal
24 hr. 80°C
No Post-anneal
7 sec. 165° Pre-heat
15 sec. 250°C Integrate
Mean = 706
% = 2.94

TABLE 14 (cont'd)

9) 1 hr. 400°C Pre-anneal
10 min. 100°C Post-anneal
No Pre-heat
15 sec. 250°C Integrate
Mean = 964
% = 2.89

10) 1 hr. 400°C Pre-anneal
10 min. 100°C Post-anneal
7 sec. 165°C Pre-heat
15 sec. 250° Integrate
Mean = 932
% = 4.27

11) 1 hr. 400°C Pre-anneal
No Post-anneal
7 sec. 165°C Pre-heat
15 sec. 250°C Integrate
Mean = 936
% = 3.20

12) 1 hr. 400°C Pre-anneal
No Post-anneal
7 sec. 165°C Pre-heat
15 sec. 250°C Integrate
Mean = 960
% = 3.82

TABLE 15

TLD ANNEALING PROCEDURE SUMMARY

TEST NO.	MEAN	STANDARD DEVIATION (Percent)
1	718	3.53
2	697	6.50
3	711	3.40
4	704	2.98
5	706	2.94
6	695	2.94
7	672	5.12
8	706	2.94
9	964	2.89
10	932	4.27
11	936	3.20
12	960	3.82

To verify that the accuracy and the stability of the dosimeters were not affected by the abbreviated annealing procedure, a calibration curve was obtained yielding a slope of 1.016 and a maximum standard deviation at the 68% confidence interval for a 10 MR exposure of ±6.0%; fading characteristics were demonstrated to be negligible in a three-month period.

The author was aided in work on this Appendix by B. L. O'Neal, Sandia Corporation, and D. Rudy, New Mexico State University.

G. INFINITE SLAB SIZE MEASUREMENTS

In order to simplify the geometry associated with beam perimeter fall-off and increasing slab size, all "infinite-size" studies were conducted with the incident beam restricted to 2.0" square at the backscatter surface. The distance from beam edge to backscatter slab edge was then increased, holding thickness constant, and the resulting albedos considered. Slab thickness effects were studied with a constant slab area. Lead slab areas of 4.0, 6.0, 7.0, 8.0, 9.0, and 10.0 inches square and thicknesses of 0.25, 0.50, 0.625, 0.75, 1.00, 1.25, 1.375, 1.50, and 2.00 inches were studied at 2.0 MeV. Slabs of 4.0, 6.0, 8.0, 12.0, and 14.0 inches square and thicknesses of 0.15, 0.35, 0.58, 0.78, 1.15, 1.40, 1.72, and 2.10 inches were studied at 60.0 MeV. Infinite size calculations were checked at 2.0 MeV for iron and steel but the full plot not made due to machine time considerations.

A hypothesis test that the iron slabs are equally effective reflectors falls well within the 95% acceptance level. The concrete results are similar (Tables 16 and 17).

TABLE 16

IRON REFLECTOR RATIOS (x 10^5)

ANGLE	SLAB SIZE 12" x 12" x 2.5"	12" x 12" x 4.125"	14" x 14" x 2.5"
150°	4.04 ± 8.35%	4.00 ± 8.30%	4.04 ± 10.05%
135°	3.96 ± 9.34%	4.04 ± 8.61%	4.16 ± 8.70%
120°	2.97 ± 9.02%	2.97 ± 7.97%	2.92 ± 9.5 %

TABLE 17

CONCRETE REFLECTOR RATIOS (x 10^5)

ANGLE	SLAB SIZE 32" x 32" x 8"	32" x 32" x 10"	36" x 36" x 8"
150°	4.59	4.60	4.55
135°	4.40	4.22	4.43
120°	3.25	2.89	3.21

The following graphs, 74, 75, 76, and 77 show results of the above experiments.

At small backscatter surface areas, an increase in albedo was noted. These measurements were made with very little collimation, which might have recorded scatter from the sides of the backscatter slab as well as the face. This effect might better be studied with a gamma source-scintillation detector arrangement.

Figure 74 2.0 MeV lead surface area effects

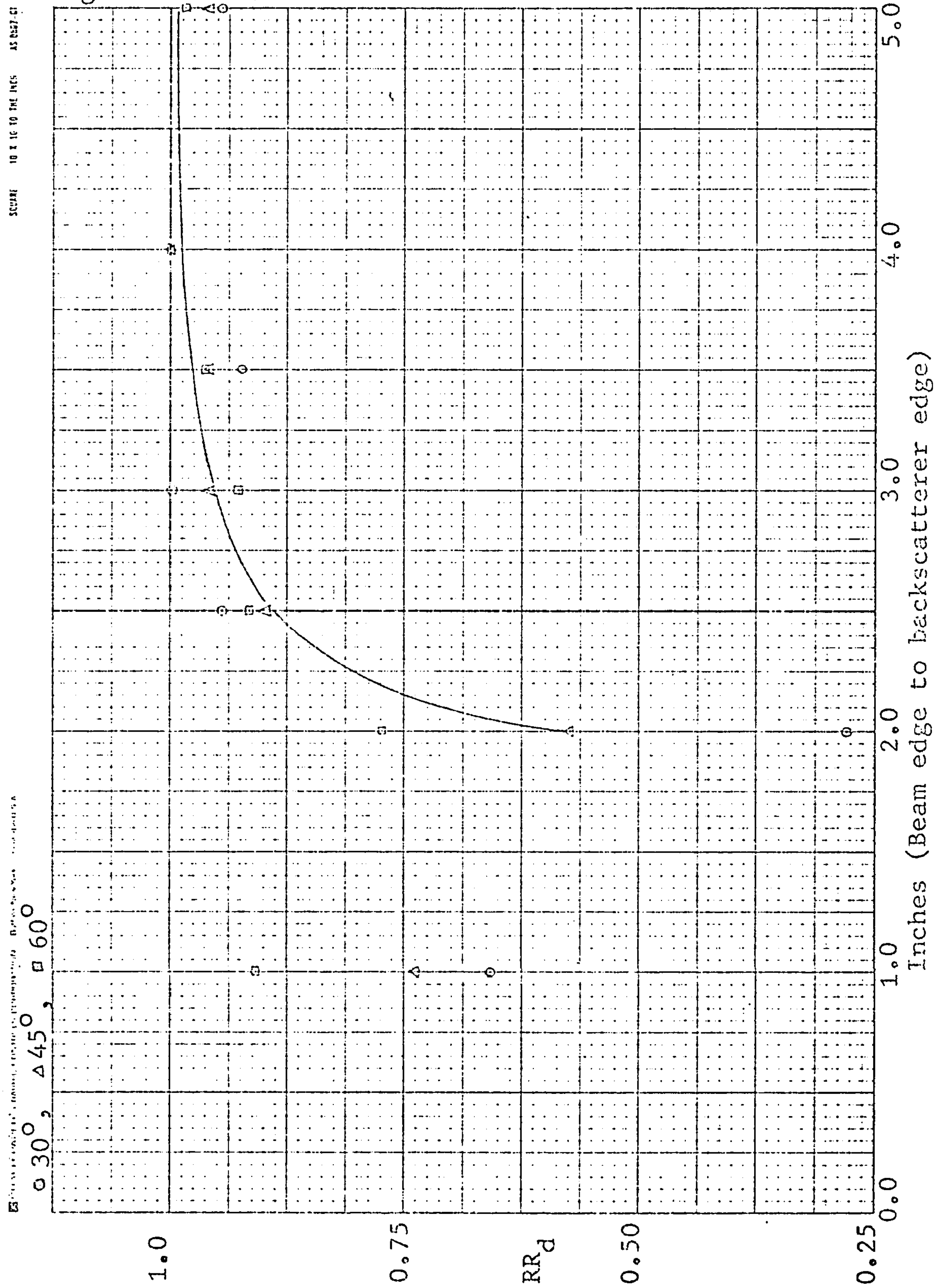

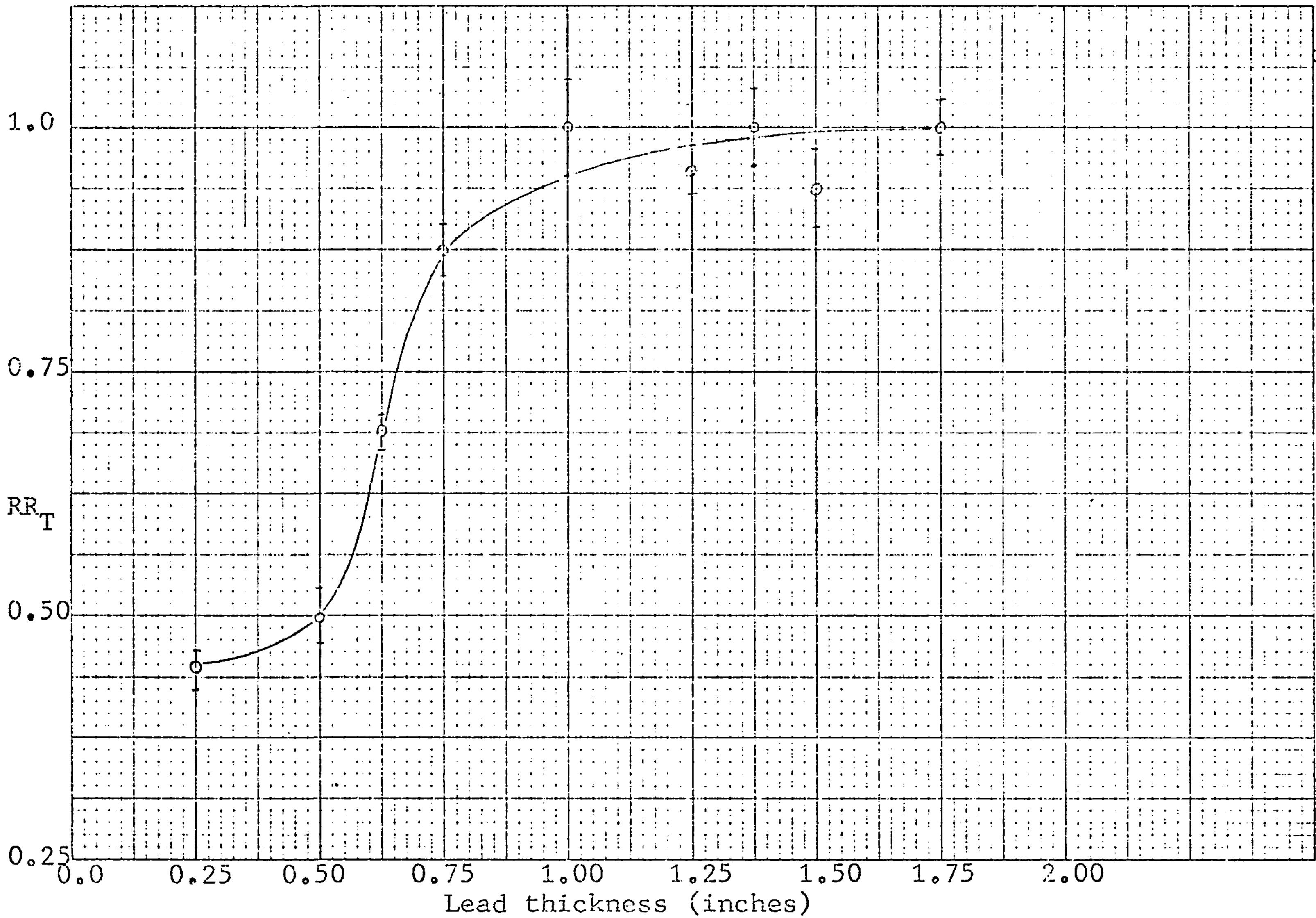

Figure 75 2.0 MeV lead thickness effects

Figure 76 60 MeV lead surface area effects

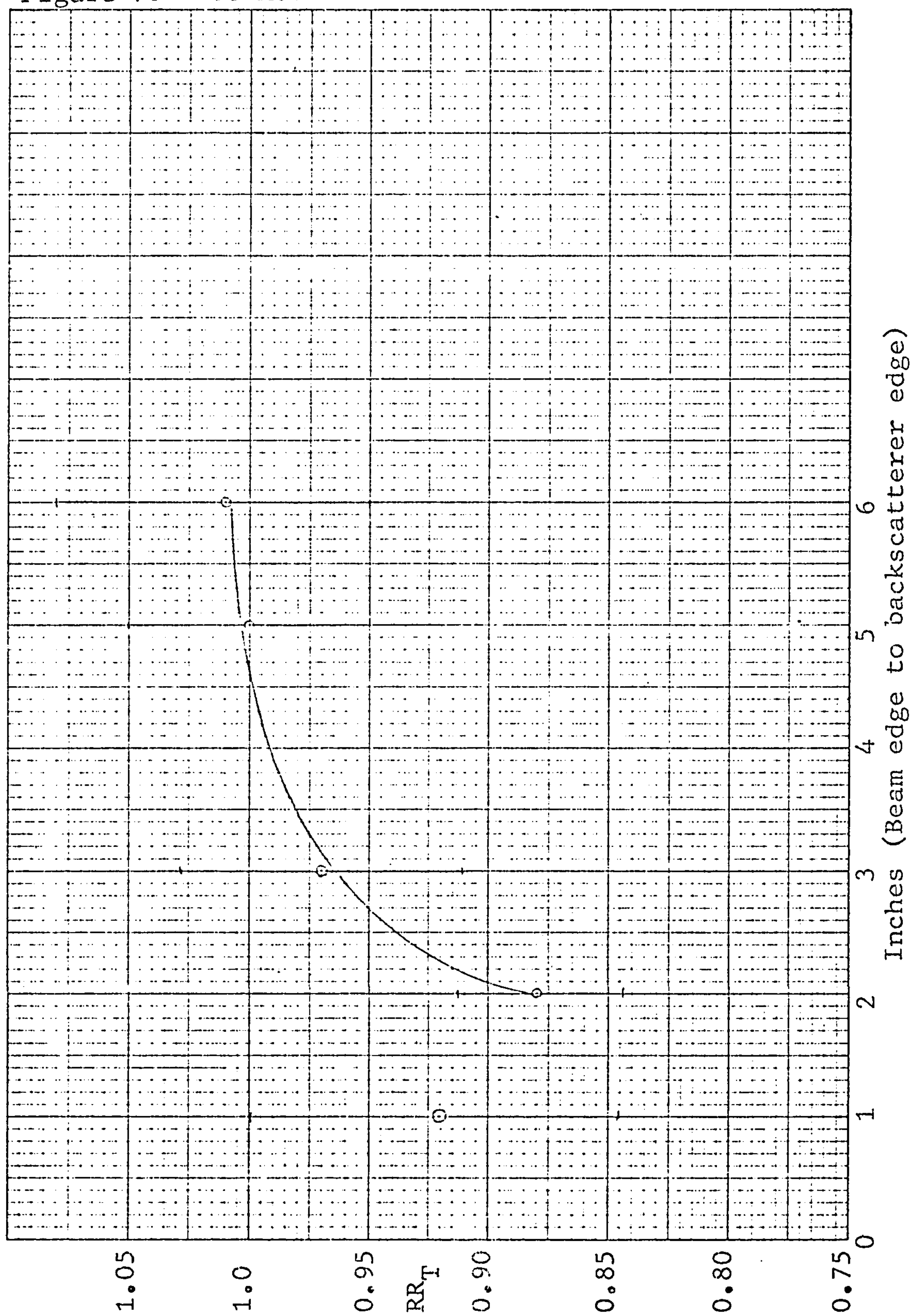

Figure 77 60 MeV lead thickness effects

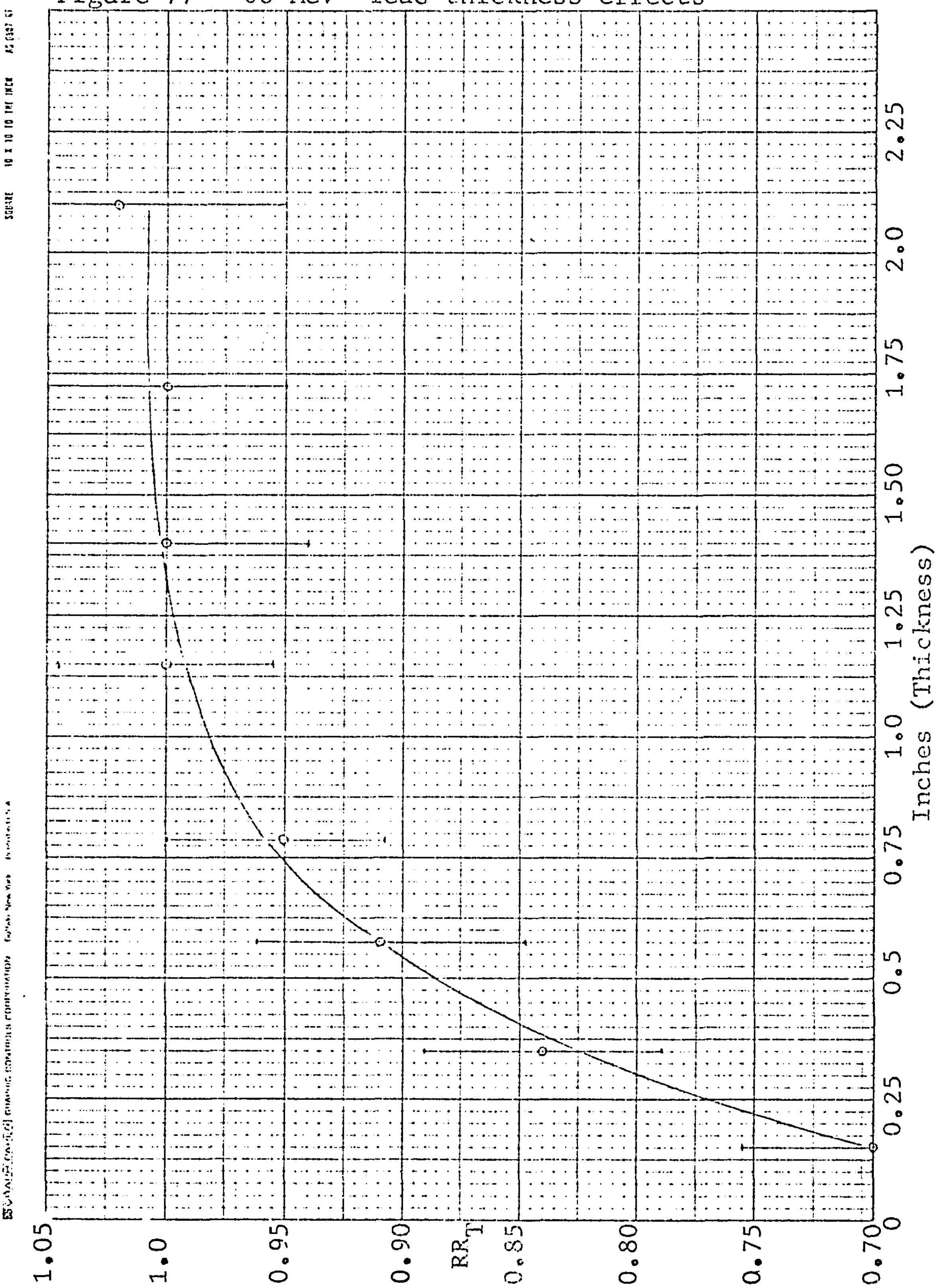

H. BEAM DIVERGENCE

X-ray beams are inherently more directional than are isotopic sources. Beam divergence is a function of the particular generating machine used. Horizontal and vertical beam cross-sections are given for the machines used (except at 10.5 MeV for which published cross-sectional measurements exist) in Figures 78 to 83. Cylindrical symmetry is then assumed and a least squares fit made to determine beam fall-off as a function of radius (Figures 84 to 86). The incident slab dose is then averaged at the center of the "effective viewed area".

Albedo would be expected to vary with the amount of semi-infinite surface irradiated, up to some point, similar to the change experienced with increased surface area. The concept of "semi-infinite irradiated surface area" is even less well established than that of semi-infinite surface. Indeed, large numbers of albedo experiments have been conducted (Section 2) in which a uniformly irradiated surface could not have been achieved. In the experiments conducted in this research, only those with concrete at

Figure 78 2.0 MeV horizontal beam divergence

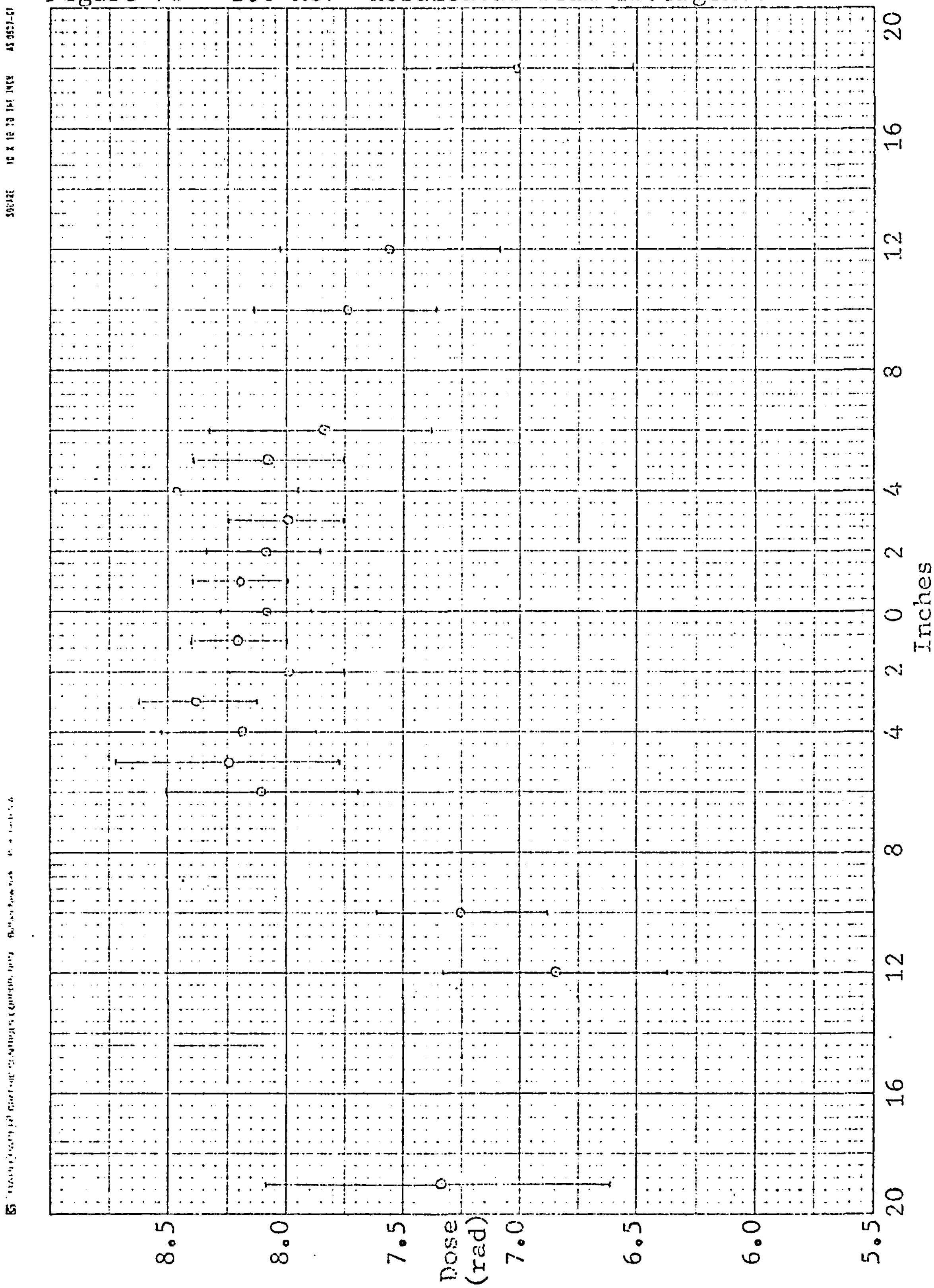

Figure 79 2.0 MeV vertical beam divergence

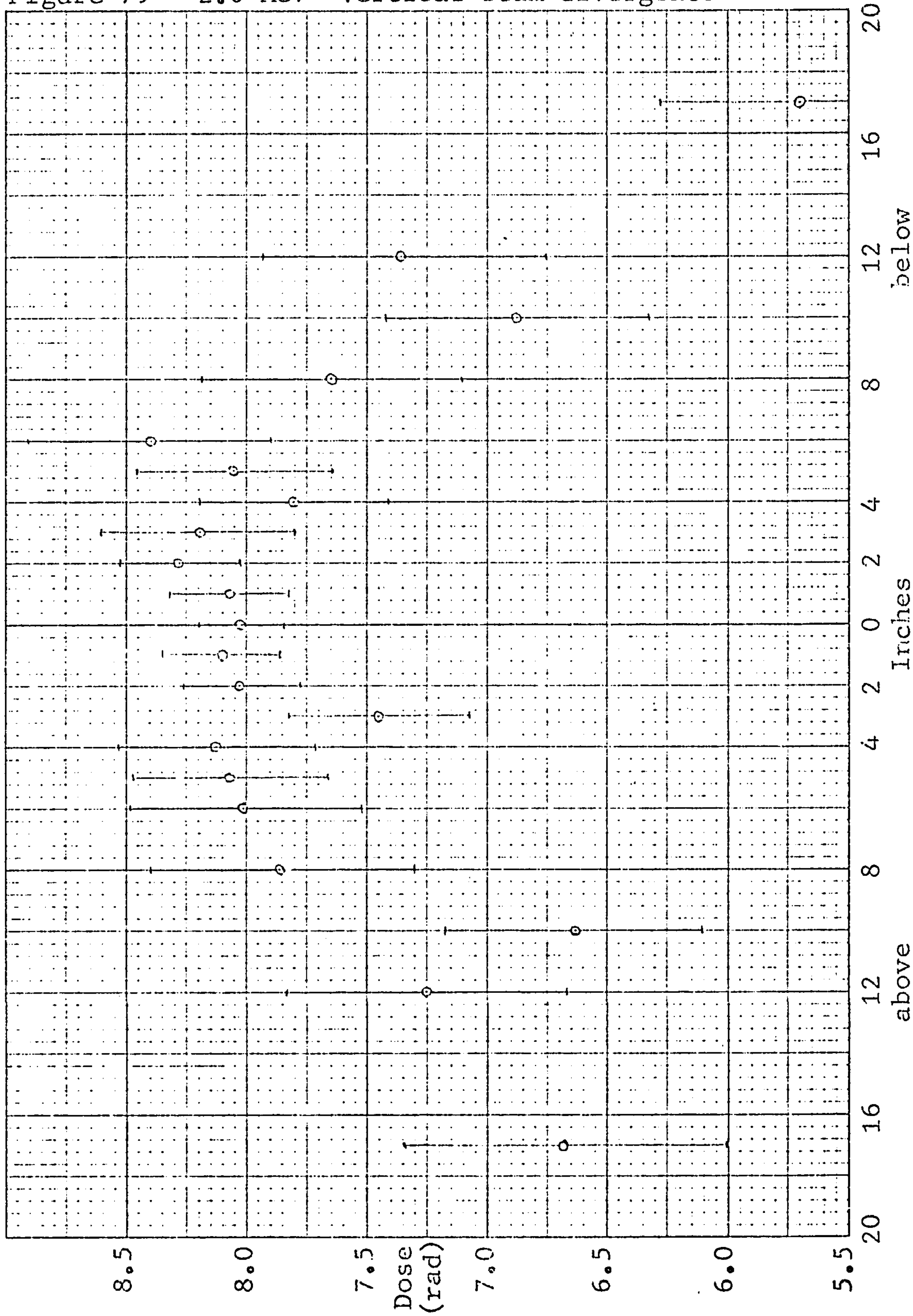

Figure 80   3.5 MeV vertical beam divergence

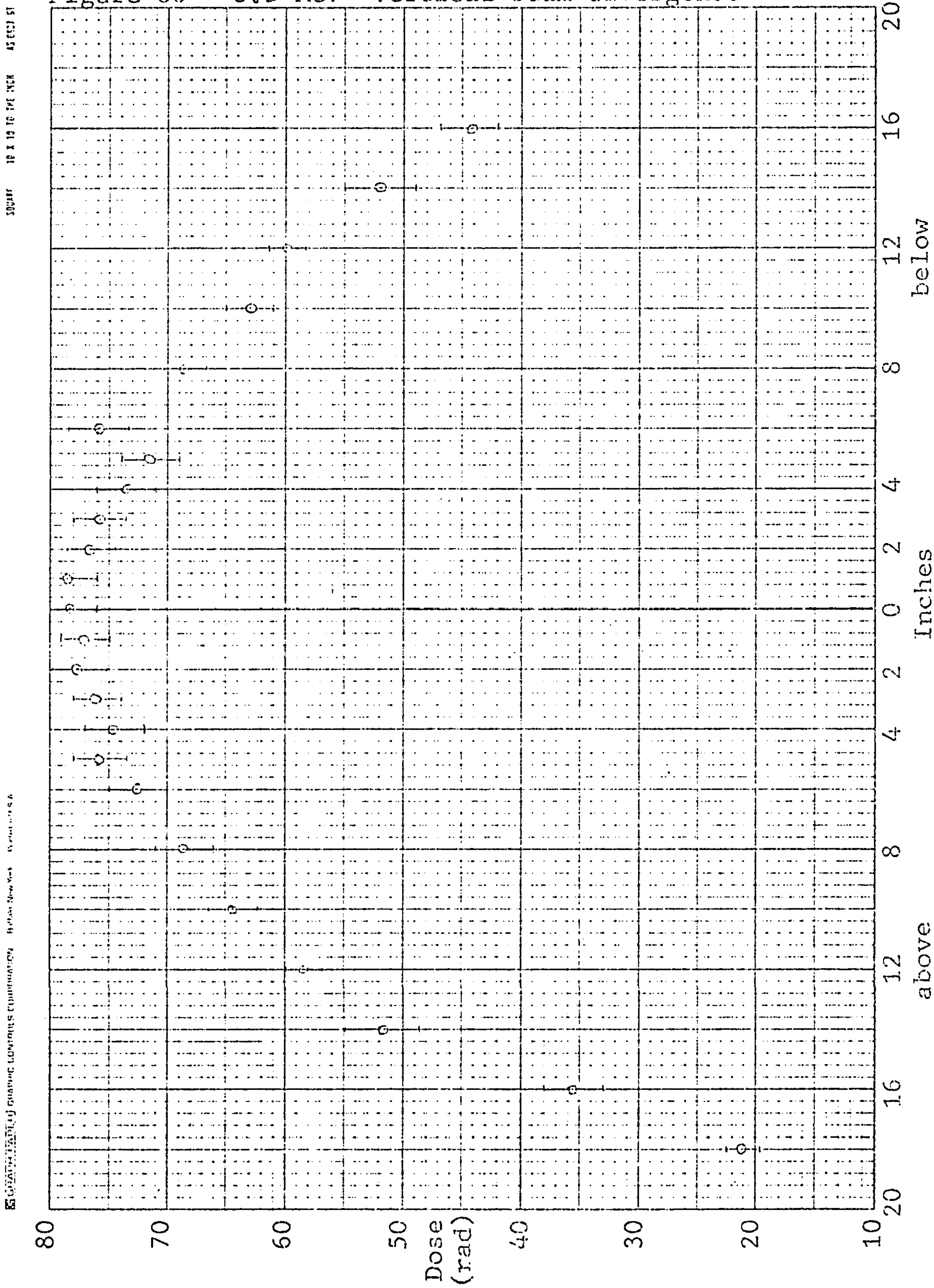

Figure 81 3.5 MeV horizontal beam divergence

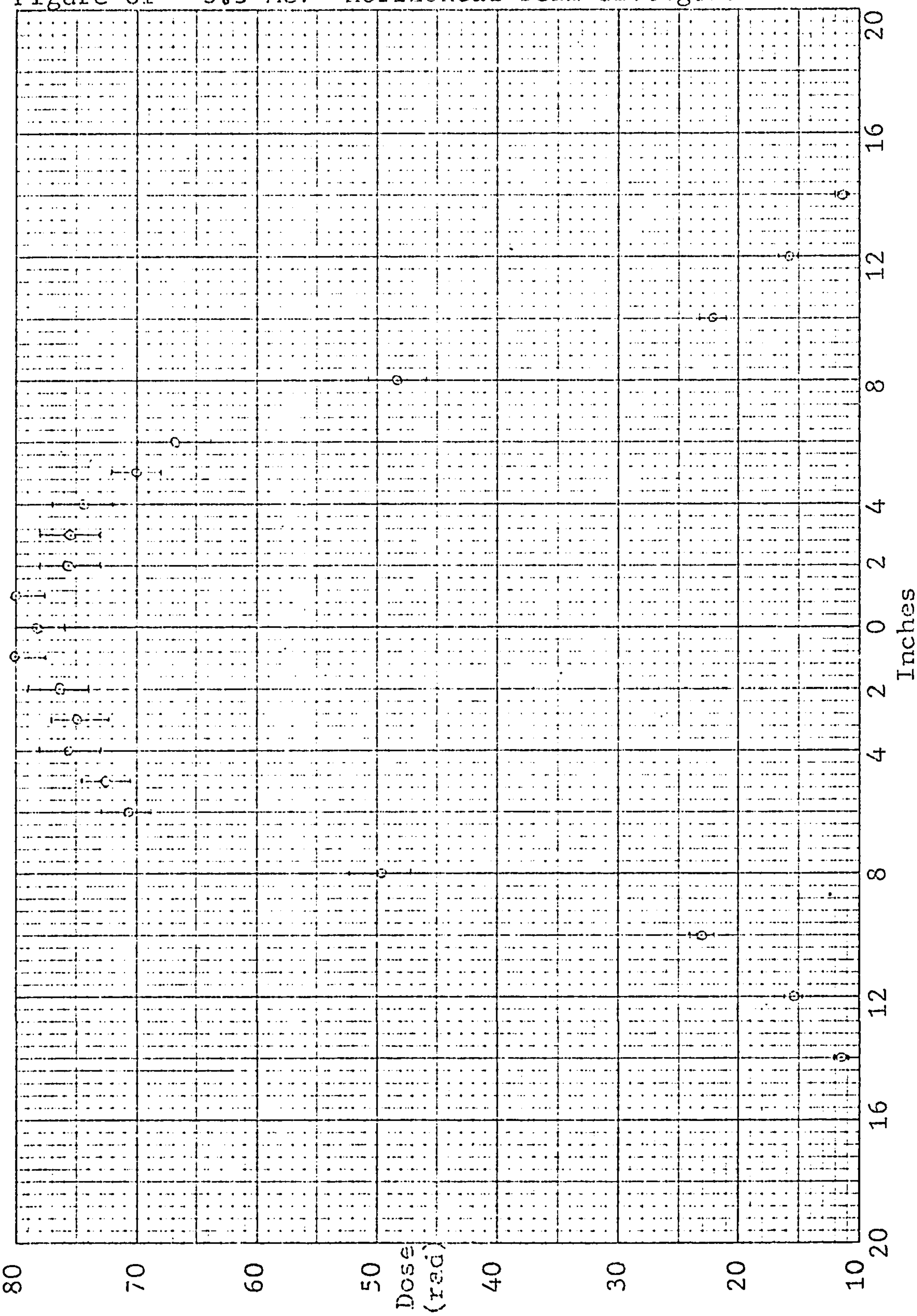

Figure 82 7.0 MeV horizontal beam divergence

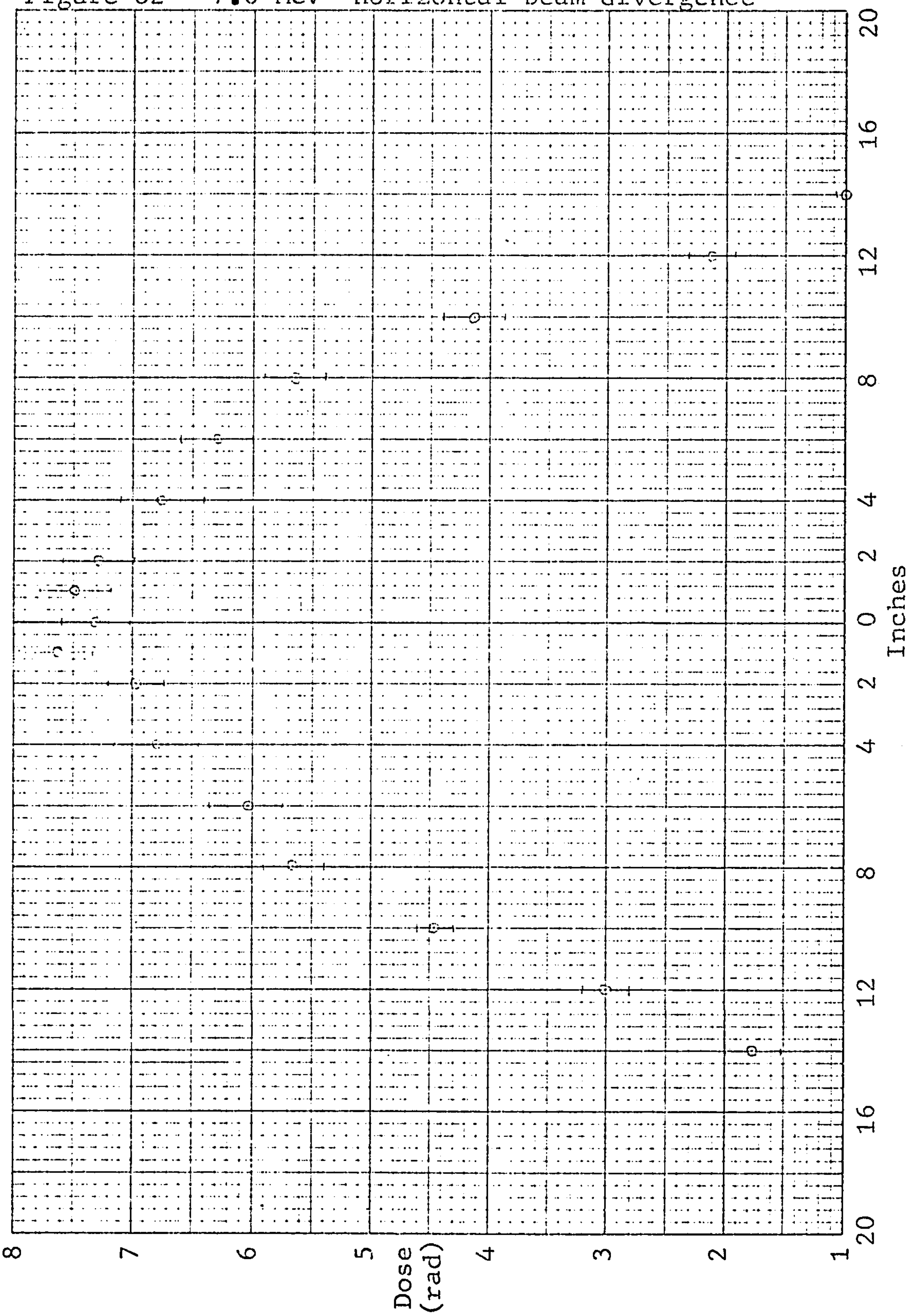

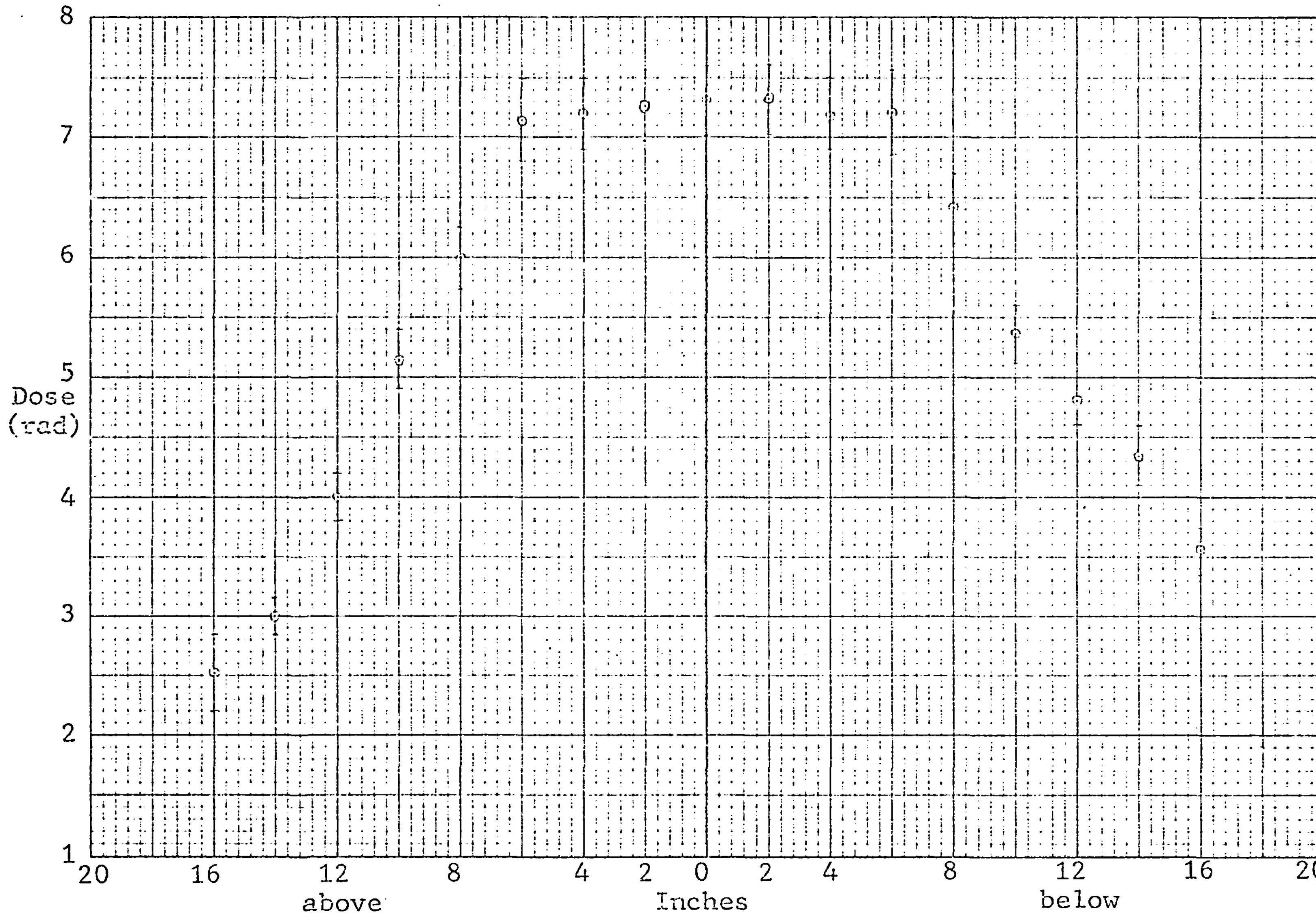

Figure 83 7.0 MeV vertical beam divergence

Figure 84 2.0 MeV beam divergence

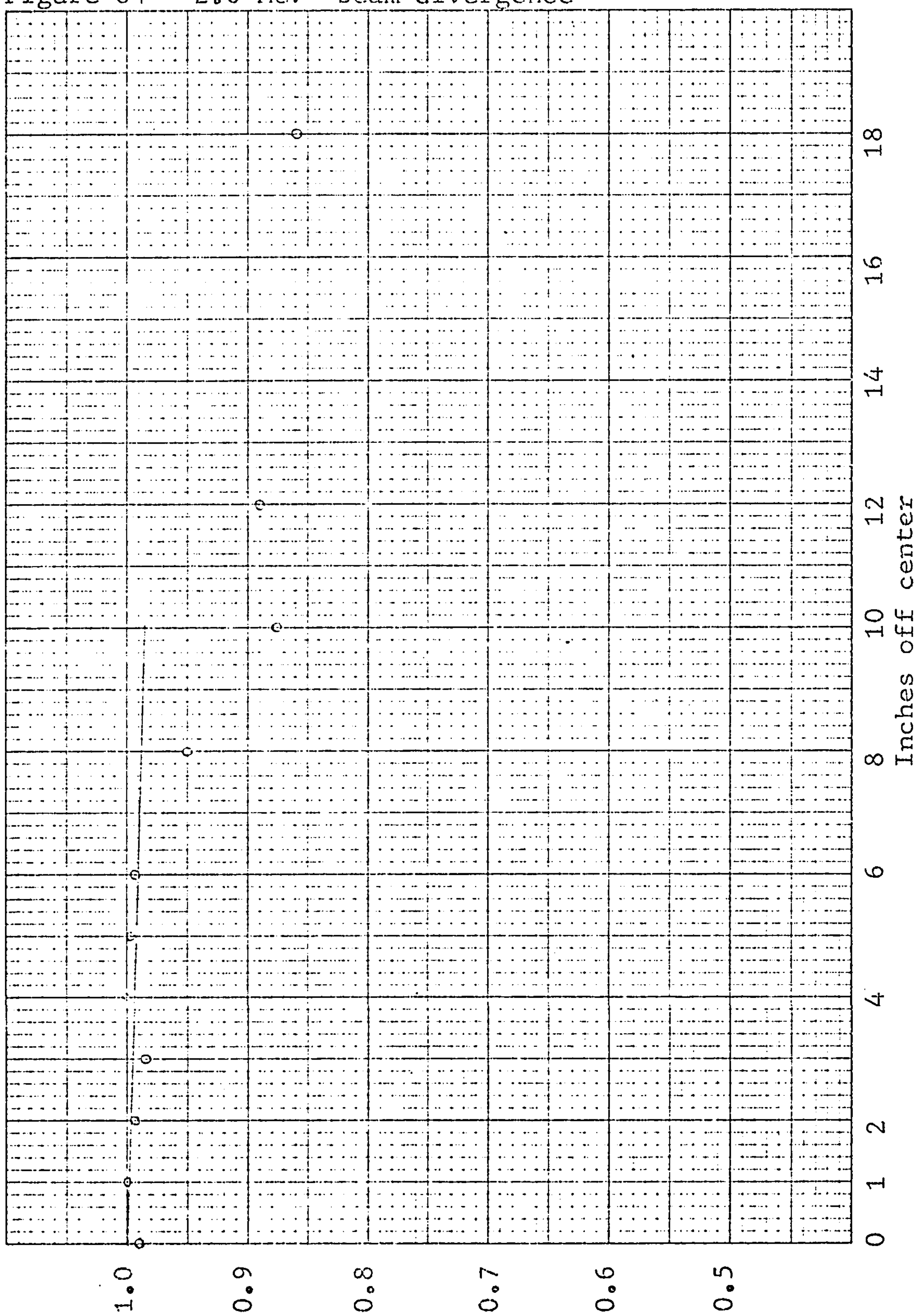

Figure 85 3.5 MeV beam divergence

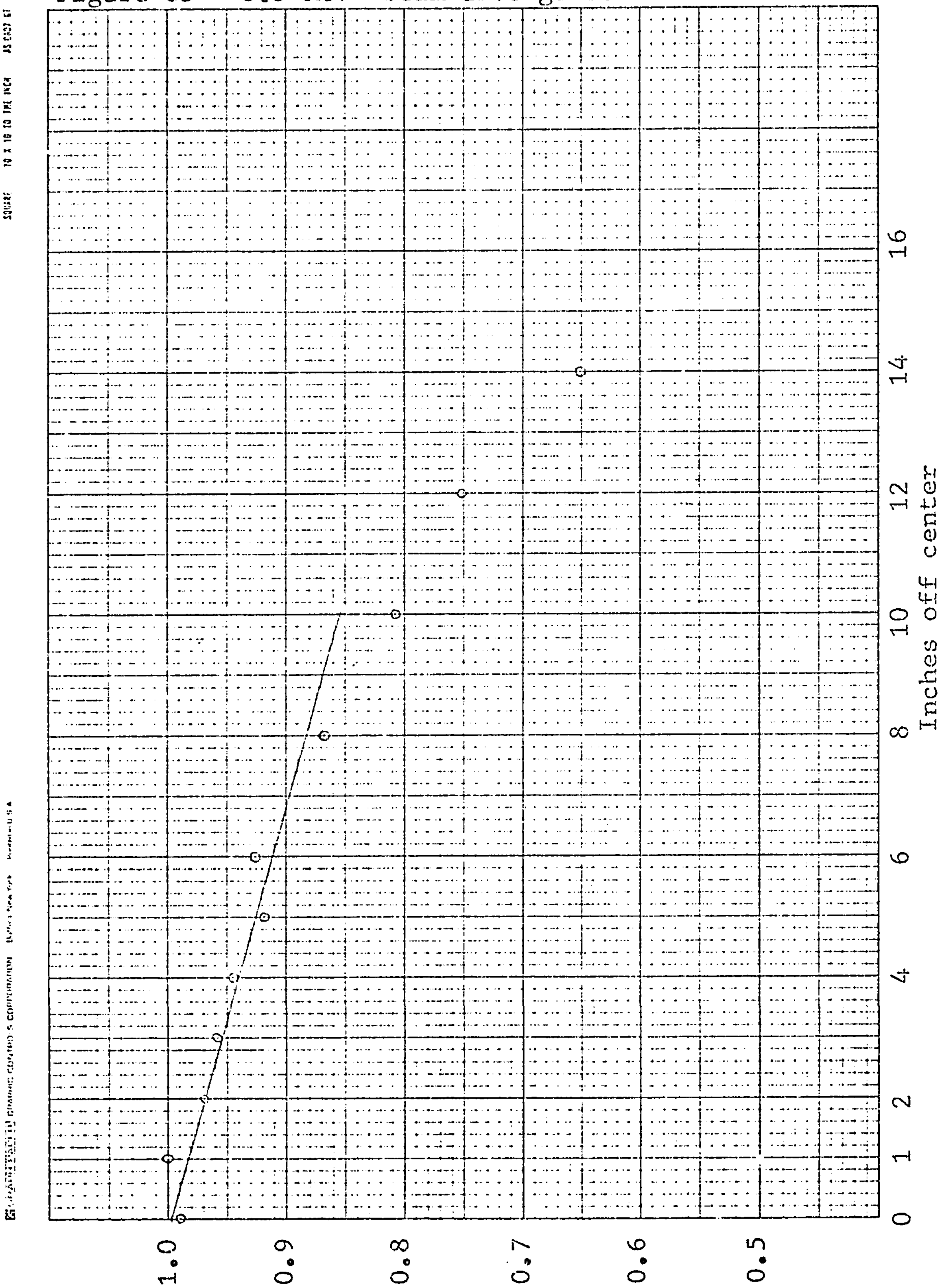

Figure 86 7.0 MeV beam divergence

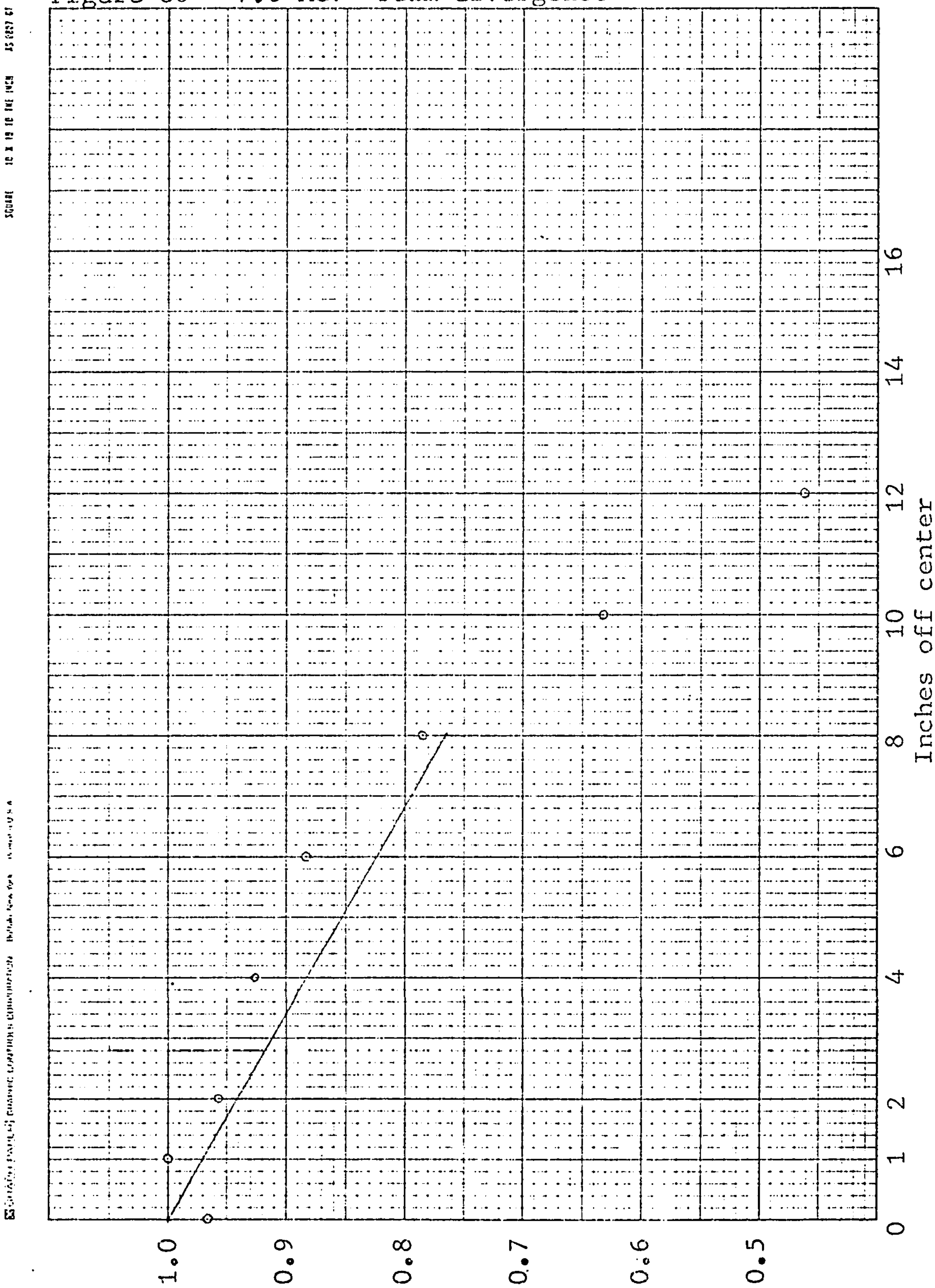

10.5 MeV are not clearly semi-infinite irradiated surface areas. And even in this case, results are not much below DTF results and the beam is as large as might generally be encountered.

I. TLD EXPERIMENTAL DATA

The following tables list the data collected in this project.

As mentioned previously, two sizes of crystals were used; these are referred to as "square" (1/8" x 1/8") and "rod" (1mm x 6mm). The locations monitored are "Beam Collimator Exit", "Backscatterer Position", and the various angular positions which have the additional notation of "Background" or "Backscatter" depending upon the measurement made. "Beam Collimator Exit" was normally 30 to 35 inches from the x-ray target. The sides of the beam were shielded somewhat to lower background levels due to scatter out of the beam. "Backscatterer Position" denotes the location at which the backscatter slab was to be placed, 60 to 75 inches from the x-ray target. The experimental configuration is discussed in Section 5.

Calibration on the crystals was repeatedly checked throughout the period of this work so as to keep the reported readings comparable.

17.1 2 MeV

17.1.1 Backscatter

17.1.1.1 Lead

LOCATION	TLD READING SQUARE	TLD READING ROD
Beam collimator exit	13939800	11369800
	15503200	11776600
	12931600	9662700
	13893600	11142500
	14839500	10335200
	13585800	10541700
Backscatterer position	1044600	894800
	973500	922600
	1150600	909200
	1047700	865100
	1152100	745900
	1236200	756300
Background @ 14", 30° 3.75" collimator	2992	
	2991	
	3653	
	3277	
Background @ 12", 40° 3.75" collimator		3020
		3018
		2495
		2892
Background @ 11", 50° 3.75" collimator	224	
	208	
	231	
	211	
Background @ 10", 60° 3.75" collimator		407
		371
		339
		372

LOCATION	TLD READING SQUARE	TLD READING ROD
Beam collimator exit	14928900	9575200
	13463800	10470300
	14424000	10695400
	13789500	10354900
	14846400	10812000
	13392100	9945700
Backscatter @ 14", 30° 3.75" collimator	4216	
	4051	
	4493	
	4533	
Backscatter @ 12", 40° 3.75" collimator		3022
		3360
		2886
		2907
Backscatter @ 11", 50° 3.75" collimator	1223	
	1353	
	1413	
	1338	
Backscatter @ 10", 60° 3.75" collimator		1150
		1119
		1242
		1092
Beam collimator exit	14889800	10441500
	13182100	10613400
	14603600	10730600
	14217200	11083800
	14906500	11726900
	14327600	11215300
Backscatterer position	1124000	776600
	1164700	764000
	1179400	856100
	1158500	857100
	1202500	890000
	1082300	824500

LOCATION	TLD READING SQUARE	TLD READING ROD
Background @ 14", 30° 3.75" collimator		7314
		7026
		7377
		6877
Background @ 12", 40° 3.75" collimator	448	
	448	
	477	
	461	
Background @ 11", 50° 3.75" collimator		125
		150
		163
		165
Background @ 10", 60° 3.75" collimator	208	
	233	
	215	
	211	
Beam collimator exit	14607400	10041300
	13355400	10525400
	14491300	11334800
	14496800	11050400
	15454400	11006400
	13785600	11440300
Backscatter @ 14", 30° 3.75" collimator		4194
		5798
		4885
		5470
Backscatter @ 12", 40° 3.75" collimator	1432	
	1410	
	1532	
	1485	
Backscatter @ 11", 50° 3.75" collimator		775
		799
		815
		885

LOCATION	TLD READING SQUARE	TLD READING ROD
Backscatter @ 10", 60° 3.75" collimator	1423	
	1397	
	1504	
	1343	
Beam collimator exit	5745500	4196400
	5401900	4079800
	5287200	4167900
	5795900	4079300
	5517800	4468300
	5364400	3949500
Backscatterer position	885100	708800
	905800	675000
	913300	748600
	991800	608700
	905300	712700
	826700	645400
Background @ 27.12", 30° 11.50" collimator		4
		3
		3
		3
Background @ 23.0", 30° 7.75" collimator	5	
	5	
	5	
	5	
Background @ 16.5", 50° 6.375" collimator		5
		4
		6
		5
Background @ 10.0", 50° 7.5" collimator	4	
	4	
	5	
	5	
Background @ 24.88", 50° 13.25" collimator		3
		3
		3
		3

LOCATION	TLD READING SQUARE	TLD READING ROD
Beam collimator exit	5984300	4293400
	5552100	4139400
	5429800	4178600
	5755500	4267400
	5096300	3465100
	5686200	4227700
Backscatter @ 27.0", 30° 11.5" collimator	12	
	13	
	11	
	12	
Backscatter @ 23.0", 30° 7.75" collimator		9
		8
		9
		8
Backscatter @ 24.81", 50° 13.25" collimator	10	
	9	
	8	
	9	
Backscatter @ 18", 50° 7.5" collimator		7
		6
		6
		7
Backscatter @ 16.62", 50° 6.375" collimator	120	
	121	
	121	
	143	
Beam collimator exit	5922300	4193900
	5515800	4429800
	5906900	4088500
	5886000	4355200
	5316000	4286300
	5651400	4161200

LOCATION	TLD READING SQUARE	TLD READING ROD
Backscatterer position	1073000	630400
	1006700	753600
	1042400	716800
	999800	716100
	947500	701000
	920800	723400
Background @ 25.25", 40° 7.375" collimator		3
		4
		3
		4
Background @ 25.19", 40° 11.625" collimator	4	
	6	
	5	
	5	
Background @ 17.69", 40° 6.375" collimator		5
		5
		6
		5
Background @ 23.5", 60° 13.25" collimator	5	
	4	
	5	
	4	
Background @ 23.44", 60° 7.50" collimator		4
		3
		4
		3
Beam collimator exit	5673000	3904800
	5329500	4340100
	5124900	4198700
	5340300	4336700
	5521100	3872100
	5892000	4243800
Backscatter @ 25.19", 40° 11.625" collimator	12	
	12	
	12	
	11	

LOCATION	TLD READING SQUARE	TLD READING ROD
Backscatter @ 25.25", 40^{o} 7.375" collimator		8
		8
		9
		9
Backscatter @ 17.69", 40^{o} 6.375" collimator	128	
	111	
	139	
	126	
Backscatter @ 23.44", 60^{o} 7.50" collimator		7
		6
		7
		8
Backscatter @ 23.50", 60^{o} 13.25" collimator	12	
	10	
	11	
	11	
Beam collimator exit	5608100	3562900
	5798300	4096800
	5159900	3605000
	5720600	3828100
	5391800	3256400
	5446200	
Backscatterer position	1022000	649800
	1029400	753500
	970300	706200
	1048700	719700
	1027500	804700
	902700	598400
Background @ 21.88", 30^{o} 5.562" collimator		8
		8
		8
		9
Background @ 18.69", 40^{o} 5.312" collimator	13	
	11	
	11	
	10	

LOCATION	TLD READING SQUARE	TLD READING ROD
Background @ 18.75", 50^{o} 7.625" collimator		5
		6
		5
		5
Background @ 15.94", 60^{o} 5.875" collimator	11	
	11	
	10	
	11	
Background @ 21.19", 70^{o} 7.875" collimator		5
		5
		4
		5
Beam collimator exit	5081800	4371500
	4928900	4421700
	5148300	3569400
	5189200	3854800
	5236000	3919700
	4891800	4033000
Backscatter @ 21.88", 30^{o} 5.562" collimator		102
		91
		98
		99
Backscatter @ 18.69", 40^{o} 5.312" collimator	211	
	218	
	216	
	227	
Backscatter @ 18.75", 50^{o} 7.625" collimator		41
		43
		41
		37
Backscatter @ 15.94", 60^{o} 5.875" collimator	170	
	172	
	154	
	173	

LOCATION	TLD READING SQUARE	TLD READING ROD
Backscatter @ 21.19", 70° 7.875" collimator		27
		25
		29
		28
Beam collimator exit	6143900	4696400
	6267800	4592300
	5677200	4331700
	6139700	4205500
	5501700	3977500
	5861100	4475500
Backscatterer position	1074900	785200
	1122600	795900
	1185400	757400
	1090500	737100
	1154700	859000
	1122700	776000
Background @ 22.62", 30° 5.875" collimator	12	
	12	
	12	
	12	
Background @ 20.50", 40° 5.312" collimator		10
		9
		9
		9
Background @ 20.12", 50° 7.688" collimator	6	
	6	
	6	
	7	
Background @ 22.19", 60° 9.688" collimator		4
		4
		4
		4

LOCATION	TLD READING	
	SQUARE	ROD
Beam collimator exit	5777300	3747600
	5933100	4476500
	5342900	4724600
	5437600	4324600
	6151100	3890700
	4913400	4466200
Backscatter @ 22.62", 30° 5.875" collimator	166	
	169	
	151	
	157	
Backscatter @ 20.50", 40° 5.312" collimator		150
		159
		181
		148
Backscatter @ 20.12", 50° 7.688" collimator	65	
	76	
	75	
	70	
Backscatter @ 22.19", 60° 9.688" collimator		18
		18
		20
		19

17.1.1.2 Iron

LOCATION	TLD READING SQUARE	TLD READING ROD
Beam collimator exit	5314100	4010400
	6179900	4253400
	5303000	4039300
	5642300	4131600
	5100300	3673700
	5494500	4298900
Backscatterer position	1110800	691300
	969400	698400
	1006300	734000
	1005300	667900
	1036800	559000
	986800	723900
Background @ 22.69", 30° 5.75" collimator		7
		7
		6
		6
Background @ 20.15", 40° 3.25" collimator	10	
	10	
	11	
	11	
Background @ 20.19", 50° 7.625" collimator		4
		5
		4
		6
Background @ 21.88", 60° 9.688" collimator	9	
	5	
	5	
	5	
Beam collimator exit	5691700	3898200
	5633900	4258900
	5797000	4211900
	5656600	4436800
	4865300	4504600
	5610400	4326800

LOCATION	TLD READING	
	SQUARE	ROD
Backscatter @ 22.69", 30^{o} 5.75" collimator		75 80 80 83
Backscatter @ 20.25", 40^{o} 5.25" collimator	144 135 125 148	
Backscatter @ 20.19", 50^{o} 7.625" collimator		44 43 43 44
Backscatter @ 21.88", 60^{o} 9.688" collimator	39 40 37 39	
Beam collimator exit	5318700 5172700 4736100 5324300 5576500 5452300	3936200 4355700 3830100 4395200 4915300 4363500
Backscatterer position	1020500 889900 948600 881700 964500 1003000	803500 669900 669500 799900 786900 721700
Background @ 22.0", 30^{o} 5.562" collimator	9 8 8 9	
Background @ 18.75", 40^{o} 5.312" collimator		7 7 7 8

LOCATION	TLD READING SQUARE	TLD READING ROD
Background @ 18.75", 50° 7.562" collimator	7	
	5	
	6	
	6	
Background @ 15.94", 60° 5.875" collimator		7
		7
		6
		6
Background @ 21.31", 70° 7.875" collimator	7	
	6	
	7	
	7	
Beam collimator exit	5023700	4387500
	5254200	4207200
	5766400	4127400
	6038500	4670100
	5772900	3886900
	5635800	3691400
Backscatter @ 22.0", 30° 5.562" collimator	109	
	128	
	124	
	121	
Backscatter @ 18.75", 40° 5.312" collimator		110
		113
		103
		106
Backscatter @ 18.75", 50° 7.562" collimator	57	
	66	
	61	
	67	
Backscatter @ 15.94", 60° 5.875" collimator		95
		93
		93
		96

LOCATION	TLD READING	
	SQUARE	ROD
Backscatter @ 21.31", 70^{o} 7.875" collimator	69 66 77 72	

17.1.1.3 Concrete

LOCATION	TLD READING SQUARE	TLD READING ROD
Beam collimator exit	6652900	5511400
	7201600	5400800
	7273400	5491600
	6833100	4900200
	5935200	5399400
	6879300	5290200
Backscatterer position	494800	339100
	443500	357800
	419800	236600
	487700	308600
	457300	347800
	442000	319100
Background @ 43.25", 30^{o} 12.0" collimator	7	6
	8	5
	7	4
	7	5
Background @ 35.62", 45^{o} 9.875" collimator	5	3
	4	4
	4	3
	4	3
Background @ 37.88", 60^{o} 14.625" collimator	5	
	4	
	5	
	4	
Beam collimator exit	6198700	5268500
	6530300	5026100
	6062200	4752500
	6098000	5049600
	6217100	4602700
	6793000	5323200
Backscatter @ 43.25", 30^{o} 12.0" collimator	17	13
	18	13
	18	14
	22	13

LOCATION	TLD READING	
	SQUARE	ROD
Backscatter @ 35.62", 45° 9.875" collimator	23	17
	24	18
	21	22
	22	19
Backscatter @ 37.88", 60° 14.625" collimator	13	11
	13	9
	12	10
	13	9

17.1.2 Copper absorption in beam

DEPTH IN COPPER	TLD READING
2.00 inches	127
	146
	137
	124
1.50	210
	215
	195
	226
1.25	315
	340
	330
	295
1.00	474
	431
	457
	471
0.875	531
	475
	487
	546
0.75	625
	669
	670
	622
0.625	724
	684
	735
	662
0.50	936
	930
	949
	904
0.25	1700
	1605
	1619

17.1.3 Infinite size determinations
(All measurements in this section were made with a 3.75" collimator)

17.1.3.1 Lead

17.1.3.1.1 4" square, 1.75" thick

LOCATION	TLD READING	
	SQUARE	ROD
Beam collimator exit	6480700	
	5735200	
	5710500	
	6423100	
	5356600	
	5896500	
	5548300	
	5576500	
	5777500	
Backscatterer position	910000	
	822600	
	963500	
	970600	
	971400	
	864200	
	909700	
	886600	
	930300	
Background @ 33.88", 30°	8	
	7	
	7	
	7	
Background @ 28.62", 45°	9	
	7	
	8	
	7	

LOCATION	TLD READING SQUARE	ROD
Background @ 23.38", 45°	7	
	8	
	9	
	8	
Background @ 22.56", 60°	10	
	7	
	7	
	9	
Beam collimator exit	6029600	
	6202700	
	6405100	
	6472100	
	6093800	
	5930100	
	6368300	
	6094400	
	6025500	
Backscatter @ 33.88", 30°	17	
	17	
	18	
	17	
Backscatter @ 28.62", 45°	20	
	21	
	18	
	20	
Backscatter @ 23.38", 45°	28	
	25	
	27	
	27	
Backscatter @ 22.56", 60°	28	
	29	
	27	
	28	

LOCATION	TLD READING	
	SQUARE	ROD
Beam collimator exit		4338300
		3227500
		4221800
		4391000
		4206300
		4361400
		4246000
		4084100
		4298800
Backscatterer position		604700
		568600
		629200
		590600
		662900
		603800
		616200
		646700
		578400
Background @ 31.52", 30°		9
		9
		11
		13
Background @ 23.81", 45°		7
		8
		7
		8
Background @ 24.81", 45°		10
		10
		10
		9
Background @ 20.75", 60°		6
		10
		7

LOCATION	TLD READING	
	SQUARE	ROD
Backscatterer position		4336800
		4206400
		3532300
		4356900
		3971800
		3756700
		4051000
		4089200
		4158800
Backscatter @ 31.52", 30°		14
		13
		14
		15
Backscatter @ 23.81", 45°		21
		19
		19
		20
Backscatter @ 24.81", 45°		19
		18
		17
		19
Backscatter @ 20.75", 60°		20
		20
		21
		20

17.1.3.1.2 6" square, 1.75" thick

LOCATION	TLD READING SQUARE	TLD READING ROD
Beam collimator exit		4459000
		4262300
		4196600
		4296100
		4167300
		4559700
		3959300
		4540100
		4407900
Background @ 34.19", 30°		8
		7
		6
		8
Background @ 28.50", 45°		6
		7
		6
		6
Background @ 22.69", 60°		7
		8
		8
		7
Beam collimator exit		4219700
		3277000
		4128100
		4480800
		5006400
		4590700
		4138400
		4405200
		4592100
Backscatter @ 34.19", 30°		11
		11
		12
		12

LOCATION	TLD READING SQUARE	TLD READING ROD
Backscatter @ 28.50", 45°		13
		15
		15
		13
Backscatter @ 22.69", 60°		17
		17
		17
		19
Beam collimator exit	5359200	
	5500800	
	5462800	
	5240900	
	5527500	
	5448500	
	4800700	
	5607800	
	5153100	
Backscatterer position	878800	
	868000	
	835500	
	790600	
	660800	
	933600	
	845400	
	836900	
	869100	
Background @ 31.75", 30°	38	
	33	
	35	
	38	
Background @ 24.19", 45°	33	
	31	
	36	
	34	

LOCATION	TLD READING SQUARE	ROD
Background @ 24.25", 45°	38	
	33	
	42	
	33	
Background @ 21.06", 60°	30	
	25	
	34	
	29	
Beam collimator exit	6368200	
	5437800	
	6056400	
	5269500	
	5870700	
	5435900	
	5563100	
	6483500	
	5944600	
Backscatter @ 31.75", 30°	42	
	35	
	39	
	44	
Backscatter @ 24.19", 45°	53	
	48	
	57	
	46	
Backscatter @ 24.25", 45°	45	
	56	
	46	
	56	
Backscatter @ 21.06", 60°	51	
	50	
	47	
	55	

17.1.3.1.3 7" square, 1.75" thick

LOCATION	TLD READING SQUARE	TLD READING ROD
Beam collimator exit	5975100	
	6275500	
	5638400	
	6404600	
	6070900	
	6045900	
Backscatterer position	932500	
	887500	
	877800	
	936400	
	857800	
	919500	
Background @ 30.25", 30^{o}	4	
	4	
	5	
	5	
Background @ 14.50", 45^{o}	6	
	5	
	5	
	5	
Background @ 19.62", 60^{o}	5	
	5	
	5	
Beam collimator exit	6319100	
	6396400	
	6025800	
	5905400	
	6037000	
	5949100	
Backscatter @ 30.25", 30^{o}	16	
	15	
	16	
	15	

LOCATION	TLD READING	
	SQUARE	ROD
Backscatter @ 14.50", 45°	76	
	72	
	82	
	67	
Backscatter @ 19.62", 60°	30	
	31	
	30	
	31	
Beam collimator exit		4340400
		4721300
		4371600
		4298700
		4203400
		4734200
Backscatterer position		765200
		727900
		649500
		611600
		642000
		643000
Background @ 30.06", 30°		3
		2
		3
		3
Background @ 14.56", 45°		4
		3
		4
		4
Background @ 19.19", 60°		4
		4
		4
		3

LOCATION	TLD READING	
	SQUARE	ROD
Beam collimator exit		4331500
		4635500
		4360300
		4901400
		4468100
		4365400
Backscatter @ 30.06", 30°		11
		12
		12
		12
Backscatter @ 14.56", 45°		55
		54
		53
		56
Backscatter @ 19.19", 60°		20
		21
		20
		21
Beam collimator exit	4843000	
	4631300	
	5108500	
	5079200	
	5375700	
	5163500	
Background @ 29.50", 30°	13	
	14	
	13	
	15	
Background @ 23.69", 45°	20	
	21	
	23	
	22	
Background @ 21.38", 60°	20	
	20	
	20	
	19	

LOCATION	TLD READING SQUARE	TLD READING ROD
Beam collimator exit	5191800	
	5565100	
	5472400	
	5284500	
	5187600	
	5522000	
Backscatter @ 29.50'', 30°	16	
	15	
	17	
	16	
Backscatter @ 23.69'', 45°	22	
	19	
	21	
	22	
Backscatter @ 21.38'', 60°	21	
	22	
	20	
	21	

17.1.3.1.4 8" square, 1.75" thick

LOCATION	TLD READING SQUARE	ROD
Beam collimator exit	5788300	
	5680300	
	4898800	
	5905100	
	5762300	
	5975700	
	6004600	
	6101300	
	5492500	
Backscatterer position	890800	
	834800	
	859700	
	881500	
	821100	
	855800	
	928200	
	876500	
	902300	
Background @ 28.81", 30°	7	
	6	
	7	
	5	
Background @ 22.38", 45°	6	
	7	
	7	
	7	
Background @ 25.00", 45°	5	
	6	
	5	
	5	
Background @ 20.19", 60°	8	
	8	
	7	
	6	

LOCATION	TLD READING	
	SQUARE	ROD
Beam collimator exit	5997300	
	5886400	
	5027700	
	5736700	
	5675700	
	6063900	
	6047700	
	5976200	
	5587300	
Backscatter @ 28.81", 30°	19	
	18	
	18	
	17	
Backscatter @ 22.38", 45°	29	
	31	
	26	
	30	
Backscatter @ 25.00", 45°	24	
	20	
	23	
	21	
Backscatter @ 20.19", 60°	30	
	30	
	30	
	26	
Beam collimator exit		3903800
		4244200
		4322700
		3935000
		4122800
		4436200
		4122900

LOCATION	TLD READING SQUARE	TLD READING ROD
Backscatterer position		645500
		627300
		625700
		635400
		623700
		619500
		612600
		657200
Background @ 31.62", 30°		5
		6
		6
		6
Background @ 24.12", 45°		5
		6
		5
		6
Background @ 24.06", 45°		9
		7
		7
		8
Background @ 21.25", 60°		6
		6
		6
		5
Beam collimator exit		4193300
		4131300
		4019800
		4555600
		3970500
		3159000
		4081600
		4070700
Backscatter @ 31.62", 30°		12
		10
		11
		11

LOCATION	TLD READING SQUARE	TLD READING ROD
Backscatter @ 24.12", 45^{o}		18
		18
		19
		20
Backscatter @ 24.06", 45^{o}		20
		16
		18
		20
Backscatter @ 21.25", 60^{o}		19
		19
		19
		18

17.1.3.1.5 10" square, 1.75" thick

LOCATION	TLD READING SQUARE	TLD READING ROD
Beam collimator exit		4201500
		4177300
		3034800
		4124500
		4347900
		4341200
		4400100
		4033000
		4202100
Backscatterer position		604400
		695200
		699000
		622300
		689900
		646900
		444900
Background @ 29.00", 30°		4
		5
		4
		5
Background @ 22.50", 45°		4
		4
		4
		3
Background @ 25.25", 45°		5
		4
		4
		5
Background @ 20.12", 60°		4
		5
		4
		4

LOCATION	TLD READING SQUARE	TLD READING ROD
Backscatter @ 29.00", 30°		14
		13
		12
		13
Backscatter @ 22.50", 45°		22
		22
		21
		24
Backscatter @ 25.25", 45°		14
		15
		15
		14
Backscatter @ 20.12", 60°		20
		22
		18
		20
Beam collimator exit	5374900	
	4996800	
	5753600	
	5252100	
	5641100	
	5262100	
	5681400	
Backscatterer position	840100	
	838100	
	841500	
	824400	
	787500	
	882900	
	806000	
Background @ 31.00", 30°	9	
	8	
	6	
	7	

LOCATION	TLD READING	
	SQUARE	ROD
Background @ 23.75", 45°	7	
	6	
	7	
	6	
Background @ 23.62", 45°	9	
	9	
	9	
	10	
Background @ 21.00", 60°	8	
	7	
	8	
	8	
Beam collimator exit	4943200	
	4709400	
	5036200	
	5343500	
	5500300	
	5866100	
	4646300	
	5543300	
Backscatter @ 31.00", 30°	12	
	14	
	15	
	17	
Backscatter @ 23.75", 45°	25	
	25	
	25	
	25	
Backscatter @ 23.62", 45°	25	
	26	
	27	
	28	
Backscatter @ 21.00", 60°	26	
	28	
	25	
	25	

17.1.3.1.6 12" square, 1.75" thick

LOCATION	TLD READING	
	SQUARE	ROD
Beam collimator exit		4179500
		4103400
		2933900
		3748700
		4084000
		3795400
Backscatterer position		569500
		584200
		664100
		665200
		582000
		507100
Background @ 29.44", 30°		2
		3
		3
		3
Background @ 23.69", 45°		3
		2
		2
		3
Background @ 21.62", 60°		3
		3
		3
		2
Beam collimator exit		4044700
		4204900
		4234200
		4302300
		4395000
		3998900
Backscatter @ 29.44", 30°		10
		11
		11
		10

LOCATION	TLD READING SQUARE	TLD READING ROD
Backscatter @ 23.69", 45°		18
		15
		16
		15
Backscatter @ 21.62", 60°		15
		15
		14
		15
Beam collimator exit	5846700	
	4800800	
	6307000	
	5969500	
	5717500	
	5906000	
Backscatterer position	982300	
	913400	
	890300	
	969600	
	851400	
	807200	
Background @ 29.25", 30°	4	
	3	
	3	
	2	
Background @ 23.50", 45°	3	
	3	
	3	
Background @ 21.25", 60°	4	
	4	
	4	
	4	

LOCATION	TLD READING	
	SQUARE	ROD
Beam collimator exit	5514400	
	5327400	
	5356800	
	5056400	
	5416600	
	6150900	
Backscatter @ 29.25", 30°	15	
	17	
	16	
	15	
Backscatter @ 23.50", 45°	23	
	22	
	21	
	20	
Backscatter @ 21.25", 60°	22	
	21	
	26	
	24	

17.1.3.1.7 9" square, 0.25" thick

LOCATION	TLD READING SQUARE	TLD READING ROD
Beam collimator exit	5916900	
	6956400	
	6050700	
	6588100	
	6426800	
	6919600	
	6147600	
	6719600	
	6291300	
Backscatterer position	910900	
	923000	
	1058600	
	1051600	
	1049700	
	1037200	
	993000	
	961500	
	819400	
Background @ 27.62", 30°	9	
	7	
	8	
	9	
Background @ 11.81", 45°	11	
	10	
	11	
	11	
Background @ 12.69", 60°	13	
	12	
	10	
Beam collimator exit	5619800	
	5128300	
	5539300	
	5371900	
	5026800	
	5852100	

LOCATION	TLD READING	
	SQUARE	ROD
Backscatter @ 27.62", 30°	21	
	22	
	23	
	21	
Backscatter @ 11.81", 45°	141	
	132	
	132	
	126	
Backscatter @ 12.69", 60°	100	
	85	
	88	
	77	

17.1.3.1.8 9" square, 0.50" thick

LOCATION	TLD READING	
	SQUARE	ROD
Beam collimator exit	6165400	
	6250900	
	6426700	
	4938000	
	5716300	
	6004100	
	5386200	
	6356600	
	5807800	
Backscatter @ 27.69", 30°	20	
	16	
	18	
	19	
Backscatter @ 11.88", 45°	125	
	119	
	120	
	121	
Backscatter @ 12.75", 60°	82	
	86	
	97	
	96	

17.1.3.1.9 9" square, 0.625" thick

LOCATION	TLD READING	
	SQUARE	ROD
Beam collimator exit		3752400
		4125300
		3733100
		4058100
		4217800
		4681900
Backscatterer position		654100
		649600
		677700
		628500
		663000
		719200
Background @ 30.00", 30°		3
		5
		3
		5
Background @ 14.50", 45°		5
		4
		5
		6
Background @ 19.25", 60°		5
		6
		6
		6
Beam collimator exit		5282000
		4378000
		4194200
		4571100
		4700800
		3526000
		4965600
		4971200
		4746300

LOCATION	TLD READING	
	SQUARE	ROD
Backscatter @ 30.00", 30°		15
		14
		13
		16
Backscatter @ 14.50", 45°		63
		68
		60
		80
Backscatter @ 19.25", 60°		97
		88
		96
		89

17.1.3.1.10 9" square, 0.75" thick

LOCATION	TLD READING	
	SQUARE	ROD
Beam collimator exit	5647500	
	5997300	
	5950300	
	5605700	
	5674900	
	6240300	
Backscatter @ 27.75", 30°	18	
	16	
	18	
	16	
Backscatter @ 11.88", 45°	122	
	112	
	107	
	103	
Backscatter @ 12.75", 60°	84	
	93	
	88	
	83	

17.1.3.1.11 9" square, 1.00" thick

LOCATION	TLD READING SQUARE	TLD READING ROD
Beam collimator exit		4485400
		4179200
		4005100
		3742500
		3981100
		4060800
		4076500
		4165300
		2964900
Backscatterer position		565400
		698200
		718800
		656700
		803100
		600100
		589100
		829100
		628200
Background @ 27.69", 30°		3
		3
		3
		4
Background @ 9.56", 45°		5
		5
		5
		5
Background @ 11.31", 60°		5
		5
		5
		5

LOCATION	TLD READING SQUARE	TLD READING ROD
Beam collimator exit		4668400
		4274200
		3947400
		4291300
		4290500
		4700800
		4788000
		4392200
		3911400
Backscatter @ 27.69", 30^{o}		14
		13
		14
		15
Backscatter @ 9.56", 45^{o}		109
		109
		116
		114
Backscatter @ 11.31", 60^{o}		150
		174
		152
		149

17.1.3.1.12 9" square, 1.25" thick

LOCATION	TLD READING SQUARE	TLD READING ROD
Beam collimator exit		3772700
		3903400
		4611300
		4182300
		3993800
		4173300
		4005000
		4161500
		4031800
Backscatter @ 27.5", 30°		22
		17
		17
		14
Backscatter @ 9.44", 45°		145
		169
		164
		169
Backscatter @ 11.25", 60°		87
		91
		90
		64

17.1.3.1.13 9" square, 1.375" thick

LOCATION	TLD READING SQUARE	TLD READING ROD
Beam collimator exit		4126300
		4430100
		4140800
		4292500
		4035800
		4127300
		4435600
		3980400
		4572000
Backscatter @ 27.62", 30°		14
		13
		14
		14
Backscatter @ 11.81", 45°		89
		97
		81
		83
Backscatter @ 12.75", 60°		54
		59
		54
		59

17.1.3.1.14 9" square, 1.50" thick

LOCATION	TLD READING SQUARE	TLD READING ROD
Beam collimator exit	6701400	
	6936700	
	5921000	
	6825300	
	6357500	
	6108500	
	6636100	
	6145900	
	6254900	
Backscatter @ 31.12", 30°	15	
	15	
	15	
	15	
Backscatter @ 23.62", 45°	27	
	27	
	27	
	26	
Backscatter @ 9.19", 45°	280	
	284	
	265	
	278	
Backscatter @ 20.62", 60°	27	
	26	
	28	
	24	
Beam collimator exit		4754300
		4658300
		4515900
		3268600
		4135600
		4261100
		4784200
		4752400
		4770900

LOCATION	TLD READING SQUARE	TLD READING ROD
Backscatter @ 31.38", 30°		17
		20
		19
		20
Backscatter @ 23.88", 45°		18
		19
		19
		18
Backscatter @ 9.62", 45°		167
		163
		166
		169
Backscatter @ 20.75", 60°		10
		12
		11
		10

17.1.3.1.15 9" square, 1.75" thick

LOCATION	SQUARE	ROD
Beam collimator exit		4041000
		3913700
		4212500
		3631600
		2898900
		4214500
		4229200
		3899300
		3831600
Backscatterer position		627100
		649200
		637800
		644400
		622700
		671600
		599300
		656900
		695900
Background @ 31.62", 30^{o}		9
		10
		8
		11
Background @ 23.75", 45^{o}		10
		9
		8
		10
Background @ 24.75", 45^{o}		10
		14
		11
		10
Background @ 20.75", 60^{o}		9
		9
		8
		9

LOCATION	TLD READING SQUARE	TLD READING ROD
Beam collimator exit	6049200	2743000
	6133600	3734900
	5863600	3852000
	5548900	4067500
	5993500	3596600
	6285000	3694200
	4933000	4059500
	5916500	3680000
	5330600	4217300
Backscatter @ 31.62", 30°	19	15
	19	14
	19	15
	17	15
Backscatter @ 23.75", 45°	28	23
	27	24
	26	21
	30	20
Backscatter @ 24,75", 45°	28	21
	26	20
	28	21
	29	21
Backscatter @ 20.75", 60°	27	23
	27	20
	28	24
	30	23

17.1.3.1.16 9" square, 2.00" thick

LOCATION	TLD READING SQUARE	ROD
Beam collimator exit	6347700	
	6077600	
	6247200	
	5567900	
	5849600	
	6068000	
	6296200	
	6619700	
	6183200	
Backscatterer position	950500	
	940300	
	1019600	
	902100	
	982000	
	960200	
	1013400	
	986100	
	1070800	
Background @ 31.25", 30°	4	
	3	
	4	
	4	
Background @ 23.75", 45°	3	
	3	
	3	
	4	
Background @ 9.38", 45°	6	
	6	
	6	
	6	
Background @ 20.69", 60°	4	
	3	
	4	
	4	

LOCATION	TLD READING SQUARE	ROD
Backscatterer position	6632000	
	6615100	
	6515000	
	6960200	
	5833500	
	6599500	
	6472200	
	6512900	
	6562600	
Backscatter @ 31.25", 30°	15	
	15	
	15	
	16	
Backscatter @ 23.75", 45°	29	
	26	
	26	
	26	
Backscatter @ 9.38", 45°	274	
	254	
	262	
	276	
Backscatter @ 20.69", 60°	27	
	29	
	29	
	29	

17.1.3.2 Iron

17.1.3.2.1 12" square, 2.50" thick

LOCATION	TLD READING SQUARE	ROD
Beam collimator exit	5921000	
	6044000	
	6743200	
	5603200	
	5559900	
	5983400	
Backscatterer position	976400	
	998400	
	920800	
	885100	
	941100	
	944700	
Background @ 29.81", 30^{o}	3	
	3	
	4	
	3	
Background @ 23.94", 45^{o}	4	
	4	
	4	
	4	
Background @ 21.62", 60^{o}	4	
	5	
	5	
	4	
Beam collimator exit	6001300	
	6251800	
	5811000	
	6397600	
	6302500	
	6274500	

LOCATION	TLD READING SQUARE	TLD READING ROD
Backscatter @ 29.81", 30°	44	
	44	
	44	
	47	
Backscatter @ 23.94", 45°	60	
	56	
	65	
	54	
Backscatter @ 21.62", 60°	54	
	69	
	59	
	60	
Beam collimator exit		4371100
		4654900
		4634000
		4631400
		4890000
		4486900
Backscatterer position		719000
		729000
		715100
		750300
		742900
		719700
Background @ 29.06", 30°		6
		5
		5
		4
Background @ 23.19", 45°		6
		6
		5
		6
Background @ 21.06", 60°		5
		6
		5
		5

LOCATION	TLD READING	
	SQUARE	ROD
Beam collimator exit		4355700
		4945900
		3539400
		4347700
		4577500
		4289900
Backscatter @ 29.06", 30°		36
		41
		36
		37
Backscatter @ 23.19", 45°		41
		44
		44
		48
Backscatter @ 21.06", 60°		47
		47
		50
		49

17.1.3.2.2 14" square, 2.50" thick

LOCATION	TLD READING SQUARE	ROD
Beam collimator exit	6231400	
	6030300	
	6646900	
	5419100	
	5863700	
	5731600	
Backscatterer position	862900	
	847400	
	1053700	
	890200	
	890600	
	850000	
Background @ 29.81", 30°	4	
	3	
	3	
	3	
Background @ 23.94", 45°	5	
	6	
	5	
	5	
Background @ 21.62", 60°	6	
	4	
	5	
	5	
Beam collimator exit	6250400	
	5622600	
	6192700	
	5500100	
	5324600	
	5860800	
Backscatter @ 29.81", 30°	44	
	39	
	45	
	51	

LOCATION	TLD READING SQUARE	TLD READING ROD
Backscatter @ 23.94", 45°	55	
	59	
	60	
	51	
Backscatter @ 21.62", 60°	55	
	58	
	62	
	52	
Beam collimator exit		4511300
		5059300
		4631200
		4763700
		4406900
		4441300
Backscatterer position		649200
		711600
		769800
		752000
		651700
		721300
Background @ 30", 30°		2
		3
		2
		2
		3
		3
Background @ 24.12" 45°		3
		3
		3
		3
		2
		3

LOCATION	TLD READING SQUARE	TLD READING ROD
Background @ 21.75", 60°		3
		3
		3
		3
		3
		3
Beam collimator exit		4418300
		4636200
		4571700
		3514400
		4617100
		4129800
Backscatter @ 30", 30°		31
		31
		32
		34
Backscatter @ 24.12", 45°		47
		37
		46
		47
Backscatter @ 21.75", 60°		45
		43
		41
		40

17.1.3.2.3 12" square, 4.125" thick

LOCATION	TLD READING SQUARE	TLD READING ROD
Beam collimator exit	6789100	4239600
	6265300	4514800
	5710000	4660900
	6600800	4692200
	6163500	4731100
	5774700	4257500
Backscatterer position	884700	726300
	1042700	766300
	937200	771500
	1011600	748400
	916400	648500
	965500	721300
Background @ 29.06", 30°	6	3
	6	3
	6	3
	7	3
Background @ 23.19", 45°	6	3
	6	3
	6	3
	6	3
Background @ 21.06", 60°	6	3
	6	3
	7	4
	7	3
Beam collimator exit	6597300	4156200
	6625100	4457600
	6235700	5006200
	6021100	4402900
	6069700	4976000
	5870100	4153200
Backscatter @ 29.06", 30°	55	33
	50	36
	53	39
	54	35

LOCATION	TLD READING	
	SQUARE	ROD
Backscatter @ 23.19", 45°	63	47
	70	41
	65	45
	71	41
Backscatter @ 21.06", 60°	67	46
	73	39
	76	47
	64	47

17.1.3.3 Concrete

17.1.3.3.1 32" square, 8" thick

LOCATION	TLD READING SQUARE	TLD READING ROD
Beam collimator exit	5344300	
	5936900	
	5568300	
	5857700	
	6239600	
	6449500	
Backscatterer position	965900	
	899800	
	863800	
	835200	
	1004700	
	778700	
Background @ 28.94", 30°	4	
	3	
	4	
	4	
Background @ 21.75", 45°	3	
	4	
	5	
	5	
Background @ 19.50", 60°	6	
	5	
	5	
	5	
Beam collimator exit	5941900	
	5607600	
	5808100	
	5559900	
	5841800	
	5549200	

LOCATION	TLD READING SQUARE	TLD READING ROD
Backscatter @ 28.94", 30°	56	
	51	
	48	
	48	
Backscatter @ 21.75", 45°	61	
	76	
	78	
	60	
Backscatter @ 19.50", 60°	67	
	78	
	60	
	78	
Beam collimator exit		4596400
		4531300
		4297800
		4185600
		4420200
		4117400
Backscatterer position		703100
		675700
		621000
		630600
		635300
		686400
Background @ 27.88", 30°		3
		2
		2
		3
Background @ 22.75", 45°		3
		3
		3
		3
Background @ 19.06", 60°		3
		3
		3
		4

LOCATION	TLD READING SQUARE	TLD READING ROD
Beam collimator exit		4640200
		4127400
		4381200
		4009500
		4181000
		4214400
Backscatter @ 27.88", 30°		38
		33
		37
		34
Backscatter @ 22.75", 45°		42
		28
		36
		43
Backscatter @ 19.06", 60°		32
		45
		41
		42

17.1.3.3.2 36" square, 8" thick

LOCATION	TLD READING SQUARE	TLD READING ROD
Beam collimator exit		4198600
		4570500
		4442700
		4005500
		4179900
		4521700
Backscatterer position		715900
		705000
		697800
		724800
		753700
		594500
Background @ 27.94", 30^{o}		4
		4
		3
		3
Background @ 21.56", 45^{o}		3
		3
		3
		3
Background @ 18.0", 60^{o}		4
		4
		3
		4
Beam collimator exit		4282000
		3797100
		4208300
		3806000
		3898800
		4334500
Backscatter @ 27.94", 30^{o}		37
		39
		42
		35

LOCATION	TLD READING SQUARE	TLD READING ROD
Backscatter @ 21.56", 45°		37
		49
		42
		47
Backscatter @ 18.0", 60°		46
		53
		53
		46
Beam collimator exit	6023700	
	6046600	
	5825700	
	6223000	
	6057000	
	6436900	
Backscatter @ 29.12", 30°	47	
	52	
	53	
	47	
Backscatter @ 21.75", 45°	60	
	66	
	73	
	50	
Backscatter @ 19.62", 60°	47	
	73	
	66	
	51	

17.1.3.3.3 32" square, 10" thick

LOCATION	TLD READING	
	SQUARE	ROD
Beam collimator exit	5540300	
	5393900	
	4830500	
	5329600	
	5248900	
	5949500	
Backscatterer position	752200	
	880800	
	927200	
	819900	
	943800	
	884700	
Background @ 27.81", 30°	4	
	4	
	4	
	5	
Background @ 22.81", 45°	4	
	6	
	5	
	5	
Background @ 19.19", 60°	5	
	5	
	6	
	7	
Beam collimator exit	5922200	
	5234100	
	5672000	
	5804900	
	5689700	
	5539400	
Backscatter @ 27.81", 30°	58	
	46	
	54	
	56	

LOCATION	TLD READING SQUARE	TLD READING ROD
Backscatter @ 22.81", 45°	63	
	48	
	43	
	62	
Backscatter @ 19.19", 60°	67	
	73	
	49	
	45	
Beam collimator exit		3848500
		4329900
		4011600
		4748900
		3734200
		4428000
Backscatter @ 27.88", 30°		31
		36
		33
		35
Backscatter @ 22.70", 45°		29
		46
		35
		41
Backscatter @ 18.94", 60°		41
		43
		30
		35

17.1.4 Beam divergence

HORIZONTAL DISPLACEMENT (inches)	TLD READING Right of Center	TLD READING Left of Center
17	72700	74857
	67600	71800
12	78900	68500
	72300	60300
10	80300	68600
	74600	76500
8	68500	69600
	67700	65400
6	83100	97300
	78300	81100
5	73000	88900
	80700	75900
4	84700	88400
	84600	78600
3	73900	89800
	79800	77800
2	71600	83700
	81900	73600
	82400	76100
	87300	73400
1	87300	84200
	77300	59700
	84400	80100
	78800	71000
Center	85600	
	85100	
	78100	
	74100	

VERTICAL DISPLACEMENT (inches)	TLD READING Above Center	Below Center
17	47500	62700
	66500	70900
12	66700	74700
	64100	72500
10	70200	61500
	62500	76000
8	79800	73200
	77500	79800
6	74300	84400
	86000	83400
5	89100	81500
	72300	89500
4	83100	78000
	79400	69100
3	71200	91600
	74500	81900
2	74900	85900
	76500	74600
	82800	72400
	86800	80300
1	83800	86900
	76800	73600
	77800	75200
	81000	87400

17.2 3.5 MeV

17.2.1 Backscatter

17.2.1.1 Lead

LOCATION	TLD READING	
	SQUARE	ROD
Beam collimator exit	2110900	1964900
	2495600	1755300
	2536900	1706400
	2320000	1719600
		1952500
		1878500
Backscatterer position	450300	317600
	455700	265100
	409900	288200
	422300	340500
	440600	330900
	341300	324700
Background @ 23.00", 30^{o} 5.625" collimator		14
		15
		14
		16
Background @ 20.38", 40^{o} 5.562" collimator	15	
	15	
	17	
	17	
Background @ 19.00", 50^{o} 6.25" collimator		7
		8
		8
		9
Background @ 18.38", 60^{o} 8.00" collimator	8	
	9	
	9	
	9	

LOCATION	TLD READING SQUARE	TLD READING ROD
Beam collimator exit	2452300	1775900
	2298700	1558600
	2381000	1633600
	2372300	1636500
	2328600	1923500
	2611600	1754700
Backscatter @ 23.00", 30° 5.625" collimator		91
		82
		87
		83
Backscatter @ 20.38", 40° 5.562" collimator	169	
	142	
	145	
	150	
Backscatter @ 19.00", 50° 6.25" collimator		71
		76
		64
		78
Backscatter @ 18.38", 60° 8.00" collimator	53	
	52	
	46	
	54	
Beam collimator exit	3976400	2914600
	3649700	2657500
	3854800	2797900
	3818900	2551600
	4013500	2677800
	4185700	2890900
Backscatter @ 23.75", 30° 5.562" collimator	164	
	168	
	158	
	170	
Backscatter @ 20.50", 40° 5.625" collimator		147
		133
		135
		122

LOCATION	TLD READING	
	SQUARE	ROD
Backscatter @ 19.50", 50°	104	
7.00" collimator	104	
	107	
	102	
Backscatter @ 19.00", 60°		47
7.812" collimator		49
		46
		42

17.2.1.2 Iron

LOCATION	TLD READING	
	SQUARE	ROD
Beam collimator exit	2234100	1585700
	2491000	1539800
	2422900	1767900
	2414300	1775000
	2302900	1720900
	2144800	1721900
Backscatterer position	456000	289300
	472300	330500
	388100	279200
	392700	270700
	393700	309200
	419700	279100
Background @ 23.25", 30° 5.562" collimator	16	
	15	
	14	
	14	
Background @ 19.94", 40° 5.625" collimator		14
		12
		13
		14
Background @ 19.62", 50° 7.00" collimator	8	
	7	
	7	
	8	
Background @ 18.38", 60° 7.75" collimator		6
		5
		6
		5
Beam collimator exit	2716600	1810900
	2612100	1681200
	2095900	1963700
	2544700	1817400
	2318800	1556000
	2477800	2055600

LOCATION	TLD READING SQUARE	TLD READING ROD
Backscatter @ 23.25", 30° 5.562" collimator	78	
	72	
	72	
	73	
Backscatter @ 19.94", 40° 5.625" collimator		51
		53
		56
		53
Backscatter @ 19.62", 50° 7.00" collimator	45	
	45	
	43	
	45	
Backscatter @ 18.38", 60° 7.75" collimator		26
		26
		26
		25
Beam collimator exit	4003300	2977500
	4064600	3253100
	4016400	3127600
	4648500	3335900
	4248900	3030000
	4224100	2967700
Backscatter @ 23.00", 30° 5.625" collimator		79
		78
		73
		72
Backscatter @ 20.50", 40° 5.50" collimator	119	
	120	
	124	
	115	
Backscatter @ 19.38", 50° 6.25" collimator		63
		58
		65
		58

LOCATION	TLD READING	
	SQUARE	ROD
Backscatter @ 18.38", 60° 8.00" collimator	46	
	52	
	43	
	46	

17.2.1.3 Concrete

LOCATION	TLD READING SQUARE	TLD READING ROD
Beam collimator exit	6728400	
	6899900	
	5948600	
	6285400	
	6052700	
	6651100	
Backscatterer position	795200	
	868500	
	890300	
	820300	
	860800	
	748800	
Background @ 25.00", 30° 6.25" collimator	244	
	236	
	202	
	244	
Background @ 23.25", 45° 7.50" collimator	15	
	15	
	14	
	16	
Background @ 26.00", 60° 9.562" collimator	16	
	18	
	18	
	18	
Beam collimator exit	5525800	
	5793600	
	5202400	
	5823000	
	5923800	
	5730600	

LOCATION	TLD READING SQUARE	TLD READING ROD
Backscatter @ 25.00", 30° 6.25" collimator	343	
	350	
	352	
	292	
Backscatter @ 23.25", 45° 7.50" collimator	73	
	65	
	71	
	71	
Backscatter @ 26.00", 60° 9.562" collimator	55	
	48	
	51	
	53	

17.2.2 Copper absorption in beam

DEPTH IN COPPER (inches)	TLD READING SQUARE	TLD READING ROD
2.50		107
		101
		97
		88
1.75	274	
	300	
	267	
	263	
1.50		203
		315
		284
		256
1.25	612	
	600	
	623	
	625	
1.125		507
		424
		530
		579
1.00	1001	
	1078	
	1044	
	1251	
0.875	935	
	895	
	1074	
	782	
0.75		589
		549
		397
		493

DEPTH IN COPPER (inches)	TLD READING SQUARE	TLD READING ROD
0.625	1434	
	1471	
	1897	
	1407	
0.50		1199
		1194
		843
		1187
0.25	2701	
	2741	
	3731	
	2625	
0.125		2036
		1474
		1941
		1652
0.0	6347	3251
	4788	2622
	6152	2951
	5082	3172
2.50		5372
		6499
		6325
		5872
1.75	9475	
	8744	
	9581	
	9127	
1.50		5815
		5708
		5669
		5874

DEPTH IN COPPER (inches)	TLD READING SQUARE	TLD READING ROD
1.25	11787	
	10808	
	10718	
	11374	
1.125		6606
		7570
		6818
		7053
1.00	12934	
	13678	
	11438	
	13270	
0.875	12772	
	11719	
	10241	
	10210	
0.75		4724
		4300
		4540
		4544
0.625	12911	
	12860	
	13843	
	12652	
0.50		6702
		7314
		6289
		6272
0.25	12509	
	13163	
	13002	
	12130	

DEPTH IN COPPER (inches)	TLD READING SQUARE	TLD READING ROD
0.125		5468
		5118
		4862
		5981
0.0	14172	7555
	13071	7779
	13162	7910
	12926	7123

17.2.3 Beam divergence

HORIZONTAL DISPLACEMENT (inches)	TLD READING	
	RIGHT OF CENTER	LEFT OF CENTER
16	7910 9001	7754 9614
14	11405 12020	11489 11738
12	15072 16898	14919 15426
10	23222 21290	22181 24097
8	46807 49645	49178 50300
6	67144 66511	71202 70743
5	67278 70701	70632 75019
4	74633 74858	75900 76889
3	75522 72251	77582 68331
2	75290 75878	75996 77564
1	82713 80425	81624 79453
Center	79675 76865	

VERTICAL DISPLACEMENT (inches)	TLD READING SQUARE	TLD READING ROD
18	21203	
	21520	
16	35552	44917
	35577	49274
14	52013	53497
	51043	50558
12	58143	59018
	58542	60972
10	64369	63785
	64483	62652
8	69170	68468
	68197	69632
6	73174	75902
	72310	75904
5	76880	73218
	72636	69605
4	75705	73732
	63805	69450
3	74771	75815
	77770	79808
2	79387	78059
	75922	74671
1	75352	84514
	78061	78408

17.3 7.0 MeV

17.3.1 Backscatter

17.3.1.1 Lead

LOCATION	TLD READING	
	SQUARE	ROD
Backscatterer position	802500	543300
	856600	599000
	872200	604700
	820000	581000
	925400	600200
	832200	622200
Background @ 26.94", 30° 5.688" collimator		1618
		1605
		1697
		1608
Background @ 26.00", 40° 5.625" collimator	1211	
	1338	
	1387	
	1473	
Background @ 26.50", 50° 6.50" collimator		101
		87
		95
		93
Background @ 30.00", 60° 9.312" collimator	617	
	509	
	613	
	552	
Backscatter @ 26.75", 30° 5.625" collimator		2078
		2104
		2051
		2083

LOCATION	TLD READING SQUARE	TLD READING ROD
Backscatter @ 25.44", 40° 5.562" collimator	2347 1919 2036 2359	
Backscatter @ 25.88", 50° 6.50" collimator		401 354 413 382
Backscatter @ 29.32", 60° 9.312" collimator	205 185 188 161	
Backscatterer position	437400 433600 405200 401600 440400 475300	303900 323300 308600 336200 273900 306700
Background @ 24.12", 30° 5.25" collimator	949 942 995 954	
Background @ 23.9", 40° 5.688" collimator		107 101 97 119
Background @ 27.50", 50° 7.75" collimator	68 60 69 63	
Background @ 26.31", 60° 8.312" collimator		107 104 94 100

LOCATION	TLD READING	
	SQUARE	ROD
Backscatter @ 24.00", 30° 5.25" collimator	3679 3253 3655 3139	
Backscatter @ 23.12", 40° 5.625" collimator		698 780 734 748
Backscatter @ 27.62", 50° 7.75" collimator	384 401 379 359	
Backscatter @ 26.50", 60° 8.312" collimator		166 194 175 156
Backscatterer position	428900 406000 371200 424900 411800 374600	303700 240900 299300 284700 271500 282700
Background @ 26.12", 30° 5.25" collimator		3048 3272 3107 2882
Background @ 25.25", 40° 5.75" collimator	38 39 37 39	
Background @ 31.37", 50° 9.625" collimator		96 95 101 88

LOCATION	TLD READING	
	SQUARE	ROD
Background @ 29.31", 60° 10.312" collimator	42	
	42	
	44	
	50	
Backscatter @ 26.12", 30° 5.25" collimator		5235
		5233
		4791
		4833
Backscatter @ 25.25", 40° 5.75" collimator	455	
	395	
	430	
	446	
Backscatter @ 31.37", 50° 9.625" collimator		104
		107
		102
		120
Backscatter @ 29.31", 60° 10.312" collimator	95	
	89	
	89	
	83	

LOCATION	TLD READING x 10^{-3}
Beam collimator exit	3609
	3610
	3960
	3718
	3793
	3716
	3700
	3527
	3551
	3915
Backscatterer position	870
	873
	885
	838
	860
	876
	887
	878
	826
	880
Beam collimator exit	4469
	4196
	4366
	4399
	4366
	4331
	4230
	4225
	4332
	4435
Beam collimator exit	2354
	2430
	2183
	2378
	2383
	2331
	2281
	2531
	2426
	2475

LOCATION	TLD READING x 10^{-3}
Backscatterer position	457
	449
	450
	470
	454
	470
	440
	443
	461
	443
Beam collimator exit	4627
	4707
	4402
	4673
	4633
	4402
	4714
	4435
	4501
	4633
Beam collimator exit	2340
	2251
	2426
	2281
	2510
	2365
	2417
	2460
	2407
	2448
Backscatterer position	431
	434
	468
	432
	422
	433
	437
	478
	426
	454

LOCATION	TLD READING x 10^{-3}
Beam collimator exit	3335
	3213
	3369
	3285
	3326
	3465
	3197
	3361
	3554
	3333

17.3.1.2 Iron

LOCATION	TLD READING SQUARE	TLD READING ROD
Backscatterer position	385700	283500
	382000	260300
	373400	289600
	387700	265500
	373300	301800
	339900	262300
Background @ 26.12", 30°		2162
5.25" collimator		1012
		2115
		1868
Background @ 25.25", 40°	34	
5.75" collimator	33	
	33	
	32	
Background @ 31.31", 50°		242
9.562" collimator		261
		256
		276
Background @ 29.25", 60°	50	
10.25" collimator	52	
	44	
	52	
Backscatter @ 26.13", 30°		5544
5.25" collimator		6137
		6601
		5589
Backscatter @ 25.25", 40°	286	
5.75" collimator	316	
	274	
	299	

LOCATION	TLD READING SQUARE	TLD READING ROD
Backscatter @ 31.38", 50^{o} 10.312" collimator		56
		55
		54
		58
Backscatter @ 29.31", 60^{o} 10.312" collimator	201	
	196	
	198	
	221	
Backscatter @ 26.94", 30^{o} 5.688" collimator		3315
		2720
		3083
		2999
Backscatter @ 26.00", 40^{o} 5.625" collimator	1690	
	1514	
	1607	
	1653	
Backscatter @ 26.50", 50^{o} 6.50" collimator		190
		214
		210
		212
Backscatter @ 30.00", 60^{o} 9.312" collimator	1690	
	1514	
	1607	
	1653	
Backscatterer position	900400	544700
	799400	631200
	844900	545200
	790600	581500
	782300	564000
	699300	549700
Background @ 24.12", 30^{o} 5.25" collimator	2149	
	1996	
	2212	
	2084	

LOCATION	TLD READING SQUARE	TLD READING ROD
Background @ 23.29", 40^{o} 5.688" collimator		220
		216
		243
		234
Background @ 27.50", 50^{o} 7.75" collimator	142	
	138	
	144	
	141	
Background @ 26.31", 60^{o} 8.312" collimator		93
		78
		85
		93
Backscatter @ 24.12", 30^{o} 5.25" collimator	1823	
	1710	
	1886	
	1681	
Backscatter @ 23.19", 40^{o} 5.688" collimator		202
		245
		235
		255
Backscatter @ 27.50", 50^{o} 7.75" collimator	148	
	146	
	162	
	153	
Backscatter @ 26.31", 60^{o} 8.312" collimator		54
		57
		48
		52

LOCATION	TLD READING x 10^{-3}
Beam collimator exit	2335
	2301
	2153
	2200
	2234
	2350
	2106
	2165
	2304
	2338
Backscatterer position	402
	411
	394
	392
	391
	413
	412
	414
	405
	417
Beam collimator exit	5167
	4985
	4607
	4644
	4364
	4736
	4401
	4629
	4955
	4805
Beam collimator exit	4203
	4161
	4530
	4399
	4057
	4533
	4255
	4609
	4356
	4468

LOCATION	TLD READING x 10^{-3}
Beam collimator exit	3960
	3985
	4207
	4057
	4200
	4113
	4059
	4061
	4212
	3806
Backscatterer position	859
	779
	826
	811
	1028
	778
	784
	832
	839
	787
Beam collimator exit	2898
	2803
	2898
	2763
	2921
	2831
	2911
	2820
	2862
	2772

17.3.2 Beam divergence

HORIZONTAL DISPLACEMENT (inches)	TLD READING RIGHT OF CENTER	TLD READING LEFT OF CENTER
16	480	
	544	
14	842	1849
	952	1773
12	2131	3195
	1670	2860
10	3975	4729
	4129	4416
8	5885	5262
	5426	5651
6	6472	5934
	6127	6023
4	6751	6952
	6789	6709
2	7297	6676
	7576	6978
1	7707	7630
	7498	7712

VERTICAL DISPLACEMENT (inches)	TLD READING ABOVE CENTER	TLD READING BELOW CENTER
16	2644 2380	3663 3517
14	3046 2977	4425 4385
12	3719 4237	5028 4629
10	5237 5031	5373 6248
8	5826 5996	6521 6429
6	7137 7158	7287 7209
4	7211 6917	7334 6987
2	7324 7298	7248 7498
Center	6181 7304	

17.4 10.5 MeV

17.4.1 Backscatter

17.4.1.1 Lead

LOCATION	TLD READING	
	SQUARE	ROD
Beam collimator exit	17660000	12305100
	18324100	13899600
	16629900	14485700
	17724400	15152800
	19311000	15299200
	18328100	13829100
Backscatterer position	3030500	2165400
	2789000	1935400
	2906200	2182000
	2665800	2084900
	2932900	2093900
	2680000	2360300
Background @ 41.31", 35° 6.687" collimator	8804	
	8590	
	7746	
	7623	
Background @ 38.06", 40° 6.00" collimator		925
		865
		879
		983
Background @ 37.81", 50° 11.062" collimator	203	
	190	
	189	
	190	
Background @ 36.19", 60° 11.938" collimator		97
		100
		107
		102

LOCATION	TLD READING SQUARE	TLD READING ROD
Beam collimator exit	29242500	22386500
	30817500	20709700
	29099000	20747600
	31044800	20511500
	29386700	23246300
	30655700	21458700
Backscatter @ 41.31", 35° 6.688" collimator	10082	
	10426	
	8100	
	10262	
Backscatter @ 38.06", 40° 6.00" collimator		2020
		2038
		1987
		1973
Backscatter @ 37.81", 50° 11.062" collimator	438	
	457	
	480	
	494	
Backscatter @ 36.19", 60° 11.938" collimator		373
		358
		345
		362
Beam collimator exit	17920700	12099200
	16397300	13602500
	16555900	14372600
	16775800	13228100
	18253000	13852500
	17377700	11729900
Backscatterer position	5282200	3859000
	4642600	3606000
	4650800	3628700
	4992300	3921600
	4395900	3788200
	5129700	3418500

LOCATION	TLD READING SQUARE	ROD
Background @ 41.31", 35° 6.688" collimator	7549	
	7152	
	7197	
	6599	
Background @ 38.06", 40° 6.00" collimator		1098
		1185
		1205
		1019
Background @ 37.81", 50° 11.062" collimator	189	
	208	
	191	
	199	
Background @ 36.19", 60° 11.938" collimator		36
		30
		38
		32
Beam collimator exit	10244300	7354600
	11017200	6690200
	9046100	7605800
	9347100	8084600
	10427900	7375200
	10059600	7196200
Backscatterer position	1810800	1367700
	1879200	1385400
	1648200	1301200
	1382900	1161400
	1859700	1391600
	1819800	1318200
Background @ 60.12", 30° 15.938" collimator		24
		23
		23
		20
Background @ 45.88", 40° 11.00" collimator		135
		144
		126
		142

LOCATION	TLD READING SQUARE	ROD
Background @ 41.06", 50° 11.688" collimator	45	
	44	
	49	
	54	
Background @ 38.38", 60° 13.75" collimator	16	
	17	
	18	
	18	
Beam collimator exit	7326900	4553100
	6926400	4481000
	6449900	5106700
	6683500	4804700
	6017000	5694500
	6536300	4430900
Backscatter @ 60.12", 30° 15.938" collimator		28
		25
		26
		29
Backscatter @ 45.88", 40° 11.00" collimator		163
		147
		174
		162
Backscatter @ 41.06", 50° 11.688" collimator	77	
	74	
	89	
	76	
Backscatter @ 38.38", 60° 13.75" collimator	44	
	43	
	46	
	48	
Beam collimator exit	8828500	1331800
	7900700	1052600
	9193500	1263500
	9254000	1330000

LOCATION	TLD READING SQUARE	TLD READING ROD
Background @ 60.12", 30° 15.938" collimator		24
		25
		27
		25
Background @ 45.88", 40° 11.00" collimator		130
		156
		144
		157
Background @ 41.06", 50° 11.688" collimator	53	
	53	
	50	
	54	
Backscatter @ 38.38", 60° 13.75" collimator	22	
	21	
	21	
	21	
Beam collimator exit	5306000	3481100
	4382600	3634500
	5191700	3332800
	5199400	3166700
	4810100	3856000
	5023000	3541000
Backscatterer position	974800	718200
	918000	589500
	781300	653700
	856600	637600
	865100	675500
	982100	738000
Background @ 58.69", 30° 15.938" collimator	21	
	25	
	22	
	24	
Background @ 44.38", 40° 11.00" collimator	302	
	294	
	281	
	254	

LOCATION	TLD READING SQUARE	TLD READING ROD
Background @ 39.44", 50^{o} 11.625" collimator		27
		26
		31
		31
Background @ 37.53", 60^{o} 13.688" collimator		9
		10
		11
		11
Beam collimator exit	9796700	6910700
	8361800	7020400
	10238200	7832300
	10822300	7330200
	10434000	6801200
	10262400	7461200
Backscatter @ 58.69", 30^{o} 15.938" collimator	45	
	46	
	47	
	44	
Backscatter @ 44.38", 40^{o} 11.00" collimator	376	
	375	
	438	
	425	
Backscatter @ 39.44", 50^{o} 11.625" collimator		88
		80
		78
		75
Backscatter @ 37.53", 60^{o} 13.688" collimator		37
		38
		34
		41

17.4.1.2 Iron

LOCATION	TLD READING SQUARE	TLD READING ROD
Beam collimator exit	15193900	10420400
	13945000	11724800
	13805700	10025500
	14254600	11539300
	15010900	11202900
	14173100	11443100
Backscatterer position	2381400	1700900
	2067500	1845900
	2241500	1651800
	2080500	1809300
	2167100	1732400
	2090400	1471100
Background @ 59.25", 30° 16.00" collimator	31	
	30	
	33	
	36	
Background @ 44.88", 40° 11.00" collimator	426	
	415	
	432	
	395	
Background @ 40.06", 50° 11.688" collimator		42
		37
		37
		38
Background @ 38.81", 60° 13.75" collimator		13
		15
		13
		11
Beam collimator exit	17877600	11242700
	17426600	11109900
	15207900	9996800
	16488100	11811000
	14324000	12960000
	14944500	12037000

LOCATION	TLD READING SQUARE	TLD READING ROD
Backscatter @ 59.25", 30° 16.00" collimator	49	
	52	
	46	
	52	
Backscatter @ 44.88", 40° 11.00" collimator	267	
	284	
	281	
	292	
Backscatter @ 40.06", 50° 11.688" collimator		71
		67
		72
		74
Backscatter @ 38.81", 60° 13.75" collimator		37
		35
		37
		35
Beam collimator exit	11921600	9126400
	12547100	8095600
	11545500	8823400
	11739300	9610900
Backscatterer position	1688300	1354500
	1889700	1279100
	1936400	1483900
	2000600	1167200
Background @ 59.25", 30° 16.00" collimator		26
		24
		22
		24
Background @ 44.88", 40° 11.00" collimator		169
		175
		165
		175

LOCATION	TLD READING	
	SQUARE	ROD
Background @ 40.06", 50° 11.688" collimator	53 50 54 58	
Background @ 38.81", 60° 13.75" collimator	20 24 23 21	
Beam collimator exit	10901600 11506000 10593300 11216100	7720800 8644400 7873800 8488500
Backscatter @ 59.25", 30° 16.00" collimator		26 31 29 33
Backscatter @ 44.88", 40° 11.00" collimator		159 187 177 183
Backscatter @ 40.06", 50° 11.688" collimator	94 82 82 80	
Backscatter @ 38.81", 60° 13.75" collimator	44 35 40 39	

17.4.1.3 Concrete

LOCATION	TLD READING	
	SQUARE	ROD
Beam collimator exit	6423700	4593000
	5285100	4226300
	4853600	3824800
	5498400	4437100
	5069700	4342800
	5170800	4319900
Backscatterer position	992800	692200
	1132900	703900
	1064700	761400
	984700	788500
	999100	672700
	936200	712400
Background @ 59.25", 30°	44	
16.00" collimator	33	
	40	
	38	
Background @ 44.88", 40°	226	
11.00" collimator	249	
	273	
	247	
Background @ 40.06", 50°		42
11.688" collimator		34
		37
		34
Background @ 38.81", 60°		15
13.75" collimator		15
		16
		16
Beam collimator exit	8934300	9863300
	12324300	9704200
	10853500	8688500
	9691200	8940000
	10719600	8374400
	11654700	7946300

LOCATION	TLD READING SQUARE	ROD
Backscatter @ 59.25", 30° 16.00" collimator	51	
	44	
	45	
	45	
Backscatter @ 44.88", 40° 11.00" collimator	238	
	212	
	222	
	261	
Backscatter @ 40.06", 50° 11.688" collimator		50
		50
		52
		50
Backscatter @ 38.81", 60° 13.75" collimator		26
		21
		25
		20
Beam collimator exit	11602600	8351900
	12111600	9134900
	10665400	7774800
	11083900	8983500
Backscatterer position	1741900	1502600
	1848700	1236100
	2054000	988800
	1869600	1135400
Background @ 59.25", 30° 16.00" collimator	33	
	31	
	27	
	28	
Background @ 44.88", 40° 11.00" collimator	187	
	217	
	208	
	179	

LOCATION	TLD READING SQUARE	TLD READING ROD
Background @ 40.06", 50° 11.688" collimator		31
		32
		37
		34
Background @ 38.81", 60° 13.75" collimator		12
		11
		13
		13
Beam collimator exit	3753900	3522100
	4599500	3698000
	3986600	3136500
	4249600	3440100
Background @ 59.25", 30° 16.00" collimator	31	
	28	
	30	
	30	
Background @ 44.88", 40° 11.00" collimator	200	
	191	
	198	
	209	
Background @ 40.06", 50° 11.688" collimator		34
		30
		34
		34
Background @ 38.81", 60° 13.75" collimator		13
		11
		14
		15
Beam collimator exit	12045300	9027100
	11189100	8379400
	10579900	9199000
	12654900	9781500

LOCATION	TLD READING SQUARE	TLD READING ROD
Backscatter @ 59.25", 30° 16.00" collimator	50	
	48	
	43	
	46	
Backscatter @ 44.88", 40° 11.00" collimator	242	
	225	
	248	
	209	
Backscatter @ 40.06", 50° 11.688" collimator		54
		52
		56
		48
Backscatter @ 38.81", 60° 13.75" collimator		26
		22
		23
		24
Beam collimator exit	12566400	10804100
	11573200	8531400
	11907500	10392200
	12226000	11114200
	11200700	8172900
	12729700	9158500
Backscatterer position	2123200	1512000
	1914900	1790100
	2210400	1519200
	2098000	1564500
	2036100	1721500
	2008000	1625300
Background @ 59.25", 30° 16.00" collimator	32	
	29	
	35	
	36	
Background @ 44.88", 40° 11.00" collimator	230	
	215	
	249	
	209	

LOCATION	TLD READING	
	SQUARE	ROD
Background @ 40.06", 50°		38
11.688" collimator		37
		37
		40
Background @ 38.81", 60°		15
13.75" collimator		11
		12
		14

17.4.2 Copper absorption in beam

DEPTH IN COPPER (inches)	TLD READING
0.0	57100
	57064
	59525
	62146
0.125	38049
	40497
	38354
	44394
0.25	43356
	42304
	44106
	40696
0.50	29291
	31003
	30111
	28917
0.75	22794
	25503
	23366
	24392
0.875	17428
	16651
	16749
	18198
1.00	19569
	17281
	19430
	18427
	13663
	13039
	13980
	12323

DEPTH IN COPPER (inches)	TLD READING
1.125	14407
	13593
	14027
	13796
1.25	16699
	16483
	14208
	14141
1.50	8855
	9453
	8994
	8912
	11619
	10575
	10863
	11805
1.75	8610
	7823
	8369
	8610
2.00	7462
	7790
	8144
	7935
2.50	5168
	5215
	5352
	5238
0.0	24446
	27186
	23500
	20089
0.0	26688
	25487
	25480
	22365

DEPTH IN COPPER (inches)	TLD READING
0.125	19994
	22068
	22436
	23764
0.25	18457
	18546
	17033
	19759
0.50	16021
	14143
	15207
	12508
0.75	10543
	9202
	10528
	9923
0.75	11539
	11994
	12978
	12157
0.875	9313
	8844
	8534
	8795
0.875	12082
	11747
	11158
	13567
1.00	9331
	9648
	9725
	8486

DEPTH IN COPPER (inches)	TLD READING
1.125	7633
	7671
	8227
	7161
1.125	10774
	9553
	10631
	11727
1.25	14595
	15907
	13587
	14181
1.25	6506
	7765
	6661
	8304
1.25	5760
	8183
	6331
	8255
1.50	6881
	6695
	6646
	5510
1.50	6293
	6374
	6190
	6084
1.75	5995
	4947
	5498
	4681

DEPTH IN COPPER (inches)	TLD READING
1.75	5535
	4838
	5655
	5296
2.50	3798
	3502
	4016
	3280
3.50	2262
	2163
	2247
	2464

BEAM MONITOR	TLD READING
1	28363
	28776
	19795
	27964
2	24949
	24148
	23413
	20948
3	18278
	16864
	19304
	18949
4	20926
	21686
	22816
	22054
5	21337
	21115
	23820
	23089
6	32239
	35034
	32786
	33579
7	24403
	23127
	22437
	19047

17.5 20 MeV

17.5.1 Lead Backscatter

LOCATION	TLD READING
Beam collimator exit	21528 21538
Backscatterer position	2621 2866
Background @ 12.0", 22.5°	43 40
Background @ 12.0", 45°	36 38
Background @ 12.0" 67.5°	37 37
Beam collimator exit	50052 51551
Backscatter @ 12.0", 22.5°	115 119
Backscatter @ 12.0", 45°	96 93
Backscatter @ 12.0", 67.5°	76 80

17.5.2 Lead - infinite size

17.5.2.1 12" square, thickness as designated

Background and backscatter measurements
@ 10.0", 67.5°

LOCATION	TLD READING
Beam collimator exit	11255
	11993
	11904
Background	34
	34
	34
Beam collimator exit	18244
	18919
	18916
Backscatter, 0.15" thick	46
	46
	48
Beam collimator exit	16083
	16796
	16253
Backscatter, 0.42" thick	46
	47
	45
Beam collimator exit	16679
	15381
	16393
Backscatter, 0.57" thick	44
	44
	45
Beam collimator exit	15726
	16307
	15253

LOCATION	TLD READING
Backscatter, 0.86" thick	45
	45
	43
Beam collimator exit	13061
	12146
	14174
Backscatter, 1.15" thick	42
	43
	44
Beam collimator exit	15806
	16941
	15639
Backscatter, 1.42" thick	45
	46
	47
Beam collimator exit	16442
	16881
	16488
Backscatter, 1.72" thick	47
	45
	46
Beam collimator exit	17258
	17147
	15385
Backscatter, 1.81" thick	47
	47
	48
Beam collimator	17469
	15879
	16803
Backscatter, 2.50" thick	47
	47
	50

LOCATION	TLD READING
Beam collimator exit	22031
	20962
	23097
Background	34
	33
	35

17.5.2.2 4.0" thick, area as designated

Background and backscatter measurements
@ 10.0", 67.5°

LOCATION	TLD READING
Beam collimator exit	10130
	10864
	10480
Background	38
	34
	32
Beam collimator exit	24819
	24206
	24368
Backscatter, 4.0" square	54
	55
	54
Beam collimator exit	13787
	14275
	13989
Background	60
	57
	59
Beam collimator exit	32048
	35767
	35383
Backscatter, 6.0" square	87
	86
	84
Beam collimator exit	24843
	27299
	25039
Background	39
	41
	44

LOCATION	TLD READING
Beam collimator exit	39737
	38883
	39883
Backscatter, 8.0" square	70
	73
	74
Beam collimator exit	18959
	16176
	18726
Background	25
	30
	28
Beam collimator exit	37433
	43698
	41218
Backscatter, 10.0" square	63
	63
	66
Beam collimator exit	13087
	13609
	12722
Background	34
	33
	34
Beam collimator exit	31428
	34260
	31282
Backscatter, 12.0" square	59
	67
Beam collimator exit	23593
	23720
	22409

LOCATION	TLD READING
Background	37
	38
	38
Beam collimator exit	40587
	37074
	41238
Backscatter, 14" square	69
	65
	72

17.6 30 MeV

17.6.1 Lead - infinite size

17.6.1.1 4.0" thick, area as designated

Background and backscatter measurements @ 10.0", 67.5°

LOCATION	TLD READING
Beam collimator exit	40519 39086 40072
Background	556 548 544
Beam collimator exit	88644 78352 74421
Backscatter, 4.0" square	825 754 733
Beam collimator exit	48000 48000 47973
Background	20 17 18
Beam collimator exit	90399 82734 82429
Backscatter, 6.0" square	86 70 77

LOCATION	TLD READING
Beam collimator exit	25908
	33677
	32829
Background	557
	585
	586
Beam collimator exit	74749
	76408
	82676
Backscatter, 8.0" square	704
	680
	696
Beam collimator exit	30201
	32691
	35421
Background	652
	644
	631
Beam collimator exit	64450
	62447
	68474
Backscatter, 10" square	676
	663
	663
Beam collimator exit	37594
	37548
	40205
Background	594
	603
	608
Beam collimator exit	51130
	57250
	55916

LOCATION	TLD READING
Backscatter, 12" square	685
	678
	668
Beam collimator exit	30192
	27610
	28660
Background	872
	699
	716
Beam collimator exit	45095
	51497
	48551
Backscatter, 14" square	358
	1062
	1063

17.6.2 Beam cross-section

HORIZONTAL DISPLACEMENT (inches)	TLD READING LEFT OF CENTER	TLD READING RIGHT OF CENTER
2.00	549	
1.50		502
1.19	2924	
0.75		1296
0.38	3921	
0.19		3160
Center	3386	

VERTICAL DISPLACEMENT (inches)	ABOVE CENTER	BELOW CENTER
2.00		574
1.50	585	
1.19		1180
0.56	2635	
0.75		3239
0.44	3628	

17.7 40 MeV

17.7.1 Lead backscatter

LOCATION	TLD READING
Beam collimator exit	55982 51498
Backscatterer position	6506 6362
Background @ 12.0", 22.5^{o}	43 44
Background @ 12.0", 45^{o}	40 43
Background @ 12.0", 67.5^{o}	41 45
Beam collimator exit	89616 93046
Backscatter @ 12.0", 22.5^{o}	153 158
Backscatter @ 12.0", 45^{o}	113 120
Backscatter @ 12.0", 67.5^{o}	86 82

17.7.2 Lead - infinite size

17.7.2.1 12.0" square, thickness as designated

Background and backscatter measurements @ 10.0", 67.5°

LOCATION	TLD READING
Beam collimator exit	31741 35690 30545
Background	22 21 23
Beam collimator exit	39941 39604 39835
Backscatter, 0.15" thick	42 44 42
Beam collimator exit	46973 45341 51020
Backscatter, 0.36" thick	54 57 59
Beam collimator exit	49006 48373 49690
Backscatter, 0.57" thick	59 59 61
Beam collimator exit	43699 43817 39169

LOCATION	TLD READING
Backscatter, 0.86" thick	59
	54
	56
Beam collimator exit	43810
	40618
	39892
Backscatter, 1.15" thick	49
	54
	55
Beam collimator exit	46309
	43357
	47239
Backscatter, 1.42" thick	57
	58
	56
Beam collimator exit	51367
	56323
	52752
Backscatter, 1.72" thick	64
	62
	61
Beam collimator exit	55867
	55275
	53278
Backscatter, 2.08" thick	61
	60
	60
Beam collimator exit	48948
	47355
	50388
Backscatter, 2.57" thick	60
	59
	58

LOCATION	TLD READING
Beam collimator exit	50150
	49913
	51811
Background	23
	23
	24

17.7.2.2 4.0" thick, area as indicated

LOCATION	TLD READING
Beam collimator exit	163105 153437 161074
Background	51 51 55
Beam collimator exit	163129 157548 172490
Background	53 53 55
Beam collimator exit	183929 155932 160574
Backscatter, 4.0" square	178 166 167
Beam collimator exit	183124 192225 173896
Background	61 59 56
Beam collimator exit	190277 182371 175496
Backscatter, 6.0" square	220 218 235

LOCATION	TLD READING
Beam collimator exit	44997
	37150
	45530
Background	28
	34
	29
Beam collimator exit	75728
	89594
	88461
Backscatter, 8.0" square	93
	94
	98
Beam collimator exit	60961
	54860
	56489
Background	559
	447
	33
Beam collimator exit	172964
	192693
	175334
Backscatter, 10.0" square	224
	212
	236
Beam collimator exit	39309
	39917
	36748
Background	19
	20
	20
Beam collimator exit	190843
	157822
	178053

LOCATION	TLD READING
Backscatter, 12.0" square	130
	136
	157
Beam collimator exit	62502
	57142
	70865
Background	19
	22
	26
Beam collimator exit	172333
	187764
	203856
Backscatter, 14.0" square	178
	171
	188

17.7.3 Beam cross-section

HORIZONTAL DISPLACEMENT (inches)	TLD READING	
	LEFT OF CENTER	RIGHT OF CENTER
2.00	310	
1.56	722	773
1.19	7525	
0.75		1150
0.38	9435	8409
0.19		9184
Center	9291 9091	

VERTICAL DISPLACEMENT (inches)	ABOVE CENTER	BELOW CENTER
2.38	282	
1.56		703
1.19	1054	
0.81	4119	
0.75		5058
0.38	8262	8550
0.19		9268

17.8 60 MeV

17.8.1 Lead backscatter

LOCATION	TLD READING
Beam collimator exit	111316 110444
Backscatterer position	9025 8136
Background @ 12.0", 22.5^o	48 55
Background @ 12.0", 45^o	44 43
Background @ 12.0", 67.5^o	40 47
Beam collimator exit	275054 272831
Backscatter @ 12.0", 22.5^o	382 360
Backscatter @ 12.0", 45^o	304 270
Backscatter @ 12.0", 67.5^o	166 160

17.8.2 Lead - infinite size

17.8.2.1 12.0" square, thickness as designated

Background and backscatter measurements @ 10.0", 67.5°

LOCATION	TLD READING
Beam collimator exit	30646 29827 28822
Background	38 37 36
Beam collimator exit	65507 67690 70239
Backscatter, 0.15" thick	71 77 76
Beam collimator exit	98671 98107 101194
Backscatter, 0.36" thick	102 102 104
Beam collimator exit	100049 95412 105191
Backscatter, 0.57" thick	110 109 104
Beam collimator exit	86741 75480 91520

LOCATION	TLD READING
Backscatter, 0.79" thick	97
	101
	92
Beam collimator exit	65329
	60036
	66151
Backscatter, 1.15" thick	89
	90
	81
Beam collimator exit	69499
	64865
	66368
Backscatter, 1.42" thick	88
	88
	91
Beam collimator exit	76791
	80212
	76251
Backscatter, 1.72" thick	99
	104
	98
Beam collimator exit	77287
	72870
	73558
Backscatter, 2.10" thick	96
	99
	93
Beam collimator exit	81958
	79575
	81459
Backscatter, 2.57" thick	92
	90
	94

LOCATION	TLD READING
Beam collimator exit	73017
	71364
	69466
Background	42
	43
	42

17.8.2.2 4.0" thick, area as designated

LOCATION	TLD READING
Beam collimator exit	97084 85156 90687
Background	107 109 108
Beam collimator exit	186002 163199 188759
Backscatter, 4.0" square	236 224 221
Beam collimator exit	19536 20349 13676
Background	314 313 330
Beam collimator exit	184787 179372 179721
Backscatter, 6.0" square	434 419 422
Beam collimator exit	133378 137203 128563
Background	107 105 104

LOCATION	TLD READING
Beam collimator exit	181783
	177818
	192393
Backscatter, 8.0" square	214
	220
	231
Beam collimator exit	9220
	7260
	2693
Background	520
	469
	583
Beam collimator exit	225300
	208864
	219958
Backscatter, 10.0" square	674
	571
	540
Beam collimator exit	76575
	79163
	82820
Background	108
	112
Beam collimator exit	149123
	176767
	181433
Backscatter, 12.0" square	239
	242
	221
Beam collimator exit	85081
	80621
	76680

LOCATION	TLD READING
Background	283
	290
	332
Beam collimator exit	200714
	180116
	181880
Backscatter, 14.0" square	155
	144
	137

17.8.3 Beam cross-section

HORIZONTAL DISPLACEMENT (inches)	TLD READING LEFT OF CENTER	TLD READING RIGHT OF CENTER
2.00		1925
1.56	17252	2999
1.19	22287	
0.75		4097
0.38	24288	5562
0.19		19073
Center	22667 20145	

VERTICAL DISPLACEMENT (inches)	ABOVE CENTER	BELOW CENTER
2.38	971	
1.56	3071	3239
1.19	4372	
0.81	18735	16972
0.38	19736	20443
0.19		21388

17.9 TLD annealing procedures

17.9.1 Annealing cycle

		TLD READING
Pre-anneal:	1 hour @ 400° C	678
	2 hours @ 100° C	729
Post-anneal:	10 min. @ 100° C	727
Pre-heat:	None	701
Read-out:	15 sec. @ 250° C	749
		744
		713
		689
		753
		732
		729
		724
		689
		728
		745
		730
		742
		663
		703
		719
		705
		739
		677
		724
		690

17.9.2 Annealing cycle

		TLD READING
Pre-anneal:	1 hour @ 400°C	709
	2 hours @ 100°C	678
Post-anneal:	10 min. 100°C	733
Pre-heat:	7 sec. @ 165°C	744
Read-out:	15 sec. @ 250°C	693
		737
		691
		697
		718
		587
		752
		733
		722
		670
		704
		698
		712
		716
		715
		709
		592
		708
		716
		584
		702

17.9.3 Annealing cycle

		TLD READING
Pre-anneal:	1 hour @ 400°C	727
	2 hours @ 100°C	723
Post anneal:	None	742
Pre-heat:	7 sec. @ 165°C	700
Read-out:	15 sec. @ 250°C	700
		705
		698
		729
		756
		672
		741
		748
		703
		701
		721
		687
		662
		737
		724
		676
		704
		699
		706
		705

17.9.4 Annealing cycle

		TLD READING
Pre-anneal:	1 hour @ 400°C	712
	24 hours @ 80°C	703
Post-anneal:	None	722
Pre-heat:	None	677
Read-out:	15 sec. @ 250°C	703
		711
		717
		684
		721
		716
		675
		707
		726
		727
		691
		717
		683
		668
		704
		737
		704
		721
		673
		738
		673

17.9.5 Annealing cycle

		TLD READING
Pre-anneal:	1 hour @ 400°C	723
	24 hours @ 80°C	744
Post-anneal:	None	750
Pre-heat:	7 sec. @ 165°C	713
Read-out:	15 sec. @ 250°C	703
		702
		740
		689
		680
		707
		683
		718
		699
		696
		705
		698
		715
		703
		720
		662
		713
		711
		684

17.9.6 Annealing cycle

		TLD READING
Pre-anneal:	1 hour @ 400°C	715
	24 hours @ 80°C	694
Post-anneal:	10 min. @ 100°C	671
Pre-heat:	None	733
Read-out:	15 sec. @ 250°C	697
		700
		688
		669
		707
		692
		698
		721
		670
		698
		713
		638
		702
		680
		714
		681
		706
		693
		719
		681
		705

17.9.7 Annealing cycle

		TLD READING
Pre-anneal:	1 hour @ 400°C	682
	24 hours @ 80°C	700
Post-anneal:	10 min. @ 100°C	713
Pre-heat:	7 sec. @ 165°C	654
Read-out:	15 sec @ 250°C	716
		694
		716
		585
		698
		592
		677
		665
		677
		684
		705
		690
		652
		633
		689
		672
		675
		656
		727
		685
		668

17.9.8 Annealing cycle

		TLD READING
Pre-anneal:	1 hour @ 400°C	723
	24 hours @ 80°C	744
Post-anneal:	None	750
Pre-heat:	7 sec. @ 165°C	713
Read-out:	15 sec. @ 250°C	703
		702
		740
		689
		680
		707
		683
		718
		699
		696
		705
		698
		715
		703
		720
		662
		713
		711
		684

17.9.9 Annealing cycle

		TLD READING
Pre-anneal:	1 hour @ 400°C	983
Post-anneal:	10 min. @ 100°C	944
Pre-heat:	None	967
Read-out:	15 sec. @ 250°C	960
		960
		929
		967
		928
		957
		950
		894
		990
		962
		1003
		962
		999
		956
		967
		974
		985
		920
		1004
		962
		965
		1015

17.9.10 Annealing cycle

		TLD READING
Pre-anneal:	1 hour @ 400°C	965
Post-anneal:	10 min. @ 100°C	918
Pre-heat:	7 sec. @ 165°C	912
Read-out:	15 sec. @ 250°C	959
		935
		947
		898
		1008
		954
		975
		967
		982
		862
		931
		924
		947
		977
		909
		829
		952
		938
		882
		923
		897
		926

17.9.11 Annealing cycle

		TLD READING
Pre-anneal:	1 hour @ 400°C	992
Post-anneal:	None	936
Pre-heat:	7 sec. @ 165°C	973
Read-out:	15 sec. @ 250°C	918
		928
		910
		931
		959
		934
		944
		921
		958
		914
		817
		905
		865
		942
		924
		941
		939
		978
		978
		972
		924
		888

17.9.12 Annealing cycle

		TLD READING
Pre-anneal:	1 hour @ 400°C	939
Post-anneal:	None	961
Pre-heat:	7 sec. @ 165°C	951
Read-out:	15 sec. @ 250°C	1026
		962
		972
		926
		970
		895
		1005
		1011
		956
		1018
		980
		966
		962
		983
		913
		972
		933
		880
		947
		909
		972
		980

In any set of experimentally obtained data, there exist points sufficiently far from the mean to be suspect. The discarding of suspect values without some firm and repeatable criteria might lead to loss of real information. The small number of measurements (four to eight) taken at each point during any one run, preclude the use of standard deviation or chi square testing for the rejection of extreme values.

Chauvenet's Criterion (128), which states: "any reading of a series of 'n' readings shall be rejected when the magnitude of its deviation from the mean of the series is such that the probability of occurrence of all deviations that large, or larger, does not exceed $\frac{1}{2n}$ ", was used in this dissertation. Chauvenet's Criterion for rejection (or more precisely, Chauvenet's Ratio) was applied to each set of TLD readings obtained and to final albedo calculations before using or reporting an average value. This procedure allows for the checking of values which appear to differ greatly from the average.

J. ERROR ANALYSIS

J.1 STATISTICAL VARIATION OF THERMOLUMINESCENT DOSIMETERS

A number of LiF crystals exposed to the same radiation dose do not emit the same amount of light upon read-out. The degree of this variance and its dependence upon the crystal's prior history are discussed in Appendix F. The error limits discussed there apply to a rather larger number of crystals exposed in each setting than was possible in the experiments conducted (Section 5). Also those limits apply to a given set of readings and the data gained by experiment required the subtraction of background, beam normalization, etc., thus possibly combining errors. Through standard techniques (reviewed below) and the method of data reduction discussed in Section 6, total variance may be calculated.

$$\left[\sigma(N_1 \pm N_2 \pm \ldots)\right]^2 = \left[\sigma(N_1)\right]^2 + \left[\sigma(N_2)\right]^2 + \ldots\ldots \qquad \text{Eq. J.1}$$

$$\left[\frac{\sigma\left(\frac{N_1}{N_2}\right)}{\left(\frac{N_1}{N_2}\right)}\right]^2 = \left[\frac{\sigma(N_1 N_2)}{N_1 N_2}\right]^2$$

$$\approx \left[\frac{\sigma(N_1)}{N_1}\right]^2 + \left[\frac{\sigma(N_2)}{N_2}\right]^2 \qquad \text{Eq. J.2}$$

$$\sigma_{\bar{x}} = \frac{\sigma}{\sqrt{n}} \qquad \text{Eq. J.3}$$

Putting Eq. 6.7 in symbols more convenient for this appendix, and leaving the energy absorption coefficient corrections for discussion in Section J.3

$$a_D \simeq \frac{DR - (DBG)\left(\frac{BCS}{BCG}\right)}{DI\left(\frac{BCS}{BCG}\right)\Omega} \qquad \text{Eq. J.4}$$

where:

a_D = the differential albedo

DR = measured reflected dose

DBG = measured background dose

BCS = measured dose at beam collimator exit during backscatter run

BCG = measured dose at beam collimator exit during background run

DI = measured dose at backscatterer position

Ω = the effective solid angle viewed

In each case the measured dose is the average of some number of readings and has associated with it some variance. The variance of α_D may then be calculated.

Rearranging Eq. J.4 and leaving the error associated with Ω for discussion in Section J.2:

$$\alpha_D \propto \frac{DR\left(\frac{BCG}{BCS}\right) - DBG}{DI} \qquad \text{Eq. J.5}$$

and adopting, for this development, the notation:

$$\frac{\sigma(N)}{N} = f\,\sigma(N) \qquad \text{Eq. J.6}$$

then

$$\left[f\,\sigma(\alpha_D)\right]^2 = \left[f\,\sigma\left(DR\left[\frac{BCG}{BCS}\right] - DBG\right)\right]^2 + \left[f\,\sigma(DI)\right]^2 \qquad \text{Eq. J.7}$$

$$\left[\sigma\left(DR\left[\frac{BCG}{BCS}\right] - DBG\right)\right]^2 = \left[\sigma\left(DR\left[\frac{BCG}{BCS}\right]\right)\right]^2 + \left[\sigma(DBG)\right]^2$$

Eq. J.8

$$\left[f\,\sigma\left(DR\left[\frac{BCG}{BCS}\right]\right)\right]^2 = \left[f\,\sigma(DR)\right]^2 + \left[f\,\sigma\left(\frac{BCG}{BCS}\right)\right]^2 \qquad \text{Eq. J.9}$$

$$\left[f\,\sigma\left(\frac{BCG}{BCS}\right)\right]^2 = \left[f\,\sigma(BCG)\right]^2 + \left[f\,\sigma(BCS)\right]^2 \qquad \text{Eq. J.10}$$

$$\sigma(\alpha_D) = \alpha_D \left\{ \left[\frac{\sigma(DI)}{DI}\right]^2 + \frac{\left[\sigma(DBG)\right]^2}{\left[DR\left(\frac{BCG}{BCS}\right) - DBG\right]^2} + \frac{\left[DR\left(\frac{BCG}{BCS}\right)\right]^2 \left[\left\{\frac{(DR)}{DR}\right\}^2 + \left\{\frac{(BCG)}{BCG}\right\}^2 + \left\{\frac{(BCS)}{BCS}\right\}^2\right]}{\left[DR\left(\frac{BCG}{BCS}\right) - DBG\right]^2} \right\}^{\frac{1}{2}}$$

Eq. J.11

This would be the standard deviation of one measurement of the differential albedo due to variation in TLD readings. As each albedo was measured at least twice and generally several times, Eq. J.3 was used to obtain the standard deviation of the average albedo due to dosimeter variation. The percent of this deviation ran from 3.8% for iron @ 2.0 MeV to 17.6% for lead @ 7.0 MeV.

J.2 PHYSICAL MEASUREMENTS

Measurement of collimator length and detector to slab distance determines the effective solid angle and viewed area used in the albedo calculation. The collimators used in this work were milled to the nearest thousandth of an inch. Variation of even five thousandths compared to the collimator dimensions would still introduce far smaller error than discussed in Section J.1. The detector to scattering center distance was made with a standard steel tape measure and checked against a second tape. The author feels an error of 0.25" in 25.0" (1.0%) would be difficult to pass unnoticed. An error of this magnitude in the measurement of dosimeter to scatter surface would cause an error of ±2.0% in the resulting calculated albedo.

An error in measuring the angular relationship of the collimator axis to the scattering slab would result in a changed area relationship and the measurement of a slightly different albedo than intended. The angles reported in this dissertation were measured from a protractor of 12.0" radius which had been checked against an engineering compass. At

12.0" the linear separation of 10^{O} is approximately 1.094" or 0.109" per degree. The author feels alignment to be well within 10% or one degree. Neither albedo nor the trigonometric relationships are rapidly varying between 30 and 60 degrees (the range of interest in this dissertation). The error in measured albedo due to ±10% alignment is considerably smaller than that due to ±1.0% distance measurement (±0.2%).

J.3 ANALYTICAL

Considered here are errors due to false assumptions, theoretical approximations and calculational mistakes. The major assumptions employed are that of semi-infinite slab area, uniform irradiation of the slab surface, and the energy absorption coefficient corrections to the dose measurements made. Extreme care has been taken to verify the required slab size by reference to previous works on this subject (Section 5.1) and experimental verification of a number of points (Appendix G). Uniform irradiation of the viewed area is demonstrated for nearly every case (Appendix H) and the one case in which uniform irradiation of the entire slab is questionable (i.e. concrete) is discussed in Appendix H.

Theoretical approximations made in the handling of the data are discussed in Appendix B and Appendix C and Section 6. The error involved in the point detector approximation is shown to be much below others of this section. The validity of applying computer generated spectra for a collimator penetration effect correction may be debated. A comparison of the spectral data given in Appendix D and of the generated spectra to the literature cited in Section 2 indicate the computer spectra certainly to be reasonable. To apply no correction would be to knowingly over-estimate the real collimator length. The corrections made decrease the albedos by 2.0% (lead @ 2.0 MeV) to 11.0% (iron @ 2.0 MeV). These values would certainly exceed the error made by performing the correction.

The mass energy-absorption coefficient correction to the absorbed dose used in Section 6 is based on both the input and reflected spectra. The coefficients of LiF and water follow very closely throughout the energy range of interest in this dissertation and are essentially identical above a few hundred KeV (Appendix E). Even with the wide variation of input spectra discussed in Appendix D the ratio of mass energy-absorption coefficients,

$$\left[\frac{\left(\frac{\mu_{en}}{\rho}\right)_{H_2O}}{\left(\frac{\mu_{en}}{\rho}\right)_{LiF}}\right]$$ varies only on the order of ±6% for any given bremsstrahlung maximum energy spectra. However, the

$$\left[\frac{\left(\frac{\mu_{en}}{\rho}\right)_{Slab}}{\left(\frac{\mu_{en}}{\rho}\right)_{LiF}}\right]$$ ratio varies greatly with the low energy portion of the energy spectra, as a glance at plots of the mass energy-absorption coefficients for the various reflecting materials would indicate. This variance is far too great to include with the measurements to which it is applied and leave any meaning in the result. Therefore, until more reliable information becomes available as to the low energy make-up of flash x-ray bremsstrahlung spectra, no error limits can realistically be assigned those measurements plotted in Figures 17 through 27.

It is also assumed that the doses measured at each point are comparable (since they are manipulated algebraically together). The TLD packaging used (~0.14 gm/cm^2) is not thick enough to create charged particle equilibrium

(CPE) to high (>1 MeV) energy photons. At the backscatter energies, the thickness of packaging is adequate. At 2.0, 3.5, and 10.5 MeV, the incident beam contains such a large number of low energy photons that a true charged particle equilibrium cannot be achieved. The absorption of low energy photons predominates the electron build-up. The packaging chosen, therefore, is desirable as the surface dose most nearly approximates the "equilibrium dose". However, the more heavily filtered 7.0 MeV incident beam does indeed show a build-up with increasing depth. Work at Kirtland (Figure 87) by EG&G indicates an "equilibrium dose" is reached at about 1.0 gm/cm^2. The measured dose is at about 0.965 of that and has been corrected accordingly, resulting in a 3.5% lowering of the albedo at that energy.

Any time a large number of computations are made, the very real possibility of human error exists. Each calculation made was repeated at a separate time and any suspect resultant values (as pointed up by the Chauvenet ratio test) were again checked. Due to the check made for extreme values (Appendix I) the author believes any prejudicing of reported values due to computational errors has been kept to a minimum.

Variance of the bremsstrahlung peak energy is

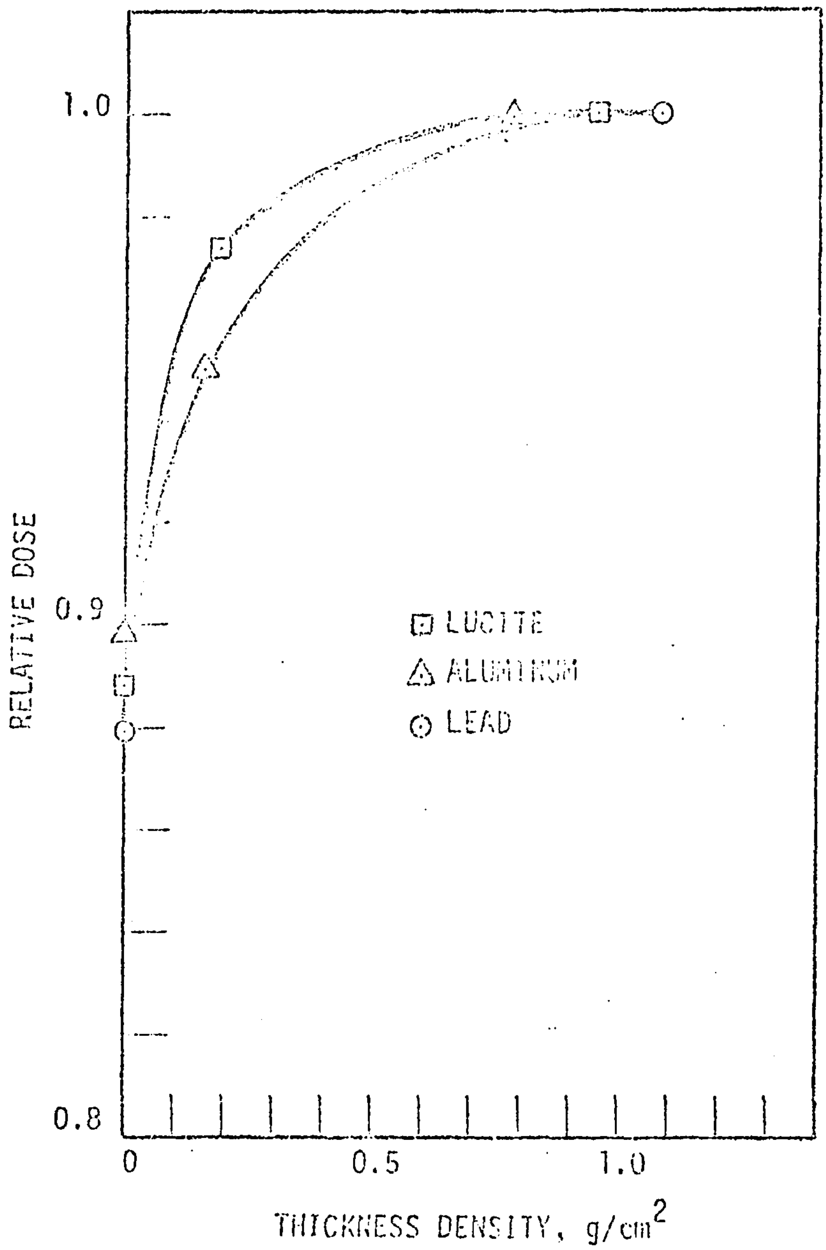

Figure 87 Charged particle equilibrium

discussed in Section 5 and results of that variance shown in Section 6.

The error bars reported in Section 6 are a statistical combination of the limits discussed in this appendix.

K. MONTE CARLO PROGRAM

The program used in this dissertation is based on a Monte Carlo adaptation of Adams and Mehl (106) used for calculating the deposition of energy by photons. The original program includes fluorescence and Compton scattering, but neglects pair production interactions. Since, at the energies of interest in this dissertation, pair production interactions are quite important, it was necessary to add a sub-routine to handle this item. Mr. K. G. Adams of Sandia Corporation was extremely helpful in adding this feature to the existing Monte Carlo program.

The program, in its updated form, is somewhat limited as to material inputs, and requires certain material data to be included in the update patch not regularly part of the input. Otherwise input is as specified in (106), allowing a wide choice of input energy (or number) spectra and various output forms.

The update to the original program (106) is included here and is for the CDC 6600 computer.

```
*IDENT KOP
*INSERT,SLAB.1191
      SIGPPT(KK+1,J) = 1.E+10
*INSERT,SLAB.31
      COMMON/PAIR/AA(8,20),ELOSS,NPAIR,IPP,IPPFL,
     1SIGPP(20),PAIRA(20),NANNIH
*DELETE,SLAB.37
     1,MALOG,IPRINT,IMP,IPP
*INSERT,SLAB.259
      NPAIR=0
      NANNIH=0
      ELOSS=0.
*INSERT,SLAB.387
      IF(IPP.NE.0) WRITE(3,7000) (SIGPP(I),I=1,NMAT)
 7000 FORMAT(/(7H SIGPP=E12.4))
      ELOSS=ELOSS*511.006
      IF(IPP.NE.0) WRITE(3,7001) NPAIR,ELOSS,NANNIH
 7001 FORMAT(/* NUMBER PAIR PRODUCTION*I10,5X*TOTAL ENERGY LOSS*
     1,F10.3,5X*ANNIHILATION PHOTONS*,I10)
      ELOSS=ELOSS/511.006
*INSERT,SLAB.389
      IF(IPP.NE.0) CALL PAIRCA(I)
*INSERT,SLAB.736
      IF(IPP.NE.0) CALL PAIRCA(M)
*INSERT,SLAB.781
      COMMON/PAIR/AA(8,20),ELOSS,NPAIR,IPP,IPPFL,
     1SIGPP(20),PAIRA(20),NANNIH
      DIMENSION XARRAY(1)
      EQUIVALENCE(X2,XARRAY(1))
*INSERT,SLAB.799
      E0=E1
      IF(E1-2.) 218,219,224
  224 IF(IPP) 218,218,220
  220 CALL SPELL1
      IF(SIGPP(M)/SIGT(M)-RAN1) 218,221,221
  221 E1=1.
      IF(E0-E1) 223,23,23
  223 IPPFL=2
      DO 222 I=1,16
  222 PAIRA(I)=XARRAY(I)
      PAIRA(17)=M
      CALL SPELL1
      COANG=1.-2.*RAN1
      ELOSS=ELOSS+(E0-E1*2)
      NANNIH=NANNIH+1
      NPAIR=NPAIR+1
      RETURN
 218  CONTINUE
*INSERT,SLAB.946
      COMMON/PAIR/AA(8,20),ELOSS,NPAIR,IPP,IPPFL,
     1SIGPP(20),PAIRA(20),NANNIH
*DELETE,SLAB.954
      IF(IPPFL-1) 8,8,9
    9 IPPFL=IPPFL-1
      PAIRA(16)=-GAM2
    8 RETURN
```

```
*INSERT,SLAB.967
      COMMON/PAIR/AA(8,20),ELOSS,NPAIR,IPP,IPPFL,
     1SIGPP(20),PAIRA(20),NANNIH
      DIMENSION XARRAY(1)
      EQUIVALENCE(X2,XARRAY(1))
      IF(IPPFL) 5003,5003,5002
 5002 DO 5004 I=1,16
 5004 XARRAY(I)=PAIRA(I)
      M=PAIRA(17)
      NANNIH=NANNIH+1
      IPPFL=IPPFL-1
      E1=1.
      RETURN
 5003 CONTINUE
*INSERT,SLAB.919
      IF(IPP.NE.0) CALL PAIRCA(I)
*INSERT,SLAB.133
      COMMON/PAIR/AA(8,20),ELOSS,NPAIR,IPP
*INSERT,SLAB.1097
      IF(IPP.NE.0) CALL PAIRPD(NOMAT)
*INSERT,SLAB.1764
      SUBROUTINE PAIRPD(NOMAT)
      COMMON/TEMPCO/TEMP(4114),AMT(30,20),NOAT(30)
C THIS SUBROUTINE CALCULATES PAIR PRODUCTION CROSS SECTIONS FROM          PAI   2
C COEFFICIENTS STORED ON CROSS SECTION DATA TAPE                         PAI   3
      COMMON/TRANS/UMU,UMUPE,UMUAB,EP,NL
      COMMON/1/B(8,20)
      COMMON/PAIR/AA(8,20),ELOSS,NPAIR,IPP,IPPFL,
     1SIGPP(20),PAIRA(20),NANNIH
C READ COEFFICIENTS FROM DATA TAPE                                       PAI   6
      DATA(NAME1=8HPAIR PRO)                                             PAI   7
      REWIND 4                                                           PAI   8
1     READ (4,2) NAME                                                    PAI   9
2     FORMAT (A8)                                                        PAI  10
      IF (NAME.NE.NAME1) GO TO 1                                         PAI  11
      DO 7 J=1,NL
    3 READ(4,4) NO,(B(I,J),I=1,7)
4     FORMAT (I3,7E11.3)                                                 PAI  14
      READ(4,5) B(8,J)
5     FORMAT (E10.3)                                                     PAI  16
      IF (NO-NOAT(J)) 3,7,6                                              PAI  17
6     REWIND 4                                                           PAI  18
      GO TO 1                                                            PAI  19
7     CONTINUE                                                           PAI  20
      DO 20 I=1,8
      DO 20 J=1,20
   20 AA(I,J)=0
      DO 25 I=1,NL
      DO 25 J=1,NOMAT
      DO 25 K=1,8
   25 AA(I,K)=AA(I,K)+AMT(J,I)*B(K,J)
      RETURN                                                             PAI  21
C CALCULATE PAIR PRODUCTION CROSS SECTION                                PAI  22
      ENTRY PAIRCA                                                       PAI  23
      FAC=(EP-1022.012)                                                  PAI  24
      IF (FAC) 8,10,10                                                   PAI  25
```

```
 8       UPP=0                                                PAI  26
      9 SIGPP(NL)=UPP
         RETURN
 10      IF (EP-1500.) 11,11,12                               PAI  28
     11 UPP = AA(NL,8)*FAC**2
         GO TO 9                                              PAI  30
 12      UPP=0                                                PAI  31
         FAC=SQRTF(FAC)                                       PAI  32
         DO 13 I=1,7                                          PAI  33
     13 UPP = UPP + AA(NL,I)*FAC**I
         UPP=UPP/(1.+1.7E-13*FAC**6)                          PAI  35
         GO TO 9                                              PAI  36
         END                                                  PAI  37-
*COMPILE SLAB
```

```
SLAB            COMMON/PAIR/AA(8,20),ELOSS,NPAIR,IPP,IPPFL,           KOR     00001    ACTIVATED
SLAB           1SIGPP(20),PAIRA(20),NANNIH                            KOR     00002    ACTIVATED
SLAB           1,NALOG,IPPINT,IMP                                     SLAB    00037    DEACTIVATED
SLAB           1,NALOG,IPPINT,IMP,IPP                                 KOR     00003    ACTIVATED
SLAB            NPAIR=0                                               KOR     00004    ACTIVATED
SLAB            NANNIH=0                                              KOR     00005    ACTIVATED
SLAB            ELOSS=0.                                              KOR     00006    ACTIVATED
SLAB            IF(IPP.NE.0) CALL PAIRCA(I)                           KOR     00007    ACTIVATED
SLAB            IF(IPP.NE.0) WRITE(3,7000) (SIGPP(I),I=1,NMAT)        KOR     00008    ACTIVATED
SLAB       7000 FORMAT(/(7H SIGPP=E12.4))                             KOR     00009    ACTIVATED
SLAB            ELOSS=ELOSS*511.006                                   KOR     00010    ACTIVATED
SLAB            IF(IPP.NE.0) WRITE(3,7001) NPAIR,ELOSS,NANNIH         KOR     00011    ACTIVATED
SLAB       7001 FORMAT(/* NUMBER PAIR PRODUCTION*I10,5X*TOTAL ENERGY LOSS*  KOR     00012    ACTIVATED
SLAB           1,E12.3,5X*ANNIHILATION PHOTONS*,I10)                  KOR     00013    ACTIVATED
SLAB            ELOSS=ELOSS/511.006                                   KOR     00014    ACTIVATED
SLAB            IF(IPP.NE.0) CALL PAIRCA(M)                           KOR     00015    ACTIVATED
SLAB            COMMON/PAIR/AA(8,20),ELOSS,NPAIR,IPP,IPPFL,           KOR     00016    ACTIVATED
SLAB           1SIGPP(20),PAIRA(20),NANNIH                            KOR     00017    ACTIVATED
SLAB            DIMENSION XARRAY(1)                                   KOR     00018    ACTIVATED
SLAB            EQUIVALENCE(X2,XARRAY(1))                             KOR     00019    ACTIVATED
SLAB            ED=E1                                                 KOR     00020    ACTIVATED
SLAB            IF(E1-2.) 218,218,224                                 KOR     00021    ACTIVATED
SLAB        224 IF(IPP) 218,218,220                                   KOR     00022    ACTIVATED
SLAB        220 CALL SPELL1                                           KOR     00023    ACTIVATED
SLAB            IF(SIGPP(M)/SIGT(M)-RAN1) 218,221,221                 KOR     00024    ACTIVATED
SLAB        221 E1=1.                                                 KOR     00025    ACTIVATED
SLAB            IF(E5-E1) 223,23,23                                   KOR     00026    ACTIVATED
SLAB        223 IPPFL=2                                               KOR     00027    ACTIVATED
SLAB            DO 222 I=1,16                                         KOR     00028    ACTIVATED
SLAB        222 PAIRA(I)=XARRAY(I)                                    KOR     00029    ACTIVATED
SLAB            PAIRA(17)=M                                           KOR     00030    ACTIVATED
SLAB            CALL SPELL1                                           KOR     00031    ACTIVATED
SLAB            SCANG=1.-2.*RAN1                                      KOR     00032    ACTIVATED
SLAB            ELOSS=ELOSS+(ED-E1*2)                                 KOR     00033    ACTIVATED
SLAB            NANNIH=NANNIH+1                                       KOR     00034    ACTIVATED
SLAB            NPAIR=NPAIR+1                                         KOR     00035    ACTIVATED
SLAB            RETURN                                                KOR     00036    ACTIVATED
SLAB        218 CONTINUE                                              KOR     00037    ACTIVATED
SLAB            COMMON/PAIR/AA(8,20),ELOSS,NPAIR,IPP,IPPFL,           KOR     00038    ACTIVATED
SLAB           1SIGPP(20),PAIRA(20),NANNIH                            KOR     00039    ACTIVATED
SLAB            RETURN                                                SLAB    00054    DEACTIVATED
SLAB            IF(IPPFL-1) 8,8,9                                     KOR     00040    ACTIVATED
SLAB          9 IPPFL=IPPFL-1                                         KOR     00041    ACTIVATED
SLAB            PAIRA(16)=-GAM2                                       KOR     00042    ACTIVATED
SLAB          8 RETURN                                                KOR     00043    ACTIVATED
SLAB            COMMON/PAIR/AA(8,20),ELOSS,NPAIR,IPP,IPPFL,           KOR     00044    ACTIVATED
SLAB           1SIGPP(20),PAIRA(20),NANNIH                            KOR     00045    ACTIVATED
SLAB            DIMENSION XARRAY(1)                                   KOR     00046    ACTIVATED
SLAB            EQUIVALENCE(X2,XARRAY(1))                             KOR     00047    ACTIVATED
SLAB            IF(IPPFL) 5003,5003,5002                              KOR     00048    ACTIVATED
SLAB       5002 DO 5004 I=1,16                                        KOR     00049    ACTIVATED
SLAB       5004 XARRAY(I)=PAIRA(I)                                    KOR     00050    ACTIVATED
SLAB            M=PAIRA(17)                                           KOR     00051    ACTIVATED
SLAB            NANNIH=NANNIH+1                                       KOR     00052    ACTIVATED
SLAB            IPPFL=IPPFL-1                                         KOR     00053    ACTIVATED
```

```
*WEOR-S, *CALLS-S AND MODIFICATIONS      08/06/70    PAGE     NO.  00007

SLAB          E1=1.                                                        KOR    00054    ACTIVATED
SLAB          RETURN                                                       KOR    00055    ACTIVATED
SLAB     5003 CONTINUE                                                     KOR    00056    ACTIVATED
SLAB          IF(IPP.NE.0) CALL PAIRCA(I)                                  KOR    00057    ACTIVATED
SLAB          COMMON/PAIR/AA(8,20),ELOSS,NPAIR,IPP                         KOR    00058    ACTIVATED
SLAB          IF(IPP.NE.0) CALL PAIRPD(NOMAT)                              KOR    00059    ACTIVATED
SLAB          STAPMT(KK+1,J) = 1.E+10                                      KOR    00060    ACTIVATED
SLAB          SUBROUTINE PAIRPD(NOMAT)                                     KOR    00061    ACTIVATED
SLAB          COMMON/TEMPCO/TEMP(4114),AMT(30,20),NOAT(30)                 KOR    00062    ACTIVATED
SLAB    C THIS SUBROUTINE CALCULATES PAIR PRODUCTION CROSS SECTIONS FROM   KOR    00063    ACTIVATED
SLAB    C COEFFICIENTS STORED ON CROSS SECTION DATA TAPE                   KOR    00064    ACTIVATED
SLAB          COMMON/TRANS/UMU,UMUPE,UMUAB,EP,NL                           KOR    00065    ACTIVATED
SLAB          COMMON/1/B(8,20)                                             KOR    00066    ACTIVATED
SLAB          COMMON/PAIR/AA(8,20),ELOSS,NPAIR,IPP,IPPFL,                  KOR    00067    ACTIVATED
SLAB         1SIGPP(20),PAIRA(20),NANNIH                                   KOR    00068    ACTIVATED
SLAB    C READ COEFFICIENTS FROM DATA TAPE                                 KOR    00069    ACTIVATED
SLAB          DATA(NAME1=8HPAIR PRO)                                       KOR    00070    ACTIVATED
SLAB          REWIND 4                                                     KOR    00071    ACTIVATED
SLAB    1     READ (4,2) NAME                                              KOR    00072    ACTIVATED
SLAB    2     FORMAT (A8)                                                  KOR    00073    ACTIVATED
SLAB          IF (NAME.NE.NAME1) GO TO 1                                   KOR    00074    ACTIVATED
SLAB          DO 7 J=1,NL                                                  KOR    00075    ACTIVATED
SLAB        3 READ(4,4) NO,(B(I,J),I=1,7)                                  KOR    00076    ACTIVATED
SLAB    4     FORMAT (I3,7E11.3)                                           KOR    00077    ACTIVATED
SLAB          READ(4,5) B(8,J)                                             KOR    00078    ACTIVATED
SLAB    5     FORMAT (E10.3)                                               KOR    00079    ACTIVATED
SLAB          IF (NO-NOAT(J)) 3,7,6                                        KOR    00080    ACTIVATED
SLAB    6     REWIND 4                                                     KOR    00081    ACTIVATED
SLAB          GO TO 1                                                      KOR    00082    ACTIVATED
SLAB    7     CONTINUE                                                     KOR    00083    ACTIVATED
SLAB          DO 20 I=1,8                                                  KOR    00084    ACTIVATED
SLAB          DO 20 J=1,20                                                 KOR    00085    ACTIVATED
SLAB       20 AA(I,J)=0                                                    KOR    00086    ACTIVATED
SLAB          DO 25 I=1,NL                                                 KOR    00087    ACTIVATED
SLAB          DO 25 J=1,NOMAT                                              KOR    00088    ACTIVATED
SLAB          DO 25 K=1,8                                                  KOR    00089    ACTIVATED
SLAB       25 AA(I,K)=AA(I,K)+AMT(J,I)*B(K,J)                              KOR    00090    ACTIVATED
SLAB          RETURN                                                       KOR    00091    ACTIVATED
SLAB    C CALCULATE PAIR PRODUCTION CROSS SECTION                          KOR    00092    ACTIVATED
SLAB          ENTRY PAIRCA                                                 KOR    00093    ACTIVATED
SLAB          FAC=(EP-1022.012)                                            KOR    00094    ACTIVATED
SLAB          IF (FAC) 8,10,10                                             KOR    00095    ACTIVATED
SLAB    8     UPP=0                                                        KOR    00096    ACTIVATED
SLAB        9 SIGPP(NL)=UPP                                                KOR    00097    ACTIVATED
SLAB          RETURN                                                       KOR    00098    ACTIVATED
SLAB    10    IF (EP-1500.) 11,11,12                                       KOR    00099    ACTIVATED
SLAB       11 UPP = AA(NL,8)*FAC**2                                        KOR    00100    ACTIVATED
SLAB          GO TO 9                                                      KOR    00101    ACTIVATED
SLAB    12    UPP=0                                                        KOR    00102    ACTIVATED
SLAB          FAC=SQRTF(FAC)                                               KOR    00103    ACTIVATED
SLAB          DO 13 I=1,7                                                  KOR    00104    ACTIVATED
SLAB       13 UPP = UPP + AA(NL,I)*FAC**I                                  KOR    00105    ACTIVATED
SLAB          UPP=UPP/(1.+1.7E-13*FAC**6)                                  KOR    00106    ACTIVATED
SLAB          GO TO 9                                                      KOR    00107    ACTIVATED
SLAB          END                                                          KOR    00108    ACTIVATED
SLAB    *WEOR                                                              SLAB   01365
```

L. DTF PROGRAM

The discrete ordinates program used in this dissertation (called DTF-69) is based on work by J. H. Renken and K. G. Adams (63) of Sandia Corporation. The program, as written, is actually two programs, a cross-section generating program (GAMLEG 69) and the photon transport program (DTF-69). The program allows a very wide range of inputs, covering any Z material and various spectra to 15 MeV, but is one dimension limited. Fluorescence, Compton scattering, and pair-production are each calculated.

The program was designed primarily for use in energy deposition and energy passage calculation. Differentiation into energy spectra and emergent angle is somewhat more complicated. DTF results in this mode often show a disturbing tendency to oscillate.

Due to the wealth of output available from DTF, transfer from the energy given to the dose desired for comparison to TLD data was unwieldy. The author is much indebted to Joann H. Flinchum of Sandia Corporation for an update to the DTF program which calculates dose in addition to the energy outputs.

The update to the DTF program (63) used in this work follows and puts DTF in a form much more useful to the health physicist interested in shielding calculations. From an input consisting primarily of the shielding material and source to be shielded, one may obtain the dose transmitted or reflected through any thickness.

The major advantage DTF holds over Monte Carlo programs is a great computer time saving. A half-hour program in Monte Carlo takes less than five minutes with DTF.

The following program is written for the CDC 6600 computer.

```
*IDENT KOR
*DELETE,UTF.342
     $FLUX),A(JXCD),A(JFLIN),A(JCK),JHM,JHM1,A(JIQB),A(JIQM1),A(JVL))
*DELETE,UTF.390
     3EDXIT,CC,JHM,JHM1,ANGFLO,ANGFTO,GB)
*DELETE,UTF.379
     COMMON/ZALL/MTAPE,NTAPE
*INSERT,UTF.389
     1,GB(1),TEMP(50),AA3B(100),S(75,50),SNU(21),SES(21)
*INSERT,UTF.398
     IF(IGC.EQ.0)READ(NTAPE,125)(AA3B(IW),IW=1,IGM)
 125 FORMAT(6E12.4)
     DO 126 IV = 1,IP
     DO 126 IW = 1,MM
 126 S(IV,IW)=0.
*INSERT,UTF.544
     S1=S2=0.
     IF(IGC.EQ.0) GO TO 131
     GO TO 132
 131 DO 133 IW = 1,MM
 133 SNU(IW)=SES(IW)=0.
132  CONTINUE
*DELETE,UTF.620
     I=IP
*INSERT,UTF.624
     TGB=(GB(IG)+GB(IG+1))/2.
     WRITE(MTAPE,110)
  110 FORMAT(1H0,11HENERGY FLUX)
     DO 111 I = 1,MM
     SNU(I)=SNU(I) + XNU(IP,I)
     TEMP(I)=XNU(IP,I) * TGB
 111 SES(I)=SES(I) + TEMP(I)
     WRITE(MTAPE,112)(TEMP(I),I=1,MM)
 112 FORMAT(8E15.6)
     S2=S2+TEMP(1)
     DO 114 I = 1,IP
     DO 115 M = 1,MM
     XNU(I,M)=XNU(I,M)*TGB*AA3B(IG)
 115  S(I,M) = S(I,M) + XNU(I,M)
 114 CONTINUE
     WRITE(MTAPE,116)
 116 FORMAT(1H0,4HDOSE//)
     DO 117 I = 1,IP
 117 WRITE(MTAPE,50)I,RA(I),(XNU(I,M),M=1,MM)
 118 FORMAT(1H0,12H NUMBER SUMS)
 130 FORMAT(1H0,12H ENERGY SUMS)
*DELETE,UTF.555
 60  WRITE(MTAPE,118)
     WRITE(MTAPE,112)(SNU(IW),IW=1,MM)
     WRITE(MTAPE,130)
     WRITE(MTAPE,112)(SES(IW),IW=1,MM)
     WRITE(MTAPE,127)
 127 FORMAT(*   DOSE SUMS*/)
     DO 128 IV = 1,IP
 128  WRITE(MTAPE,50)IV,RA(IV),(S(IV,IW),IW=1,MM)
     WRITE(MTAPE,119)
```

```
119  FORMAT(1H0,2H G,22H  INCIDENT ENERGY FLUX,5X,26HINCIDENT ENERGY DO
    1SE/)
     S1=S2=0.
     DO 120 I = 1,IGM
     TGM=(GM(I)+GM(I+1))/2.
     T1=FLUX(I)*TGM
     T2=T1 * AABS(I)
     S1 = S1 + T1
     S2 = S2 + T2
120  WRITE(MTAPE,121)I,T1,T2
121  FORMAT(I3,E18.6,E25.6)
     WRITE(MTAPE,122) S1,S2
122  FORMAT(1H0,2X,E18.6,E25.6)
     IF(JMM-IMM)61,62,61
*COMPILE DIF
```

```
DIF         SFLUX),A(JVSG),A(JFLIN),A(JSK),JMM,JMM1,A(JIGB),A(JIGB1))            DIF   00342  DEACTIVATED
DIF         SFLUX),A(JVSG),A(JFLIN),A(JSK),JM4,JMM1,A(JIGB),A(JIGB1),A(JVL))     KOR   00001  ACTIVATED
DIF         3LJXIN,SG,JMM,JMM1,ANGFLO,ANGFTO)                                    DIF   00355  DEACTIVATED
DIF         3LJXIN,SG,JMM,JMM1,ANGFLO,ANGFTO,G3)                                 KOR   00002  ACTIVATED
DIF          COMMON/ALL/MTAPE                                                    DIF   00370  DEACTIVATED
DIF          COMMON/ALL/MTAPE,NTAPE                                              KOR   00003  ACTIVATED
DIF         1,GB(1),TEMP(50),AABB(100),S(75,50),SNU(21),SES(21)                  KOR   00004  ACTIVATED
DIF          IF(ICS.EQ.0)READ(NTAPE,125)(AABB(IW),IW=1,IGM)                      KOR   00005  ACTIVATED
DIF     125  FORMAT(6E12.4)                                                      KOR   00006  ACTIVATED
DIF          DO 126 IV = 1,IP                                                    KOR   00007  ACTIVATED
DIF          DO 126 IW = 1,MM                                                    KOR   00008  ACTIVATED
DIF     126  S(IV,IW)=0.                                                         KOR   00009  ACTIVATED
DIF          S1=S2=0.                                                            KOR   00010  ACTIVATED
DIF          IF(ICS.EQ.0) GO TO 131                                              KOR   00011  ACTIVATED
DIF          GO TO 132                                                           KOR   00012  ACTIVATED
DIF     131  DO 133 IW = 1,MM                                                    KOR   00013  ACTIVATED
DIF     133  SNU(IW)=SES(IW)=0.                                                  KOR   00014  ACTIVATED
DIF     132  CONTINUE                                                            KOR   00015  ACTIVATED
DIF     60   IF (J-M-IHM) 61,62,61                                               DIF   00555  DEACTIVATED
DIF     60   WRITE(MTAPE,111)                                                    KOR   00016  ACTIVATED
DIF          WRITE(MTAPE,112)(SNU(IW),IW=1,MM)                                   KOR   00017  ACTIVATED
DIF          WRITE(MTAPE,133)                                                    KOR   00018  ACTIVATED
DIF          WRITE(MTAPE,112)(SES(IW),IW=1,MM)                                   KOR   00019  ACTIVATED
DIF          WRITE(MTAPE,127)                                                    KOR   00020  ACTIVATED
DIF     127  FORMAT(*    DOSE SUMS*/)                                            KOR   00021  ACTIVATED
DIF          DO 128 IV = 1,IP                                                    KOR   00022  ACTIVATED
DIF     128   WRITE(MTAPE,60)IV,RA(IV),(S(IV,IW),IW=1,MM)                        KOR   00023  ACTIVATED
DIF          WRITE(MTAPE,119)                                                    KOR   00024  ACTIVATED
DIF     119  FORMAT(1H0,2H G,22H  INCIDENT ENERGY FLUX,5X,20HINCIDENT ENERGY DO  KOR   00025  ACTIVATED
DIF         1SE/)                                                                KOR   00026  ACTIVATED
DIF          S1=S2=0.                                                            KOR   00027  ACTIVATED
DIF          DO 120 I = 1,IGM                                                    KOR   00028  ACTIVATED
DIF          TGB=(GB(I)+GB(I+1))/2.                                              KOR   00029  ACTIVATED
DIF          T1=FLUX(I)*TGB                                                      KOR   00030  ACTIVATED
DIF          T2=T1 * AABB(I)                                                     KOR   00031  ACTIVATED
DIF          S1 = S1 + T1                                                        KOR   00032  ACTIVATED
DIF          S2 = S2 + T2                                                        KOR   00033  ACTIVATED
DIF     120  WRITE(MTAPE,121)I,T1,T2                                             KOR   00034  ACTIVATED
DIF     121  FORMAT(I3,E16.6,E25.6)                                              KOR   00035  ACTIVATED
DIF          WRITE(MTAPE,122) S1,S2                                              KOR   00036  ACTIVATED
DIF     122  FORMAT(1H0,2X,E16.6,E25.6)                                          KOR   00037  ACTIVATED
DIF          IF(J-M-IHM)61,62,61                                                 KOR   00038  ACTIVATED
DIF          DO 75 I=1,IP                                                        DIF   00620  DEACTIVATED
DIF          I=IP                                                                KOR   00039  ACTIVATED
DIF          TGB=(GB(IG)+GB(IG+1))/2.                                            KOR   00040  ACTIVATED
DIF          WRITE(MTAPE,110)                                                    KOR   00041  ACTIVATED
DIF      110 FORMAT(1H0,11HENERGY FLUX)                                          KOR   00042  ACTIVATED
DIF          DO 111 I = 1,MM                                                     KOR   00043  ACTIVATED
DIF          SNU(I)=SNU(I) + XNU(IP,I)                                           KOR   00044  ACTIVATED
DIF          TEMP(I)=XNU(IP,I) * TGB                                             KOR   00045  ACTIVATED
DIF     111  SES(I)=SES(I) + TEMP(I)                                             KOR   00046  ACTIVATED
DIF          WRITE(MTAPE,112)(TEMP(I),I=1,MM)                                    KOR   00047  ACTIVATED
DIF     112  FORMAT(8E15.6)                                                      KOR   00048  ACTIVATED
DIF          S2=S2+TEMP(1)                                                       KOR   00049  ACTIVATED
DIF          DO 114 I = 1,IP                                                     KOR   00050  ACTIVATED
```

```
DTF        DO 115 M = 1,MM                               KOR   00051   ACTIVATED
DTF        XND(I,M)=XND(I,M)*TGB*AABB(IG)                KOR   00052   ACTIVATED
DTF   115   S(I,M) = S(I,M) + XND(I,M)                   KOR   00053   ACTIVATED
DTF   114  CONTINUE                                      KOR   00054   ACTIVATED
DTF        WRITE(MTAPE,116)                              KOR   00055   ACTIVATED
DTF   116  FORMAT(1H0,4HDOSE//)                          KOR   00056   ACTIVATED
DTF        DO 117 I = 1,IP                               KOR   00057   ACTIVATED
DTF   117  WRITE(MTAPE,60)I,RA(I),(XND(I,M),M=1,MM)      KOR   00058   ACTIVATED
DTF   115  FORMAT(1H0,12H NUMBER SUMS)                   KOR   00059   ACTIVATED
DTF   130  FORMAT(1H0,12H ENERGY SUMS)                   KOR   00060   ACTIVATED
```

M. A COMPARISON OF MONTE CARLO AND DTF TO PREVIOUSLY PUBLISHED EXPERIMENTAL RESULTS

Due to the less than perfect fit of the experimental data of this dissertation to the computer runs, a few runs were made to examine the closeness of fit with experimental data of other researchers.

Figures 88 and 89 are plots of DTF and Monte Carlo results compared to results of two experimenters who used NaI scintillators in their albedo measurements. Figure 88 shows the results for an incident energy of 0.662 MeV and a lead reflector. Figure 89 is for 1.33 and 1.17 MeV reflected from iron. The experimental design of the two experimenters differs somewhat and is discussed in detail in Section 2. The design of Steyn closely resembles that of the present research.

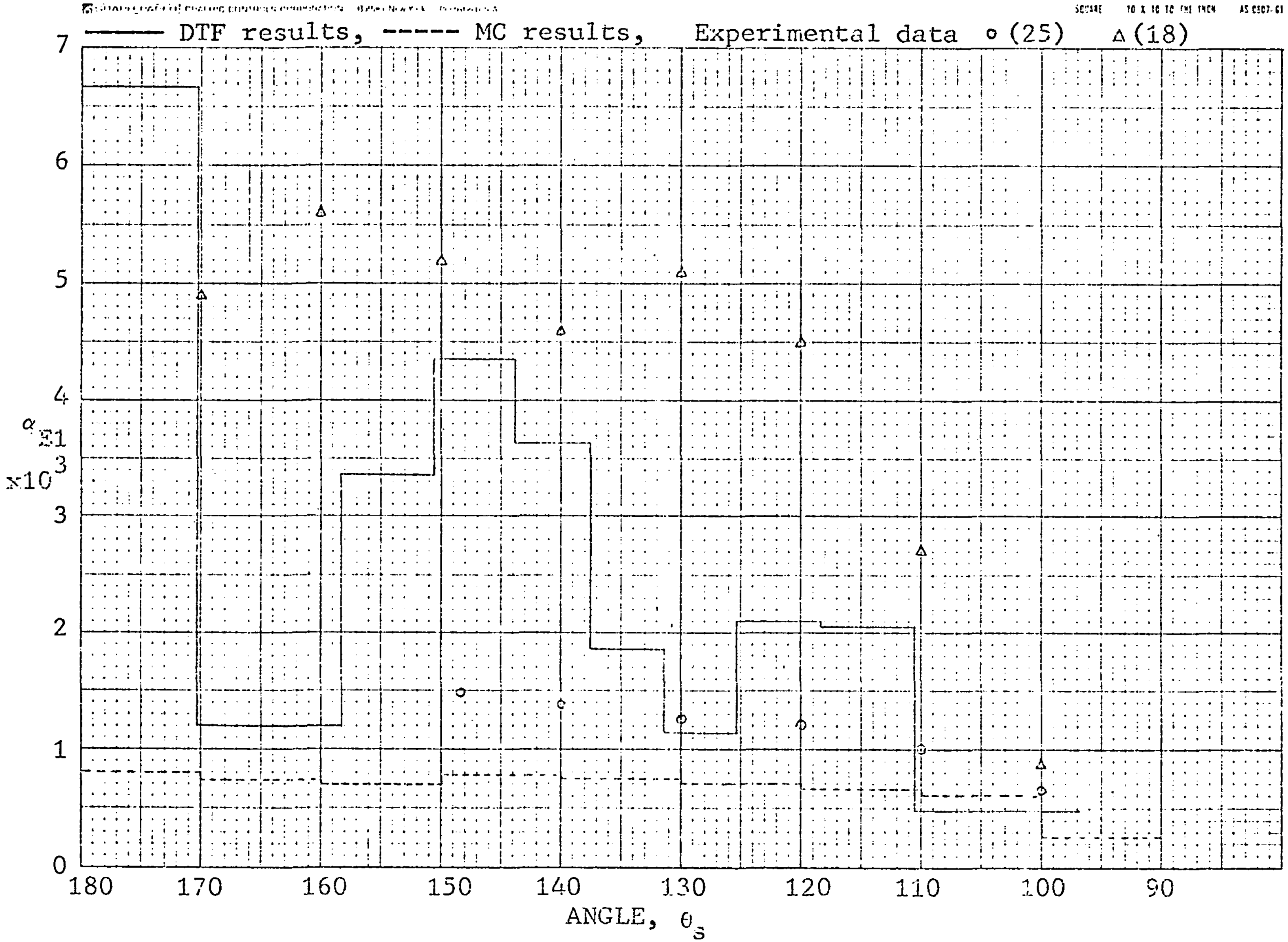

Figure 88 α_{E1} vs Angle for Cs-137 lead scatterer

Figure 89 α_{E1} vs Angle for Co-60, iron scatterer

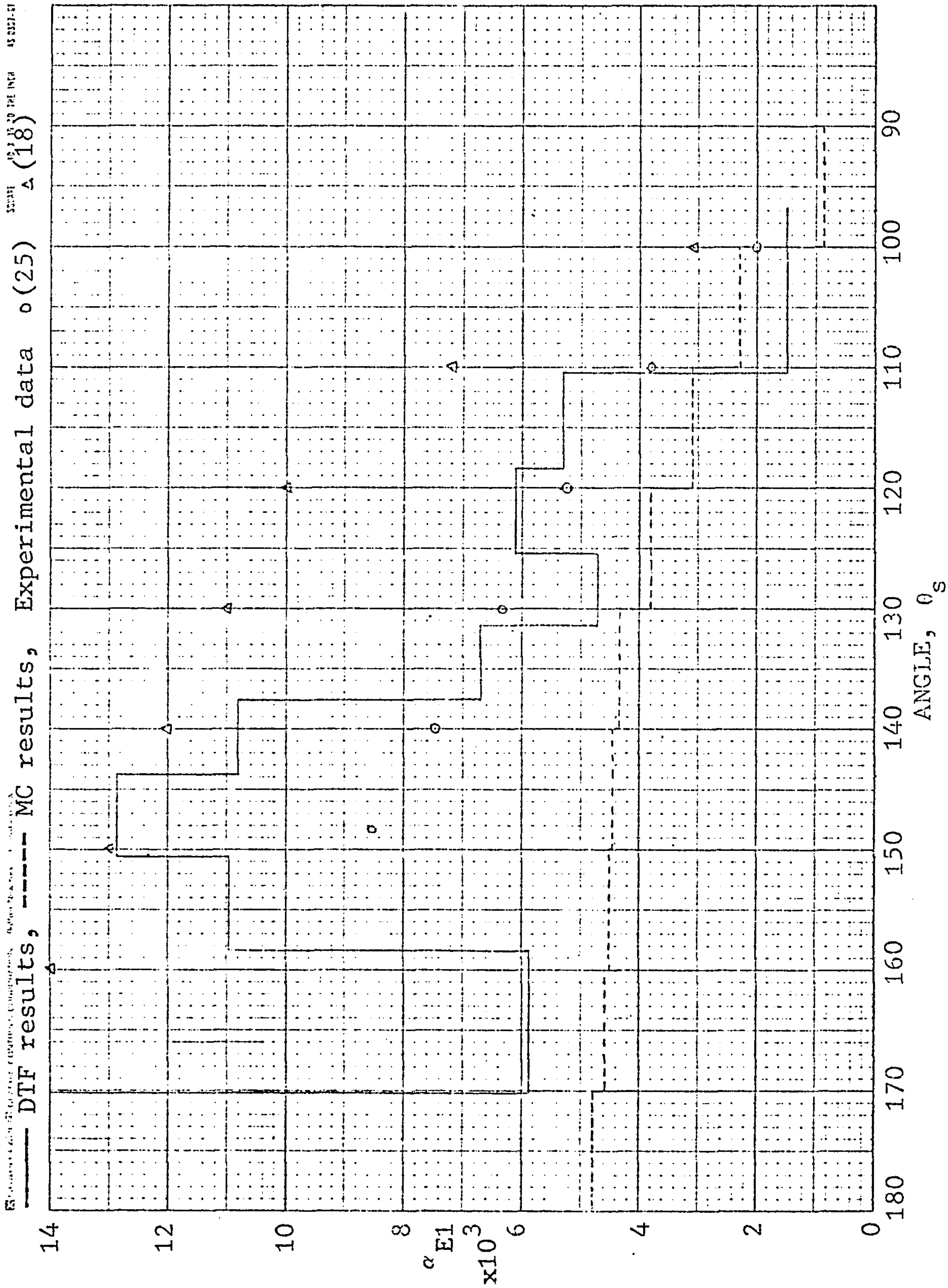

N. RESULTS OF THE CHILTON-HUDDLESTON EQUATIONS APPLIED TO THE "EFFECTIVE" ENERGIES OF THE PRESENT WORK

The Chilton-Huddleston formulation is discussed in Section 4. The formula, as given there, is:

$$a_D = \frac{C\ K(\theta_s)\ 10^{26} + C'}{1 + \cos\theta_o \sec\theta} \qquad \text{Eq. N.1}$$

Values for C and C' have been published for 0.2, 0.66, 1.0, 2.5, and 6.13 MeV. To obtain values for the energies of this work, Figures 90, 91, and 92 were made. Table 18 notes the values of C and C' used for the calculations made in this appendix. $K(\theta_s)\ 10^{26}$ was calculated as indicated in reference 11 and values are tabulated in Table 19. Results of Eq. N.1 are tabulated in Table 20 and plotted with the experimental and computer results in Section 6.

Figure 90 Lead C and C' vs Energy

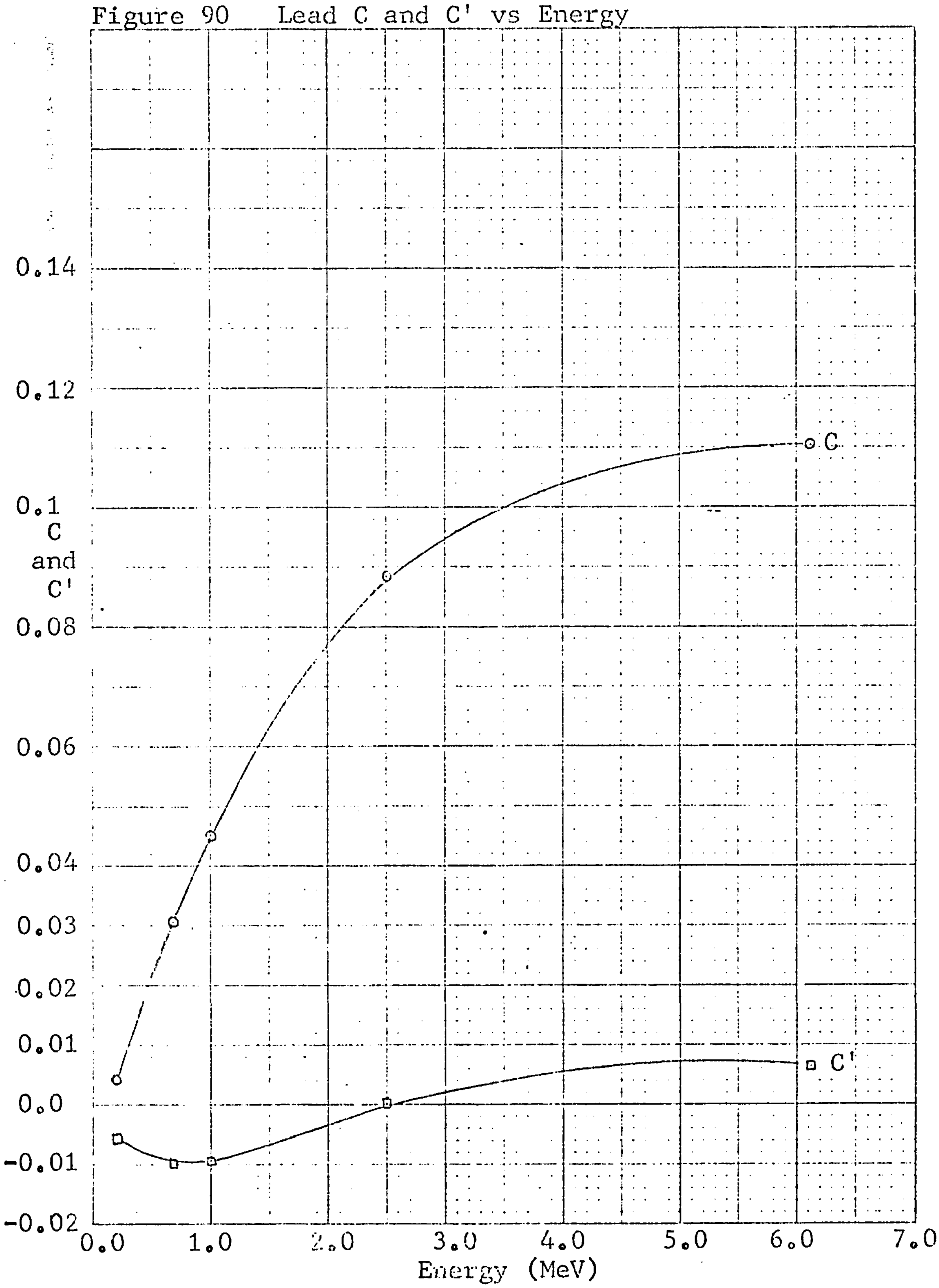

Figure 91 Iron C and C' vs Energy

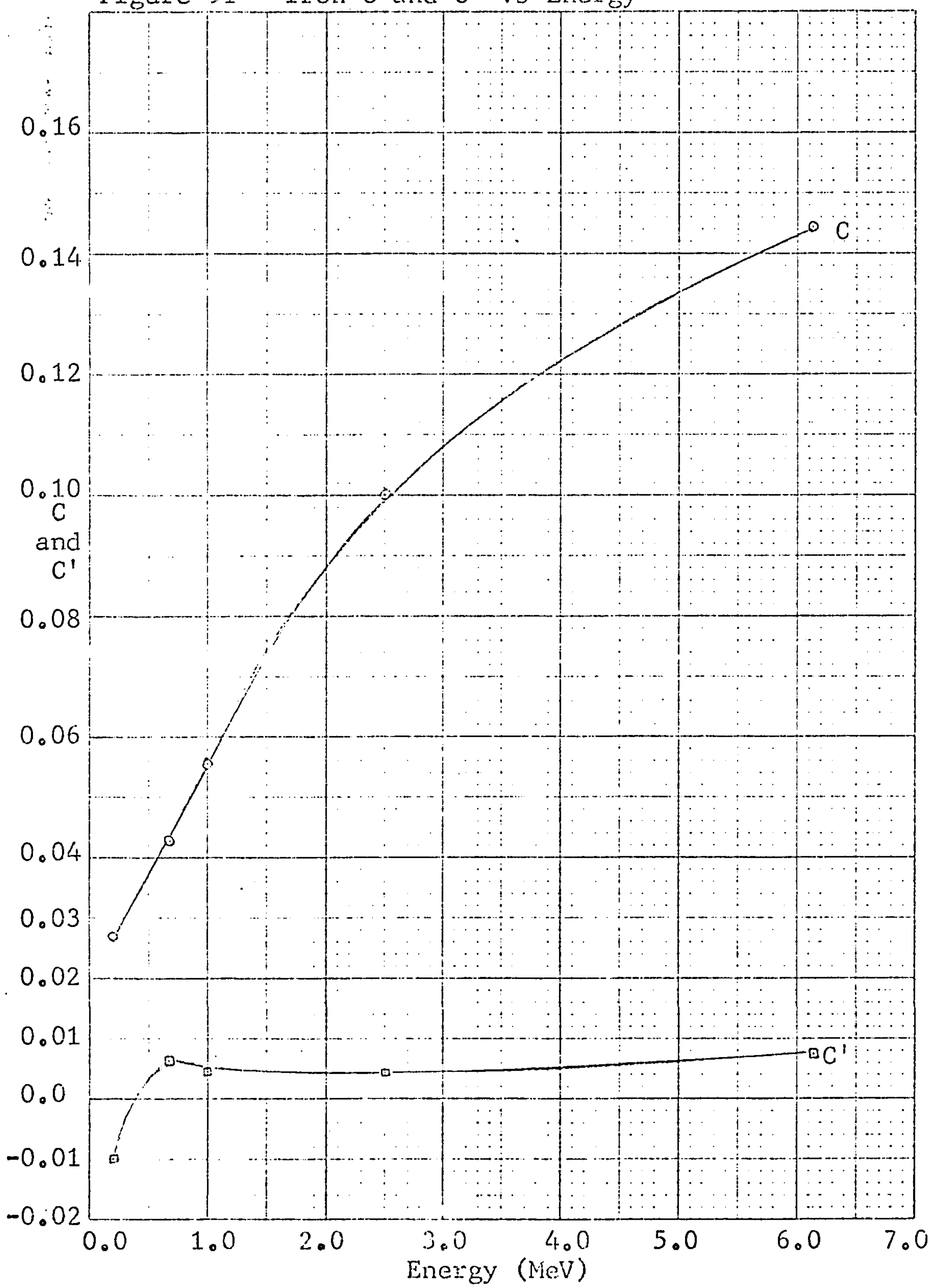

Figure 92 Concrete C and C' vs Energy

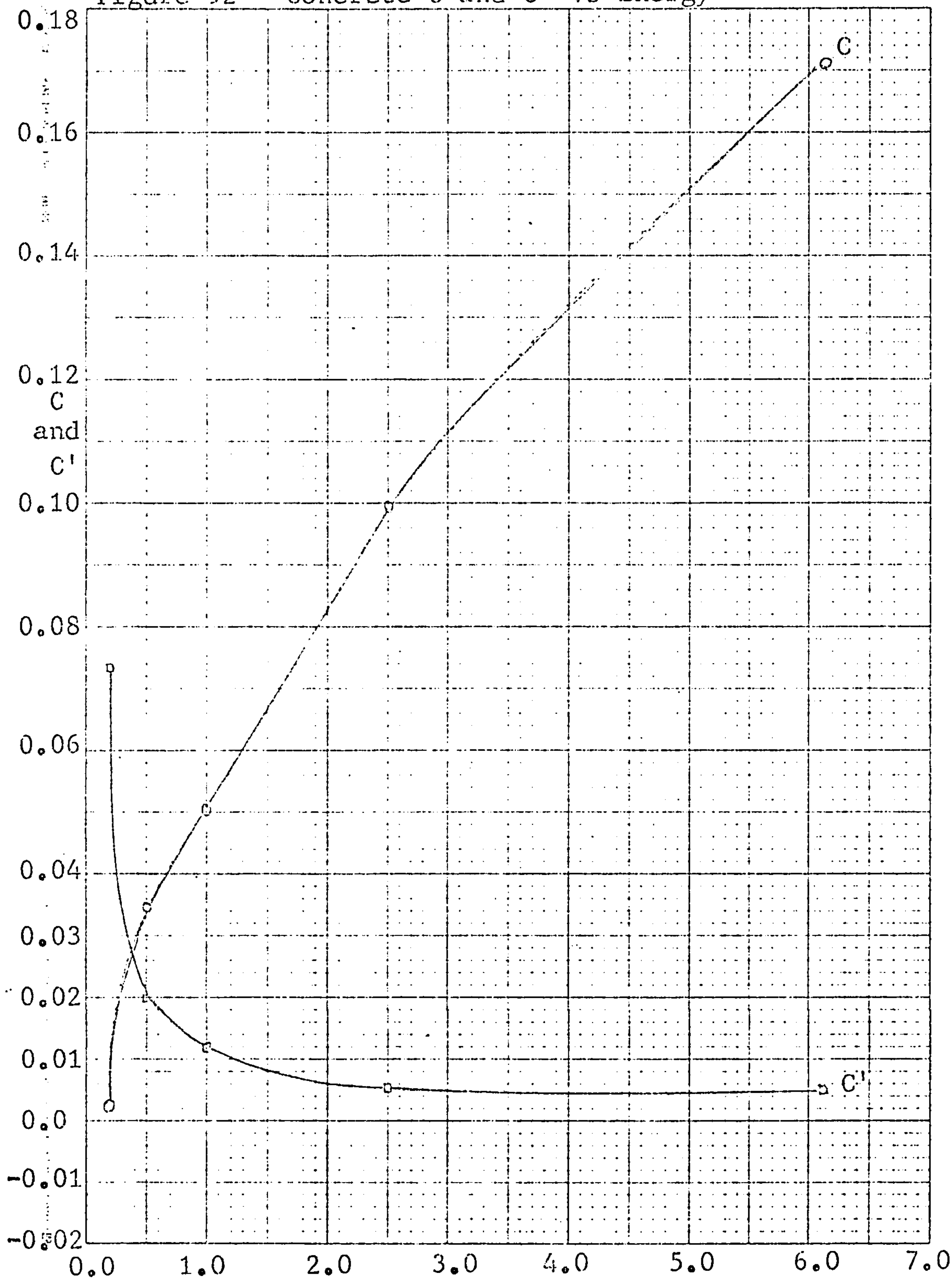

TABLE 18

CHILTON-HUDDLESTON PARAMETERS

EFFECTIVE ENERGY (MeV)	BACKSCATTER MATERIAL	C	C'
0.24	Lead	0.0062	-0.0055
	Iron	0.0281	-0.008
	Concrete	0.016	0.051
0.28	Lead	0.010	-0.0061
	Iron	0.0298	-0.006
	Concrete	0.020	0.038
0.85	Lead	0.039	-0.0095
	Iron	0.050	0.0052
	Concrete	0.0453	0.0137
1.34	Lead	0.0563	-0.0074
	Iron	0.0666	0.004
	Concrete	0.0612	0.009
4.1	Lead	0.1059	0.005
	Iron	0.1302	0.0059
	Concrete	0.132	0.0051

TABLE 19

KLEIN-NISHINA CROSS-SECTIONS

EFFECTIVE ENERGY (MeV)	SCATTERING ANGLE	$\frac{K(\theta_s)\ 10^{26}}{d\Omega}$
0.24	120°	1.2977
	135°	1.2604
	150°	1.2357
0.28	120°	1.0880
	135°	1.0692
	150°	1.0641
0.85	120°	0.2819
	135°	0.2525
	150°	0.2354
1.34	120°	0.14339
	135°	0.1232
	150°	0.1114
4.1	120°	0.02216
	135°	0.01784
	150°	0.01538

TABLE 20

CHILTON-HUDDLESTON ALBEDO VALUES

EFFECTIVE ENERGY (MeV)	BACKSCATTER MATERIAL	SCATTERING ANGLE	$a_D \times 10^3$
0.24	Lead	120°	1.18
		135°	0.959
		150°	0.720
	Iron	120°	13.21
		135°	11.36
		150°	8.91
	Concrete	120°	33.31
		135°	29.48
		150°	23.59
0.28	Lead	120°	2.22
		135°	1.90
		150°	1.51
	Iron	120°	12.26
		135°	10.71
		150°	8.57
	Concrete	120°	27.73
		135°	24.60
		150°	19.76
0.85	Lead	120°	0.693
		135°	0.144
		150°	Negative
	Iron	120°	8.95
		135°	7.38
		150°	5.66
	Concrete	120°	12.28
		135°	10.41
		150°	8.12

TABLE 20 (cont'd)

EFFECTIVE ENERGY (MeV)	BACKSCATTER MATERIAL	SCATTERING ANGLE	$\alpha_D \times 10^3$
1.34	Lead	120°	0.312
		135°	Negative
		150°	Negative
	Iron	120°	6.29
		135°	5.06
		150°	3.81
	Concrete	120°	8.25
		135°	6.85
		150°	5.27
4.1	Lead	120°	3.72
		135°	3.09
		150°	2.38
	Iron	120°	4.00
		135°	3.41
		150°	2.42

O. 20 - 60 MeV BACKSCATTER

A few preliminary measurements were made with a medical Synchrotron unit. The maximum bremsstrahlung edge was adjustable from 20 to 60 MeV. A thick target, thin window arrangement was used with standard Schiff spectra expected.

The experimental set-up was similar to that discussed in Section 5, but the detectors were essentially uncollimated and the incident beam restricted to four square inches at the backscatter slab. Slabs of lead and concrete were used. The concrete was built up of light weight cinder block and thus those results are not comparable to the rest of this dissertation. That data is not presented. Results with lead at 20, 40, and 60 MeV follow.

Due to the experimental configuration chosen, backgrounds were much higher, resulting in greater error limits for the data. One standard deviation for the data presented here varies from 10 to 20% on the TLD measurements. Results presented here are not directly comparable to other results of the dissertation due to the narrow beam arrangement used, but are presented here for possible comparison elsewhere. Because of the nature of Schiff spectra at low (<250 KeV) energies, no dose absorption corrections are made for $\alpha_{(slab)}$ calculations. The results presented in Table 21 are differential dose flux albedo, $\alpha_{D3(H_2O)}$ as discussed in Section 6, for the specific experimental configuration considered here.

The results appear to be a bit lower than those of Table 3, but are similarly grouped, despite the change in E_{max}.

TABLE 21

DIFFERENTIAL DOSE FLUX ALBEDO

BACKSCATTER ANGLE LEAD SCATTERER

20.0 MeV Incident Spectra Bremsstrahlung Maximum

θ_s	$^{a}D3(H_2O) \times 10^3$
157.5°	9.56
135.0°	7.70
112.5°	5.12

40.0 MeV Incident Spectra Bremsstrahlung Maximum

θ_s	$^{a}D3(H_2O) \times 10^3$
157.5°	9.44
135.0°	6.17
112.5°	3.00

60.0 MeV Incident Spectra Bremsstrahlung Maximum

θ_s	$^{a}D3(H_2O) \times 10^3$
157.5°	13.84
135.0°	10.80
112.5°	4.93